INAUGURAL - DISSERTATION
Zur
Erlangung der Doktorwürde
der
Gesamtfakultät für Mathematik,
Ingenieur- und Naturwissenschaften
der
Ruprecht-Karls-Universität
Heidelberg

Vorgelegt von
Kölsch-Kurtz, Leonard, MSc.

Tag der mündlichen Prüfung: 27.11.2025

Thema

Hydrology Of a Densely Forested Area Under Climate Change - Multi Model Approach

Gutachter: Prof. Dr. Lucas Menzel
Prof. Dr. James Craig

Acknowledgements

I would like to express my sincere gratitude to **Prof. Dr. Lucas Menzel** (University of Heidelberg) for his supervision, the provision of essential data, and many insightful and in-depth discussions throughout the course of this work.

I also thank **Prof. Dr. James Craig** (University of Waterloo) for his valuable supervision, as well as for insightful discussions and information regarding the Raven model.

My special thanks go to my colleague **Dr. Lea Bussière** for her continuous support and for always pushing me forward with motivation and encouragement.

I am also grateful to my colleagues **Menghao Wang, Li Han, Jianfeng Luo, Guyen Battuvshin,** and **Ying Yi** for the helpful discussions and their openness throughout this journey.

Lastly, I thank my wife, **Verena Magdalena Kölsch**, for her unwavering daily motivation and support.

Contents

Tables

Figures

Abstract

To improve understanding of how climate change affects forested catchment hydrology through interactions between climate, vegetation, and water balance processes, this dissertation investigates historical and projected hydrological dynamics in the Eyach catchment, a 52 km² forested watershed in Germany's northern Black Forest.

A comprehensive multi-model approach is applied using four hydrological models—TRAIN, HBV-Light, LWF-Brook90, and Raven-HMETS—to simulate key components of the water cycle including evapotranspiration, soil moisture, streamflow, and snow cover duration. The analysis spans the period 1975–2050, combining a historical climate and hydrology assessment (1975–2019) with future projections (2020–2050) under RCP 2.6, 4.5, and 8.5 climate scenarios. Historical climate data reveal statistically significant warming and rising solar radiation, while precipitation trends remain non-significant. These atmospheric shifts are reflected in the hydrological simulations: evapotranspiration and soil moisture show strong interannual variability, but clear long-term drying signals are found in soil moisture.

A multi-model ensemble represents structural diversity across hydrological process models. TRAIN delivers high-resolution evapotranspiration and soil moisture simulations; HBV-Light provides robust discharge estimates; LWF-Brook90 allows species-specific representation of canopy fluxes and soil processes; and Raven-HMETS best captures interannual variability in snow cover dynamics, though it tends to underestimate total snow duration.

Model evaluation against observational and satellite-based datasets—including GLEAM, ERA5 and snow cover records—demonstrates that each model performs differently depending on process and variable. TRAIN exhibits the most balanced performance in simulating snow cover duration, with the lowest root mean square error and minimal bias. Raven-HMETS, while underestimating absolute snow duration, achieves the highest correlation with observed interannual variability—highlighting how structural features such as refreezing algorithms and spatial discretization influence snow dynamics across models.

Species-specific simulations using LWF-Brook90 reveal clear hydrological differences between Norway spruce (*Picea abies*), European beech (*Fagus sylvatica*), and oak (*Quercus robur*). Deciduous species consistently show lower evapotranspiration and higher soil moisture retention than evergreen conifers under identical conditions, highlighting the role of forest composition in drought resilience and water availability.

Future scenario analyses indicate that under high-emission conditions (RCP 8.5), evapotranspiration increases modestly but begins to plateau, while soil moisture declines significantly due to enhanced atmospheric demand and warming-induced limitations on water availability. While Evapotranspiration projections from TRAIN and LWF-Brook90 converge, their soil moisture outputs diverge—emphasizing the importance of internal model structure in shaping subsurface hydrological sensitivity.

Overall, this study fulfils six integrated objectives: from historical trend analysis to multi-model evaluation, species-specific simulation, and scenario-based forecasting. The findings underscore the dual importance of climatic drivers and vegetation composition in shaping catchment hydrology. The integrative approach—including model validation, species comparisons, and scenario simulations—provides a robust foundation for understanding and managing water dynamics in temperate forested regions under climate change.

Zusammenfassung

Zur besseren Verständigung der Auswirkungen des Klimawandels auf die Hydrologie bewaldeter Einzugsgebiete – insbesondere durch das Zusammenspiel von Klima, Vegetation und Wasserhaushaltsprozessen – untersucht diese Dissertation die historischen und zukünftigen hydrologischen Dynamiken im Eyach-Einzugsgebiet, einem 52 km² großen, waldreichen Gebiet im nördlichen Schwarzwald.

Ein Multi-Modell-Ansatz mit vier hydrologischen Modellen – TRAIN, HBV-Light, LWF-Brook90 und Raven-HMETS – wird angewandt, um zentrale Wasserhaushaltsgrößen wie Evapotranspiration, Bodenfeuchte, Abfluss und Schneebedeckungsdauer zu simulieren. Die Analyse umfasst den Zeitraum 1975–2050 und verbindet eine historische Bewertung (1975–2019) mit Projektionen bis 2050 unter den Szenarien RCP 2.6, 4.5 und 8.5. Die Klimadaten zeigen signifikante Erwärmung und steigende Globalstrahlung, während sich bei Niederschlägen keine robusten Trends erkennen lassen. Diese Entwicklungen spiegeln sich in den Simulationen wider: Evapotranspiration und Bodenfeuchte zeigen hohe Variabilität, während insbesondere Bodenfeuchte klare langfristige Rückgänge aufweist.

Die Modelle unterscheiden sich strukturell und funktional: TRAIN liefert hochaufgelöste Ergebnisse für Evapotranspiration und Bodenfeuchte, HBV-Light bietet zuverlässige Abflussabschätzungen, LWF-Brook90 ermöglicht artenspezifische Simulationen von Kronen- und Bodenprozessen, und Raven-HMETS bildet die interannuelle Variabilität der Schneedecke am besten ab – unterschätzt jedoch deren Gesamtdauer.

Die Validierung mit Beobachtungs- und Fernerkundungsdaten – darunter GLEAM, ERA5 und langjährige Schneereihen – zeigt: Jedes Modell hat prozessspezifische Stärken. TRAIN simuliert die Schneebedeckungsdauer am präzisesten (geringster RMSE, geringer Bias), während Raven-HMETS die zeitliche Dynamik am besten trifft (höchste Korrelation). Unterschiede bei Refreezing, Energiehaushalt und räumlicher Auflösung prägen die Modellgüte.

Artenspezifische Simulationen mit LWF-Brook90 zeigen deutliche Unterschiede zwischen Fichte (*Picea abies*), Buche (*Fagus sylvatica*) und Eiche (*Quercus robur*). Laubbaumarten zeigen durchweg geringere Evapotranspiration und höhere Bodenfeuchte als Nadelbäume unter gleichen Bedingungen – was auf eine größere Resilienz gegenüber Dürre hindeutet.

Zukunftsszenarien unter RCP 8.5 zeigen: Evapotranspiration steigt nur moderat und erreicht ein Plateau, während die Bodenfeuchte durch steigende atmosphärische Nachfrage und Wasserverfügbarkeitsgrenzen deutlich sinkt. Während sich ETA-Projektionen von TRAIN und LWF-Brook90 ähneln, divergieren deren Bodenfeuchteverläufe – ein Hinweis auf strukturelle Unterschiede in der Submodellierung.

Die Arbeit erfüllt sechs übergreifende Ziele – von der Trendanalyse über Multi-Modell-Vergleiche bis zur szenarienbasierten und artenspezifischen Modellierung. Die Ergebnisse verdeutlichen die kombinierte Bedeutung klimatischer Steuerung und Vegetationsstruktur für die Wasserhaushaltsdynamik bewaldeter Einzugsgebiete und liefern eine belastbare Grundlage für das Management unter sich wandelnden Klimabedingungen.

Chapter 1

1. Introduction

1.1 Background

Forests play a crucial role in regulating water availability, and any shifts in the water balance due to climate change could have significant implications for water resources, ecosystem health, and regional climate patterns (Feng, 2016; Lucas-Borja et al., 2022; Sunderlin et al., 2008; Zema et al., 2022). Water is indispensable for forest ecosystems, as it facilitates nutrient transport and supports essential biochemical processes (Hörmann, 1996; Schäfer et al., 2023). Trees grow most effectively in environments with ample water, as short dry periods and favorable temperatures optimize growth and enhance overall ecosystem function. Therefore, water availability is closely tied to tree growth rates, emphasizing the critical relationship between forests and the hydrological cycle (Khaine and Woo, 2015; Toledo et al., 2011).

However, climate change increasingly disrupts this balance. Rising global temperatures and changing precipitation patterns—primarily driven by greenhouse gas emissions—are shifting the dynamics of the global water cycle (Germer et al., 2011.; Hanna et al., 2021; Intergouvernemental panel on climate change, 2007; Kurzweil et al., 2021; Weiskopf et al., 2020).While efforts to mitigate emissions continue, the impacts of past industrial activity have already set many regions on a path of continued warming and climate alterations (Intergouvernemental panel on climate change, 2007). These changes affect not only temperature and precipitation but also the timing, distribution, and intensity of water availability. Elevated temperatures heighten evaporation and evapotranspiration demands, intensifying the effects of water stress, particularly in ecosystems already vulnerable to water scarcity (Germer et al., n.d.; Hanna et al., 2021; Kurzweil et al., 2021)

Thus, understanding the water balance in forest ecosystems is increasingly urgent. Forests influence key hydrological processes such as evapotranspiration, infiltration, and soil moisture retention (Lucas-Borja et al., 2022; Sunderlin et al., 2008; Zema et al., 2022; Jones et al. 2020). As climate change disrupts these processes, understanding how forest ecosystems will respond to such shifts becomes essential for maintaining ecosystem health and ensuring sustainable water management (Zhang et al., 2017; Jones et al. 2020). By deepening our knowledge of these dynamics, strategies for forest and water resource management can be developed to address the challenges posed by a warming climate (Keenan, 2015; Pachauri et al., 2015).

1.2 Climate Change

Climate change stands as one of the most profound and urgent challenges of the 21st century, exerting transformative pressures on natural systems, human well-being, and the global economy. The most recent Intergovernmental Panel on Climate Change (IPCC) Sixth Assessment Synthesis Report (Calvin et al., 2023) unequivocally affirms that human-induced greenhouse gas emissions—chiefly carbon dioxide (CO_2), methane (CH_4), and nitrous oxide

(N_2O)—have been the dominant drivers of observed global warming since the pre-industrial era. Global mean surface temperature during the decade 2011–2020 was approximately 1.1°C above pre-industrial levels, with warming over land outpacing that over oceans.

Anthropogenic climate change is already manifesting across every continent and ocean, affecting both natural and managed systems. Calvin et al., (2023) and earlier assessments, such as Rosenzweig et al., 2007 document a wide array of observed impacts: melting glaciers, rising sea levels, changing precipitation regimes, and increased frequency and intensity of extreme events such as heatwaves, droughts, and heavy rainfall. These physical changes are accompanied by ecological shifts including phenological alterations, species range shifts, and disruptions to ecosystem functioning, particularly in sensitive biomes such as mountain, polar, and Mediterranean regions.

Changes in the hydrological cycle — a central theme in both reports — are particularly noteworthy. Rising temperatures are intensifying evapotranspiration, reducing snowpack, and altering soil moisture dynamics, with cascading effects on agricultural productivity, water availability, and ecosystem stability. Observed shifts in streamflow timing, notably earlier spring peak discharge in snow-fed rivers, further illustrate the systemic nature of hydrological change (Rosenzweig et al., 2007; Calvin et al., 2023).

Importantly, climate change does not affect all regions or populations equally. The IPCC AR6 underscores with high confidence that vulnerable groups—such as those in the Global South, Indigenous communities, and populations in low-lying coastal areas—bear a disproportionate burden of climate impacts despite having contributed the least to global emissions. This reflects deep-rooted inequalities in exposure, sensitivity, and adaptive capacity.

The evidence base for these conclusions is vast and multidisciplinary. As early as 2007, Rosenzweig et al. highlighted over 500 studies documenting climate-related changes across terrestrial, freshwater, and marine systems—from poleward species migrations to altered agricultural phenology. The IPCC AR6 further strengthens this link by employing improved attribution methods that connect observed ecological and physical shifts to anthropogenic climate forcing. Understanding the complex interplay between climate drivers and ecological responses remains crucial for anticipating future impacts and guiding adaptive management strategies.

1.3 Climate Change, Forests, and the Water Balance

Forests are both impacted by and play a critical role in mitigating the effects of climate change. They serve as major carbon sinks and are fundamental regulators of the terrestrial water cycle, influencing evapotranspiration, infiltration, surface runoff, and soil moisture dynamics (Calvin et al., 2023). Forests enhance infiltration and delay surface runoff, acting as natural buffers in the hydrological cycle. However, climate change introduces uncertainties and stressors that can alter these functions and reduce their effectiveness.

Changes in temperature and precipitation directly affect forest hydrology. Higher temperatures accelerate evaporation rates and lead to earlier snowmelt, which reduces soil water retention and extends drought periods within forest ecosystems (Calvin et al., 2023). Simultaneously, declines in summer precipitation—as observed in regions like Central Europe—exacerbate soil moisture deficits, increasing forest vulnerability to heat stress and drought. In mountainous

areas such as the Black Forest in Germany, these impacts are further compounded by elevation-dependent warming and changing snowfall patterns (Calvin et al., 2023).

The sensitivity of forest hydrological functions to tree species composition introduces a crucial dimension to climate change adaptation. Coniferous species, for example, typically exhibit higher annual evapotranspiration rates compared to deciduous species, primarily due to year-round transpiration. This has direct implications for soil water availability and groundwater recharge under increasingly dry conditions (Calvin et al., 2023). As such, forest composition and structure become important levers for water resource management under future climates, making species selection a key tool in climate-resilient forest management strategies.

In addition to species differences, site-specific conditions greatly influence how forests impact hydrology. Andréassian, (2004) emphasized that the hydrological effects of forests are not uniform across all landscapes but depend on several prerequisites: soil properties must allow deep rooting for trees to have a competitive water uptake advantage, and climate regimes must include both surplus and deficit periods to reveal differences in vegetation water use. Physiological characteristics, such as species-specific transpiration rates and stand age, further influence forest water dynamics.

Moreover, historical perspectives reveal persistent myths and misunderstandings about forest–water interactions, often arising from local overgeneralizations (Andréassian, 2004). While forests can enhance infiltration and stabilize hydrological regimes, their overall impact on streamflow can vary widely depending on factors like forest density, age, management practices, and soil-forest interactions. For instance, afforestation often leads to a reduction in annual water yield due to increased interception and transpiration, whereas deforestation may temporarily increase runoff but cause long-term degradation of soil and watershed function (Andréassian, 2004).

Recent research has further highlighted the intricate role forests play in regulating not only local water balances but also regional and even continental climates. Forests contribute significantly to atmospheric moisture recycling through evapotranspiration, influencing rainfall patterns and cloud formation over large areas (Ellison et al., 2017). Loss of forest cover can reduce regional rainfall and exacerbate drought conditions far beyond the immediate area of deforestation. Conversely, maintaining or restoring forest cover can enhance precipitation and contribute to cooling effects via increased latent heat fluxes. Thus, forests act as active drivers of both the hydrological and energy cycles, reinforcing their critical role in sustaining water availability and moderating climate extremes (Ellison et al., 2017).

The feedback loops between climate change, forest structure, and hydrological functioning underscore the urgent need for integrated assessments using hydrological models, as employed in this research. Understanding the nuanced and site-specific roles forests play in regulating water balance and atmospheric processes is critical for developing adaptive management strategies that ensure the sustainability of water resources and forest ecosystems under changing climatic conditions (Andréassian, 2004; Calvin et al., 2023; Ellison et al., 2017).

1.4 Hydrological Modeling

Hydrological modeling plays an indispensable role in predicting and understanding the distribution and movement of water across various scales. Models simulate crucial processes, including net-precipitation, evaporation, transpiration, infiltration, runoff, and groundwater

movement, essential for water resource management and environmental forecasting. Hydrological models serve as simplified representations of physical systems, aiming to replicate processes that govern the movement of water. These models can vary in complexity, from conceptual frameworks to advanced, physically-based models, incorporating principles such as mass and energy conservation to simulate the movement of water across the landscape. Forests specifically affect hydrological processes through canopy interception and evapotranspiration, directly affecting soil infiltration. The forest canopy intercepts rainfall, retaining water on its surface, which either evaporates or slowly infiltrates the soil. This reduces the amount of water that directly reaches the ground, influencing surface runoff and groundwater forest recharge. Forests also contribute to evapotranspiration, where trees release water vapor into the atmosphere. Furthermore, forests promote water infiltration, helping to recharge groundwater supplies and mitigate surface runoff during rainfall events. These processes influence the timing, quantity, and quality of water moving through a landscape, making forests a crucial component in hydrological studies (Dingman, 2015).

Hydrological models designed for forested watersheds integrate these processes to simulate how water behaves under various scenarios. They can predict how changes in forest cover, such as deforestation or afforestation, will influence hydrological outcomes. Deforestation, for example, typically leads to higher surface runoff and reduced groundwater recharge due to the loss of interception and transpiration. On the other hand, afforestation increases water retention in the soil and reduces runoff, promoting groundwater recharge. These models help inform strategies for sustainable land use, particularly under changing climate conditions (Bruijnzeel, 2004; Green, 2002; Scott et al., 2004).

The foundational scientific principles behind hydrological models include the conservation of mass, energy, and momentum. The modeling process typically involves three stages: conceptualization, where key processes are identified and represented; parameter estimation, which involves calibrating the model using observed data to ensure accuracy; and validation, which tests the model's predictive ability. Hydrological models are invaluable in assessing the impacts of climate change. By simulating different climate scenarios, these models provide critical insights into how forests and watersheds will respond to future environmental conditions (Dingman, 2015).

Recent advances in hydrological modeling have been driven by the need to address gaps in model resolution. Xu, (2000) notes that the coarse resolution of Global Circulation Models (GCMs) limits their usefulness for assessing local-scale hydrological impacts of climate change. GCMs are effective at simulating large-scale atmospheric processes but struggle to represent regional features crucial for hydrological assessments (Dingman, 2015; Kour et al., 2016; Xu, 2000, in Dingman, 2015). To overcome this, techniques such as downscaling are employed to generate high-resolution meteorological data for use in hydrological models.

The integration of downscaling methods, both statistical and dynamical, has improved the ability of hydrological models to simulate water systems under future climate scenarios. Kour et al., (2016) emphasize the importance of using downscaled climate data to improve the resolution of hydrological forecasts, particularly in regions where local scale climate dynamics are critical for water management (Dingman, 2015; Kour et al., 2016, in Dingman, 2015). Statistical downscaling uses large-scale climate variables to predict local climate variables such as precipitation and temperature, which are directly relevant for hydrological modeling (Dingman, 2015; Xu, 2000, in Dingman, 2015).

Dynamic downscaling uses high-resolution regional climate models (RCMs) to generate finer spatial resolutions necessary for hydrological impact assessments. These downscaled climate inputs are then used with hydrological models to more accurately simulate the effects of climate change on regional water resources. Owing to their improved ability to represent local meteorological variables, RCMs are increasingly employed in hydrological studies (Dingman, 2015; Xu, 2000, in Dingman, 2015).

In the context of hydrological modeling, Milly et al., (2008) emphasize the need for models that account for non-stationary conditions, as the assumption that hydrological conditions will remain constant is no longer valid in the face of rapid climate change. Advances in model calibration and the use of ensemble approaches, as well as sensitivity analysis, help improve the reliability and robustness of hydrological predictions under dynamic and uncertain conditions (Dingman, 2015; Kour et al., 2016, in Dingman, 2015).

Moreover, recent developments in macroscale hydrological modeling focus on integrating hydrological models across large spatial domains. This includes the simulation of river flows at continental and global scales, which is essential for understanding the broader impacts of climate change on water systems (Dingman, 2015; Xu, 2000, in Dingman, 2015). Gleick, (1986) highlights the flexibility of hydrological models in assessing climate change impacts, particularly in regions with complex hydrological processes. This flexibility allows for the application of various models depending on data availability and study objectives.

1.5 Objectives

The first objective of this research is the analysis of historical climate data for the Eyach catchment in the northern Black Forest, Germany. This analysis provides the climatic foundation for understanding long-term trends and variability in key variables such as temperature, precipitation, and solar radiation, which are essential for interpreting past hydrological responses and informing future model simulations. The Eyach catchment, located about 17 km southeast of Baden-Baden in western Baden-Württemberg, reaches up to 900 m in elevation and covers an area of approximately 52 km². The dataset spans from 1975 to 2019, offering valuable insight into multi-decadal climate dynamics relevant to hydrological modelling and scenario analysis.

The second objective is the application of a hydrological model named TRAIN, developed by Prof. Dr. Lucas Menzel (Menzel, 1999). TRAIN is a well-established model designed to simulate key components of the water cycle, such as evaporation, transpiration, snowfall, infiltration, and soil moisture. Applying TRAIN allows for a process-based understanding of how climate variability influences water fluxes in forested catchments on a long-term scale.

The third objective is to apply additional hydrological models—namely the RAVEN-HMETS Emulation (Craig et al., 2020), HBV-Light (Bergström, 1976) and LWF-Brook90 (B90) (Schmidt-Walter et al., 2020)—to establish a robust multi-model approach. These models differ in their hydrological representations, conceptual frameworks, and process complexity. Applying them in parallel allows for a more comprehensive analysis of the region's water balance by capturing a broader range of modelling perspectives and simulating hydrological processes from multiple angles.

The fourth objective is the comparison, evaluation, and validation of these hydrological models to determine their suitability and accuracy in simulating hydrological processes in

forested regions under changing climatic conditions. This includes validating key output parameters such as evapotranspiration, soil moisture and snow cover—essential indicators of forest–water cycle interactions—by comparing model outputs with observed data to ensure reliable predictions.

The fifth objective is the species-specific simulation of different tree species using the LWF-Brook90 model. A unique and valuable feature of this model is the ability to simulate different tree species, allowing an exploration of how various forest types respond to climate change. These simulations provide critical insights for forest resilience and adaptive management. As climate change continues to alter environmental conditions, forest managers and policymakers require data-driven guidance on optimal tree species selection. By using LWF-Brook 90 to test various compositions, this research supports decision-making for reforestation, afforestation, and sustainable forest management (Keenan et al. 2015).

The sixth objective is the integration of future climate scenarios to assess the projected impacts of climate change on the water balance in the Black Forest region through 2050. This includes simulations under various CO_2 emission scenarios (RCP 2.6, 4.5, and 8.5), enabling a robust assessment of possible future hydrological conditions and supporting broader efforts to assess potential impacts of future climate scenarios (Brocca et al., 2017; Dong et al., 2022). These projections provide valuable insights into the challenges that forested regions like the Black Forest may face in the coming decades.

1.6 Scientific Context and Rationale

Climate change is exerting unprecedented pressure on regional and global water cycles, with cascading effects on forest ecosystems. Forests, while critical regulators of hydrological processes, are also highly sensitive to climatic shifts—particularly regarding evapotranspiration, soil moisture dynamics, and species resilience. This research addresses these challenges through a multi-model hydrological approach, combining process-based simulations with forest-specific scenarios.

By integrating historical climate trends, model comparisons, and species-level analyses under future emissions scenarios, the study contributes to a more robust understanding of how forested catchments may evolve under intensifying climate stress. These insights are essential not only for scientific modelling but also for informing adaptive water and forest resource management strategies aimed at enhancing ecosystem resilience in regions like the Black Forest.

In sum, these objectives collectively address past, present, and future aspects of forest hydrology under climate change.

1.7 Thesis Structure

This thesis is structured into six chapters, each contributing to the overarching objective of understanding climate–hydrology–vegetation interactions in a forested catchment under climate change. Chapter 1 introduced the research background, outlined six core objectives, and explained the relevance of climate change for hydrological and ecological systems. Chapter 2 presents the methodology, including a description of the study area, datasets, data processing and the hydrological models applied—TRAIN, Raven-HMETS, LWF-Brook90, and HBV-Light—detailing their characteristics, inputs, and outputs. Chapter 3 addresses Objectives 1

through 4. It begins with an evaluation of historical climate data for the Eyach catchment (1975–2019), followed by the spatial application of the TRAIN model to simulate evapotranspiration, soil moisture, and snow water equivalent. It also introduces a multi-modelling framework to assess model behaviour across spatial scales using Raven, LWF-Brook90, and HBV-Light. Moreover, it covers the intercomparison and validation of hydrological model outputs with a focus on evapotranspiration, soil moisture, and snow cover days. These are benchmarked against observational and remote-sensing datasets to assess model performance and structural differences. Chapter 4 fulfils Objective 5 by investigating species-specific differences in water balance responses using the LWF-Brook90 model. Simulations for Norway spruce *(Picea abies)*, European beech (*Fagus sylvatica)* and oak (*Quercus robur)* provide insights into how forest composition influences evapotranspiration, soil moisture, and drought resilience. Chapter 5 addresses Objective 6 by integrating future climate scenarios (RCP 2.6, 4.5, and 8.5) to examine projected changes in meteorological and hydrological conditions up to 2050 using TRAIN and LWF-Brook90. Finally, Chapter 6 synthesizes the findings, discusses model strengths and uncertainties, highlights key trends in forest–climate interactions, and offers an outlook for future research and forest–water resource management. Supplementary figures, and calibration data are provided in the appendices.

Chapter 2

This chapter outlines the methodological framework of the study, detailing the steps undertaken to analyze the impact of climate change on the hydrological regime of the Eyach catchment. It describes the geographical setting, the datasets used, and the hydrological modeling approaches implemented to achieve the objectives outlined in Chapter 1.

The chapter begins by introducing the Eyach catchment as the study area, including its geographical location, topographical characteristics, land cover, soil properties, and climatic conditions. These physical attributes are crucial for understanding the region's hydrological behavior and for selecting appropriate modeling strategies.

Subsequently, the various data sources used throughout the study are presented. These include long-term meteorological datasets, spatial land cover and soil data, and discharge records. The procedures for data acquisition, preprocessing, and interpolation are described in detail, with particular emphasis on the spatial resolution and consistency required for reliable hydrological modeling.

The core section of the chapter focuses on the hydrological models applied in the study. Four models are described: the spatially distributed TRAIN model, and the point-scale models Raven-HMETS, LWF-Brook90, and HBV-Light. For each model, the theoretical background, model structure, input and output requirements, and implemented hydrological processes are discussed. The rationale for using a multi-model approach lies in the complementary strengths of the models and their ability to represent diverse aspects of the soil–vegetation–atmosphere system under varying climate and land cover conditions.

In addition to model descriptions, this chapter outlines the parametrization, model setup, and methodological choices made to adapt each model to the specific conditions of the Eyach catchment. Emphasis is placed on the integration of land cover and soil data into the models and on ensuring comparability and consistency across different simulation frameworks.

Overall, this chapter provides the methodological foundation for the simulations and analyses conducted in the subsequent chapters, establishing a transparent and reproducible basis for understanding the hydrological impacts of climate variability and change in the study region.

2. Methodology

2.1 Study Area

The Eyach catchment is located about 17 km southeast of the city Baden-Baden in western Baden Württemberg in southwest Germany (Figure 1). It is part of the northern Black Forest and obtains a size of roughly 52 km^2. The draining River Eyach is about 14 km in length and contributes to the Enz River north of the village Höfen an der Enz. The Eyach catchment mostly obtains sandy soils and loamy sand soils lying over "Geröllsandstein-Formationen" and "Badischer Bausandstein". Elevation within the catchment ranges from approximately 356 m to 954 m a.s.l., and the area is hydrologically structured into five subcatchments.

High rainfall and cold temperatures with annual precipitation characterize the northern Black Forest region sums reaching 2000 mm a year and mean annual temperatures ranging between 5 and 10 °C (Ludemann, 2014). The Eyach catchment obtains a mean annual temperature of

7.4 °C (reference period 1975 – 2019) and mean annual precipitation sums up to 1209.3 mm (reference period 1975 – 2019). Moreover, forested areas mostly obtain coniferous forest (64 %) with *Picea abies* being the predominant species. The remaining part (21 %) consists of a mixed forest and deciduous trees as e.g. *Fagus sylvatica* (3.5 %) (UBA,2019).
This catchment was selected for several reasons. First, it offers excellent data availability, including a continuous long-term streamflow time series (1975–2019), which is essential for parameterizing and evaluating hydrological models that require discharge calibration (e.g., HBV-Light and Raven-HMETS). Additionally, observational snow cover data are available for part of the simulation period, enabling partial validation of modelled snow dynamics. The site also benefits from ongoing research activities within the framework of the research group led by Prof. Dr. Lucas Menzel, ensuring a robust scientific context and data infrastructure.

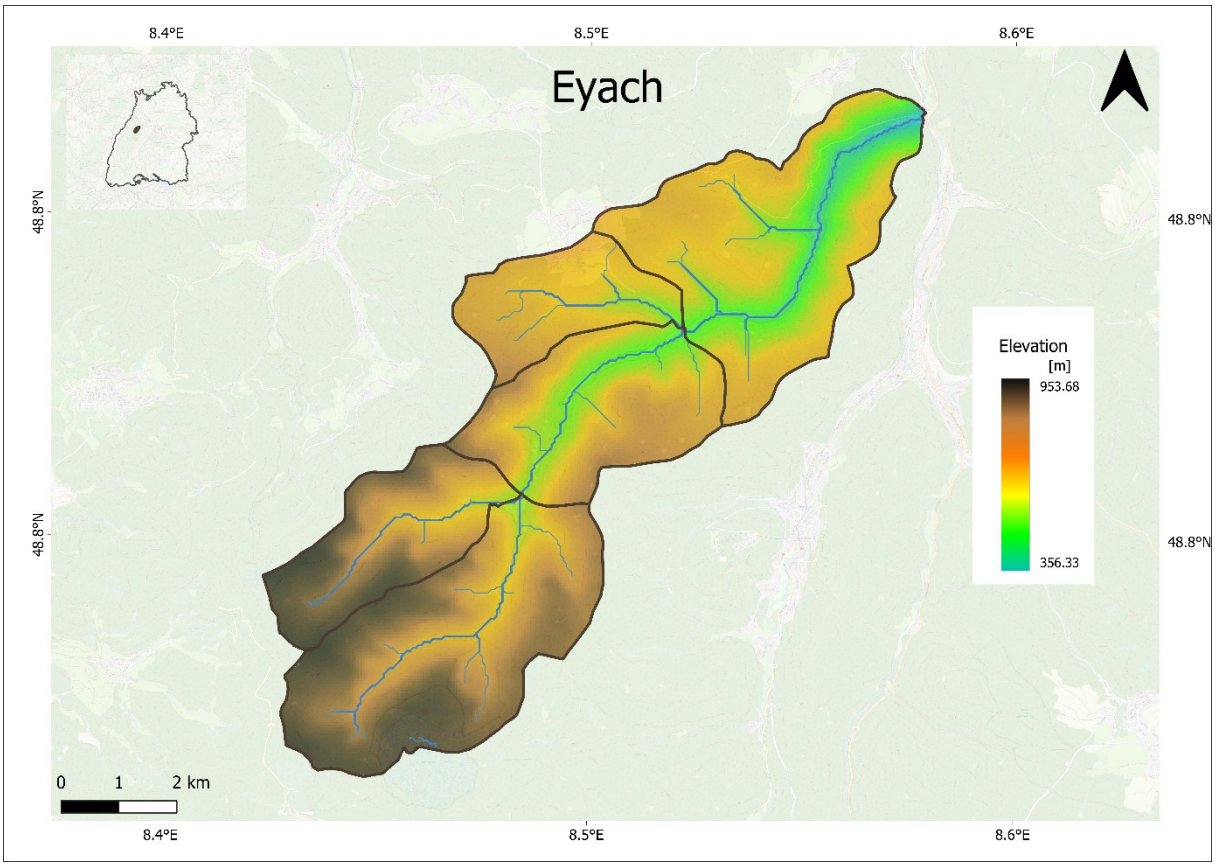

Figure 1. Map of the Eyach catchment, the study area of this dissertation, showing elevation, stream network, and delineated subcatchments.

2.2 Data Source

This study utilizes a long-term dataset spanning the period from 1975 to 2019. This time frame was selected because all relevant forcing data were complete, free of data gaps, and thus ready for use as input for the applied hydrological models. Precipitation data P [mm] was taken from the REGNIE (Regionalisierte Niederschlagshöhen) dataset (Rauthe et al., 2013) and originates from the climate data center of the German Weather Service. Moreover, station-based meteorological observations of relative humidity RH [%], temperature T [°C], and wind speed U [m/s] also stem from the climate data center of the German Weather Service (DWD, 2019).

Global radiation data RG [W/m²] was taken from the SARAH dataset and derived from the Satellite Application Facility on Climate Monitoring (Pfeifroth et al., 2019 a,b). Using the software INTERMET (Dobler et al., 2004), station-based meteorological observations (DWD, 2019) were interpolated to grids of T, U, RH, and RG. INTERMET employs kriging-based methods to interpolate meteorological variables to a 1 km resolution grid (Tijdeman and Menzel, 2021). For detailed catchment-scale modelling, these datasets were subsequently resampled to 50 × 50 m resolution grids using bilinear interpolation. Daily potential evapotranspiration (ETp) was derived from the ERA5-Land Daily Aggregated Reanalysis dataset provided by Copernicus Climate Change Service (C3S) Climate Data Store (CDS) (CDS, 2024), using the variable *potential_evaporation_sum*, which represents potential evapotranspiration in meters per day. The dataset provides global land surface coverage at a spatial resolution of 0.1° (~9 km).

Elevation data with a resolution of 50 x 50 m were obtained from Sonny Light detection and ranging (LiDAR) Digital Elevation Models (DTM). Vectorized land cover data from 2018 originate from the Corine-2006 dataset and were downloaded from the European Union's Copernicus Land Monitoring Service information (CLMS, 2018). Moreover, most soil properties (field capacity, air capacity, wilting point, and root zone depth) were derived from the BK-50 (scale of 1:50,000) dataset provided by the Federal State Office for Geological Resources and Mining (LGRB, 2019). Some soil properties, as e.g. bulk density, was taken from the SoilGrids250 dataset (Hengl et al., 2017), which provides global soil property estimates at a 250-meter resolution. Discharge data stem from the Environment Agency of Baden-Württemberg (LUBW).

The ERA5-Land dataset from the Copernicus Climate Change Service (C3S) Climate Data Store (CDS) (Muñoz Sabater, J. (2019), CDS, (2024)) and the Global Land Evaporation Amsterdam Model (GLEAM) dataset Miralles et al., (2025) were utilized for the validation of the simulation results. ERA5-Land provides high-resolution atmospheric and land surface variables at 0.1° spatial resolution (~9 km), while the GLEAM dataset offers satellite-based estimates of terrestrial evaporation at 0.25° resolution (~25 km).

For the validation of snow cover simulations, additional in situ observations were incorporated. Snow cover day records for the periods 1975–1985 and 2013–2019 were provided by a local observer (W. Roos) residing near the study area. These systematically collected observations were compiled and shared in tabular format with Prof. Dr. Lucas Menzel, offering valuable ground-based data for snow model validation.

For the analysis of future climate scenarios, the EURO-CORDEX, regional model 2009 (REMO 2009) dataset from the Copernicus Climate Change Service (C3S) Climate Data Store (CDS) was used (CDS, 2019). The dataset provides regional climate projections at a spatial resolution of 0.11° (~12.5 km) for Europe. This dataset provides regional climate model data on single levels, specifically designed for assessing climate projections at regional scales. The CORDEX REMO 2009 dataset offers high-resolution simulations that were utilized to evaluate potential climate changes under various future scenarios. All datasets utilized in this study are summarized in Table 1, which provides an overview of their sources, spatial resolution, temporal resolution, and application within the modeling and validation framework.

Table 1. Summary of Input and Validation Datasets.

Category	Variable / Dataset	Source / Provider	Spatial Resolution	Time Resolution
Forcing Data	Precipitation (P) – REGNIE	DWD / Climate Data Center (Rauthe et al., 2013)	1 km (REGNIE native)	daily
	Temperature (T), Relative Humidity (RH), Wind Speed (U)	DWD / Climate Data Center (DWD, 2019)	Station-based, interpolated	daily
	Global Radiation (RG) – SARAH	CM SAF / DWD (Pfeifroth et al., 2019a,b)	0.05° (~5 km) native; interpolated	daily
	Potential Evapotranspiration (ETp) – ERA5-Land	C3S / CDS	0.1° (~9 km)	daily
Elevation Data	DEM	SONNY's LiDAR TERRAIN MODELS of EUROPE	50 m	-
Land Cover	Corine Land Cover (CLC)	German Environment Agency (UBA, 2019)	Vectorized	yearly
Discharge	Streamflow / Discharge	Environment Agency of Baden-Württemberg (LUBW)	Point-based (gauges)	daily
Soil Data	Soil Physical Properties – BK50 (field capacity, wilting point, etc.)	State Office for Geology and Mining (LGRB, 2019)	Scale 1:50,000 (~20–50 m)	-
	Bulk Density, Other – SoilGrids250	ISRIC / Hengl et al., 2017	250 m	-
Future Climate Scenarios	Regional Climate Projections – REMO2009 (CORDEX)	C3S / CORDEX via CDS	0.11° (~12.5 km)	daily
Validation Data	ERA5-Land Reanalysis (Evaporation & Soil Moisture)	C3S Climate Data Store (Muñoz Sabater, 2019)	0.1° (~9 km)	yearly
	GLEAM v3.7a (Evaporation)	GLEAM / Miralles et al. (2025)	0.25° (~25 km)	yearly
	Snow Cover Days (SCD) – Local Observations	Observer: W. Roos / compiled by Prof. Dr. Lucas Menzel	Point-based (Eyach region)	Yearly(1975–1985, 2013–2019)

2.3 Hydrological Models

2.3.1 TRAIN: Soil-Vegetation-Atmosphere Transfer Model

The TRAIN SVAT-model (Soil-Vegetation-Atmosphere Transfer) was developed by Prof. Dr. Lucas Menzel (1999) to simulate water budgets spatially or locally. In this work, the model is applied in its spatially distributed form. It focuses on key hydrological processes, such as evapotranspiration, interception, and soil water dynamics, under varying meteorological and land use conditions. TRAIN's flexibility allows its application to a wide range of studies, including site-specific research, irrigation planning, and regional water resource management (Menzel, 1996, 1999).

2.3.1.1 Model Abstraction

The TRAIN model captures the interactions between the soil, vegetation, and atmosphere by focusing on vertical water and energy exchanges. At the core of its simulations are soil water dynamics, which are governed by the following equation (Menzel and Rötzer, 2007):

$$\Delta\psi = rr - et_t - int - ro + cr + irr \quad [1]$$

where:

*$\Delta\psi$: Change in soil water content [mm*day^{-1}]*
*rr: Precipitation [mm*day^{-1}]*
*et_t: Actual evapotranspiration [mm*day^{-1}]*
*int: Interception loss [mm*day^{-1}]*
*ro: Runoff [mm*day^{-1}]*
*cr: Capillary rise [mm*day^{-1}]*
*irr: Irrigation [mm*day^{-1}]*

This equation represents the balance of water within the soil layer, incorporating inputs like precipitation and irrigation, as well as losses through evapotranspiration, interception, and runoff.
A basic soil module is characterized by field capacity, wilting point, and rooting depth. Furthermore, the daily capillary rise, as described by (Giese et al., n.d.), is determined based on soil type, groundwater depth, and rooting depth, with consideration of the current soil water content.
A snow module incorporates snowfall and melt processes, simulating a delay in precipitation's effect on the water balance, with snow impacting the balance only upon melting. Accumulation occurs when temperatures fall below 2°C and precipitation is present, while ablation (melt) occurs when temperatures rise above 0°C and there is water in the snowpack. The meltwater amount is determined using the degree-day factor, as described by (Hock, 2003) in the next section.
For regional applications, TRAIN uses a grid-based structure with flexible resolutions, typically ranging from 500 meters to 1 kilometer. Vegetation and soil are treated as dynamic components, with properties such as leaf area index (LAI), albedo, and soil moisture updated throughout the simulation based on meteorological inputs and seasonal phenology.

2.3.1.2 Input Files

The TRAIN model requires various input data to accurately simulate hydrological processes:

1. Meteorological Data: Essential climate inputs include daily or hourly precipitation, mean temperatures, relative humidity, wind speed, and solar radiation (or sunshine duration). For snow-covered regions, temperature thresholds determine whether precipitation is rain or snow.
2. Vegetation Properties: Dynamic vegetation parameters, such as LAI, albedo, and plant height, are provided directly or calculated internally using phenological models. Seasonal changes, like growth and senescence, are based on temperature or time-dependent curves.
3. Soil Characteristics: Soil inputs include field capacity, usable field capacity, wilting point, root zone depth, soil depth and hydraulic conductivity. These parameters determine water retention, movement, and availability to plants.
4. Spatial Data: For regional applications, digital elevation models (DEMs), land use maps, and soil grids are necessary to define the study area's topography and land cover distribution.

2.3.1.3 Outputs

After executing TRAIN, a set of output data is generated, including five parameters: Evapotranspiration (in mm), Snow Water Equivalent (mm), Soil Moisture (in %), Soil Moisture (in mm), and Water Availability (Evapotranspiration minus Precipitation in mm) for each day.

2.3.1.4 Hydrological Processes

Interception and Evapotranspiration, snow store change, soil moisture change, and runoff generation are the four processes considered within the TRAIN model.
Evapotranspiration (ET) is calculated using the Penman-Monteith equation**,** describing the movement of moisture and its regulation between grassland canopy and a reference height (Menzel, 1996):

$$\lambda E = \frac{(R_n - G) + \frac{pc_p D_{ref}}{r_a}}{\Delta + \gamma(1 + \frac{r_c}{r_a})} \quad [2]$$

where:

λE: *Vapor flux [kg*m^{-2}s^{-1}]*
λ*: Latent heat of vaporization [(J*kg^{-1}]*
R_n*: Net radiation [J*m^{-2}s^{-1}]*
G*: Soil heat flux [J*m^{-2}s^{-1}]*
$\triangle$*: Slope of saturation vapor pressure [hPa*K^{-1}]*
γ*: Psychometric heat constant [hPa*K^{-1}]*
p*: Density of dry air [kg*m^{-3}]*
c_p*: Special heat of dry air [J*kg^{-1}K^{-1}]*
D_{ref}*: Specific humidity deficit at reference height [hPa]*

r_a: *Aerodynamic resistance [s*m^{-1}]*
r_c: *Canopy resistance [s*m^{-1}]*

r_c is influenced by soil moisture status, vegetation growth and weather conditions (Menzel, 1996):

$$r_c = r_a(1 + \frac{\Delta}{y})(\frac{E_p}{E_a} - 1) \quad [3]$$

where:

$E_p = Maximal\ evaporation\ rate\ [mm/day]$
$E_a = Maximal\ evaporation\ rate\ [mm/day]$

(Menzel, 1996) indicates that the canopy's capacity to retain water is governed by the seasonal dynamics of the Leaf Area Index (LAI). The rate of interception-driven evaporation is simulated as a variable process, influenced by both the volume of water currently stored within the canopy and the surrounding meteorological conditions.
Furthermore, the TRAIN model estimates soil water dynamics and percolation based on the conceptual framework of the HBV model (Bergström, 1976). This approach treats the soil as a single homogeneous column, rather than dividing it into stratified layers. Soil moisture content is determined by evaluating the difference between incoming precipitation and outgoing evapotranspiration, using field capacity and the wilting point to guide the calculation:

$$\frac{Q}{P} = (\frac{SM}{F_c})^{\beta} \quad [4]$$

where:

$\frac{Q}{P}$ = *Runoff coefficient*
Q= *Runoff [mm]*
P= *Precipitation [mm]*
SM= *Soil moisture [mm]*
F_c= *Maximum soil moisture storage [mm]*
$^{\beta}$ = *Shape parameter associated to soil characteristics [-]*

Snowmelt is calculated using a temperature-index approach, in which melt is linearly related to air temperature above a defined threshold. This method, commonly referred to as the degree-day method, is implemented in TRAIN using the following equation (Hock, 2003):

$$M = DDF * (T_a - T_{thres}) for T_a > T_{thres} \quad [5]$$

where:

M= *Melt rate [mm/day]*
M= *Degree-day factor [mm °C^{-1} day^{-1}]*
T_a= *Mean daily air temperature [°C]*
T_{thres}= *Melt threshold temperature, typically 0 °C*

2.3.1.5 Strengths and Advanced Features

TRAIN's modular design makes it highly versatile, with applications ranging from site-specific studies to regional hydrological assessments. Key features include:

1. Dynamic Vegetation Modeling: Seasonal phenology is incorporated to capture vegetation's role in water and energy exchange.
2. Snow and Interception Modules: Detailed processes for snowmelt and interception enhance accuracy in forests and mountainous regions.
3. Scalable Applications: TRAIN supports both hourly site-level studies and large-scale regional analyses.
4. Validation and Calibration: Outputs can be validated against field measurements, improving confidence in simulation results.

2.3.1.6 Applications

Applications of TRAIN are featured in hydrological mapping projects across multiple countries, including the Hydrological Atlas of Switzerland (Menzel, 1999, Fig. 3) and the Hydrological Atlas of Rheinland-Pfalz (LfU, 2005), particularly in connection with the implementation of the European Water Framework Directive.

Beyond mapping, TRAIN has been extensively applied under contrasting climatic and environmental conditions: in the semi-arid Jordan River basin (Menzel and Rötzer, 2007), in permafrost-affected basins in southern Siberia and Mongolia (Han and Menzel, 2022), and in the boreal Aldan catchment where permafrost degradation alters hydrological regimes. Additionally, TRAIN is used for scenario studies evaluating the impact of climate change (Menzel and Lang, 2005) and land-use changes on hydrological processes.

For example, Wimmer et al., (2009) applied TRAIN in northern Mongolia to assess the impacts of climate change on snow sublimation under IPCC A1B scenarios, showing that sublimation accounted for up to 80% of snowfall and is projected to increase with rising winter precipitation in future climates. These findings underscore TRAIN's capacity to simulate snow processes under sparse data conditions and across varied topographic gradients.

Recent research also highlights its utility in climate impact assessments and extreme event analysis. For example, Wang et al., (2023) used TRAIN to simulate evapotranspiration and root zone soil moisture at 1 km resolution for flash drought detection in southwestern Germany, revealing significant increases in flash drought frequency under compound heatwave conditions. Similarly, Tijdeman and Menzel, (2021) employed TRAIN to explore soil moisture stress persistence during droughts over agricultural regions in Baden-Württemberg, linking stress duration and onset dynamics to rooting depth and soil water capacity. Furthermore, Stork and Menzel, (2016) conducted a multi-site model intercomparison using TRAIN across forested catchments in Germany and confirmed its strong performance in replicating site-specific soil moisture and evapotranspiration dynamics for both deciduous and coniferous vegetation types. Overall, TRAIN's physically based SVAT structure and high spatial resolution make it well suited for capturing spatial variability and vegetation-climate interactions—attributes particularly valuable in complex catchments such as the Eyach catchment.

2.3.1.7 Model Setup and Implementation in the Eyach Catchment

Parameter Classification

Based on the values extracted from the BK50 (such as usable field capacity, field capacity, air capacity, hydraulic conductivity, soil depth, and rootability), the classification of these values into specific categories was done according to the classification system established by the GeoFachdaten BW – Bodenkunde and the Bodenkundliche Kartieranleitung (Soil Mapping Guidelines) from the Landesamt für Geologie, Rohstoffe und Bergbau (LGRB). This classification system was designed by AG BODEN and used in the state of Baden-Württemberg, Germany, as outlined in publications from the Geologisches Landesamt Baden-Württemberg (1995) and the Landesanstalt für Umwelt, Messungen und Naturschutz Baden-Württemberg (2010). The following categories were applied to the key soil parameter (Table2):

Table 2. Soil Hydraulic and Physical Property Classification Scheme.

Parameter	Class Code	Description
Field Capacity	1	Very low < 130 mm (l/m²)
	2	Low 130 – 260 mm (l/m²)
	3	Medium 260 – 390 mm (l/m²)
	4	High 390 – 520 mm (l/m²)
	5	Very high > 520 mm (l/m²)
Usable Field Capacity	1	Very low < 50 mm (l/m²)
	2	Low 50 – 90 mm (l/m²)
	3	Medium 90 – 140 mm (l/m²)
	4	High 140 – 200 mm (l/m²)
	5	Very high > 200 mm (l/m²)
Air Capacity	1	Very low < 3 Vol.%
	2	Low 3 – 7 Vol.%
	3	Medium 7 – 12 Vol.%
	4	High 12 – 18 Vol.%
	5	Very high > 18 Vol.%
Hydraulic Conductivity	1	Very low < 1 cm/d
	2	Low 1 – 10 cm/d
	3	Medium 10 – 40 cm/d
	4	High 40 – 100 cm/d
	5	Very high 100 – 300 cm/d
	6	Extremely high > 300 cm/d
Soil Depth	1	Very shallow < 1.5 dm
	2	Shallow 1.5 – 3 dm
	3	Medium-depth 3 – 6 dm
	4	Moderately deep 6 – 10 dm
	5	Deep > 10 dm

Parameter	Class Code	Description
Rootability	1	Moderately rootable
	2	Poorly rootable
	3	Very poorly rootable
	4	Empty = Rootability not restricted

Land Cover Classification

The CORINE Land Cover (CLC) data was used as a foundation for land use classification. The CLC data were aggregated and adapted for use with the TRAIN model based on the land-use aggregation scheme developed by Prof. Dr. Lucas Menzel (Table3)**.** The land use types were mapped according to this specific aggregation scheme to align with the requirements of the TRAIN model. This classification approach was essential for ensuring that the CLC data could be properly integrated and used for hydrological simulations within the context of the model:

Table 3. Land Use Classification Based on CLC and TRAIN Codes.

CLC Class Code	CLC Class Name	TRAIN Code	TRAIN Class Name	Particular Feature
111	Dense urban areas	5	Dichte Besiedlung (Populous / Highly Urban)	-
112	Sparsely urbanized areas	6	Lockere und mittlere Bebauung (Urban)	-
121, 122, 123, 124	Industrial and commercial areas	7	Industrie- und Gewerbeflächen (Industrialized)	-
131, 132, 133	Quarries and landfills	15	Abbauflächen und Deponien (Landfill, Deteriorated Area)	-
141, 142	Green spaces	20	Sonstige Grünflächen (Green Spaces)	-
211, 242, 243	Arable land	30	Ackerland (Arable Land, Undifferentiated)	-
221	Orchards and vineyards	40	Obst- und Gartenbau (Orchards and Wine-growing)	Treated together with wine-growing (50)
222	Vineyards	50	Weinbau (Wine-growing)	Treated together with orchards (40)
231, 321, 322, 333	Grassland	60	Wiesen, Weiden, Grünland (Pastureland, Grassland)	-
311, 0	Deciduous forests	70	Laubwald (Deciduous Forest)	-

312	Coniferous forests	80	Nadelwald (Coniferous Forest)	-
313, 324	Mixed forests	90	Mischwald (Mixed Forest)	-
511, 512, 411	Water bodies	95	Gewässer (Open Water Bodies)	-

In addition to the CLC-based aggregation, Menzel (2013) introduced a comprehensive applied code number system for the TRAIN model, accommodating a wide range of land-use classes beyond standard CORINE definitions. The current classification in TRAIN is a hybrid system that integrates elements from CORINE, Moderate Resolution Imaging Spectroradiometer (MODIS), and earlier internal schemes, reflecting the model's use across diverse research initiatives such as the Global Change in the Hydrological Cycle (GLOWA) Jordan River project and the Rheinland-Pfalz (RLP) regional hydrology studies. Despite this mixture of numbering conventions, no inconsistencies arise in the parameterization of land-use classes, as each class is uniquely linked to a defined set of hydrological parameters. In cases where MODIS-derived classes occurred only in negligible areas, they were reclassified into more common land-use types for modeling purposes. For example, woody savannas (code 55) and forest (code 22) were reassigned to shrublands (33), set-aside areas (21) were mapped to barren land (66), and wetlands (99) were reclassified as open water bodies (class 3). The full applied code number list used in TRAIN can be found in Appendix D, Table 41.

2.3.2 Raven Hydrologic Modeling Framework

The Raven hydrologic modeling framework is a flexible software tool developed for watershed simulation. Originally created by J. R. Craig at the University of Waterloo (Craig et al., 2020), Raven is a mixed lumped and semi-distributed model that offers significant versatility for hydrological analysis. It enables users to investigate the behavior of watersheds under various environmental scenarios, including the impacts of climate change, land use shifts, or specific storm events. With Raven, users can assess a wide range of outcomes, such as groundwater recharge rates, soil water availability, and flood potential, while also creating detailed mass, water, and energy balances to support water quality assessments and resource management decisions.

As a flexible framework, Raven provides a library of customizable subroutines and algorithms representing components of the water cycle. This enables modelers to choose from a variety of methods and even mimic existing hydrological models such as the UBC Watershed Model, HBV, HMETS, SAC-SMA, MOHYSE, HYMOD, GR4J, Brook90, VIC, SWAT, and PRMS. The ability to emulate these models allows researchers to compare results or expand upon existing approaches. Raven also integrates tools to interpolate meteorological forcing data, simulate runoff processes, and route water downstream. This high degree of customization makes Raven suitable for applications ranging from simple watershed simulations to complex analyses involving thousands of hydrological response units (HRUs).

2.3.2.1 *Model Abstraction*

Raven represents watersheds as a collection of subbasins, which are further divided into HRUs. Each HRU represents a unique combination of land use, vegetation, soil, and terrain type, and these units serve as fundamental building blocks in the model. HRUs function as discrete storage compartments for water and energy, which may include snowpacks, glaciers, wetlands, soils, and aquifers. These units are defined by geometric and topographic properties, such as area, slope, aspect, and coordinates, along with soil profiles and vegetation characteristics. Each HRU's storage compartments are linked to specific hydraulic processes that simulate the redistribution of water in response to atmospheric forcings such as precipitation and temperature.

To ensure spatial consistency, Raven interpolates meteorological inputs across all HRUs using built-in methods such as nearest-neighbour or inverse-distance weighting. Catchment-level outputs are then computed by aggregating HRU-specific results using area-weighted means, allowing the model to produce representative watershed-scale values.

At the core of Raven's water redistribution logic are mass and energy balances that are rigorously solved at each time step. Within each HRU, changes in storage compartments are computed using a system of ordinary and partial differential equations (that represent the dynamic exchange of water and energy between components such as the soil, atmosphere, and surface water.

Soil water dynamics in Raven follow a generalized mass balance formulation, where the rate of change in soil water content is determined by the net sum of fluxes. For instance, the water balance in the surface ponded water compartment can be represented as:

$$\frac{\partial \phi_{DS}}{\partial t} = P - E - I - R \qquad [6]$$

where:

P= Precipitation Input [mm]
E= Evaporation [mm]
I= Infiltration [mm]
R= Overflow / Surface Runoff [mm]

Each term in the equation is derived from process-specific algorithms that may depend on current state variables (e.g., saturation), parameters (e.g., soil conductivity), and atmospheric forcing (e.g., temperature, radiation).

The overall system of balance equations for each HRU is represented in matrix form as:

$$\frac{\partial \vec{\phi}}{\partial t} = M_G(\vec{\phi}, \vec{P}, \vec{F})\ \{1\} \qquad [7]$$

where:

$M_G = Global\ symmetric\ matrix\ with\ rate\ of\ change\ functions$
$\vec{\phi}$= *Rate of change of state variables*

$\vec{P}$ = *Rate of change of system parameters*
$\vec{F}$ = *Rate of change of forcing functions*
{1}= Column vector filled with ones

Within each HRU, water is redistributed between storage compartments based on user-defined processes, and runoff is routed into subbasin channels. Raven tracks water, mass, and energy fluxes over time, enabling both cumulative and instantaneous diagnostics. Its modular design allows processes like infiltration and evapotranspiration to function independently while ensuring a globally consistent, mass- and energy-conserving solution. Whether simulating a single-layer or multi-layer soil profile, Raven integrates vertical water and energy exchanges within the watershed system. This balance of structure and flexibility makes it suitable for both simple and complex hydrological applications.

2.3.2.2 Input Files

Simulating a watershed in Raven requires several input files, each providing critical data about the model's structure and processes:

1. RVI File (Primary Input): This file serves as the starting point of the model, specifying the simulation duration, time steps, water routing methods, and soil column structure. Users define hydrological processes, the algorithms used to represent them, and optional outputs for diagnostics and analyses.
2. RVH File (HRU/Subbasin Definitions): The RVH file includes the number of HRUs and subbasins, their connectivity, and physical properties. It specifies vegetation, soil, and aquifer classes, creating a detailed map of the watershed's structure.
3. RVT File (Time Series/Forcing Functions): This file provides meteorological data, such as precipitation, temperature, radiation, and humidity, which are interpolated across HRUs. Gridded data, such as NetCDF files, can also be used, requiring additional metadata about spatial relationships between grids and the landscape.
4. RVP File (Class Parameters): This file groups hydrological parameters into classes (e.g., soil, land use, vegetation) and assigns them to HRUs. Each HRU corresponds to specific classes that define properties like porosity, conductivity, and other coefficients critical to simulating hydraulic behavior.
5. RVC File (Initial Conditions): This optional file sets the initial values for state variables such as snowpack depth or soil moisture. If left blank, Raven assumes zero initial conditions and uses a spin-up period to reach equilibrium.

Optional input files, such as live (.rvl) or ensemble (.rve) files, support advanced configurations, including real-time forecasting and ensemble simulations.

2.3.2.3 Outputs

Raven produces a variety of outputs to meet diverse modeling needs. By default, the framework generates:

- Hydrograph.csv: Tracks flow rates at subbasin outlets throughout the simulation.
- WatershedStorage.csv: Logs average water storage across all compartments.

- Solution.rvc: Captures the final state of the system, allowing it to be used as initial conditions for subsequent runs.
- RavenErrors.txt: Details errors and warnings encountered during the run, helping users identify issues such as flawed input data or parameter conflicts.

In addition, users can request specific outputs, such as energy fluxes, reservoir mass balances, or stream water levels. Advanced options, like the :CustomOutput command, enable tracking user-defined variables or spatially and temporally aggregated data. Outputs can be formatted as CSV, NetCDF, or Green Kenue-compatible .tb0 files, supporting integration with visualization or analysis tools.

2.3.2.4 Hydrological Processes

Raven includes an extensive library of hydrological processes, such as precipitation partitioning, infiltration, runoff, evapotranspiration, and snowmelt. These processes interact to solve mass and energy balance equations for each HRU. The framework supports both simple and complex routing methods:

- In-Catchment Routing: Transfers water from HRUs to subbasin channels, often using unit hydrographs or convolution methods.
- In-Channel Routing: Simulates water flow between subbasin channels, employing algorithms such as Muskingum-Cunge, lag-and-route, or more advanced approaches for reservoir and lake routing.

Additional features include reservoir management, irrigation modeling, and contaminant transport. Depending on the chosen method, corresponding algorithms for the hydrological processes are used.

In the scope of this study, the Raven – Hydrological Model of École de technologie supérieure (HMETS) (Martel et al., 2017.) was chosen. Within the HMETS model the following hydrological processes are considered.

Potential Evapotranspiration (PET) is calculated by the Penman-Monteith equation (Monteith, 1965) that estimates PET over a reference vegetation:

$$PET = \frac{1}{\lambda_v \rho_w} * \left[\frac{\Delta}{\Delta+\gamma*} R_n + \frac{p_a C_{atm}}{\Delta+\gamma}(e_s - e)\right] \quad [8]$$

where:

λ_v = *Latent heat of vaporization of water [MJ*kg^{-1}]*
ρ_w = *Density of water [kg*m^{-1}]*
$\Delta = de_s/dT$ = *Slope of saturated vapor pressure*
$R_n = S_n + L_n$ *[MJ*kg^{-1}]*
p_a = *Air density [kg*m^{-3}]*
C_a = *Specific heat of air [MJ*kg^{-1}]*
C_{atm} = *Atmospheric conductance [m*d^{-1}]*
e = *Vapor pressure of the atmosphere [kPa]*
$e_s(T)$ = *Current saturated vapor pressure of the atmosphere, function of T [kPa]*
$\gamma*$ = *Psychrometic constant [kPa/°C]*

where:

$$\gamma* = \left(1 + \frac{C_{atm}}{C_{con}}\right)\gamma$$

where:

C_{con} = Canopy conductance [m*day^{-1}]

$$C_{atm} = v * \frac{k^2}{ln\left(\frac{z_{ref}-z_0}{z_{rough}}\right) ln\left(\frac{z_{ref}-z_0}{z_{vap}}\right)}$$

where:

k = *Von Karman constant [0.42]*

z_{ref} = *Reference height [m]*

v = *Wind velocity [m*day^{-1}]*

z_0 = *Zero-plane displacement height [m]*

z_{rough} = *Roughness height [m]*

z_{vap} = *Vapor Roughness height [m]*

These parameters are primarily derived from ground surface roughness and canopy height characteristics. Canopy conductance is subsequently estimated as a function of the vegetative LAI (Dingman, 2002):

$$C_{con} = 0.5 * c_{leaf} * LAI$$

where:

c_{leaf} = *Leaf conductance (m/d) calculated after Dingman 2002*

Within the HMETS model, Infiltration is calculated the following (Martel et al, 2017):

$$M_{inf} = R * \left(1 - \alpha * \frac{\phi_{soil}}{\phi_{soil}^{max}}\right) \quad [9]$$

where:

$M_{inf} = Infiltration\ rate$ *[mm*day^{-1}]*

R = *Rainfall/snowmelt rate [mm*day^{-1}]*

α = *Unitless land use parameter HMETS_RUNOFF_COEFF*

ϕ_{soil} = *Top soil layer water content [mm]*

ϕ_{max} = *Maximum soil storage [mm]*

where:

$$\phi_{max} = Hn(1 - SF)$$

where:

H = *Soil layer thickness [mm]*

n = *porosity*

SF = *Stone fraction (typically 0)*

Percolation denotes the net downward movement of water from one soil or aquifer layer to another, primarily driven by moisture potential gradients. Within HMETS a linear percolation algorithm is chosen:

$$M_{perc} = k\phi_{soil} \quad [10]$$

where:

M_{perc}? $Percolation\ rate$ *[mm*day^{-1}]*
*k = Soil Parameter PERC_COEFF [1*day^{-1}]*
ϕ_{soil} *= Top soil layer water content [mm]*

Moreover, baseflow represents the contribution of water from an aquifer or deeper soil layers to surface water bodies, typically driven by a hydraulic head gradient between fully saturated subsurface zones and the stream channel. It can be conceptualized as the combined effect of deep groundwater discharge and delayed release from streambank storage. In HMETS, a common linear approach is used where baseflow is proportional to storage:

$$M_{base} = k\phi_{soil} \quad [11]$$

where:

$M_{base} = Baseflow\ rate$ *[mm*day^{-1}]*
k = Baseflow coefficient BASEFLOW_COEFF [1/d]
ϕ_{soil} *= Water storage in soil or aquifer layer [mm]*

Next, soil evapotranspiration refers to the transfer of water from soil layers to the atmosphere through the combined processes of evaporation and plant transpiration. The rate of evapotranspiration is influenced by factors such as soil moisture availability, vegetation type, phenological stage of the plants, and meteorological conditions including solar radiation, wind speed, humidity, and air temperature. Within Raven-HMETS, soil evapotranspiration is estimated via an uncorrected evaporation algorithm, where soil water is depleted at the maximum rate until the soil moisture is exhausted:

$$M_{evap} = PET \quad [12]$$

where:

*PET = Potential evapotranspiration rate [mm*day^{-1}]*

Canopy evaporation involves the transformation of intercepted water on the vegetative canopy into atmospheric water vapor. The rate of this process is governed by plant species, phenological stage, and environmental conditions including solar radiation, wind speed, humidity, and air temperature. HMETS calculates canopy evaporation via a complete canopy evaporation algorithm where all moisture intercepted by the canopy is assumed to evaporate instantaneously, resulting in the immediate return of this water to the atmosphere. This assumption also applies in the absence of a canopy. For snow canopy evaporation, intercepted snowfall evaporates instantaneously, contributing to atmospheric moisture.
Another process included in HMETS is a convolution algorithm. Convolution governs the release of water from a convolution unit - where it may have been added by other hydrological processes – to any designated storage compartment. It is calculated by the transfer function *UH*:

$$UH(t) = \frac{1}{t}\frac{(\beta t^{a})}{T(a)}\exp(-\beta t) \quad [13]$$

where:

α and β are land use parameters (GAMMA_SHAPE and GAMMA_SCALE)
t= time

T= Tempaerature [°C]

Lastly, a snow balance process is included. Snow balance algorithms are employed to simulate the tightly coupled mass and energy balance equations that govern snowpack melting, refreezing, and the dynamics of liquid water within the snow matrix. Within HMETS, the snowmelt model outlined in Martel et al., (2017.) is a simplified, single-layer approach incorporating degree-day freezing. It tracks both the liquid water content within the snowpack and the snow water equivalent (SWE). The refreeze rate, which is limited by the availability of water, is expressed as follows:

$$M_{rf} = K_f * (T_{rf} - T_{di})^{\,f} \quad [14]$$

where:

$M_{rf} = refreeze\ rate\ [mm*day^{-1}]$
K_f = *Land use property REFREEZE_FACTOR*
T_{rf} = *Degree day refreeze factor (land use property DD_REFREEZE_TEMP)*
f = *Land Use Parameter REFREEZE_EXP*

The water retention capacity, or the maximum liquid water content in the snow, fluctuates throughout the year, depending on the cumulative snowmelt:

$$SWI = \max(SWI_{min}, SWI_{max} * (1 - \alpha * M_{cumul}) \quad [15]$$

where:

SWI_{min} *and* SWI_{max} = *Land use parameters SNOW_SWI_MIN and SNOW_SWI_MAX*
α = *Land use parameter SWI_REDUCT_COEFF*
M_{cumul} = *Cumulative melt since last period of zero snow*

2.3.2.5 Strengths and Advanced Features

The Raven framework is unique in its ability to emulate established hydrological models, providing a platform for comparative analyses or extending existing models. Its modular design allows users to select only the components relevant to their study, ensuring efficiency and precision. Raven supports gridded meteorological data, making it ideal for incorporating climate models or regional forecasts. It also offers diagnostic tools to ensure accuracy and evaluate the appropriateness of model configurations.
Advanced users can leverage tools like RavenR, Ostrich, and BasinMaker to streamline calibration, analyze uncertainties, and manage large datasets. These tools, combined with Raven's flexible input and output options, make it a powerful resource for hydrological research and watershed management.

2.3.2.6 Applications

Several studies have applied the Raven hydrological modelling framework in practical watershed management and climate impact analysis, demonstrating its flexibility and process-based strengths across diverse hydrologic conditions and data availability levels.

A notable application by (Chernos et al., 2023) illustrates how Raven can support forest management planning by improving upon traditional Equivalent Clearcut Area (ECA) approaches. Using a semi-distributed HBV-type model within Raven, the study assessed the hydrological impacts of forest disturbance and climate change in a mountainous British Columbia watershed. The model outperformed the ECA method by capturing spatial and temporal variability in streamflow response and identifying high-elevation areas as more hydrologically sensitive. Simulations under projected climate scenarios further highlighted risks of earlier freshet timing and lower summer flows. This demonstrates Raven's utility for risk-based land use planning, especially under changing environmental conditions.
In a related study, (Chernos et al., 2017) proposed an efficient, semi-distributed workflow using Raven to simulate streamflow in data-scarce catchments. By combining simplified HBV-type modelling, modular input preparation, and automated calibration, the study showed how hydrological processes like snowmelt and soil storage dynamics can be effectively represented with low computational cost. This makes Raven suitable not only for detailed studies but also for applied watershed management tasks in practice.
(Chlumsky et al., 2021) extended Raven's application by developing a blended model approach that simultaneously calibrates both hydrological process representations and their parameters. This method allows for automated identification of dominant processes and reduces structural uncertainty, enhancing model robustness across varying catchment conditions.
(Goodbrand et al., 2022) applied Raven to investigate hydrological responses to forest harvesting in foothill conifer forests under summer-dominated precipitation regimes. Their study emphasized the importance of teleconnections, subsurface storage, and precipitation timing in shaping streamflow responses, and demonstrated Raven's strength in representing these complex interactions within variable climates and landscapes.
(Taheri et al., 2023) advanced the Raven framework by integrating a physically based emulation of fill-and-spill processes common in depression-dominated catchments. Their analytical formulation enables the representation of threshold-driven runoff generation from small surface storages at the catchment scale, providing an efficient and scalable approach particularly suited for prairie and boreal regions.
In Summary, Raven ensures a semi-distributed, customizable perspective in the model ensemble, complementing the other models.

2.3.2.7 Model Setup and Implementation in the Eyach Catchment

Model Discretization

The Raven model, using the HMETS conceptualization, was configured in a semi-distributed setup with multiple Hydrologic Response Units (HRUs) representing the Eyach catchment. To ensure full transparency and reproducibility, the five essential template input files were fully customized for the study (see Appendix A), where both the input file structures and summary tables of their calibrated parameters are provided.
The .rvi file defines the general model configuration, including the simulation period (1975–2019), selected hydrological processes (e.g., snow balance, multilayer soil moisture dynamics), routing settings, and output diagnostics. Custom outputs such as daily snow water equivalent and soil moisture levels were configured to support the evaluation of water balance components.

The model was set up with a three-layer soil profile (SOIL_MULTILAYER 3), consistent with stratifications observed in the Eyach catchment according to the BK50 soil mapping series.
The RVH file captures the spatial discretization of the catchment. Since the Eyach catchment naturally comprises five distinct subbasins, the model structure reflects this by defining five subbasins, each assigned to a single Hydrologic Response Unit (HRU). No additional delineation was performed. The physical properties of the HRUs, including area, elevation, slope, aspect, land use class, and soil profile, were derived through GIS analysis based on input datasets, namely land use data, the BK50 soil mapping series, and a digital elevation model (DEM).
The RVP file specifies the land surface and soil characteristics used in the simulations. Soil profiles were constructed based on land use classifications and soil property information obtained from the BK50 dataset. One of the most abundant soil types in the Eyach catchment, according to the BK50 soil map, is Braunerde, which was also dominant across the catchment. For the Raven-HMETS model setup, the soil type "b15" was chosen to represent this classification. Relevant soil attributes, including physical properties for the defined layers, were exported from an Excel database provided by the Federal State Office for Geological Resources and Mining (LGRB, 2019). Land use and vegetation classes were similarly parameterized based on classified land cover data for the study area.
The RVC file sets the initial conditions for the simulation period, prescribing uniform initial soil moisture levels across all soil layers and initial snowpack values, ensuring model stability during the spin-up and calibration phases.
For model evaluation, specific time periods were defined using the :EvaluationPeriod command in the RVI file. A warm-up period was established from 1st January 1975 to 31st December 1977, ensuring the model reached dynamic equilibrium before calibration. The calibration period was set from 1st January 1978 to 31st December 1999, during which model parameters were optimized using the OSTRICH calibration tool (detailed on page 28). Subsequently, a validation period was defined from 1st January 2000 to 31st December 2019 to independently test model performance.
The RVT file organizes the links to the meteorological forcing data and observed discharge data required for model operation and calibration. For meteorological inputs, the file redirects to four separate forcing files containing daily time series for temperature **(**BW6BroNT.rvt**),** relative humidity (BW6BroRELH.rvt**),** wind speed (BW6BroWIND.rvt**),** and global radiation (BW6BroRAD.rvt**).** In addition, observed streamflow data are included via redirection to two files: BW6Observed.rvt and BW6Observed_2.rvt**.** These contain discharge measurements for the main Eyach River and the Brotenaubach tributary, respectively, and were essential for calibrating the model based on observed runoff behavior during the calibration period.
Evaluation metrics, including the Nash-Sutcliffe Efficiency (NSE), Root Mean Square Error (RMSE), and Percent Bias (PBIAS), were configured directly in the RVI file to facilitate objective assessment of model performance. The detailed procedures for calibration, model evaluation, and statistical performance analysis are described in the following sections.

Nash- Sutcliffe efficiency (NSE)

The Nash-Sutcliffe efficiency (NSE), originally introduced by Nash and Sutcliffe, (1970) is a widely used performance metric in hydrology for evaluating how well a model simulates

observed streamflow. It measures the proportion of the variance in observed discharge explained by the model, with a value of 1 indicating a perfect match, and a value of 0 meaning the model performs no better than using the mean of the observed values (Nash & Sutcliffe, 1970). In this study, the NSE was calculated following the conventional formulation as used in (Törnros and Menzel, 2010):

$$R^2 = 1 - \frac{\sum_{t=1}^{T}(Q_{sim,t} - Q_{obs,t})^2}{\sum_{t=1}^{T}(Q_{obs,t} - \overline{Q}_{obs})^2} \quad [16]$$

where:

$Q_{sim,t}$ = *Simulated discharge at time step t [m³*s⁻¹]*
$Q_{obs,t}$ = *Observed discharge at time step t [m³*s⁻¹]*
$\overline{Q}_{obs}$ = *Mean of observed discharge [m³*s⁻¹]*
T= Total number of time steps

This formula offers a quantitative framework for assessing model performance across different climatic conditions and periods. Its strength lies in its sensitivity to peak flow reproduction and its ability to evaluate model adequacy in terms of both magnitude and temporal variation of discharge, making it especially suitable for hydrological applications involving runoff simulation under variable climatic regimes (Törnros & Menzel, 2010).

Root mean Square Error (RMSE)

The root mean square error (RMSE) is a widely used statistical metric for model evaluation, particularly when the underlying error distribution is assumed to be Gaussian. RMSE emphasizes larger errors due to its squared term, making it a more sensitive measure of model performance when compared to the mean absolute error (MAE). It is especially effective in reflecting the variance and distribution of model residuals. RMSE is computed as (Chai and Draxler, 2014):

$$RMSE = \sqrt{\frac{1}{n}\sum_{i=1}^{n}(e_i)^2} \quad [17]$$

where:

e_i = *difference between observed and simulated values*
n= Total number of data points or observations in the dataset

According to Chai and Draxler (2014), RMSE is not ambiguous in its interpretation and satisfies the triangle inequality, qualifying it as a valid distance metric. It is therefore considered appropriate and informative for model performance assessment in geoscientific applications, including hydrological modelling.

Percent Bias (PBIAS)

The Percent Bias (PBIAS) statistic measures the average tendency of the simulated flows to be larger or smaller than their observed counterparts do. The optimal value is 0.0, with positive values indicating a model bias toward underestimation, while negative values indicate a bias toward overestimation. It is calculated as (Gupta Hoshin Vijai et al., 1999):

$$PBIAS = \frac{\sum_{i=1}^{n}(Q_i^{sim} - Q_i^{obs}) * 100}{\sum_{i=1}^{n} Q_i^{obs}} \quad [18]$$

where:

Q_i^{obs} = *Observed flow at the i-th time step [m³*s⁻¹]*

Q_i^{sim} = *Simulated flow at the i-th time step [m³*s⁻¹]*

n= Total number of Observations

Calibration with OSTRICH

The Optimization Software Toolkit for Research Involving Computational Heuristics (OSTRICH) (Matott, 2017) is a versatile, model-independent tool designed to automate the processes of model calibration and optimization without the need for users to develop additional software. With a user-friendly interface, OSTRICH requires minimal user input, typically limited to filling out essential sections of the input file (ostIn.txt) and creating template model input files. The program also offers a wide range of optional features, including parallel processing, model pre-emption, algorithm restarts, parameter statistics, and predictive uncertainty analysis. These capabilities are designed to enhance the flexibility and efficiency of model optimization. OSTRICH implements a variety of algorithms, including deterministic local search methods, heuristic global search techniques, and sampling methods aimed at defining parameter probability distributions. Some algorithms, like Levenberg-Marquardt, are specialized for non-linear least-squares calibration, while others, such as Pareto Archive Dynamically Dimensioned Search (DDS) and Simple Multi-Objective Optimization Test Heuristic (SMOOTH), are suitable for multi-objective optimization and calibration. Additionally, sampling-based algorithms like Generalized Likelihood Uncertainty Estimation, Rejection Sampling, and Metropolis-Hastings Markov Chain Monte Carlo are designed for uncertainty-based calibration. These algorithms offer flexibility to handle a range of problems with real-valued, combinatorial, and integer parameters. For this study, the Pareto Archive Dynamically Dimensioned Search (DDS) algorithm was chosen and executed with 5,000 function evaluations to calibrate model parameters efficiently.

The DDS algorithm is a stochastic, single-solution global optimizer designed for efficient calibration of computationally expensive models. It starts with a broad search across many parameters and progressively narrows to a local search by dynamically reducing the number of parameters perturbed. Perturbations are randomly applied using normal distributions, and boundary constraints are enforced via reflection. DDS is particularly effective when the goal is to find good near-optimal solutions (Tolson & Shoemaker, 2007).

The Generalized Composite Objective Function (GCOP) structure was used to enable multi-objective calibration against two discharge datasets by minimizing a combined cost function (SumNS). The Additive Penalty Method (APM) was specified as a required placeholder.

To set up and run OSTRICH effectively, several key files and configurations are required. Below is a table (Table 4) summarizing the primary files needed for an OSTRICH setup, based on the general structure and requirements of the program.

The ostIn.txt configuration file and all associated template files are provided in Appendix A.

Table 4. Description of Key Files Used in the Ostrich Optimization Framework.

File	Description	Example
ostIn.txt	The main input file for OSTRICH, where the user specifies the program type, objective function, calibrated parameters and their bounds, optimization algorithms, and respective configurations as e.g. perturbation values, maximum iterations, etc.	`ostIn.txt`
ModelExecutable	The batch file or executable that runs the model being calibrated or optimized. This is the main model file that OSTRICH interacts with.	`Ost-RAVEN.bat`
Template Model Files	The model input files that contain the necessary data or template information for the simulation model. These files are used to initialize model variables during optimization.	`BW6.rvp.tpl`, `BW6.rvt.tpl`
Model Output Files	Output files where results from the model simulation will be written (e.g., diagnostic outputs, model performance metrics).	`Raven_HMETS_Diagnostics.csv`
Batch or Script Files	Scripts that handle various tasks, such as saving the best model during optimization or pre-processing data before running the optimization.	`save_best.bat`, `initParams.bat`
Response Variable Files	Files containing the model's output variables to track performance metrics (e.g., Nash-Sutcliffe efficiency) during optimization.	`Raven_HMETS_Diagnostics.csv`
External Tools (Optional)	If using external optimization or model interfacing tools (e.g., PIGEON), additional configuration files may be required for these integrations.	Depends on external tools used

2.3.3 Brook 90 & LWF-BROOK90

BROOK90 is a physically based, one-dimensional hydrological model developed to simulate vertical water movement and evapotranspiration within the soil–plant–atmosphere system. Originally written in FORTRAN by Federer (1995) and later refined by Federer et al. (2003), the model emphasizes detailed representation of water fluxes at a single location.(Vorobevskii et al., 2022, 2020). In 2001, Hammel and Kennel introduced LWF-BROOK90, an extension that incorporated parameterizations for soil hydraulic functions based on Mualem, (1976) and Van Genuchten, (1980), along with dynamic representations of vegetation attributes such as leaf area index and stand density. Further advancements led to the integration of LWF-BROOK90 into the R programming environment by Schmidt-Walter in 2020, resulting in the LWFBrook90R package, which facilitates model execution and analysis within R.

2.3.3.1 Model Abstraction

BROOK90 operates as a lumped, one-dimensional model focused on simulating vertical hydrological fluxes within the soil–plant–atmosphere system. Designed to represent processes at a single point location, it partitions precipitation into interception, infiltration, percolation, and runoff components. Net throughfall and snowmelt can infiltrate the soil matrix, bypass the matrix via macropore flow, or contribute directly to surface runoff and downslope flow. The model supports detailed soil characterization using up to 25 distinct layers, each with unique hydraulic properties (Vorobevskii et al., 2022, 2020).
Soil water movement is resolved using Richards' equation (Richards, 1931), which governs vertical unsaturated and saturated flow in porous media by combining Darcy's law (in section 2.3.3.4 Hydrological Processes) with the continuity equation. The general mixed-form of Richards' equation is given as:

$$\frac{\delta\theta}{\delta t} = z\left[K(\theta)\left(\frac{\delta\psi}{\delta z}+1\right)\right] \quad [19]$$

where:

θ = *Volumetric water content* $[m^3 * m^{3-1}]$
$K(\theta)$ = *Unsaturated hydraulic conductivity* $[m * s^{-1}]$
ψ = *Soil water pressure head [m]*
z = *Vertical Coordinate [m]*
t = *time [s]*

This formulation, described in Farthing and Ogden, 2017 allows the model to simulate dynamic moisture redistribution between soil layers based on water potential gradients and soil-specific conductivity.
Although BROOK90 does not explicitly express a full water balance equation as a single formula, the model simulates a complete balance of inputs and outputs within the root zone. This can be summarized as:

$$\Delta\theta = P+M-E-R-D \quad [20]$$

where:

$\Delta\theta = Change\ in\ soil\ water\ storage\ [mm]$
P= Precipitation input [mm]
M= Snowmwelt [mm]
E= Evapotranspiration [mm]
R= Surface runoff or lateral flow [mm]
D= Deep percolation to groundwater [mm]

This water balance logic is implemented across all soil layers and supports the simulation of key processes such as transpiration, infiltration, and drainage. The LWF-BROOK90 extension incorporates dynamic vegetation parameters, enabling responsive simulation of plant–soil–atmosphere interactions (Schmidt-Walter et al., 2020, Hammel & Kennel, 2001). Its implementation in the LWFBrook90R package Schmidt-Walter et al., 2020 facilitates model setup, execution, and output analysis within the R environment.

2.3.3.2 Input Files

The model requires daily meteorological inputs such as precipitation, maximum and minimum air temperature, solar radiation, vapor pressure, and wind speed. These inputs drive the simulation of hydrological processes within the model (Vorobevskii et al., 2022, 2020). Moreover the model , combined, requires over 50 general, vegetation and soil parameters (Schmidt-Walter et al., 2021, 2020).

2.3.3.3 Outputs

Upon execution, LWF-BROOK90 generates a comprehensive set of output data detailing various hydrological components, including transpiration, interception, soil and snow evaporation, streamflow, and soil water fluxes through the soil profile. These outputs are essential for analysing the water balance and understanding the dynamics within the soil–plant–atmosphere system.

2.3.3.4 Hydrological Processes

The BROOK90 model employs the Shuttleworth-Wallace approach (Shuttleworth and Wallace, 1985) to estimate evaporation, representing an advancement over the traditional Penman–Monteith equation by separately calculating evaporation from a closed canopy (PM_c) and from the underlying bare substrate (PM_s), each using a Penman–Monteith-type formulation.:

$$\lambda E = C_c PM_c + C_s PM_s \quad [21]$$

where:

*λE = Total evaporation of the crop [W*m^{-2}]*
$PM_c = \Delta A + \left\{pc_p D - \Delta r_a^c A_s\right\} / \left(r_a^a + r_a^c\right)/\Delta + \gamma\{1 + r_s^c / \left(r_a^c\right)\}$ *[kg*m^{-2}*s^{-1}]*
$PM_s = \Delta A + \left\{pc_p D - \Delta r_a^s (A - A_s)\right\} / \left(r_a^a + r_a^s\right)/\Delta + \gamma\{1 + r_s^s / \left(r_a^a + r_a^s\right)\}$ *[kg*m^{-2}*s^{-1}]*
$C_c = \{1 + R_c R_a / R_s(R_c + R_a)\}^{-1}$ *[-]*
$C_s = \{1 + R_s R_a / R_c(R_s + R_a)\}^{-1}$ *[-]*

where:

$R_a = (\Delta + \gamma) r_a^a$ *[s*m⁻¹]*
$R_c = (\Delta + \gamma) r_a^c + \gamma r_s^c$ *[s*m⁻¹]*
$R_s = (\Delta + \gamma) r_a^s + \gamma r_s^s$ *[s*m⁻¹]*

where:

$r_s^c = r_{ST} / 2L$ *is the bulk stomatal resistance of the canopy*
$r_a^c = r_b / 2L$ *is the resistance of the canopy*

in which:

A = Total energy flux leaving the complete crop as sensible latent heat per unit ground area [W m^{-2}]
A_s = Total energy flux leaving the substrate as sensible latent heat per unit ground area [W m^{-2}]
c_p= Specific heat at constant pressure [J kg^{-1} K^{-1}]
D = Vapor pressure deficit at reference height: [e_w (T_x) - e_x] [mb]
e_w (T) = Saturated vapor pressure at temperature T (T = T_x, T_0, T_s) [mb]
L = Projected area of leaf per unit ground area (leaf area index) [dimensionless]
r_{ST} = Mean stomatal resistance [s m^{-1}]
r_b = Mean boundary layer resistance per unit area of vegetation [s m^{-1}]
r_a^a = Aerodynamic resistance between canopy source height and reference level [s m^{-1}]
r_a^c = Bulk boundary layer resistance of the vegetative elements in the canopy [s m^{-1}]
r_a^s = Aerodynamic resistance between the substrate and the canopy source height [s m^{-1}]
r_s^c= Bulk stomatal resistance of the canopy [s m^{-1}]
r_s^s = Surface resistance of the substrate [s m^{-1}]
γ = Psychrometric constant [mb (K)$^{-1}$]
ρ = Density of air [kg m^{-3}]

The BROOK90 model simulates infiltration and vertical water flow using a physically based approach that integrates both classical soil physics and enhancements to account for soil heterogeneity, such as macropore flow. Vertical fluxes are driven by Darcy's law (Darcy, 1856) and are resolved across multiple soil layers, allowing detailed tracking of water movement through the unsaturated zone. BROOK90 computes vertical water flux between soil layers using a Darcy-type formulation, where the interlayer hydraulic conductivity *K* is the geometric mean of the conductivities of two adjacent layers K_i and K_{i+1} (Haverkamp and Vauclin, 1979). The hydraulic gradient *G* is calculated as (Federer et al., 2003):

$$G = \frac{\psi_i - \psi_{i+1}}{\min(D_i, D_{i+1})} \quad [22]$$

where:

G= Hydraulic gradient [-]

$\psi = Total\ water\ potential$
$D = Thickness\ of\ respective\ soil\ layer\ [m]$

This formulation allows for robust computation of unsaturated flow in heterogeneous soil profiles. The model uses an adaptive time step (minimum of 0.5 days or time to equilibrium between layers) to ensure numerical stability and precision. Drainage from the lowest soil layer is calculated using the saturated hydraulic conductivity of that layer and a gravitational gradient (Federer et al., 2003).

Infiltration is modelled using both classical top-down infiltration and an alternative macropore-assisted vertical infiltration method. The latter addresses the non-uniform movement of water in structured or heterogeneous soils (Beven and Clarke, 1986). When macropore flow is enabled, incoming water is distributed across soil layers from the surface down to a defined depth D_t, typically set equal to the effective root depth D_r. The fractional infiltration F_i into a given layer *i* is determined by:

$$F_i = (\frac{D_i}{D_t})^{\alpha} - (\frac{D_{i-1}}{D_t})^{\alpha} \quad [23]$$

where:

α= *Shape parameter controlling depth distribution of infiltrating water*

For example, α = 0 simulates a sharp wetting front (classic infiltration), α = 0.3 represents exponential decay with depth, and α = 1 assumes uniform infiltration throughout the root zone. This dual infiltration framework enables BROOK90 to represent both conventional and preferential flow dynamics, making it especially suitable for simulating forested or structured soils with vertical heterogeneities (Federer et al., 2003).

BROOK90 simulates snow accumulation and melt using a temperature-index (degree-day) method. Precipitation is partitioned into rainfall or snowfall based on a threshold air temperature. When air temperature falls below the defined snow threshold (typically ~0°C), precipitation is classified as snow and added to the snowpack. Conversely, when temperature exceeds this threshold, melt is initiated at a rate proportional to the difference between air temperature and the threshold. The model does not explicitly track snowpack energy states but simulates snowmelt via (Hock, 2003):

$$M = DDF * (T - T_{melt}), for\ T > T_{melt} \quad [24]$$

where:

M = Daily snowmelt [mm]
DDF = Degree-day factor [mm °C⁻¹ day⁻¹]
T = Daily mean air temperature [°C]
T_{melt} *= Melt temperature threshold [°C]*

2.3.3.5 Strengths and Advanced Features

LWF-Brook90 stands out among hydrological models for its capacity to represent the complexity of forest ecosystems through a combination of detailed biophysical parameterization and flexible structure. One of its most notable strengths lies in its species-specific parametrization, allowing for realistic simulation of both monospecific and mixed forest stands. Vegetation processes are dynamically modelled based on species-dependent attributes such as phenological development, rooting depth, leaf area index (LAI), and stomatal behaviour, enabling nuanced simulation of transpiration and interception processes across different forest types (Groh and Puhlmann, 2013; Schmidt-Walter et al., 2020).

The model also features a flexible soil representation, which divides the soil profile into up to 25 vertical layers. This structure allows a highly resolved simulation of water fluxes and storage changes across the unsaturated zone. LWF-Brook90 uses the Mualem–van Genuchten parameterization to define soil hydraulic properties, thereby supporting accurate simulation of soil moisture retention and percolation processes under diverse soil textures and conditions (Federer et al., 2003; Schmidt-Walter et al., 2020).

Evapotranspiration in LWF-Brook90 is computed using the Shuttleworth–Wallace framework, an energy-balance method that separates canopy transpiration from soil evaporation based on resistances and radiation partitioning. This approach provides a more realistic representation of evapotranspiration, especially in heterogeneous or sparse canopies typical of managed or natural forest stands (Federer et al., 2003; Shuttleworth and Wallace, 1985).

Another advanced capability is the model's suitability for scenario-based climate impact assessments. LWF-Brook90 has been effectively applied in combination with downscaled climate projections (e.g., RCP 4.5 and RCP 8.5 scenarios), enabling exploration of long-term changes in forest water balance, evapotranspiration, and drought risk under anticipated climate trends (Schmidt-Walter et al., 2020; Weis et al., 2023). This functionality positions the model as a valuable tool for forest water resource planning in the face of global environmental change.

2.3.3.6 Applications

(Schmidt-Walter et al., 2020) introduced LWF-Brook90R, an R-based implementation of the LWF-Brook90 soil–vegetation–atmosphere transfer model, designed for reproducible simulations and parameter sensitivity analysis. The model was applied to a short-rotation poplar plantation to investigate seasonal water balance dynamics. Results showed strong agreement between modelled and observed soil moisture, with notable seasonal drought stress, demonstrating the model's applicability in agroforestry and forest hydrology contexts.

(Lamacova et al., 2022) evaluated the performance of LWF-Brook90 in a forested headwater catchment dominated by Norway spruce. While the model effectively simulated streamflow and soil moisture, it notably underestimated interception losses, which accounted for over a quarter of the precipitation. The study highlighted the need to refine canopy process representations in order to improve predictive accuracy in forested systems with high interception potential.

Morales-Santos et al., 2025) applied LWF-Brook90R to simulate water balance components in a mixed forest in the Hessian Ried, Germany. Using long-term climate, soil, and vegetation data from pine, oak, and beech plots, the study assessed species-specific differences in

transpiration, interception, and soil water storage. The model performed well in simulating throughfall and highlighted greater drought stress in deciduous stands and lower drainage in pine due to canopy and soil effects. The results emphasize the importance of forest composition in water balance modelling under climate change conditions.
(Vorobevskii et al., 2024) developed and implemented a high-resolution operational soil moisture monitoring system for forests in central Germany using the LWF-Brook90 model. By integrating detailed forest inventory data, high-resolution soil maps, and daily meteorological inputs, the model simulates soil moisture conditions at 250 m resolution across large forest areas. The output is provided via an online platform to support forest management. Validation against soil moisture sensors at 51 stations showed strong agreement (median Pearson correlation of 0.76), with higher accuracy in deciduous than coniferous stands. The system enables real-time assessment of drought stress and supports adaptive forest management under climate change.
(Bauwe et al., 2012) applied LWF-Brook90 to simulate long-term soil moisture dynamics and drought risk in Scots pine (*Pinus sylvestris*) stands across northeastern Germany. Using daily climate data from 1951 to 2009, detailed soil information, and site-specific forest structure parameters, the model was run for 24 forest sites to assess spatial and temporal drought patterns. Results showed increasing drought frequency over time, particularly after the 1980s, and highlighted stronger drought effects in drier, sandier eastern locations. Sites with high LAI and shallow rooting were especially sensitive. The study demonstrates LWF-Brook90's suitability for evaluating forest drought risk under long-term climate variability.
LWF-Brook90's capacity to simulate different tree species makes it invaluable for exploring Objective 5.

2.3.3.7 Model Setup and Implementation in the Eyach Catchment

Model Discretization

The species considered in this work is *Picea abies*, chosen because it is the most abundant tree species in the Eyach catchment. Furthermore, to determine the vegetation period for *Picea abies*, two widely used phenological methods were applied: the Menzel method for budburst and the von Wilpert method for leaf fall. These methods rely on temperature data to estimate the start and end of the growing season. The Menzel method estimates the onset of the growing season by accumulating degree days based on daily mean temperature. A threshold temperature, typically 5°C, is used, and once a specified number of degree days is reached, budburst is predicted to occur, marking the beginning of the vegetation period (Menzel, 1997). The von Wilpert method calculates the end of the growing season by identifying when daily mean temperatures consistently fall below 5°C for several consecutive days, which signals the onset of dormancy and leaf fall (von Wilpert, 1990). These methods were applied using the `calc_vegperiod` function, which integrates the daily mean temperature (Tmean) data to determine the vegetation period. The species considered was *Picea abies,*, and a prior estimation of 3 years **(**est.prev = 3**)** was used to adjust for historical climatic conditions.
For the LWF-Brook90 model, soil input data were prepared using an Excel file that specifies the soil characteristics for the defined layers. The soil profiles were constructed based on land use classifications and soil property information obtained from the provided soil data. The data

file includes detailed soil attributes such as horizon, texture, bulk density (bd), gravel content, and the particle size distribution (sand, silt, and clay).

The bulk density data were derived from the SoilGrids dataset, which provides global soil properties at a 250-meter resolution. The rasters for the relevant depth ranges of 0-60 cm and 60-100 cm were extracted for the area surrounding the Eyach catchment. To focus on the specific area of interest, the rasters were cropped to match the boundary of the subcatchment where the model's central input cell is located.

For the 0-60 cm depth range, the rasters for 0-5 cm, 5-15 cm, 15-30 cm, and 30-60 cm were combined to calculate an average bulk density value for the entire range. Similarly, for the 60-100 cm depth range, the corresponding raster was used to determine the average bulk density for that layer.

The bulk density values were initially provided in centigrams per cubic centimeter (cg/cm^3). To align with the model's unit system, these values were converted to grams per cubic centimeter (g/cm^3) by dividing by 100. The resulting values were then used in the LWF-Brook90 model, providing an accurate representation of soil bulk density for the specified depth ranges.

The remaining soil attributes, including the physical properties for the defined layers, were applied as in the Raven-HMETS model setup, using the same values for the soil type Braunerde.

For the LWF-Brook90 model, the location- and site-specific parameters, the species-specific parameters, and the general model parameters were largely adopted from Weis et al., (2023), as detailed in Appendix B. Their work offers a well-calibrated and species-specific framework for temperate forest ecosystems, which served as a valuable foundation for this study. Since no site-specific observed parameters were available for the Eyach catchment, relevant parameters were extracted from their published setup and adapted for use within the R implementation of LWF-Brook90. Unlike their original use of the standard LWF-Brook90 interface, this study employed the R-based version of the model, requiring partial translation and selection of parameters. The specific parameter configuration used in this study is documented in Appendix B. Two exceptions were made to the Weis-based setup. First, the LAI values were not taken from Weis et al. (2023) but instead derived from regional observations reported by Battuvshin and Menzel, (2022). Their study, conducted in the central Black Forest at approximately 900 m elevation, reported maximum growing season LAI values of up to 3.2 m^2/m^2 using both hemispherical photography and LiDAR-derived metrics. Accordingly, a rounded maximum summer LAI of 3.0 m^2/m^2 was applied in this study. Second, the maximum rooting depth was set to 1.0 m to match the soil profile depth defined in the model setup.

As a final step, the precipitation data were corrected for wind and evaporation errors using the correct_prec function, following the methodology outlined by Richter (1995). This correction process ensures that rain gauge precipitation data is adjusted for potential biases due to wind exposure and evaporation effects, enhancing the accuracy of the precipitation measurements used in the model.

Addressing objective 5, LWF-B90 was applied to simulate hydrological response of different tree species. In this context, *Fagus sylvatica* and *Quercus robur w*ere chosen. Respective parameters were adapted based on the same source of *Picea abies.*

2.3.4 HBV-Light

The HBV model (Bergström, 1976, 1992; Lindström et al., 1997)) is a widely used conceptual model. It is named after the Hydrologiska Byråns Vattenavdelning unit at the Swedish Meteorological and Hydrological Institute (SMHI). The HBV-light version was developed in 1993 at Uppsala University using Microsoft Visual Basic and has since become widely adopted in educational programs at various universities (Seibert and Vis, 2012).

2.3.4.1 Model Abstraction

HBV is a semi-distributed model, allowing to divide a catchment into different sub catchments, vegetation zones as well as different elevation zones. The model is composed of several routines that simulate catchment discharge, typically on a daily time step. Snow accumulation and melt are determined using a degree-day approach within the snow routine. Depending on whether the temperature exceeds or falls below a specified threshold (P_{TT} °C), precipitation is classified as either rain or snow. Simulated Snow underlies a correction factor P_{SCF}, compensating snowfall measurements as well as snowpack evaporation. The soil routine models groundwater recharge and actual evaporation, depending on the available water storage. Runoff is calculated as a function of water storage within groundwater. Lastly, the routing routine uses a triangular weighting function to simulate runoff movement towards the catchment outlet (Seibert and Vis, 2012).
To represent these processes, HBV-light internally resolves a simplified water balance over time, capturing the dynamic change in storage as a function of incoming and outgoing fluxes. This can be generalized as:

$$\Delta S = P + M - E - Q \qquad [25]$$

where:

$\Delta S = Change\ in\ catchment\ storage\ [mm]$
*P= Precipitation [mm*day^{-1}]*
*M= Snowmelt [[mm*day^{-1}]*
*E= Actual Evapotranspiration [mm*day^{-1}]*
*Q= total runoff [mm*day^{-1}]*

HBV-light incorporates a preliminary adjustment phase, allowing state variables to shift from default starting values to levels that align with meteorological conditions and model parameters. Typically, a one-year duration is adequate for this initialization process (Seibert and Vis, 2012).

2.3.4.2 Input Files

The model can be run by implementing monthly or daily time series of air temperature, precipitation and potential evaporation rates, stored in the "ptq" file. Observed Streamflow may be added.

2.3.4.3 Outputs

Executing HBV-Light provides several output files:

- Dis.txt: Precipitation, temperature, snow, snowmelt, soil moisture, actual Evapotranspiration and Recharge results
- Peaks.txt: a comparison of observed and simulated streamflow
- Results.txt: detailed daily results of all output parameters (see table)
- Summary.txt: results of water balance analysis and model performance metrics

2.3.4.4 Hydrological Processes

Actual Evaporation (E_{act}) is calculated based on the water content in the soil box (Seibert and Vis, 2012). When the soil water content is above a certain threshold (P_{LP}), actual evaporation equals potential evaporation (E_{pot}). When the soil moisture content is lower, a linear reduction in evaporation is used. The Potential Evaporation (E_{pot}) is adjusted using a correction factor (P_{CET}), which accounts for deviations in the temperature from the long-term average. This correction factor helps simulate how temperature changes impact evaporation on any given day.

$$E_{act} = E_{pot} * \min\left(\frac{S_{SOIL(t)}}{P_{FC} * P_{LP,1}}\right) \quad [26]$$

where:

E_{act}: *Actual Evapotranspiration [mm]*
E_{pot}: *Potential Evaporation [mm]*
$S_{SOIL(t)}$: *current water content of the soil box [mm]*
P_{FC}: *maximum value of water content [mm]*
$P_{LP,1}$: *threshold of soil water content [mm]*

$$E_{pot} = \left(1 + P_{CET} * (T(t) - T_M)\right) * E_{POT,M,} but\ 0 > E_{POT(t)} < 2 * E_{POT,M} \quad [2]$$

where:

$E_{pot\ (t)}$: *Potential Evapotranspiration [mm]*
P_{CET}: *Correction factor*
$T(t)$: *Deviation of temperature on certain day*
T_M: *Long term mean of temperature*
$E_{POT,M,}$: *long term mean values of potential evapotranspiration*

The snow routine simulates the accumulation and melt of snow using the degree-day method (Seibert and Vis, 2012). A degree-day factor (P_{CFMAX}) is used to calculate snowmelt based on the temperature difference from a threshold temperature (P_{TT}). Snowmelt is simulated as long the temperature exceeds P_{TT}:

$$M = P_{CFMAX} * (T(t) - P_{TT} \quad [27]$$

where:

M = *Snowmelt [mm]*
P_{CFMAX} = *degree-day-factor [mm/d /°C]*
$T(t)$ = *Deviation of temperature on certain day*
P_{TT} = *Threshold temperature [°C]*

Meltwater and rain remain in the snowpack until they surpass a set fraction P_{CWH} [-] of its water equivalent. When temperatures fall below P_{TT}, refreezing of liquid water in the snowpack, R [mm d^{-1}], is determined using the refreezing coefficient P_{CFR} [-] (Seibert and Vis, 2012).

$$R = P_{CFR} * P_{CFMAX} * (P_{TT} - T(t)) \quad [28]$$

where:

R = *Amount of refreezing liquid water within snowpack [mm*day^{-1}]*
P_{CFR} = *Refreezing coefficient [-]*
P_{CFMAX} = *Degree-day-factor [mm*day^{-1} *°C^{-1}]*
P_{TT} = *Threshold temperature [°C]*
$T(t)$ = *Deviation of temperature on certain day*

Based on the sum of rain and snowmelt, the groundwater flux F(t) at a certain time step I(t) is computed, while the residual part of P(t) is allocated to the soil storage compartment. The partitioning is governed by the ratio of the soil box's current water content, S_{SOIL}(t) (mm), to its maximum capacity, P_{FC} (mm) (Seibert and Vis, 2012).

$$\frac{F(t)}{I(t)} = \left(\frac{S_{SOIL}(t)}{P_{FC}}\right)^{P_{BETA}} \quad [29]$$

where:

$F(t)$ = *Groundwater flux [mm/d]*
$I(t)$ = *Groundwater flux at certain time step [mm*day^{-1}]*
$S_{SOIL}(t)$ = *Current water content of soil box [mm]*
P_{FC} = *Maximum value of water content [mm]*
P_{BETA} = *Non-linearity exponent [-]*

Groundwater recharge is directed into the upper groundwater box (S_{UZ}, mm), with the maximum percolation rate to the lower groundwater box (S_{LZ}, mm) regulated by P_{PERC} (mm/d). Runoff from the groundwater boxes is calculated using two or three linear outflow equations (P_{K0}, P_{K1}, and P_{K2}), depending on whether S_{UZ} exceeds the threshold P_{UZL} (mm) (Seibert and Vis, 2012):

$$Q_{GW(t)} = P_{K2} * S_{LZ} + P_{K1} * S_{UZ} + P_{K0} * \max(S_{UZ} - P_{UZL,0}) \quad [30]$$

where:

$Q_{GW(t)}$ = *Groundwater recharge [mm]*
P_{K2} = *Otflow equation [day^{-1}]*
P_{K1} = *Outflow equation [day^{-1}]*
P_{K0} = *Outflow equation [day^{-1}]*
S_{LZ} = *Lower groundwater box [mm]*
S_{UZ} = *Upper groundwater box [mm]*
$P_{UZL,0}$ = *Threshold value [mm]*

The runoff is ultimately converted into simulated runoff [mm/d] using a triangular weighting function defined by the parameter P_{MAXBAS}.

$$Q_{sim(t)} = P_{MAXBAS} \sum i = 1c(i) * Q_{GW(t-i+1)} \quad [31]$$

where:

$$c(i) = \int_{i-1}^{i} \frac{2}{P_{MAXBAS}} - u - \frac{P_{MAXBAS}}{2} * \frac{4}{p_{MAXBAS}^2} du$$

$Q_{sim(t)}$ = *Simulated Runoff [mm*day^{-1}]*
P_{MAXBAS} = *Base width of unit hydrograph [day]*

2.3.4.5 Strengths and Advanced Features

HBV-Light includes a simple glacier melt module based on Konz and Seibert, (2010), which activates once the seasonal snowpack has fully melted. Glacier ice melt is then simulated using an enhanced degree-day approach that accounts for the lower albedo of ice by applying a melt factor greater than that used for snow. Additionally, the model incorporates an aspect correction to reflect the influence of slope orientation on melt rates.

Moreover, regarding the upper groundwater box outflows, one single outflow may be introduced:

$$Q_{GW(t)} = P_{K2} * S_{LZ} + P_{K1} * S_{UZ\ ALPHA}^{P} \quad [32]$$

where:

$Q_{GW(t)}$ = *Groundwater recharge [mm]*
P_{K2} = *Outflow equation [day^{-1}]*
P_{K1} = *Outflow equation [day^{-1}]*
S_{LZ} = *Lower groundwater box [mm]*
$S_{UZ\ ALPHA}^{P}$ = *Upper groundwater box [mm]*

The configuration of groundwater storage can be adjusted (Uhlenbrook et al., 1999). In a single-box model, groundwater is stored in one compartment, with outflows triggered only when storage exceeds certain thresholds. A three-box setup consists of stacked compartments, where flow between them is regulated by specific parameters. Another approach splits recharge into two fractions: one enters storage immediately, while the other is gradually added over multiple time steps to a separate storage unit. This method is particularly useful for catchments with deeper groundwater flow paths (Seibert, 2000; Seibert and McDonnell, 2010; Seibert and Vis, 2012).

Using multiple elevation zones is advisable when temperature variations within a catchment are influenced by altitude differences. Each zone typically covers around 100 meters in elevation. This approach is generally sufficient for educational purposes, while research applications may require testing and comparing different configurations for improved accuracy and performance.

2.3.4.6 Applications

HBV-Light has been extensively applied in hydrological research worldwide, demonstrating its adaptability across diverse climatic and geographical conditions (Jenicek et al., 2018; Muauz et al., 2024; Usman et al., 2022).

Muaz et al. (2024) utilized HBV-Light to estimate groundwater recharge in the upper Awash River Basin, Ethiopia. By incorporating daily temperature, precipitation, and evapotranspiration data, the model effectively simulated streamflow dynamics. Their findings provided crucial insights into regional water balance and potential recharge zones, supporting sustainable water resource management in the basin. Similarly, Khan et al. (2022) applied HBV-Light for streamflow simulation in the Soan River Basin, Pakistan. The model was calibrated and validated using data from 2001 to 2013, with performance assessed through Nash-Sutcliffe Efficiency and Kling-Gupta Efficiency metrics. The study highlighted HBV-Light's suitability for semi-arid environments, demonstrating reliable hydrological modelling under variable climatic conditions.

In a different setting, Jenicek et al. (2018) applied HBV-Light to 14 alpine catchments in Switzerland to assess how future reductions in snowpack may affect spring and summer low flows. Using CH2011 climate scenarios, they projected substantial decreases in maximum snow water equivalent (up to 75% below 2200 m a.s.l.) and earlier melt timing by up to four weeks. These shifts weakened the contribution of snowmelt to summer runoff, especially at lower elevations, highlighting the model's ability to simulate elevation-dependent snow dynamics and drought sensitivity under climate change.

2.3.4.7 Model Setup and Implementation in the Eyach Catchment

Model Discretization

For model discretization, the standard configuration of the HBV-Light model was applied. This setup includes two groundwater boxes, which represent the rapid and delayed components of the catchment's groundwater response to precipitation and evapotranspiration. A one-year model warm-up period was implemented from 01/01/1975 to 31/12/1975 to allow initial conditions to stabilize. Consequently, the simulation outputs and all subsequent analyses were based on the period from 1976 to 2019. For simplification, the model was discretized using a single elevation zone and a single vegetation zone, reflecting average catchment characteristics.

Calibration

The HBV-Light model was calibrated using two optimization techniques. The first approach, GAP, is a hybrid method that initially employs a genetic algorithm to evolve a population of parameter sets through selection and recombination. Following this, Powell's method, a derivative-free optimization technique, is used to fine-tune the parameter sets to achieve optimal model performance. This method is integrated into the HBV-Light software and has been extensively described in the literature (Vidmar et al., 2020) For comparison, the model was also calibrated using Powell's method alone, which is well-suited for optimizing complex, nonlinear functions without the need for derivative information.

Each calibration approach was executed 10,000 times to ensure robustness and to assess the variability in the parameter estimates. The calibration process focused on two main categories of parameters: Vegetation Zone Parameters, which are related to the characteristics of the vegetation within the catchment area, and Catchment Parameters, which describe the physical and hydrological properties of the catchment, such as soil moisture storage, groundwater response, and runoff coefficients. Detailed values and ranges for these parameters can be found in Table 5.

Table 5. Parameter boundaries for HBV-Light model calibration.

Parameter	Lower Limit	Upper Limit	Description
TT	-1	2.5	Temperature threshold (°C) for snow/rain separation
CFMAX	0	10	Degree-day factor (mm/°C/day) for snowmelt
SP	0	1	Snow pack water-holding capacity (fraction)
SFCF	0	5	Snowfall correction factor
CFR	0	0.1	Refreezing coefficient (fraction of meltwater refreezing)
CWH	0	0.2	Water-holding capacity of snow (fraction of SWE)
FC	100	300	Field capacity of the soil (mm)
LP	0	1	Threshold for limiting evapotranspiration (fraction of FC)
BETA	0.1	6	Shape parameter for soil runoff relationship
PERC	0	10	Percolation rate to lower groundwater zone (mm/day)
UZL	0	100	Threshold for quick runoff from upper groundwater (mm)
K0	0	0.5	Recession coefficient for quick runoff (1/day)
K1	0	0.3	Recession coefficient for upper groundwater (1/day)
K2	0	0.3	Recession coefficient for lower groundwater (1/day)
MAXBAS	1	10	Routing parameter (days) for triangular weighting function
PCALT	0	10	Precipitation lapse rate (mm/km)
TCALT	-1	10	Temperature lapse rate (°C/km)
Elev. of P	500	600	Elevation at which precipitation is measured (m)
Elev. of T	500	600	Elevation at which temperature is measured (m)

In summary, the methodology integrates a distributed SVAT model (TRAIN), a flexible semi-distributed model (Raven-HMETS), a species-specific process model (LWF-Brook90), and a conceptual model (HBV-Light).

2.4 Data Processing

2.4.1 Data Processing for Historical Climate Analysis

To investigate historical climate conditions in the Eyach catchment over the period 1975–2019, daily gridded meteorological datasets were processed using R Studio and QGIS. Spatial masking was applied using the catchment shapefile to ensure that all analyses were restricted to the defined watershed area. Subsequent processing and statistical evaluation focused on temperature, precipitation, and global radiation, which were aggregated spatially and temporally to evaluate interannual and seasonal climate dynamics.

Daily values were first aggregated to obtain annual and seasonal averages or totals, depending on the variable. To evaluate long-term trends, Mann-Kendall Mann, (1945) tests were performed on all time series, supported by Sen's slope Sen, (1968) estimates to quantify the magnitude of detected trends. These non-parametric methods are robust to non-normal distributions and are commonly used in hydroclimatic trend analysis (Hamed and Ramachandra Rao, 1998; Koudahe et al., 2017). Temperature anomalies were computed as deviations from a 1981–2010 climatological baseline, following guidelines by the World Meteorological Organization 2017 (WMO, 2017), to contextualize warming trends over time.

Beyond mean conditions, temperature extremes were evaluated by computing the annual number of hot days (Tmax > 30°C) and frost days (Tmin < 0°C)

This integrative analysis enabled the quantification of long-term climate dynamics across multiple variables and scales, serving as a foundation for the further application of hydrological models in the catchment.

2.4.2 Data Processing for Future Climate Analysis

For future climate scenario analysis, daily projections of temperature, precipitation, and global radiation were obtained from the CORDEX REMO 2009 dataset. The data were provided in NetCDF format using a rotated coordinate system, which is commonly employed in regional climate models to reduce numerical artifacts and maintain quasi-uniform grid spacing over the European domain (Jacob et al., 2013). This required conversion to standard geographical coordinates to enable spatial alignment with the Eyach catchment.

To identify relevant grid cells corresponding to the catchment area, a rectangular bounding box was defined using the coordinate system EPSG:31467 (DHDN / Gauss-Kruger zone 3), with corner coordinates ranging from 3455000 m to 3470000 m in the west–east direction and from 5396000 m to 5411000 m in the south–north direction.

These corner coordinates were converted into rotated coordinates using the AgrimetSoft transformation tool, allowing precise localization of the relevant CORDEX grid cells. Grid cells spanning indices 213 to 216 (rotated latitude) and 201 to 204 (rotated longitude) were determined to cover the study area.

To retrieve data from the rotated grids, Panoply was used to extract latitude and longitude arrays. These were exported to Excel, where the catchment’s bounding coordinates were matched with the nearest grid cells. Once identified, the extracted data were transformed back into non-rotated coordinates. This was achieved by transposing the spatial matrix and reversing its columns, using the transformation:

rotate <- function(x) { apply(t(x), 2, rev) }

This operation ensures the spatial alignment of the dataset with the standard coordinate reference system of the catchment. Following the coordinate transformation, the extracted grids were resampled to a finer spatial resolution of 50 × 50 meters using bilinear interpolation to ensure compatibility with the spatial resolution required for input into the TRAIN model and other hydrological simulations.

After spatial alignment and resampling, the datasets were processed analogously to the historical datasets. This included the computation of seasonal and annual means or totals, derivation of anomalies relative to a climatological baseline, and statistical trend analyses using the Mann-Kendall test and Sen's slope estimator. This consistent methodological approach allowed for a robust comparison between historical and projected climate dynamics within the Eyach catchment.

2.4.3 Data Processing for Historical Hydrological Simulations

For the TRAIN model, gridded meteorological forcing data were first spatially clipped to a rectangular area covering the Eyach catchment (see section 2.4.2). These inputs were required on a daily timestep, as specified by TRAIN.

In addition to meteorological data, multiple environmental datasets were rasterized:

- Land cover data was rasterized to match the study area's extent.
- Soil data (BK50), including key parameters like usable field capacity, field capacity, air capacity, hydraulic conductivity, soil depth, and rootability, as well as aspect and slope, were rasterized.
- The Digital Elevation Model (DEM) was also clipped accordingly.

All spatial datasets were harmonized to a 50 × 50 m grid resolution, yielding 300 rows × 300 columns (90,000 total cells), ensuring sufficient detail for simulating catchment-wide hydrological processes.

Raven (using the HMETS configuration) was driven by spatially averaging the daily meteorological forcing data masked by the catchment's boundary. This averaging allowed the model to simulate processes across multiple Hydrological Response Units (HRUs), despite HRUs sharing nearly identical properties (except minor vegetation differences), effectively functioning like a point-based model.

One notable conversion was required for global radiation data, which originally came in W/m²/day format (as for TRAIN). It was converted to MJ/m²/day by multiplying the original data with 0.0864. This factor accounts for the conversion from watts to megajoules and from seconds to days (1 W/m² = 0.0864 MJ/m²/day).

To meet the Raven-HMETS input formatting, each meteorological variable was stored in a separate forcing file:

- Temperature → BW6BroNT.rvt
- Global Radiation → BW6BroRAD.rvt
- Wind Speed → BW6BroWIND.rvt
- Relative Humidity → BW6BroRELH.rvt

LWF-Brook90 used the same spatially averaged daily meteorological data as Raven. However, for temperature input, the model required daily minimum and maximum temperatures (Tmin

and Tmax). These were derived by extracting the lowest and highest values from the gridded temperature dataset for each day.
For calculating vapor pressure, the saturated vapor pressure $e_s(T)$ was first determined using the following formula for temperatures above 0 °C (Monteith and Unsworth, 2013):

$$e_s(T) = 0.6108\ exp\left(\frac{17.27*T}{T+237.3}\right) \quad [33]$$

where:

$e_s(T) = Saturation\ vapor\ pressure\ [kPa]$
$T = Air\ Temperature\ [°C]$
$0.6108 = Reference\ saturation\ vapor\ pressure\ at\ 0°C\ [kPa]$
$17.27 = Empirical\ constant$
$237.3 = Temperature\ scaling\ constant$

For temperatures below 0 °C, the following formula was used (Murray, 1967) :

$$e_s(T) = 0.6108\ exp\left(\frac{21.875*T}{T+265.5}\right) \quad [34]$$

where:

$e_s(T) = Saturation\ vapor\ pressure\ [kPa]$
$T = Air\ Temperature\ [°C]$
$0.6108 = Reference\ saturation\ vapor\ pressure\ at\ 0°C\ [kPa]$
$21.875 = Empirical\ constant$
$265.5 = Temperature\ scaling\ constant$

The actual vapor pressure e_a was then calculated by applying the relative humidity using the formula (Food and Agriculture Organization of the United Nations, 1998):

$$e_a = \frac{RH*e_s}{100} \quad [35]$$

where:

$e_{a=}\ Actual\ vapor\ pressure\ [kPa]$
$RH =\ Relative\ Humidity\ [\%]$
$e_{s=}\ Saturated\ vapor\ pressure\ [kPa]$

For HBV-Light, the ptq file containing the the model's forcing inputs was generated on a daily timestep. Data processing for Daily potential evapotranspiration (ETp) was carried out in Google Earth Engine. The ERA5-Land data was filtered for the period 1975–2019, reprojected to EPSG:31467, and resampled to a spatial resolution of 50 × 50 meters using bilinear interpolation for the desired are around the catchment (section 2.4.2). The images were subsequently clipped to the Eyach catchment boundary. Afterwards, For each day, mean ETp values across the catchment were computed and converted from meters to millimetres per day. This ensured both spatial and temporal consistency between forcing and model domain.
Additionally, parameterization for vegetation zone 1 was included, with calibration carried out using Genetic Algorithm and Powell (GAP) optimization (detailed setup in the calibration section). Key calibrated parameters included:

Table 6. Calibrated HBV-Light Input parameters for Vegetation Zone 1.

Parameter	Value	Description
TT	0.589	Temperature threshold (°C) for snow/rain separation
CFMAX	4.710	Degree-day factor (mm/°C/day) for snowmelt
SP	0.364	Snow pack water-holding capacity (fraction)
SFCF	0.426	Snowfall correction factor
CFR	0.037	Refreezing coefficient (fraction of meltwater refreezing)
CWH	3.46×10^{-9}	Water-holding capacity of snow (fraction of SWE)
FC	265.107	Field capacity of the soil (mm)
LP	0.691	Threshold for limiting evapotranspiration (fraction of FC)
BETA	1.024	Shape parameter for soil runoff relationship
PERC	9.466	Percolation rate to lower groundwater zone (mm/day)
UZL	24.276	Threshold for quick runoff from upper groundwater (mm)
K0	0.284	Recession coefficient for quick runoff (1/day)
K1	0.239	Recession coefficient for upper groundwater (1/day)
K2	0.051	Recession coefficient for lower groundwater (1/day)
MAXBAS	2.069	Routing parameter (days) for triangular weighting function

The output data from the hydrological models TRAIN, LWF-BROOK90, Raven-HMETS, and HBV-Light were post-processed in R to enable a comparative evaluation of key hydrological variables across the Eyach catchment. The focus was placed on three primary variables relevant to catchment-scale water dynamics: evapotranspiration (ETA), soil moisture (SM), and snow water equivalent (SWE), with the latter used to assess snow cover duration.

For the grid-based model TRAIN, all simulated output parameters were spatially averaged across the entire catchment to produce a single representative time series per variable. This averaging step ensured comparability with the semi-distributed or lumped structure of the other models.

The model outputs were aggregated to annual and seasonal timescales. For evapotranspiration and soil moisture, annual totals and means were computed for each hydrological year. Seasonal statistics were calculated by grouping the data into meteorological seasons (DJF, MAM, JJA, SON), enabling the identification of intra-annual variability and potential shifts in seasonal hydrological dynamics.

For snow analysis, snow cover duration was estimated from daily SWE output by counting the number of days per winter season (October through March) where SWE exceeded 1 mm. This threshold approach was applied consistently across all models. To allow comparison with available in-situ snow cover observations, a single grid cell from the TRAIN model located at the southwestern ridge of the Eyach catchment (approx. 900–1,000 m a.s.l.)—where the snow measurements were taken—was extracted and used as the reference point.

To investigate long-term changes, non-parametric Mann-Kendall trend tests were applied to the annual time series of ETA, SM, and SWE-derived snow cover duration. This method is widely

used in hydrological studies due to its robustness against non-normal data distributions and its ability to detect monotonic trends. The corresponding Sen's slope estimator was also computed to quantify the magnitude of observed trends in mm/year or days/year, depending on the variable.

In addition to absolute values, anomaly time series were calculated relative to the 1981–2010 baseline, following the WMO-recommended climatological standard. For both evapotranspiration and soil moisture, annual anomalies were derived by subtracting the 1981–2010 mean from each year's value. This enabled a clearer interpretation of deviations from long-term norms.

In addition to the core analysis, further model-specific evaluations were performed where additional output variables were available. For Raven-HMETS and HBV-Light, simulated discharge data were processed to assess streamflow performance. The Raven model produced hydrograph output files containing simulated discharge (m^3/s) for gauged subbasins, which were analysed using RStudio with the RavenR package. Discharge time series were evaluated against observed flow data from the Eyach River and Brotenaubach Creek, allowing for both calibration and validation-phase assessments. The evaluation employed established hydrological R packages including airGR, hydroTSM, hydroGOF, and hydroPSO to compute performance metrics (e.g. NSE, KGE, RMSE), apply optimization routines, and visualize simulated versus observed hydrographs. In contrast, HBV-Light discharge analysis was limited to the calibration period due to the absence of a predefined validation split. Nonetheless, the same statistical methods and visual comparison techniques were applied to ensure consistency with the Raven-HMETS assessment framework.

Beyond discharge, the LWF-BROOK90 model allowed for an additional evaluation of phenological dynamics. Based on the model's daily temperature input, the annual onset and end of the vegetation period for *Picea abies* were derived using the Menzel and von Wilpert method, implemented via the calc_vegperiod() function. This function identifies temperature-based thresholds to determine the start and end of the growing season in terms of day-of-year (DOY). The extracted DOY values for each year between 1975 and 2019 were subsequently analysed for long-term trends and correlated with mean annual temperatures, following the same processing steps applied to hydrological variables. This allowed the detection of potential shifts in vegetation period timing as a response to changing climatic conditions, based on internally consistent input data.

These additional analyses supported a broader evaluation of model performance and climate sensitivity, complementing the catchment-wide comparisons of hydrological fluxes and storage components.

Where available, modelled data were validated against independent reference datasets. For evapotranspiration and soil moisture, validation was conducted using ERA5-Land reanalysis data and the GLEAM satellite-based product, while snow cover duration outputs were compared to long-term observational records collected by a local observer at the southwestern ridge of the Eyach catchment.

Where available, modelled data were validated against independent reference datasets. For evapotranspiration and soil moisture, validation was conducted using ERA5-Land reanalysis data and the GLEAM satellite-based product, while snow cover duration outputs were compared to long-term observational records collected by a local observer at the southwestern ridge of the Eyach catchment.

These comparisons served not only to verify the plausibility of the model results but also to assess relative model performance. By combining these validations with a comprehensive intercomparison of the hydrological outputs across all models, the analysis provided insight into the consistency, variability, and climate sensitivity of each modelling approach under the same environmental conditions.

As part of this validation, key performance metrics including root mean square error (RMSE), bias, Pearson correlation coefficient (r), and the coefficient of determination (R^2) were computed for each model-reference combination. Following Krause et al., (2005) the coefficient of determination was calculated as the squared value of the Pearson correlation coefficient (Bravais–Pearson), describing the proportion of observed variance explained by the model:

$$R^2 = \left(\frac{\sum_{i=1}^{n}(O_i - \bar{O})(P_i - \overline{P})}{\sqrt{\sum_{i=1}^{n}(O_i - \overline{O})^2} * \sqrt{\sum_{i=1}^{n}(P_i - \overline{P})^2}} \right)^2 \quad [36]$$

where:

$O_i = Observed\ values$

P_i= Predicted values

$\overline{O} = Respective\ mean$

$\overline{P} = Respective\ mean$

The correlation coefficient (r) was likewise calculated as the Bravais–Pearson correlation. Bias was computed as the arithmetic mean of the difference between predicted and observed values:

$$Bias = \frac{1}{n}\sum_{i=1}^{n}(P_i - O_i) \quad [37]$$

where:

$O_i = Observed\ values$

P_i= Predicted values

2.4.4 Data Processing for Future Hydrological Simulations

Future hydrological simulations were carried out using the TRAIN and LWF-BROOK90 models, based on climate projections under three Representative Concentration Pathways (RCP 2.6, RCP 4.5, RCP 8.5). The post-processing of model output followed the same methodological framework as for historical simulations. This included aggregation of key hydrological variables—evapotranspiration (ETA) and soil moisture (SM)—to annual and seasonal scales, anomaly calculation relative to the 1981–2010 baseline, and trend detection using the Mann-Kendall test and Sen's slope estimator.

The forcing data preparation for both models followed the spatial processing steps outlined in Section 2.4.2: CORDEX REMO 2009 NetCDF datasets were converted from rotated to standard coordinates using matrix transformation, resampled to a 50 m spatial resolution, and

clipped to the Eyach catchment. The resulting gridded climate fields (T, P, radiation, etc.) were used either directly (TRAIN) or spatially averaged (LWF-BROOK90), depending on the model structure.

A critical addition for the TRAIN model was the derivation of relative humidity (RH), since the CORDEX REMO 2009 dataset does not provide RH directly. Instead, RH was computed based on specific humidity (q) and atmospheric pressure (p), both of which were available in the REMO dataset. This was done by first computing the saturation vapor pressure e_s in dependence on the air temperature via the Bolton Formula (Bolton 1980):

$$e_s(T) = 6.112\ exp\left(\frac{17.67*T}{T+243.5}\right) * 100 \quad [38]$$

where:

$e_s(T) = Saturation\ vapor\ pressure\ [Pa]$
$T = Air\ Temperature\ [°C]$
$6.112 = Reference\ saturation\ vapor\ pressure\ at\ 0°C\ [hPa]$
$17.67 = Empirical\ constant$
$243.5 = Temperature\ scaling\ constant$

followed by the actual vapor pressure e calculated from specific humidity and atmospheric pressure (both available through the CORDEX REMO 2009 dataset):

$$e = \left(\frac{q*p}{0.622}\right) \quad [39]$$

where:

$e = Actual\ vapor\ pressure\ [Pa]$
$p = Atmospheric\ pressure\ [Pa]$
$0.622 = Ratio\ of\ molecular\ weight\ of\ water\ vapor\ in\ dry\ air$

Relative humidity was then calculated as the ratio of actual to saturation vapor pressure, capped at 100% to avoid unrealistic values (Lawrence 2005):

$$RH = \frac{e}{e_s} * 100 \quad [40]$$

where:

$RH = Relative\ Humidty\ [\%]$
$e = Actual\ vapor\ pressure\ [Pa]$
$e_s = Saturation\ vapor\ pressure\ [Pa]$

For the LWF-BROOK90 model, all climate variables were spatially averaged over the catchment from the same processed REMO data used by TRAIN. Tmin and Tmax were directly available in the CORDEX dataset, so no interpolation was necessary. As in the historical setup (see Section 2.4.4), vapor pressure (e_a) was calculated based on saturated vapor pressure and relative humidity, using the same temperature-dependent formulation.

To reflect species-specific hydrological responses, simulations were conducted individually for the three dominant tree species in the Eyach catchment: *Picea abies*, *Fagus sylvatica*, and

Quercus robur. Each species was parameterized separately to assess differences in evapotranspiration (ETA) and soil moisture (SM) dynamics under future climate conditions. This stratified approach enabled a more ecologically differentiated understanding of vegetation–climate interactions across scenarios.
Simulations were run for each of the three RCP scenarios. To isolate the effect of climate forcing, all model parameters were kept identical to those used for historical simulations.
By harmonizing the climate forcing inputs—including the manual derivation of relative humidity—and applying a consistent processing approach across models and RCP scenarios, the resulting time series enabled robust and comparable projections of hydrological responses in the Eyach catchment.

2.4.5 Data Processing for Model Validation

To enable model evaluation and validation, ERA5-Land and GLEAM datasets were processed to derive time series of actual evapotranspiration (ETA) and soil moisture (SM) for the Eyach catchment. These datasets were then used for comparison with simulated outputs from the hydrological models described in earlier chapters.
For the comparison step, both annual and daily average values of ETA and SM were derived from the ERA5-Land dataset using Google Earth Engine. The data was first filtered to match the study period (1975–2019) and spatially clipped to two extents: the bounding box defined in section 2.4.2 and the catchment boundary itself. All datasets were reprojected to the local coordinate system (EPSG:31467) with a 50 m resolution to ensure consistency with model outputs. For ETA, annual sums and daily averages were calculated and spatially aggregated using zonal statistics. For SM, daily values from the three soil layers provided by ERA5 were summed per timestep and averaged across layers, producing a single annual SM value per pixel, which was then aggregated spatially.
In parallel, GLEAM data was processed using R to supplement validation of ETA only, as GLEAM soil moisture values were excluded due to consistently unrealistic magnitudes in the study region. Instead of a lack of data, the exclusion was based on quality concerns: GLEAM-derived soil moisture was found to be nearly twice as high as ERA5 across key periods, rendering it unsuitable for validation purposes. GLEAM data (1980–2019) was extracted from NetCDF files, cropped and masked using the same bounding box as defined in section 2.4.2, projected into UTM coordinates, and resampled to 50 m resolution. Yearly mean ETA values were then calculated and compiled into a validation dataset.
For the validation of snow simulations, observational data from Wolfgang Roos—from the southwestern ridge of the catchment—was used. Roos recorded snow cover days (SCD) over two periods: 1975–1985 and 2013–2019. Since his observations correspond to a high-altitude zone (900–1000 m), a representative single grid cell from the TRAIN simulations, located close to this ridge, was first selected. From this cell, daily snow water equivalent (SWE) values were extracted and used to calculate annual SCD, defined as the number of days with SWE > 1 mm. These simulated annual SCD sums were then directly compared to the observed values recorded by Roos.
In a second step, outputs from all other hydrological models were included in the comparison. However, it is important to note that these models were driven by spatially averaged forcing data (based on TRAIN meteorological inputs), and therefore their snow-related outputs

represent catchment-wide averages rather than localized high-altitude conditions. To maintain consistency, SCD values were also calculated from these simulations by counting the number of days with SWE > 1 mm, averaged over the entire catchment. The TRAIN model's main simulation was included in this aggregated comparison as well. These simulated catchment-wide annual SCD values were then compared to the observational SCD dataset provided by Roos, with the necessary caution regarding spatial representativeness.

To evaluate the accuracy and robustness of the hydrological models, simulated outputs were compared to these observational reference datasets using both visual and statistical techniques. This included boxplot comparisons of simulated versus observed annual means for ETA, SM, and SCD, allowing assessment of model bias, interannual variability, and agreement with benchmark datasets. For SM, validation was performed against ERA5 only; for ETA, both ERA5 and GLEAM were used; for snow, the observational SCD records by Roos served as the primary benchmark. These intercomparison and validation steps are jointly presented in Chapter 3 and are essential for identifying systematic deviations and enhancing confidence in model-derived hydrological estimates under both historical and future climate conditions.

Chapter 3

This chapter presents the climatic and hydrological dynamics of the Eyach catchment under historical conditions from 1975 to 2019. It forms the empirical and methodological foundation for evaluating model performance under past climate forcing and sets the stage for later assessments of future hydrological changes. The chapter is structured around the first four research objectives and combines climatological analyses with multi-model hydrological simulations and validation.

The first objective is addressed through a comprehensive analysis of historical climate data in the Eyach catchment. Using gridded daily data, key climate variables such as temperature, precipitation, and global radiation are examined for trends and variability through statistical techniques including the Mann–Kendall trend test and Sen's slope estimation. This analysis provides insight into long-term changes in atmospheric drivers relevant to ecohydrological processes.

To fulfil the second objective, the physically based hydrological model TRAIN is applied in a spatially distributed configuration. TRAIN simulates key components of the water balance—including evapotranspiration, snow cover duration, and soil moisture—based on gridded meteorological inputs and high-resolution spatial data on vegetation, topography, and soils. Its spatial resolution allows for the exploration of intra-catchment variability and climatic sensitivity across elevation gradients. For comparative purposes, the model outputs were subsequently averaged over the entire catchment area to align with the scale of the point-scale models used in the ensemble.

The third objective broadens the modelling approach by incorporating three additional point-scale hydrological models: Raven-HMETS, HBV-Light, and LWF-Brook90. These models differ in conceptual structure, ranging from the simplified rainfall–runoff representation of HBV-Light, to the modular semi-distributed framework of Raven-HMETS, and the physically detailed vegetation–soil interactions in LWF-B90. Each model was forced with spatially averaged meteorological inputs to ensure consistency across configurations. The inclusion of these structurally diverse models enables a comprehensive assessment of uncertainty and process representation, without designating any single model as a baseline. Instead, the ensemble provides multiple perspectives on the Eyach catchment's historical hydrological dynamics under identical climatic conditions.

The fourth objective involves evaluating and validating model performance under historical conditions. Key hydrological outputs—such as evapotranspiration, soil moisture, snow cover duration, and streamflow—are assessed against observed and reanalysis datasets, including ERA5, GLEAM, in-situ snow cover measurements, and long-term discharge records. Model skill is quantified using statistical metrics (RMSE, bias, R^2, and correlation), allowing for cross-comparison and performance benchmarking across hydrological variables and model structures.

By integrating climatological trend analysis with multi-model hydrological simulation and validation, this chapter provides a comprehensive baseline of the Eyach catchment's hydro-climatic behavior. The results not only highlight model capabilities and limitations but also offer critical insights into how historical climate variability has shaped key water cycle components—thereby fulfilling the first four research objectives and setting the stage for future scenario-based assessments.

3. Historical Ensemble Modelling and Validation

3.1 Historical Climate Conditions

3.1.1 Temperature

The analysis of temperature dynamics in the Eyach catchment reveals a clear and statistically significant warming trend over the period 1975–2019. Figure 2 shows the annual mean temperatures alongside a fitted Sen's slope estimate of +0.06 °C/year, with a highly significant p-value (< 0.0001), confirming the presence of a strong monotonic warming trend. While some interannual variability is evident—especially in the earlier decades—mean temperatures after the mid-1990s are consistently above the 1981–2010 baseline average of 7.26 °C.

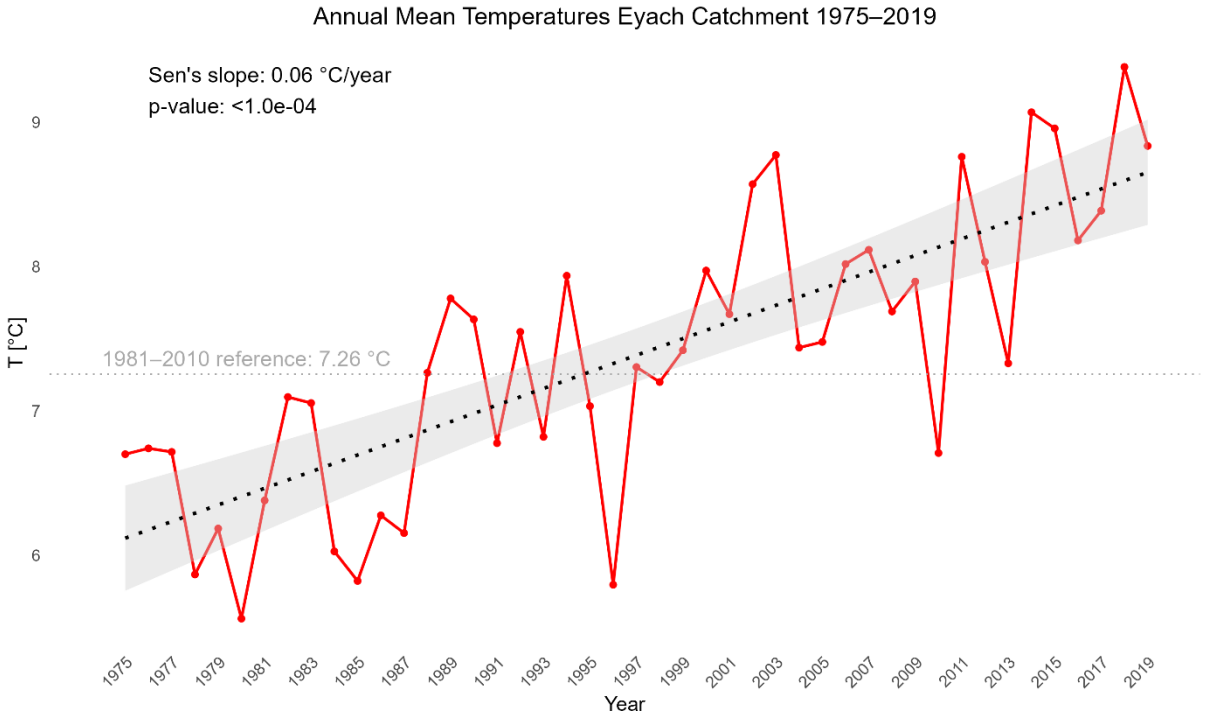

Figure 2. Annual mean air temperature time series for the Eyach catchment (1975–2019) with fitted linear warming trend (black dotted line). The shaded grey area represents the 95% confidence interval of the linear regression. The horizontal dashed line marks the 1981–2010 baseline reference (7.26 °C).

Seasonal mean temperatures, depicted in Figure 3 (p. 54), further underline this pattern. Spring and summer display the steepest increases, each with a Sen's slope of +0.082 °C/year and p-values below 0.0001, indicating very strong significance. Autumn also shows a robust warming signal (+0.043 °C/year, p = 1e-4). Winter, although also warming, does not exhibit a statistically significant trend (Sen's slope = +0.026 °C/year, p = 0.12), highlighting a seasonally asymmetric warming pattern. This seasonal divergence aligns with broader regional trends across Central Europe and supports findings by Spinoni et al., (2015) and Beniston et al., (2007), who report

stronger warming of maximum and mean temperatures in spring and summer, as well as more moderate changes in winter.

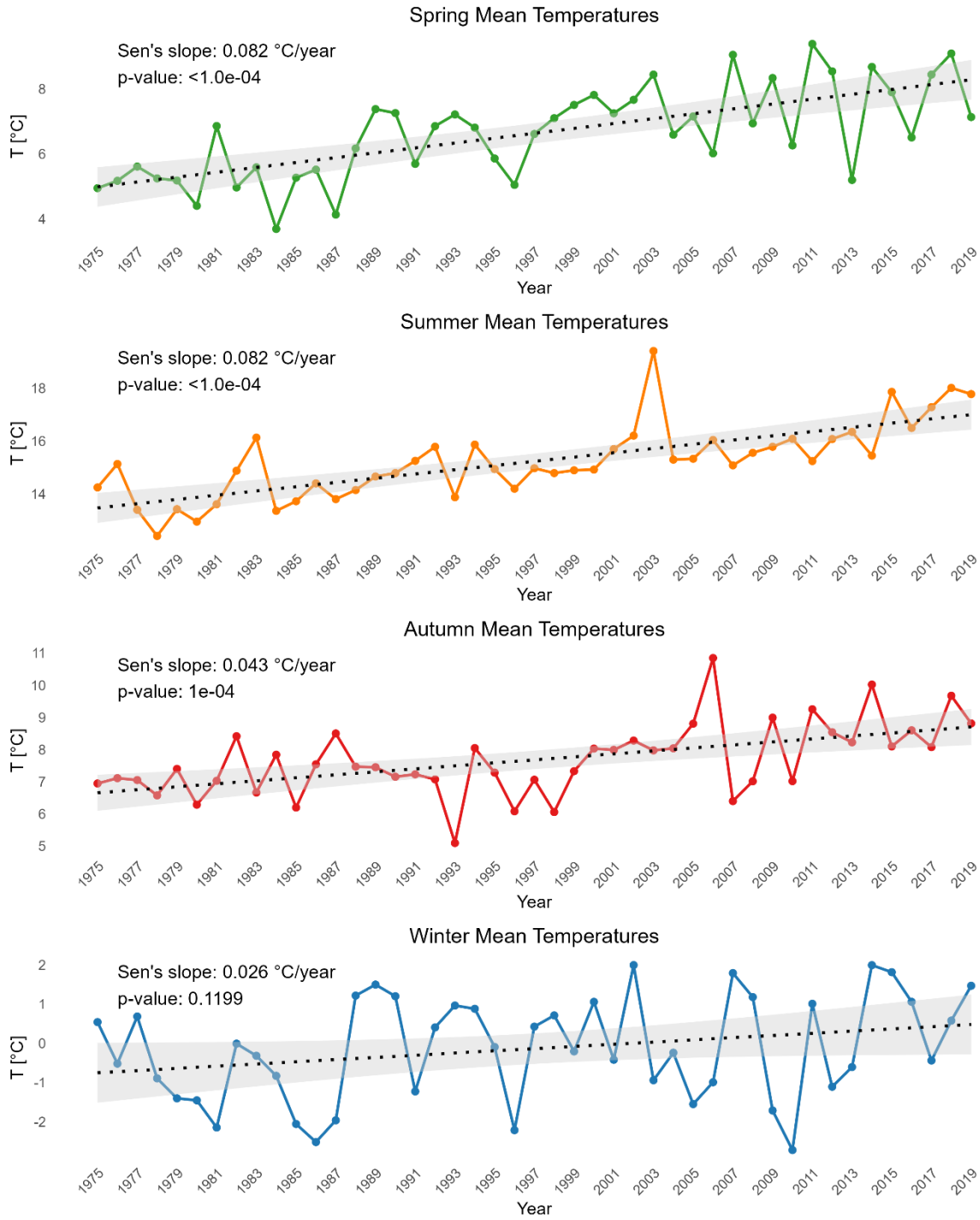

Figure 3. Seasonal mean air temperature time series for the Eyach catchment (1975–2019) for spring, summer, autumn, and winter. The black dotted lines indicate the fitted linear warming trends based on Sen's slope, with the grey shaded areas representing the 95% confidence intervals of the linear regressions.

The intra-annual and long-term distribution of temperature is visualized in Figure 4 (p. 55) through a temperature heatmap. Monthly average temperatures reveal a clear temporal shift toward warmer spring and summer periods in the more recent decades, with July and March in particular exhibiting intensification. The colour gradient progression illustrates a progressive retreat of cold winter extremes and expansion of warmer seasons. These shifts are consistent

with the trajectory highlighted by the Intergovernmental Panel On Climate Change (Ipcc), 2023a which attributes such regional warming patterns primarily to anthropogenic forcing.

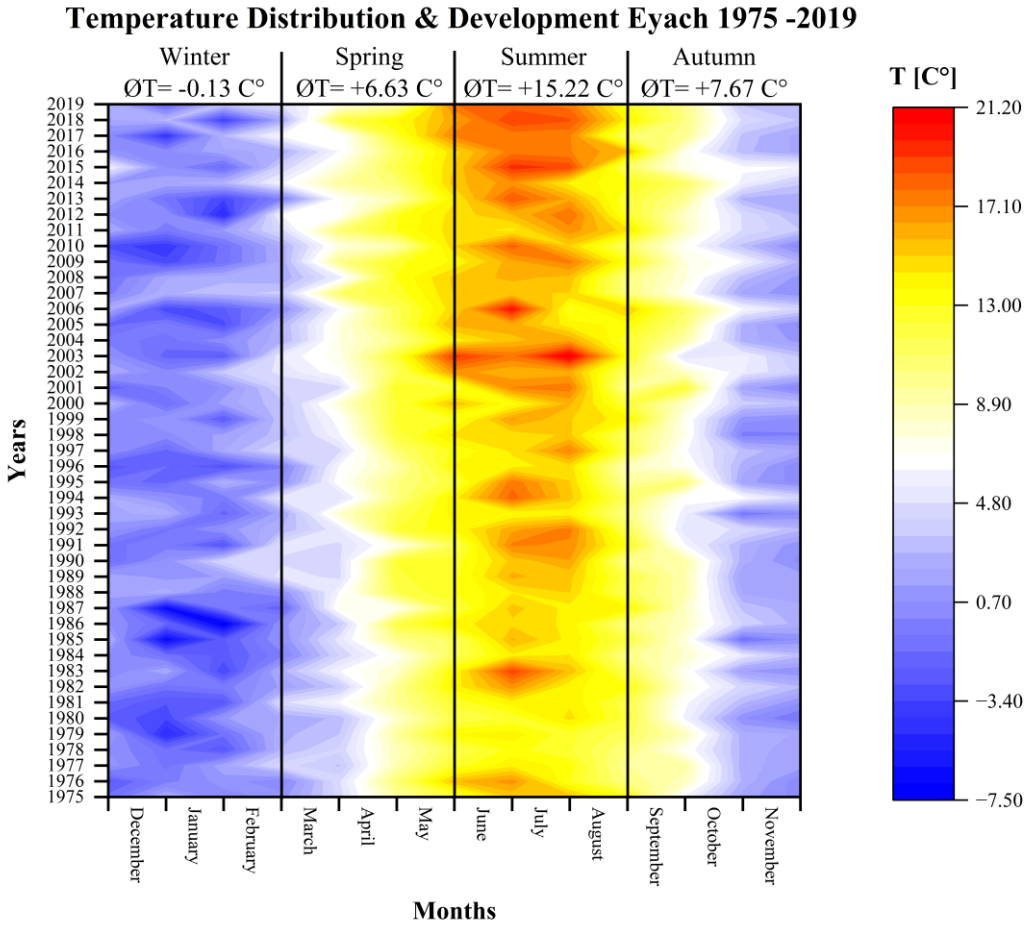

Figure 4. Heatmap of average daily temperatures in the Eyach catchment from 1975 to 2019, displayed by month and year. Colors represent temperature intensity, with seasonal boundaries marked and mean seasonal temperatures (ØT) indicated.

The frequency of temperature extremes is examined in Figure 5 (p. 56), which plots the annual number of frost days (Tmin < 0 °C) and hot days (Tmax > 30 °C). Frost days exhibit substantial interannual variability, ranging from ~25 to 90 days/year, with a gradual visual decline in more recent decades, suggesting fewer cold extremes. Hot days, on the other hand, remain nearly absent throughout the study period, consistently hovering near zero, indicating that extreme heat events have not yet become prominent in this montane region. This asymmetry—declining cold extremes without a corresponding rise in hot extremes—further supports the notion of minimum temperatures increasing more than maximum temperatures, a trend documented in European studies by Beniston et al. (2007) and Zhang et al. (2017).

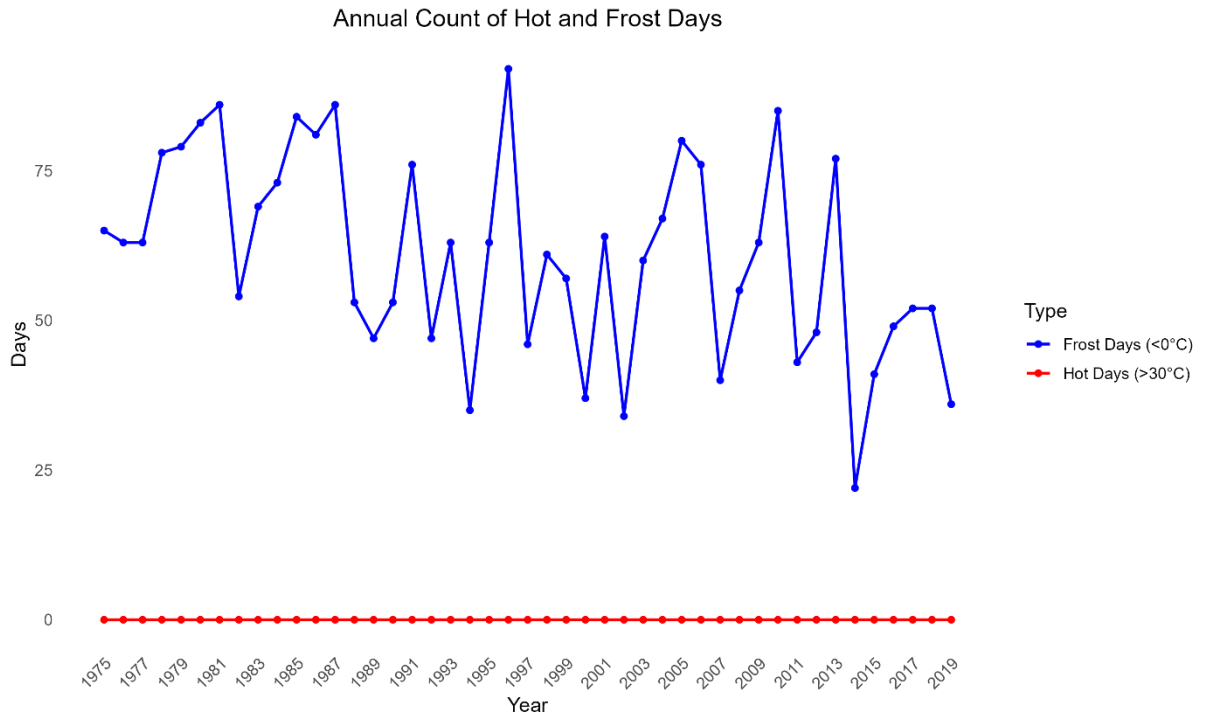

Figure 5. Annual counts of frost days and hot days in the Eyach catchment (1975–2019)

Together, these results confirm that the Eyach catchment has undergone pronounced and seasonally differentiated warming since the mid-1970s. The findings support broader evidence that regional climate change is altering thermal regimes in Central Europe, with implications for snow dynamics, evapotranspiration, and forest phenology. As Reyer et al., (2015) note, such changes can reduce forest resilience and push ecosystems toward tipping points, emphasizing the relevance of translating climatic trends into adaptive management responses (Gray, 2007).

3.1.2 Precipitation

The long-term development of precipitation in the Eyach catchment from 1975 to 2019 is illustrated in Figures 6 (p. 57) and 7 (p. 58). Figure 6 shows the annual precipitation sums, which reveal considerable interannual variability across the study period. Despite pronounced year-to-year fluctuations, a statistically significant negative trend emerges, as indicated by the Mann–Kendall test ($p = 0.0015$) and quantified by a Sen's slope of –7.9 mm/year. The linear trend line and declining trajectory suggest a general reduction in annual precipitation amounts over the last four decades, diverging from earlier assessments that suggested a positive or neutral trend. Notably, the observed values increasingly fall below the 1981–2010 reference average of 1234 mm, highlighting a potential drying tendency in recent decades.

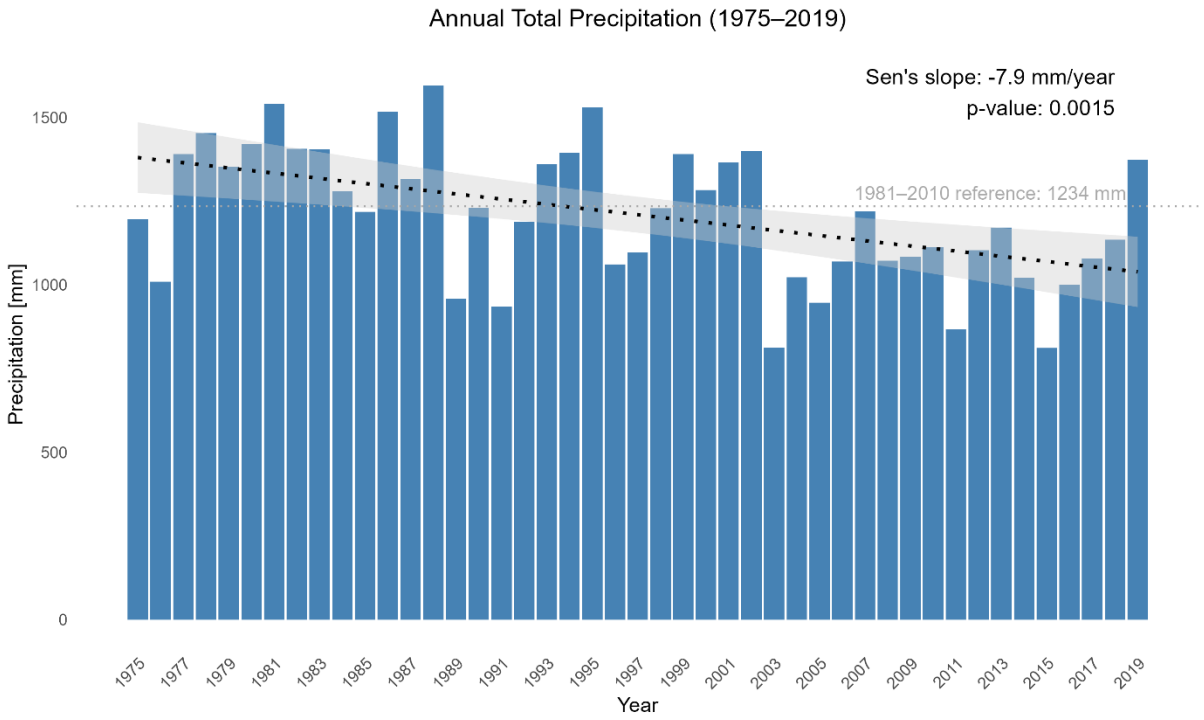

Figure 6. Annual total precipitation in the Eyach catchment (1975–2019) with fitted linear trend based on Sen's slope (black dotted line). The grey shaded area indicates the 95% confidence interval of the linear regression. The horizontal dashed line represents the 1981–2010 baseline reference (1234 mm).

Figure 7 displays seasonal precipitation totals for winter, spring, summer, and autumn. All seasons exhibit varying degrees of interannual variability, with a general tendency toward declining precipitation across all four seasonal windows. However, only winter (Sen's slope = –2.56 mm/year, p = 0.0493) and autumn (Sen's slope = –2.21 mm/year, p = 0.0264) show statistically significant negative trends. The trends for spring and summer are also negative (–1.94 mm/year and –1.41 mm/year, respectively), but do not reach statistical significance at the 95% confidence level. These results mark a notable contrast to previous analyses, where spring and summer had been identified as contributing to increases. Instead, the current findings suggest that precipitation reductions are becoming more seasonally widespread, albeit strongest in the colder half of the year.

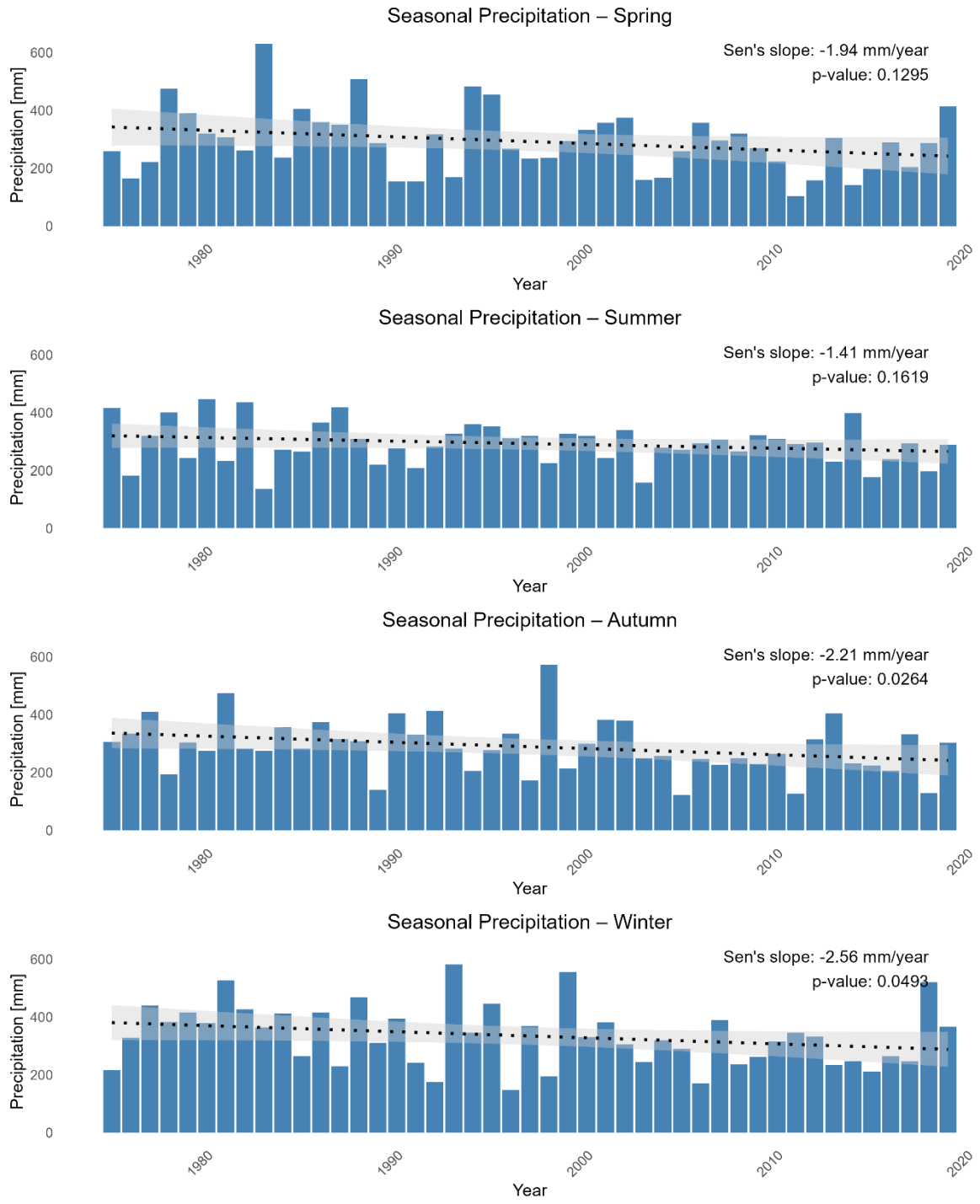

Figure 7. Seasonal total precipitation in the Eyach catchment (1975–2019) for spring, summer, autumn, and winter. Black dotted lines represent fitted linear trends based on Sen's slope, with grey shaded areas indicating the 95% confidence intervals of the linear regressions.

These declining trends in annual and seasonal precipitation align with other regional observations of increasing hydroclimatic stress in Central Europe and suggest possible shifts in large-scale atmospheric circulation patterns (Feldmann et al., 2008). The results are particularly relevant for understanding potential impacts on hydrological processes, including soil moisture dynamics, groundwater recharge, and vegetation water availability—especially when interpreted alongside observed warming trends. According to Zampieri et al., (2009) such drying signals during the winter and shoulder seasons can significantly affect soil water storage

entering the growing season, thereby altering the annual water balance and exacerbating drought risk.
Overall, the findings underscore the emergence of a drying trend in the Eyach catchment's precipitation regime, with potential consequences for both natural and managed ecosystems. As such, they contribute to a broader understanding of hydroclimatic vulnerability in the context of ongoing climate change and support the need for adaptive water resource planning and monitoring frameworks.

3.1.3 Global Radiation

Global radiation (RG) is a key component of the surface energy balance and directly controls evapotranspiration dynamics in terrestrial systems. Figure 8 illustrates the development of annual mean global radiation across the Eyach catchment from 1975 to 2019. The dataset exhibits pronounced interannual variability, with annual totals ranging between approximately 3000 W/m² and over 3600 W/m². Despite this variability, a statistically significant increasing trend is apparent (Sen's slope: +6.17 W/m²/year, $p < 0.001$), indicating a long-term shift toward greater surface radiation availability. This trend aligns with broader observations of atmospheric brightening in Central Europe since the 1980s, likely related to reductions in aerosol concentrations and changes in cloud cover (Wild, 2009).

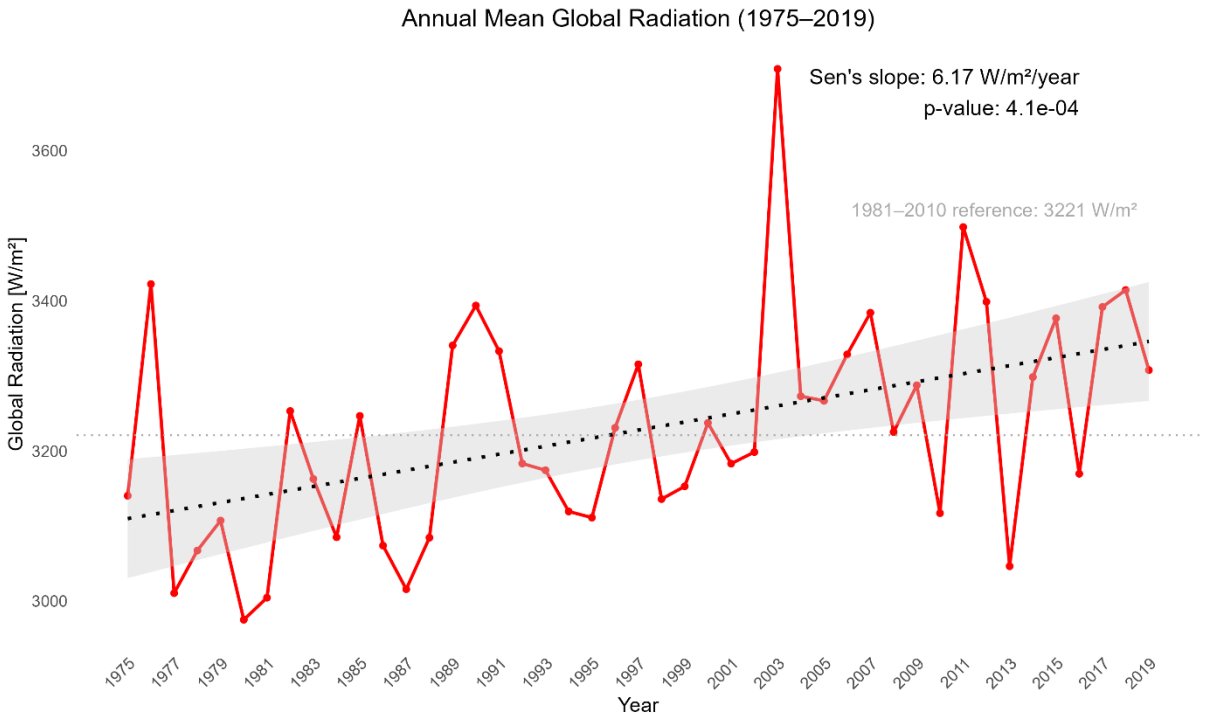

Figure 8. Annual mean incoming global radiation for the Eyach catchment (1975–2019) with fitted linear trend based on Sen's slope (black dotted line). The grey shaded area represents the 95% confidence interval of the linear regression. The horizontal dashed line shows the 1981–2010 baseline reference (3221 W/m²).

Seasonal global radiation patterns are presented in Figure 9 (p. 60). As expected, the highest values occur during summer, with means consistently exceeding 5000 W/m², followed by spring, autumn, and winter. While all seasons show variability, only summer exhibits a statistically significant positive trend (Sen's slope: +7.75 W/m²/year, $p = 0.035$), suggesting enhanced energy inputs during the warm season. Autumn also shows a moderate increasing tendency (Sen's slope: +3.04 W/m²/year, $p = 0.090$), though not statistically significant at the

0.05 level. Spring and winter display relatively stable patterns, with no significant trends detected (p-values > 0.1).

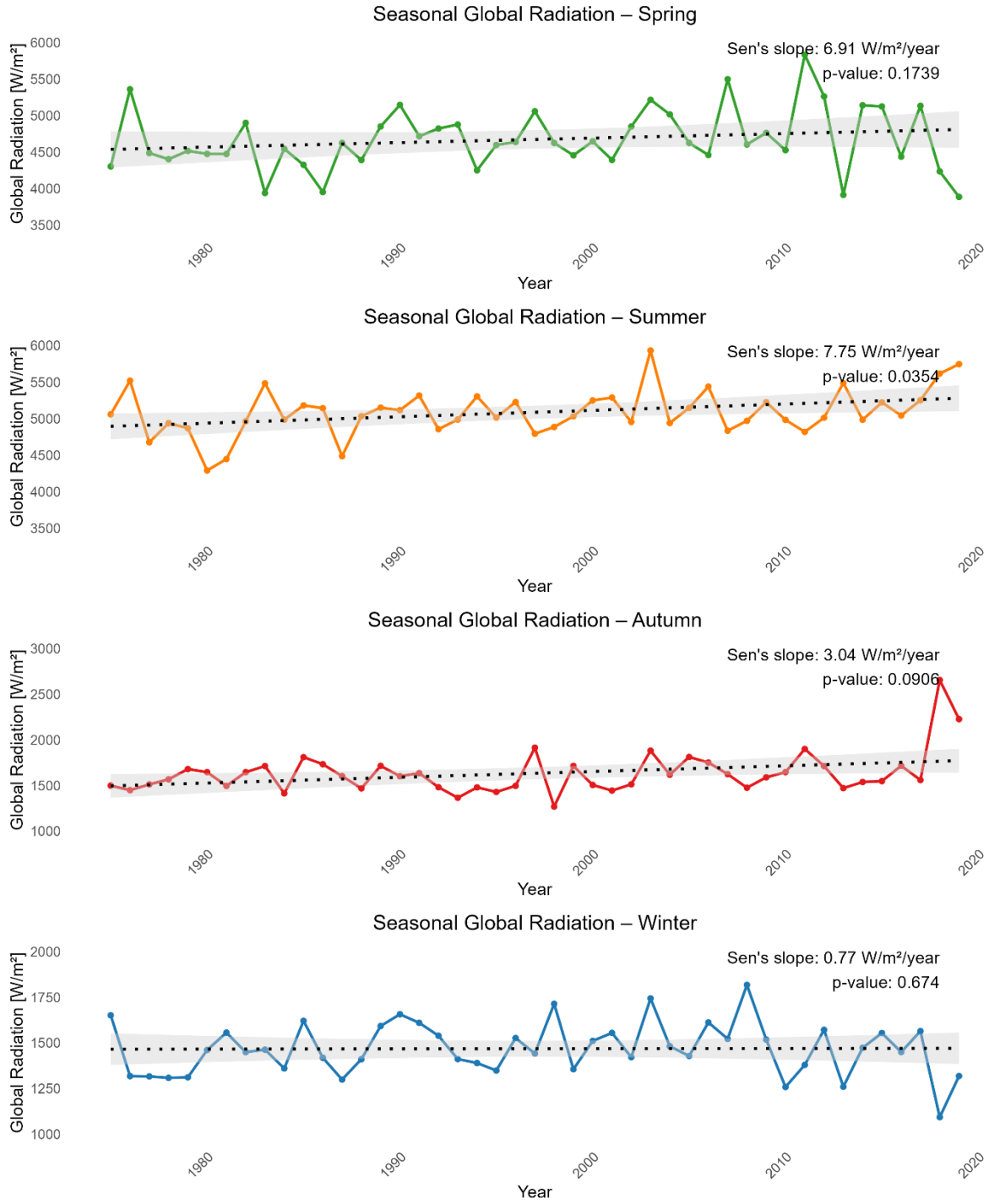

Figure 9 Seasonal mean incoming global radiation in the Eyach catchment (1975–2019) for spring, summer, autumn, and winter. Black dotted lines represent fitted linear trends based on Sen's slope, with grey shaded areas indicating the 95% confidence intervals of the linear regressions..

Overall, the observed rise in annual and summer global radiation may have important implications for surface energy balance processes in the catchment, particularly during the growing season. The enhanced radiation input is likely to increase atmospheric demand and could amplify evapotranspiration and soil moisture losses, a relationship further investigated in the hydrological modelling results discussed in the following section.

3.2 Historical Hydrological Simulations – Comparison & Validation

3.2.1 Evapotranspiration

The comparison of actual evapotranspiration (ETA) across the four hydrological models—LWF-Brook90 (B90), HBV-Light, Raven-HMETS, and TRAIN—reveals substantial structural divergence in both the magnitude and temporal behaviour of simulated fluxes (Figure 10, p. 62, Figure 11, p. 63). These differences stem from the models' varying complexity in representing land–atmosphere exchange, vegetation control, and soil moisture processes.

Figure 10 shows the annual total ETA time series for all models. LWF-B90 simulates by far the highest ETA values throughout the period, typically exceeding 900 mm year^{-1} and reaching annual totals above 1100 mm in several years. This high magnitude can be attributed to the model's process-based treatment of evapotranspiration, which includes species-specific transpiration, interception losses, and detailed root water uptake. While such physical realism can be beneficial under well-calibrated conditions, it also introduces considerable sensitivity to parameter uncertainty. Saavedra et al. (2022) note that physically-based models, although theoretically more accurate, often produce divergent internal fluxes if vegetation parameters or soil hydraulic properties are not rigorously constrained. Similarly, Orth et al. (2015) showed that overestimation of ET is common in complex models under conditions of abundant water supply.

By contrast, HBV-Light consistently produces the lowest ETA estimates (around 550–650 mm), reflecting its simple conceptual ET formulation based on temperature indices and a bucket-type soil water accounting scheme. This design limits responsiveness to changing energy and vegetation conditions, resulting in persistent underestimation—an issue often noted in conceptual models (Orth et al., 2015). TRAIN and Raven-HMETS exhibit intermediate magnitudes (roughly 600–750 mm), although Raven-HMETS displays more pronounced interannual variability. In TRAIN, evapotranspiration is calculated using the Penman–Monteith method within a vertically explicit SVAT structure that accounts for canopy conductance, dynamic LAI, and radiation exchange (Menzel, 1996). Raven-HMETS also applies the Penman–Monteith equation but does so within a modular semi-distributed system where actual evapotranspiration is tied to conceptual soil moisture routines. These structural differences likely explain the broader variability in Raven-HMETS output despite a shared PET formulation.

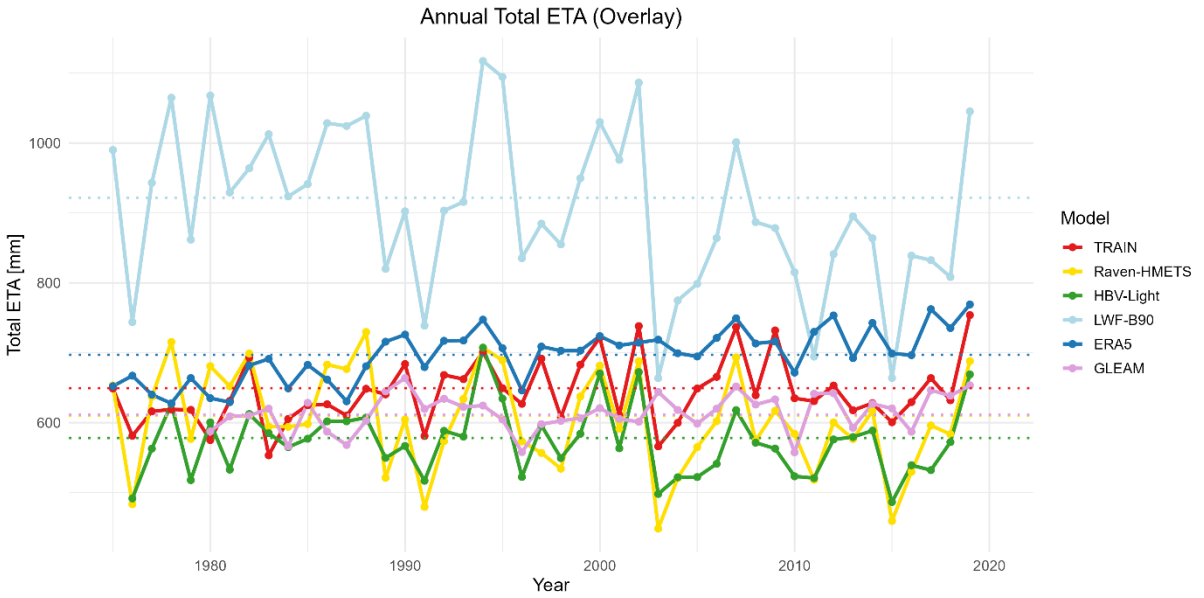

Figure 10. Annual total actual evapotranspiration (ETA) in the Eyach catchment (1975–2019) simulated by four hydrological models: HBV-Light, LWF-B90, Raven-HMETS, and TRAIN, along with two reference datasets: ERA5 and GLEAM. The coloured dotted horizontal lines indicate each model's or dataset's 1981–2010 baseline mean ETA..

Long-term ETA trends differ markedly across models (Figure 11). LWF-B90 displays a statistically significant declining trend (Sen's slope = –3.28 mm year^{-1}, p = 0.011), despite its overall high magnitude. In contrast, TRAIN shows a weakly increasing trend (+1.03 mm year^{-1}, p = 0.059), while HBV-Light and Raven-HMETS trends are negative but not statistically significant. These divergent responses suggest differing model sensitivities to climatic drivers such as temperature and radiation, as well as differences in vegetation parameterization and soil moisture representation.

Reference datasets show opposing tendencies: ERA5 exhibits a significant increasing trend (+2.07 mm year^{-1}, $p < 0.001$), while GLEAM shows a weak, non-significant increase (+0.79 mm year^{-1}, p = 0.061).

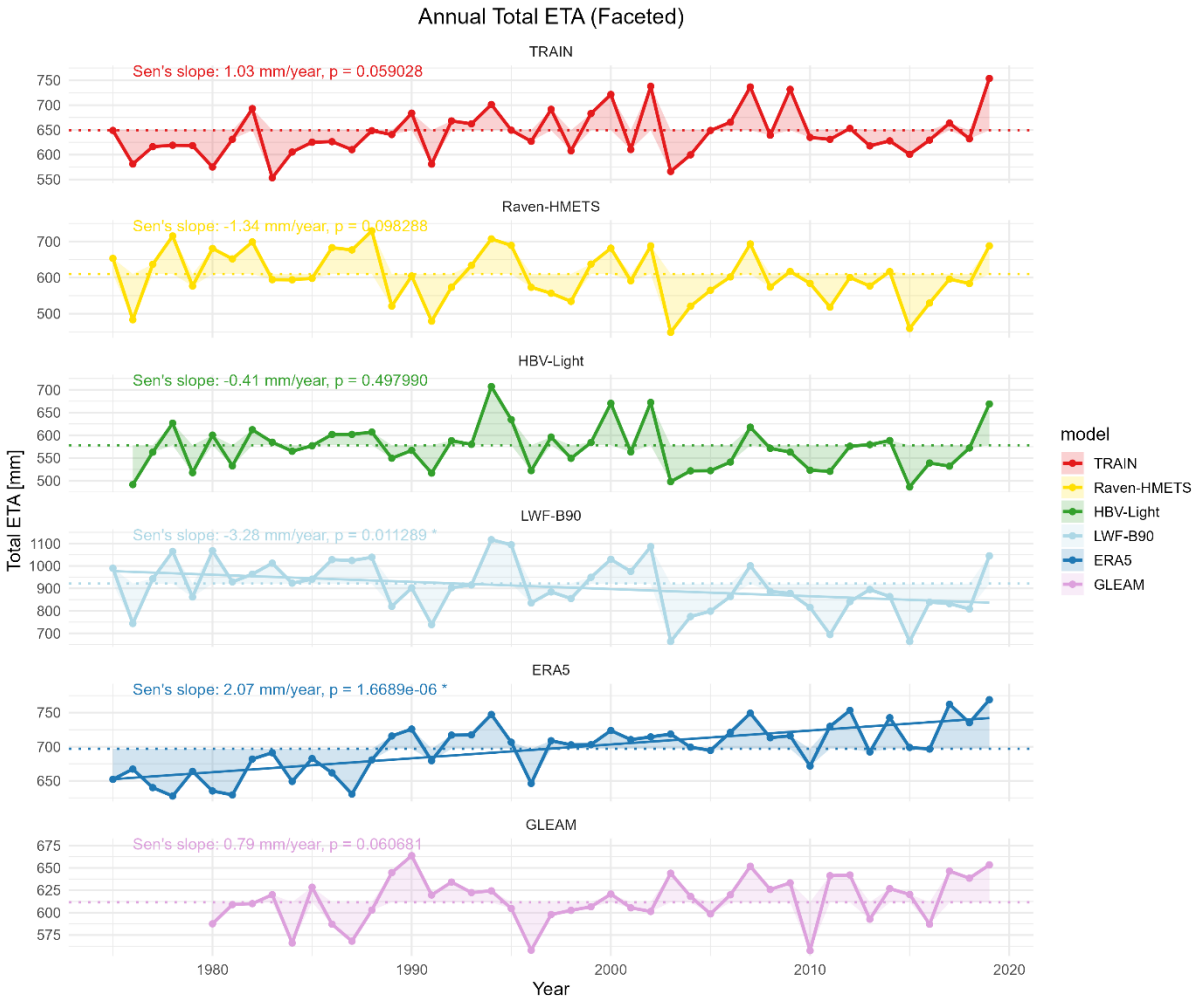

Figure 11. Long-term trends in annual actual evapotranspiration (ETA) in the Eyach catchment (1975–2019), simulated by four hydrological models (TRAIN, Raven-HMETS, HBV-Light, and LWF-B90) and compared with reference datasets ERA5 and GLEAM. Coloured dotted lines indicate model-specific baseline means for the reference period 1981–2010; bold trend lines are shown where significant ($p < 0.05$) according to Sen's slope and the Mann-Kendall test.

The magnitude differences between models are further summarized in Figure 12 (p. 64), which shows the distribution of annual ETA values via boxplots. LWF-B90 again stands out with a median value near 950 mm and wide interquartile range (IQR), followed by TRAIN, Raven-HMETS, and HBV-Light. When ERA5 and GLEAM reference datasets are included for comparison, it becomes evident that TRAIN is the only model whose ETA distribution substantially overlaps with both benchmarks. LWF-B90 clearly overestimates evapotranspiration relative to observations, while HBV-Light underestimates and Raven-HMETS remains variable but slightly low-biased.

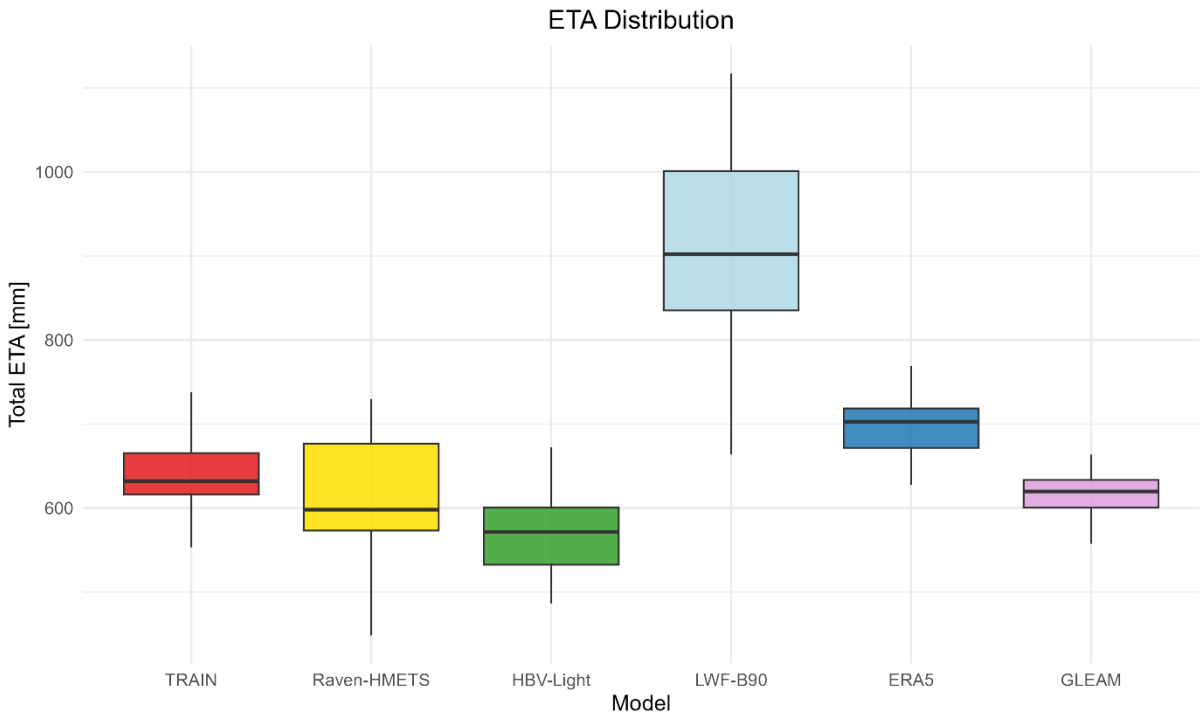

Figure 12. Distribution of annual actual evapotranspiration (ETA) values for all models and reference datasets (ERA5, GLEAM) (1975–2019).

These discrepancies are quantitatively evaluated in Table 7, which presents validation metrics (RMSE, bias, R^2, and correlation) for all model-reference combinations. TRAIN shows the best agreement with both ERA5 and GLEAM, achieving the lowest RMSE (68.1 mm vs. ERA5, 56.4 mm vs. GLEAM), moderate correlation (r = 0.52 vs. ERA5), and the smallest bias in both magnitude and sign (–54 mm vs. ERA5, +32 mm vs. GLEAM). HBV-Light and Raven-HMETS both show negative biases and higher RMSE values, while LWF-B90 is positively biased by over 200 mm relative to ERA5 and exhibits a very weak correlation (r = –0.14). These results are consistent with previous findings by Saavedra et al., (2022), who emphasized that differences in structural complexity and parameter sensitivity across models lead to large variability in simulated fluxes, even when discharge performance is satisfactory.

Table 7. Model Performance Comparison Against ERA5 and GLEAM Reference Datasets.

Model	Reference	RMSE [mm]	Bias [mm]	R^2	Correlation r
TRAIN	ERA5	**68.075**	–53.956	**0.272**	**0.522**
Raven-HMETS	ERA5	124.020	–92.404	0.010	–0.097
HBV-Light	ERA5	136.753	–125.416	0.050	0.223
LWF-B90	ERA5	243.809	209.564	0.019	–0.139
TRAIN	GLEAM	**56.431**	32.044	**0.099**	**0.315**
Raven-HMETS	GLEAM	77.584	–10.766	0.012	–0.111
HBV-Light	GLEAM	66.556	–39.407	0.004	0.064
LWF-B90	GLEAM	314.949	290.505	0.031	–0.175

To further explore seasonal dynamics, a heatmap of monthly ETA simulated by the TRAIN model is shown in Figure 13. Given that TRAIN showed the best agreement with both ERA5 and GLEAM (Table 7), its intra-annual pattern is considered relatively robust among the evaluated models. The heatmap reveals a strong seasonal cycle: low values during winter, rising in spring, peaking in summer, and declining again in autumn. Notably, the spring months—particularly April and May—exhibit increasing evapotranspiration intensity over time, as seen in the darker shading of recent decades.

This seasonal amplification is consistent with the Mann–Kendall trend analysis, where spring was the only season with a significant positive trend ($p = 0.011$). This development likely reflects earlier vegetation onset and increased atmospheric demand during spring, both of which are widely reported in the literature. For example, Wang et al., (2025) show that earlier leaf-out and accelerated phenological transitions lead to enhanced transpiration in spring months—both directly by extending the vegetation's active period and indirectly through climate–phenology interactions. Similarly, Vorobevskii et al., (2022) highlight the role of climate warming in shifting evaporative demand. These findings suggest that seasonal flux shifts are important indicators of climate–vegetation feedbacks, which may affect not only water availability but also land surface energy balance and runoff regimes.

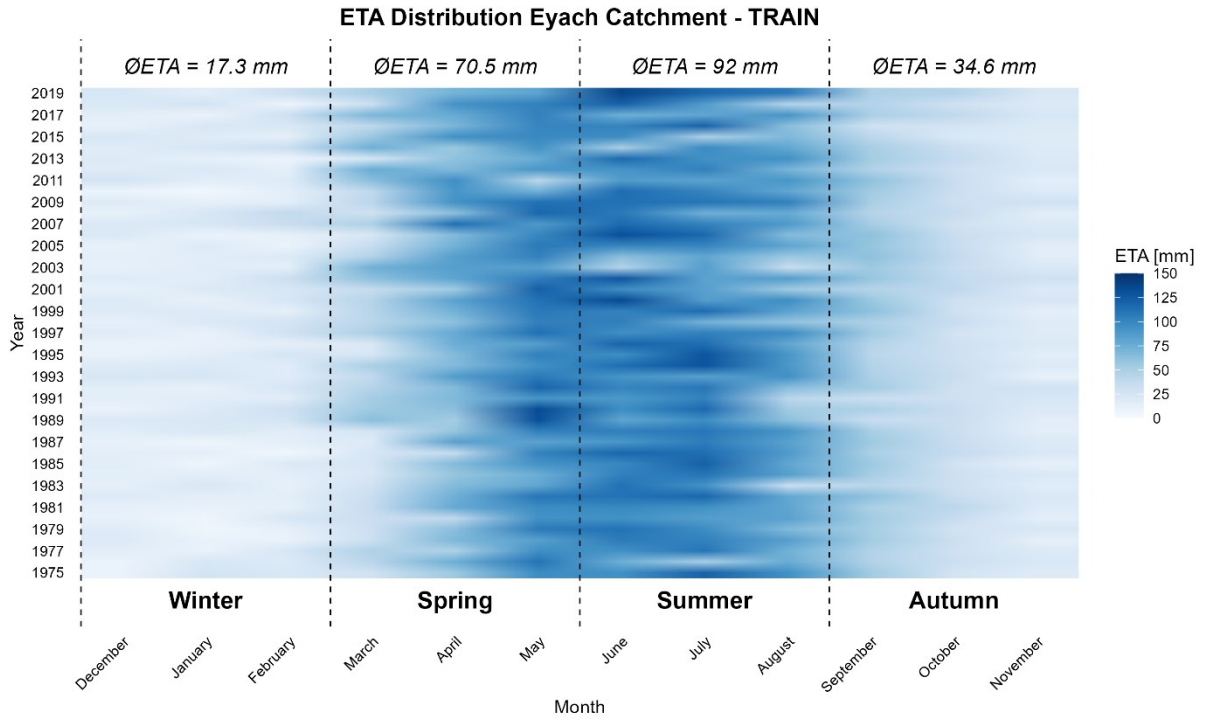

Figure 13. Heatmap of monthly actual evapotranspiration (ETA) from the TRAIN model (1975–2019).

Supporting this, Table 8 (p. 66) presents Mann-Kendall seasonal trend results for simulated evapotranspiration (ETA) from 1975 to 2019. The table lists Sen's slope values (in mm/year) and associated p-values, with statistically significant trends marked by an asterisk.

In spring, only TRAIN shows a statistically significant positive ETA trend, while the other models exhibit no significant changes. This suggests that increasing evapotranspiration during early growing season is not a consistent signal across models, but may still reflect earlier vegetation onset and enhanced atmospheric demand in TRAIN.

In summer, all models show negative ETA trends, but none of them are statistically significant. In winter, only TRAIN shows a statistically significant positive ETA trend. This may reflect the impact of reduced snow cover or patchy snow conditions, which have been shown to increase cold-season evapotranspiration by exposing soil and vegetation to atmospheric demand and allowing intermittent meltwater evaporation—even under subfreezing conditions (Kraft and McNamara, 2022).
In autumn, LWF-B90 is the only model that shows a statistically significant negative trend.

Table 8. Seasonal Trends in Simulated Evapotranspiration (Sen's Slope in mm/year, 1975–2019). Values in parentheses indicate Mann-Kendall p-values; asterisks denote significant trends at $p < 0.05$.

Model	Season	Sen's Slope (mm/year)	p-value
HBV-Light	Winter	+0.005	0.091
	Spring	–0.001	0.731
	Summer	–0.005	0.284
	Autumn	–0.002	0.448
LWF-B90	Winter	–0.002	0.660
	Spring	–0.013	0.077
	Summer	–0.010	0.286
	Autumn	**–0.008**	**0.041***
Raven-HMETS	Winter	–0.004	0.129
	Spring	+0.003	0.525
	Summer	–0.008	0.265
	Autumn	–0.005	0.107
TRAIN	**Winter**	**+0.003**	**0.045***
	Spring	**+0.010**	**0.008***
	Summer	–0.003	0.660
	Autumn	+0.002	0.200

Taken together, these results underscore that ETA estimates are highly sensitive to model structure. While conceptually simpler models like HBV-Light underestimate ETA due to their limited representation of vegetation and soil moisture dynamics, highly detailed models like LWF-B90 may overestimate when vegetation parameters are not rigorously constrained. TRAIN achieves a more consistent middle ground, likely benefiting from its balanced representation of energy and canopy processes.

3.2.2 Soil Moisture

Figure 14 presents the annual time series of total soil moisture (SM) for the four hydrological models—TRAIN, Raven-HMETS, HBV-Light, and LWF-Brook90—as well as the ERA5 reference dataset, over the period 1975–2019. Dotted horizontal lines indicate baseline averages from 1981–2010. LWF-B90 consistently simulates the highest SM values, generally above 220 mm, with low interannual variation. In contrast, HBV-Light shows the lowest values (~120 mm), while TRAIN and Raven-HMETS exhibit intermediate ranges with more pronounced year-to-year variability. The ERA5 reference lies between the HBV-Light and TRAIN outputs. These differences highlight how model structure and storage representation shape simulated water availability over time.

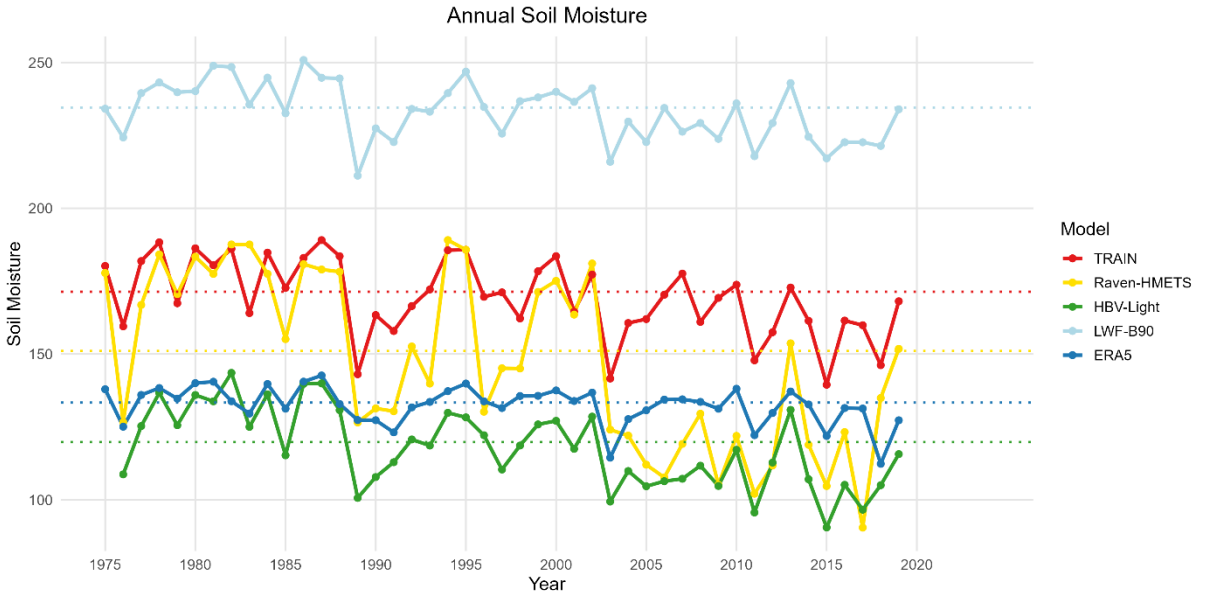

Figure 14. Annual mean soil moisture for each hydrological model (TRAIN, HBV-Light, LWF-B90, Raven-HMETS) and the reference dataset ERA5 for the period 1975–2019. Dotted horizontal lines indicate baseline mean soil moisture (1981–2010) for each dataset.

Figure 15 (p. 68) illustrates long-term SM trends in faceted form, including fitted linear trend lines and Sen's slope estimates. All models and the ERA5 dataset show statistically significant negative trends, although magnitudes vary. Raven-HMETS displays the steepest decline (–1.51 mm/year, $p < 0.001$), followed by HBV-Light (–0.69 mm/year), TRAIN (–0.48 mm/year), LWF-B90 (–0.40 mm/year), and ERA5 (–0.16 mm/year).

This consistent downward pattern suggests a robust response to hydroclimatic changes across structurally different models. Despite differences in soil moisture magnitude and variability, all models reproduce the broader decline observed in the reanalysis data, reinforcing confidence in their long-term sensitivity to climatic drying.

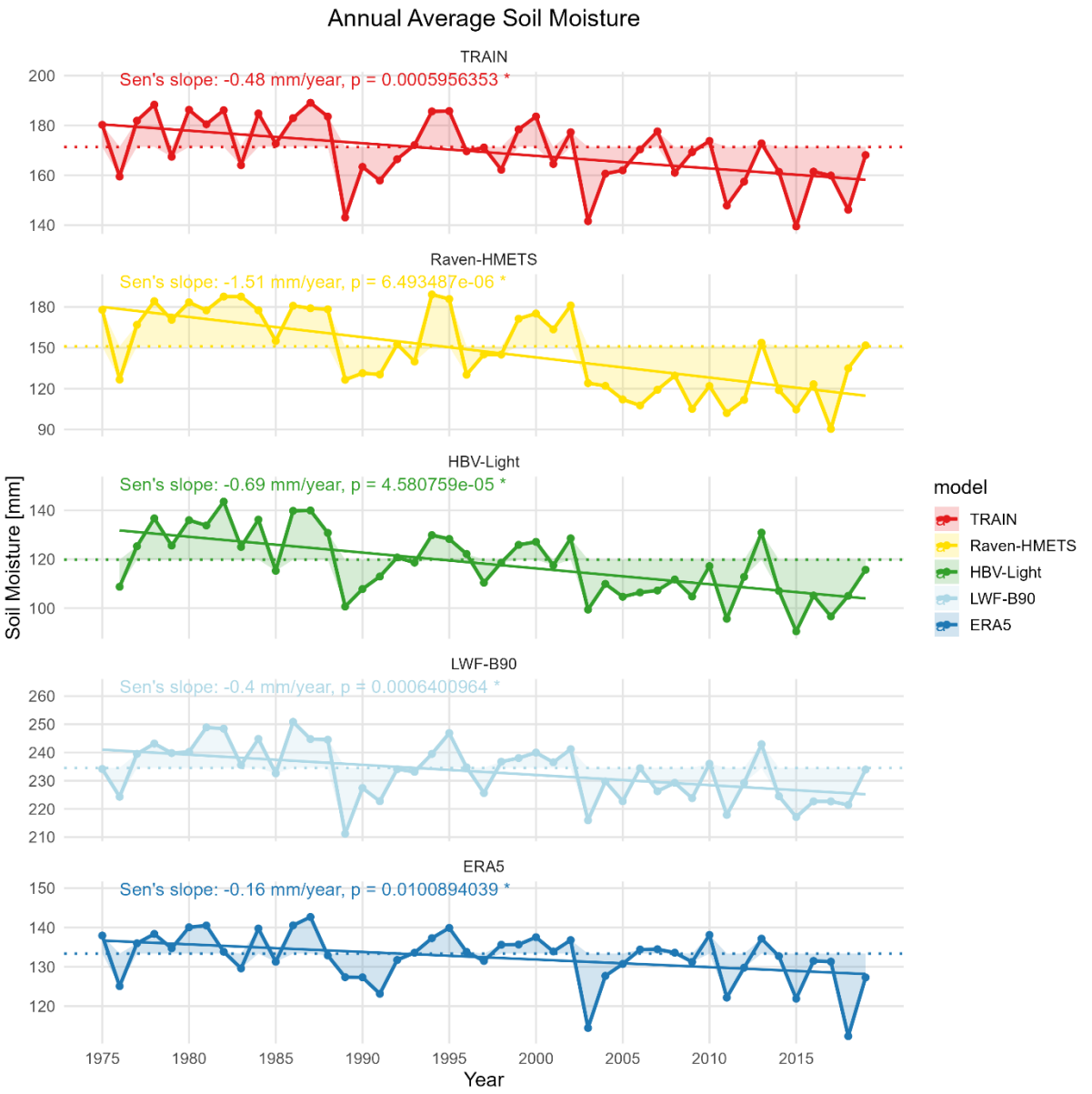

Figure 15. Long-term trends in annual mean soil moisture for each hydrological model (TRAIN, Raven-HMETS, HBV-Light, LWF-B90) and the ERA5 reference dataset for the period 1975–2019. Sen's slopes and associated p-values are shown for each time series. All trends are statistically significant, indicating widespread drying..

The corresponding boxplot (Figure 16, p. 69)) shows the distribution of annual SM values across all datasets. LWF-B90 again stands out with the highest median and narrowest spread, suggesting strong internal buffering and retention. Raven-HMETS exhibits the widest interquartile range, indicating higher sensitivity to climate inputs or model parameterization. HBV-Light and ERA5 display similar central tendencies, but ERA5 shows lower variability.

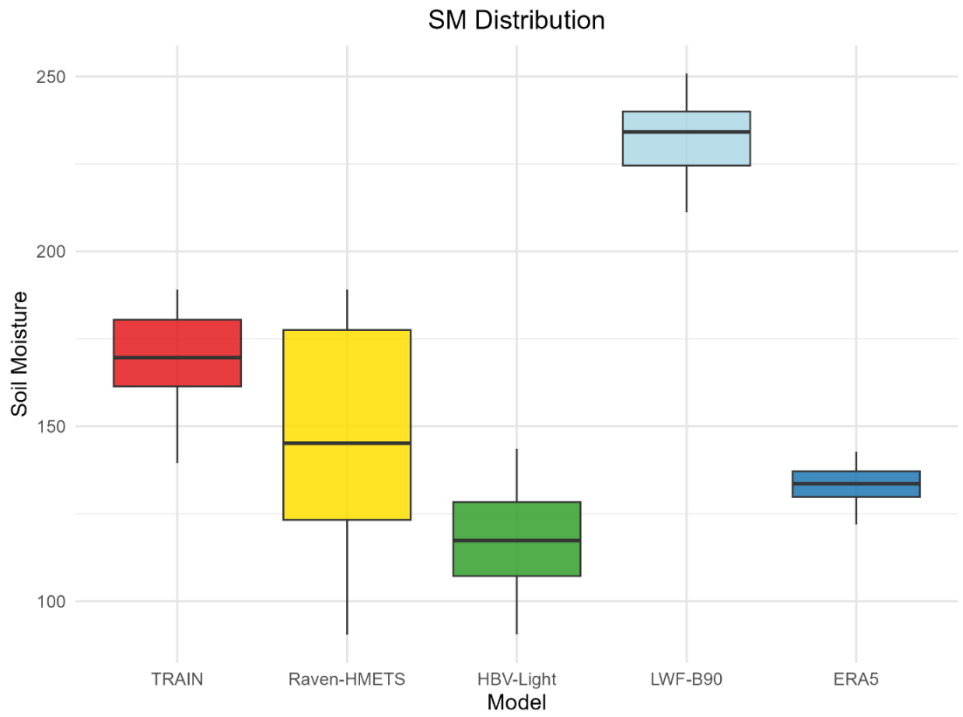

Figure 16. Distribution of annual mean soil moisture for each hydrological model (TRAIN, Raven-HMETS, HBV-Light, LWF-B90) and the ERA5 reference dataset over the period 1975–2019.

Validation metrics against ERA5 (Table 9) support these findings. While LWF-B90 shows the largest bias (+100.7 mm) and highest RMSE (100.9 mm), it also reaches a strong correlation ($r = 0.78$). HBV-Light has the smallest bias (–14.4 mm) and lowest RMSE (17.3 mm), but slightly weaker correlation ($r = 0.73$). TRAIN exhibits the best overall agreement in temporal dynamics ($r = 0.85$), although with a moderate positive bias. Raven-HMETS again appears as the most variable, with mid-range metrics.

Table 9. Model Performance Metrics for Simulated Soil Moisture Compared to ERA5.

Model	RMSE (mm)	Bias (mm)	R^2	Correlation r
TRAIN	37.82	36.91	0.728	**0.853**
Raven-HMETS	29.92	14.98	0.329	0.574
LWF-B90	100.88	100.69	0.613	0.783
HBV-Light	17.32	–14.43	0.538	0.733

Only the TRAIN model's soil moisture heatmap is shown in the main text, as it exhibits the highest temporal correlation with ERA5 (Table 9), making it best suited to illustrate seasonal patterns and long-term shifts—particularly the pronounced drying trend observed in spring. These visual patterns reinforce the statistically significant seasonal trends reported earlier in Table 8, where spring and summer exhibited the strongest declines across all models.

Figure 17 presents a heatmap illustrating the monthly and interannual variability of average daily soil moisture (SM) in the Eyach catchment, simulated by the TRAIN model for the period 1975 to 2019.

Above each section, the average seasonal soil moisture (ØSM) is indicated, with highest values in spring (154.2 mm) and autumn (172.5 mm), and lowest in summer (117.4 mm). A clear

seasonal cycle is evident, with regular wetting in winter/spring followed by drying in summer. However, recent decades exhibit a visible intensification of summer drying and reduced spring moisture, signalling a shift in seasonal hydrological dynamics.

These trends are consistent with earlier studies (Seneviratne et al., 2010; Xu et al., 2022), which link increased evapotranspiration and climate warming to declining soil moisture, particularly in the warm season. Furthermore, the seasonal and interannual variability visualized here aligns with global findings by Mondal and Mishra (2024) and Zhou et al. (2019), who show that precipitation dominates SM variability during cooler seasons, whereas evapotranspiration and land–atmosphere feedbacks govern variability and drought sensitivity in summer. The TRAIN model captures these patterns clearly, further supporting its credibility for ecohydrological applications in seasonally dynamic regions.

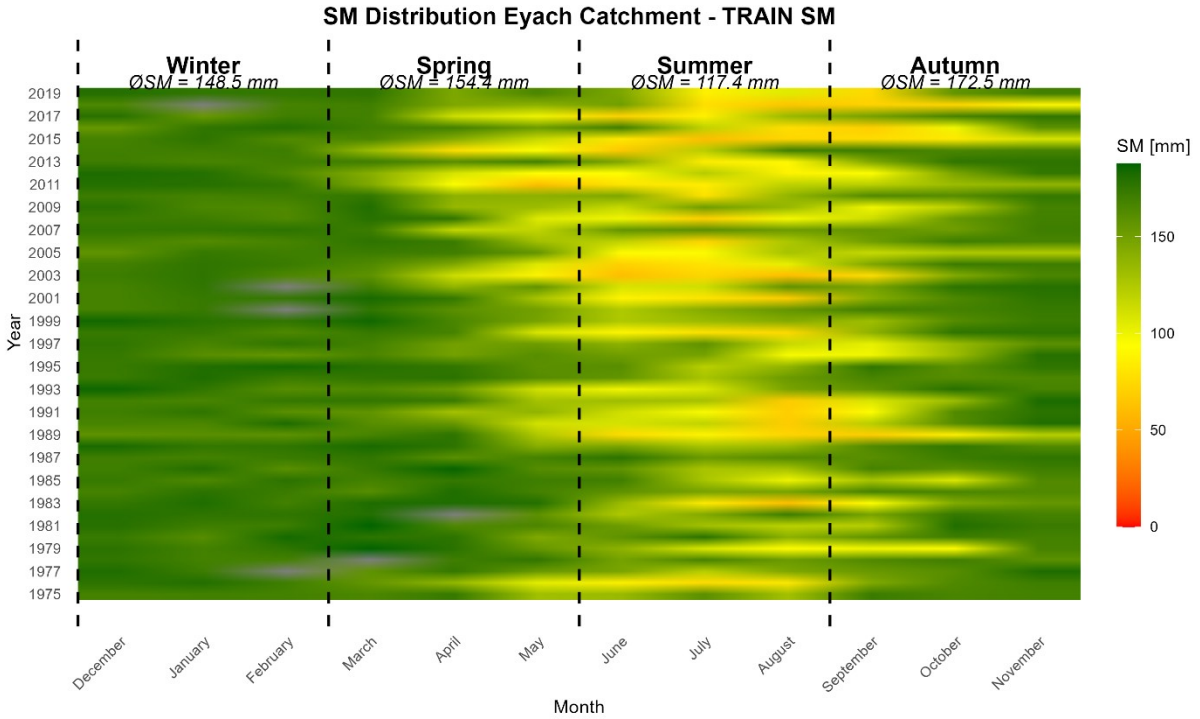

Figure 17. Heatmap of average daily soil moisture in the Eyach catchment from 1975 to 2019, displayed by month and year. Colors represent SM intensity, with seasonal boundaries marked and mean seasonal values (ØSM) indicated.

Supporting this, Table 10 (p. 71) presents Mann–Kendall seasonal trend results, with Sen's slope values indicating the rate of soil moisture change (mm/year) and corresponding p-values in parentheses. Statistically significant negative trends ($p < 0.05$) are most consistent in summer, where all models except LWF-B90 show significant declines. Spring trends are also negative across all models, with significant decreases for all four models.

In winter, Raven-HMETS, HBV-Light and LWF-B90 exhibit significant drying trends, while TRAIN shows no clear pattern.

Autumn shows weaker and less consistent changes, with only Raven-HMETS presenting a significant decline.

These results highlight the increasing influence of atmospheric demand during warmer months, as opposed to cooler seasons where trends are generally weaker and less consistent.

These patterns reflect broader global findings: Mondal and Mishra, (2024) show that precipitation is the primary driver of soil moisture dynamics in cooler seasons, while

evapotranspiration dominates during warmer periods; similarly, Zhou et al., (2019) emphasize that land–atmosphere feedbacks intensify summer variability and drought risk.

Table 10. Seasonal Trends in Simulated Soil Moisture (Sen's Slope in mm/year, 1975–2019). Values indicate Sen's slope estimates of soil moisture change per year, with corresponding p-values in parentheses. Asterisks (*) denote statistically significant trends at p < 0.05.

Model	Season	Sen's Slope (mm/year)	p-value
TRAIN	Autumn	–0.262	0.087
	Spring	**–0.519**	**0.0002843***
	Summer	**–0.812**	**0.011***
	Winter	–0.043	0.363
Raven-HMETS	**Autumn**	**–1.135**	**0.0004133***
	Spring	**–2.143**	**0.0001416***
	Summer	**–1.438**	**3.505e-05***
	Winter	**–1.288**	**4.914e-05***
LWF-B90	Autumn	–0.314	0.145
	Spring	**–0.642**	**0.006***
	Summer	–0.132	0.244
	Winter	**–0.404**	**0.017**
HBV-Light	Autumn	–0.442	0.063
	Spring	**–1.089**	**0.0001898***
	Summer	**–0.501**	**0.011***
	Winter	**–0.620**	**0.001***

Taken together, HBV-Light matches ERA5 best in magnitude, while TRAIN excels in replicating temporal patterns. Raven-HMETS balances the two but is more variable, and LWF-B90 tends to overstore moisture. These results confirm that structural choices—e.g., layering, canopy processes and soil moisture representation—strongly influence SM simulation fidelity and must be accounted for in ecohydrological model evaluation.

3.2.3 Snow Cover Duration

Figure 18 (p. 72) presents long-term trends in simulated and observed annual snow cover duration (SCD) for the period 1975–2019 across five hydrological model configurations—TRAIN, Raven-HMETS, HBV-Light, LWF-Brook90, and a high-altitude cell extracted from the TRAIN model (TRAIN-HT)—as well as in situ observations. A clear negative trend is evident across all configurations and the observed dataset, indicating a general decline in snow cover presence over time. The steepest decline is simulated by TRAIN-HT (–3.83 days/year, $p = 0.010$), followed by HBV-Light (–1.15 days/year, $p = 0.009$), Raven-HMETS (–0.97 days/year, $p = 0.001$), TRAIN (–0.89 days/year, $p = 0.003$), and LWF-Brook90 (–0.83 days/year, $p = 0.017$). Observed data also exhibit a statistically significant decline (–0.68 days/year, $p = 0.010$). These results underscore a consistent and significant reduction in SCD

across both modeled and observed records, highlighting the sensitivity of snow processes to changing climatic conditions in the study region.

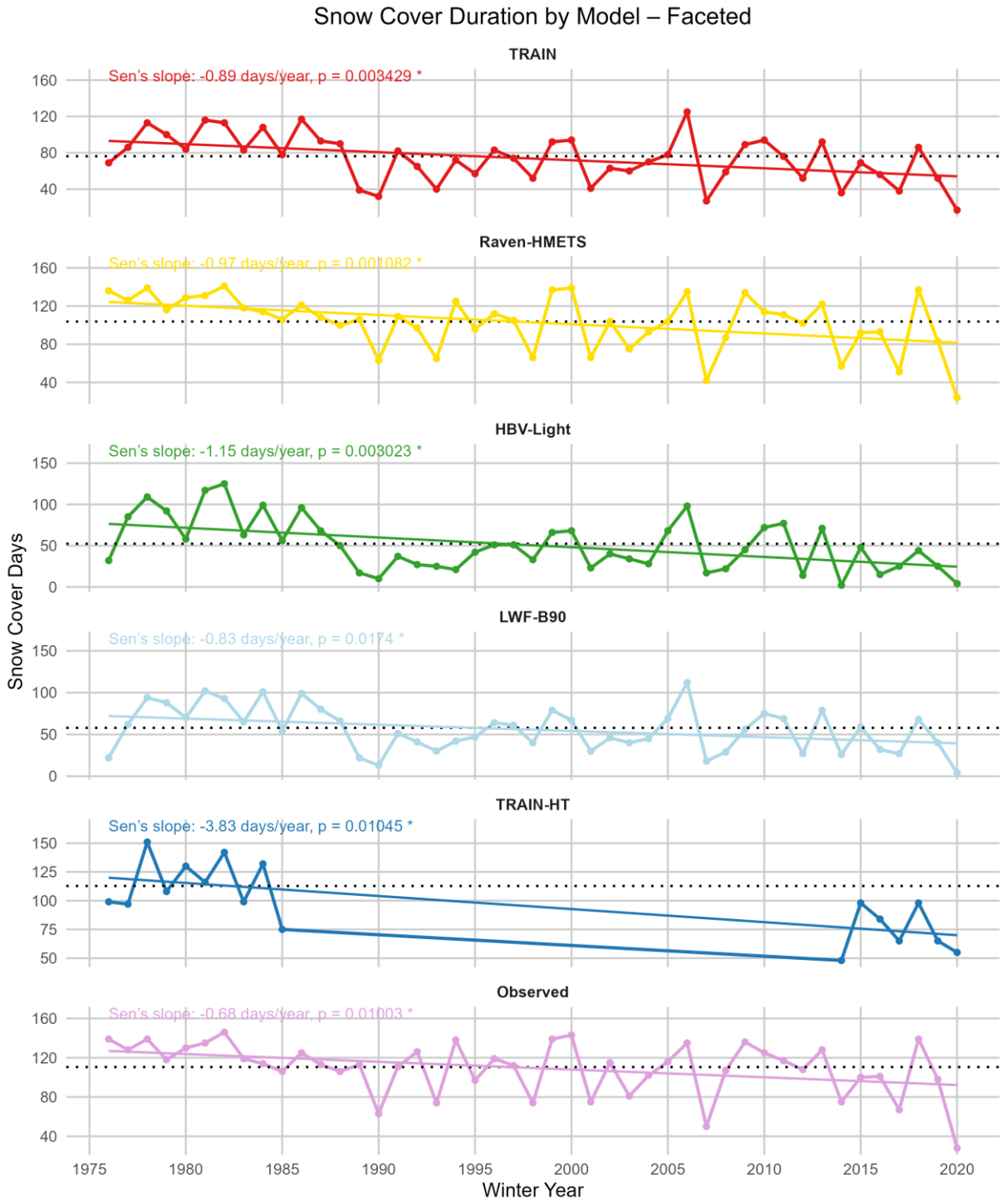

Figure 18. Sen's slope trends of annual snow cover duration (1975–2019) from five model configurations (HBV-Light, LWF-B90, Raven-HMETS, TRAIN, TRAIN-HT) and observed data(1975-1985 & 2013-2019.; Sen's slopes and p*-values are annotated in matching colors.*

Figure 19 (p. 73) shows the distribution of annual snow cover duration (SCD) for all hydrological models and the observed dataset, restricted to overlapping years. TRAIN and TRAIN-HT again exhibit the highest medians (~120 and ~130 days, respectively), highlighting their strong snow persistence. Observed data fall slightly below TRAIN-HT (~95 days median)

but align well in terms of interquartile range, supporting the representativeness of the high-elevation TRAIN cell used for comparison. Raven-HMETS performs moderately, with a median around 90 days. In contrast, HBV-Light and LWF-B90 simulate markedly fewer snow-covered days (medians ~65 and ~60 days, respectively), suggesting underestimation of snow accumulation or premature melt. Overall, the models exhibit distinct snow dynamics under shared climatic conditions, with TRAIN configurations best approximating observed snow cover at higher elevations.

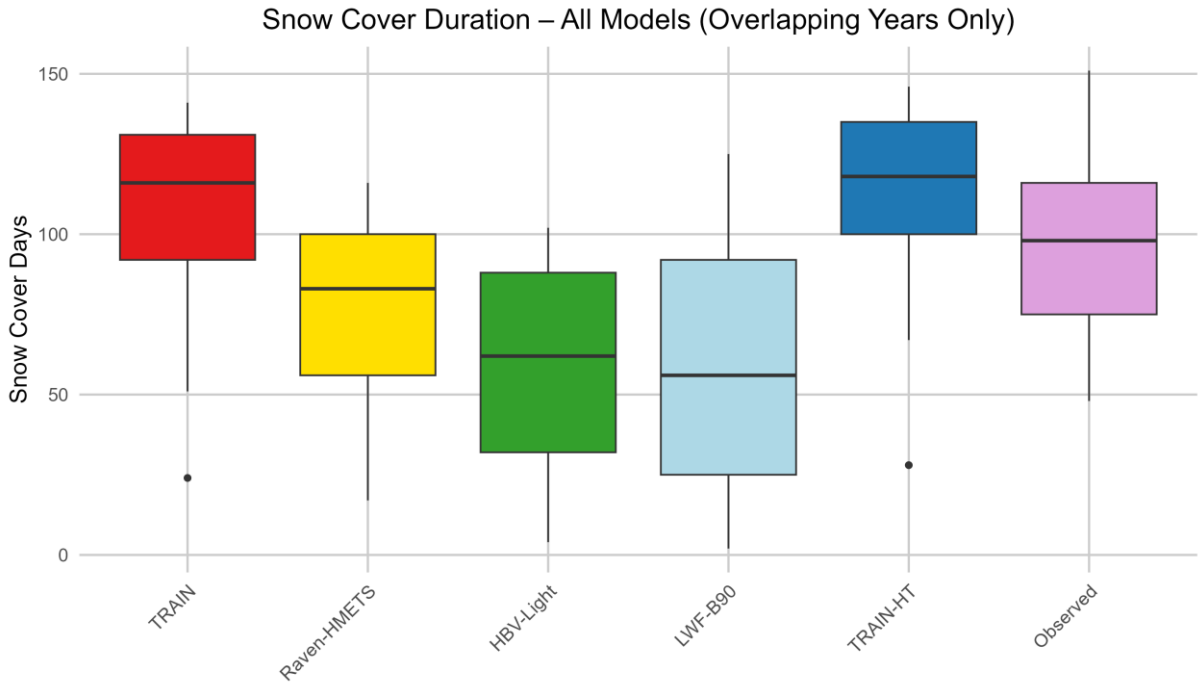

Figure 19. Distribution of winter snow cover duration by model and observed data for overlapping years (1975–2019).

Performance metrics for snow cover duration (SCD) relative to observed data are summarized in Table 11 (p. 74). Among all model configurations, TRAIN exhibits the best overall performance, with the lowest RMSE (20.99 days) and a small positive bias (+7.71 days), indicating strong accuracy in reproducing the magnitude of observed snow cover duration. Its correlation coefficient ($r = 0.82$) and R^2 (0.66) further suggest reasonable skill in capturing interannual variability. TRAIN-HT, which represents a high-elevation cell, also performs well in terms of RMSE (23.51 days) and bias (+12.94 days), aligning closely with the observed median and interquartile range. However, its slightly lower correlation ($r = 0.78$) points to reduced sensitivity to year-to-year fluctuations.

Raven-HMETS achieves the highest correlation with observations ($r = 0.89$) and the highest R^2 (0.80), suggesting that it captures temporal variability particularly well. Nonetheless, its substantial negative bias (–21.06 days) and elevated RMSE (24.95 days) indicate consistent underestimation of snow duration. In contrast, HBV-Light and LWF-B90 perform weakest overall, with large biases (–38 to –39 days) and the highest RMSE values (>41 days). Despite moderately high correlation values ($r = 0.84$–0.85), these models consistently underestimate snow cover duration, likely due to differences in parameterization, model sensitivity, or how they simulate snow accumulation and melt under local climate and elevation conditions.

Taken together, these results highlight TRAIN as the most robust and balanced model in reproducing observed snow cover dynamics, while TRAIN-HT offers valuable high-elevation insights despite slightly lower correlation.

Table 11. Validation Statistics for Simulated Snow Cover Days (SCD) against Observations.

Model	RMSE (days)	Bias (days)	R^2	Correlation r
TRAIN	**20.99**	**+7.71**	0.664	0.815
Raven-HMETS	24.95	–21.06	**0.798**	**0.893**
HBV-Light	41.89	–38.53	0.711	0.843
LWF-B90	44.04	–39.00	0.726	0.852
TRAIN-HT	**23.51**	**+12.94**	0.612	0.783

3.2.4 Vegetation Period Dynamics – Start and End of Growing Season

The vegetation period characteristics of *Picea abies* were analysed to evaluate interannual variability and long-term trends in phenological timing with the help of LWF-B90. Figure 20 illustrates the annual start of the vegetation period, measured as day of year (DOY), over the simulation period. The data show substantial year-to-year fluctuations, ranging approximately between DOY 125 and 160. However, despite short-term variability, a long-term trend toward earlier start dates is clearly visible—a finding that is consistent with the European-wide pattern reported by Menzel et al. (2006), who found that increasing temperatures advance the onset of spring phenological phases across species and regions (Menzel et al., 2006).

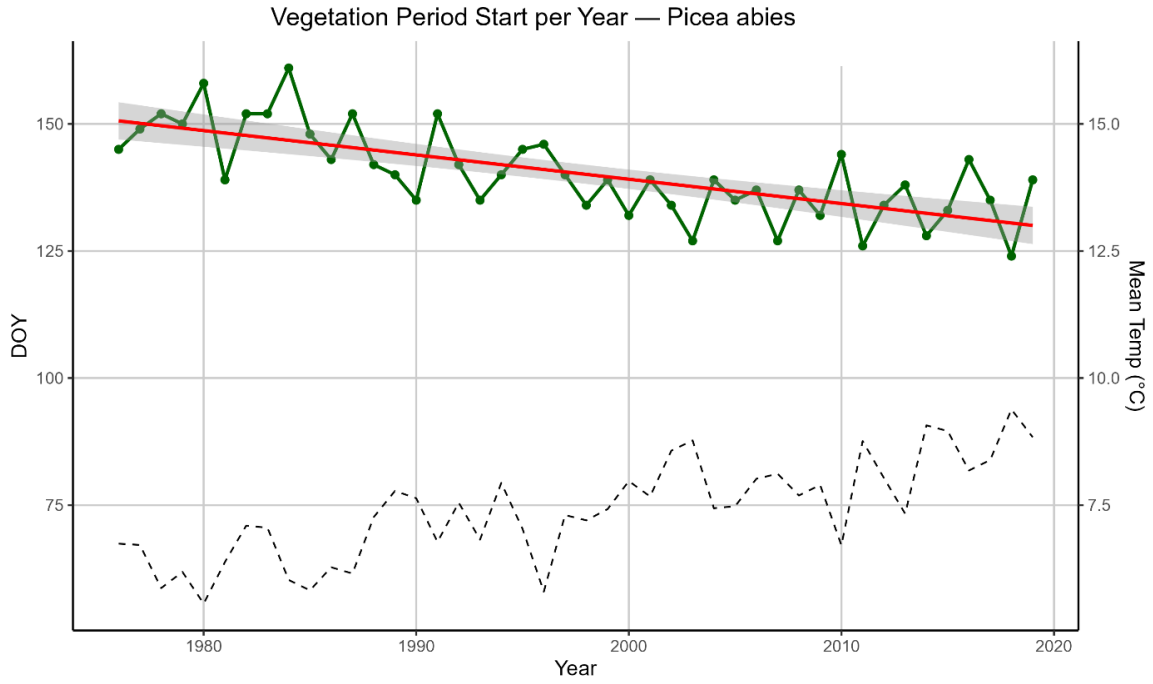

Figure 20. Annual start of vegetation (growing) period (DOY) for Picea abies (in green) and mean air temperature (black dotted line) (LWF-B90 simulation, 1975–2019).

This trend is confirmed by the linear regression shown in Figure 21. The slope indicates a steady advancement of the growing season onset over time, consistent with warming climate

conditions. Similar phenological shifts have also been documented by Parmesan and Yohe, (2003), who synthesized global studies and reported a widespread advance of spring events in response to recent warming Parmesan & Yohe (2003), and by Richardson et al., (2013) for temperate and boreal forests (Richardson et al. 2013).

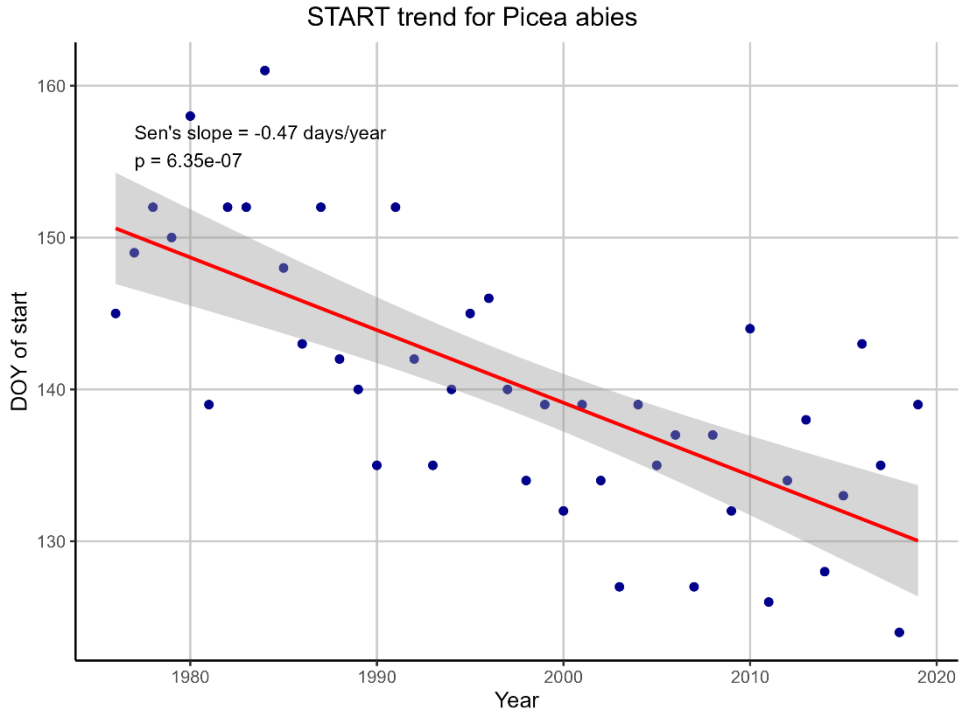

Figure 21. Linear trend of vegetation period start date (day of year) over time (1975–2019).

To further explore the climatic influence on phenology, Figure 22 displays the correlation between the mean spring temperature and the start of the vegetation period. The negative linear relationship suggests that higher spring temperatures are associated with earlier phenological onset. Years with warmer spring conditions consistently exhibit lower DOY values, confirming the temperature sensitivity of vegetation development.

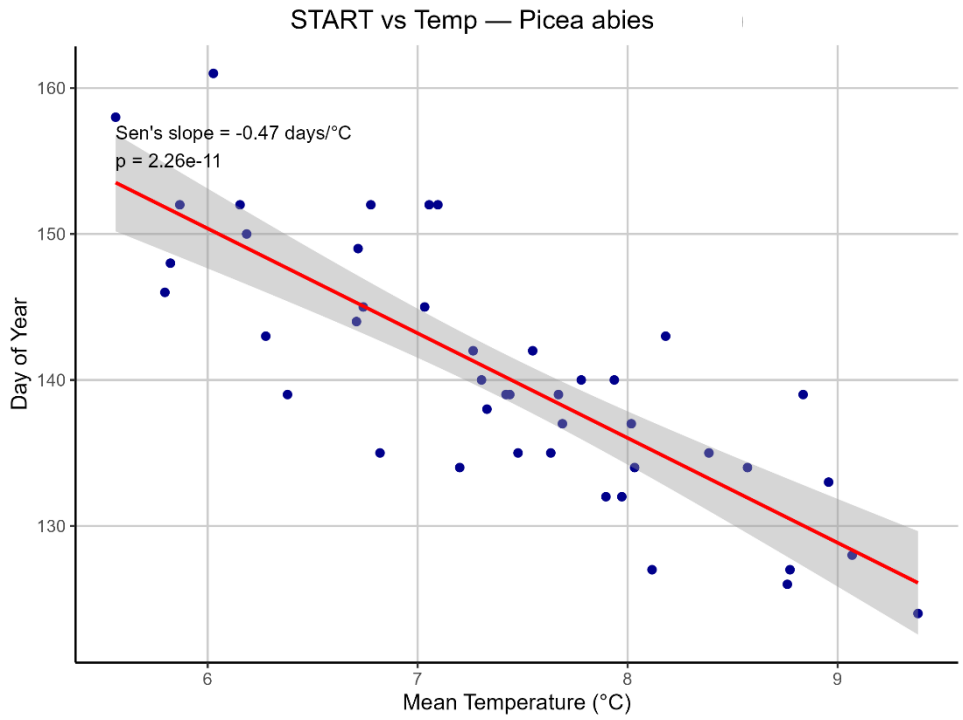

Figure 22. Scatter plot of mean spring temperature versus start of vegetation period (DOY) (1975–2019).

In contrast, the end of the vegetation period appears more stable over time. Figure 23 shows little interannual variability in end DOY, with most values clustering around DOY 275 to 280. This seasonal endpoint remains largely consistent across the full timespan, despite increases in mean annual temperature. The relative lack of trend suggests that while *Picea abies* responds to warming by initiating growth earlier in the year, the end of the active period does not extend substantially further into autumn. This stability of autumn phenology is likewise noted in Menzel et al. (2006), who found little evidence for significant changes in the end of the vegetation period at the continental scale.

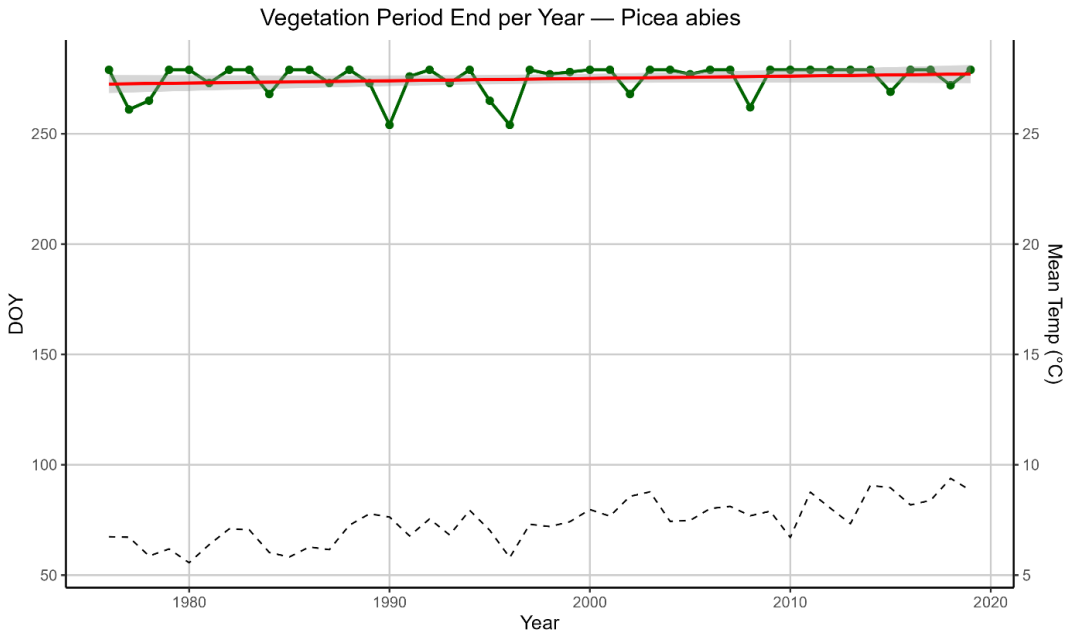

Figure 23. Annual end of vegetation (growing) period (day of year) for Picea abies (LWF-B90 simulation, 1975–2019).

Together, these results indicate an asymmetric shift in the vegetation period of *Picea abies*, primarily driven by earlier spring activation. This has important implications for species-level water and carbon dynamics, as a longer growing season could amplify transpiration or resource demand during early-season periods. Notably, this phenological advancement aligns with the increasing spring evapotranspiration trends observed in Section 3.2.1, particularly in the TRAIN model. The earlier onset of canopy activity likely contributes to enhanced transpiration during April and May, supporting the interpretation that rising spring ETA is linked to vegetation-climate interactions. This coherence between phenological and hydrological responses highlights the importance of integrated ecohydrological assessment when evaluating climate change impacts.

3.2.5 Discharge Calibration and Model Performance

Raven-HMETS

To assess the hydrological performance of the Raven-HMETS model, a calibration and validation approach was applied using observed discharge data from the Eyach catchment. The simulation period spans from 1975 to 2020 and includes a three-year warm-up phase (1975–1977) to minimize initial condition uncertainty. The calibration was performed for the period 1978–1999, while the subsequent years (2000–2020) were used for model validation. The model was calibrated using the Dynamically Dimensioned Search (DDS) algorithm with 5000 iterations to identify an optimal parameter set. To enhance spatial representativeness and improve model robustness, discharge data from both the Eyach catchment outlet and the Brotenaubach subbasin were included during calibration. However, the performance results and plots presented in the following section refer exclusively to the Eyach outlet discharge.
Overall, the model demonstrated good performance in reproducing streamflow during both the calibration and validation periods. The Nash–Sutcliffe Efficiency (NSE) reached 0.64 during calibration and 0.58 during validation, indicating a good level of agreement between observed and simulated discharge. The model's Root Mean Square Error (RMSE) values were moderate, and percent bias (PBIAS) remained within acceptable limits, showing slight overestimation during calibration (+10 %) and underestimation during validation (–12 %). These metrics suggest that the model can capture the dominant hydrological dynamics of the catchment (Table 12).

Table 12. Performance Metrics for Raven-HMETS Discharge Simulation in the Eyach Catchment

Period	**NSE**	**RMSE**	**PBIAS**
Warm-up	–3.05	0.96	+42.9 %
Calibration	0.64	0.45	+10.4 %
Validation	0.58	0.46	–11.9 %
Full period	0.44	0.54	+2.7 %

Calibration

Cumulative flow analysis (Figure 24) reveals a close agreement between observed and simulated streamflow volumes over the calibration period. The simulated cumulative discharge follows the observed trajectory with minimal long-term divergence, suggesting that the model effectively captures the total water balance of the Eyach catchment. This consistency across multiple hydrological years indicates that the model is well-calibrated with respect to runoff generation and routing and is capable of reproducing catchment-scale water yield over extended timescales.

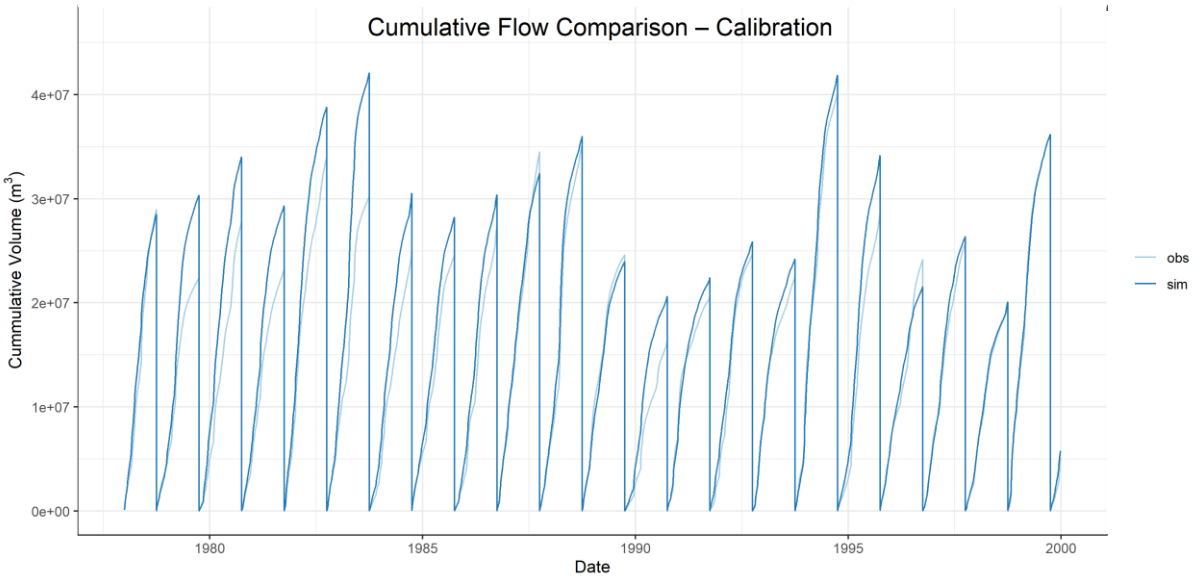

Figure 24. Cumulative observed vs. simulated discharge volumes (1975–2019) within calibration.

Figure 25 (p. 79) compares simulated and observed annual peak discharges for the calibration period. While the majority of points are distributed near the 1:1 reference line, especially for moderate events, the model tends to underestimate larger peaks. This pattern may reflect challenges in simulating fast runoff responses or capturing extreme precipitation events. Still, the overall agreement suggests that Raven-HMETS captures peak flow dynamics reasonably well under calibration conditions, supporting its applicability for flood-related analysis.

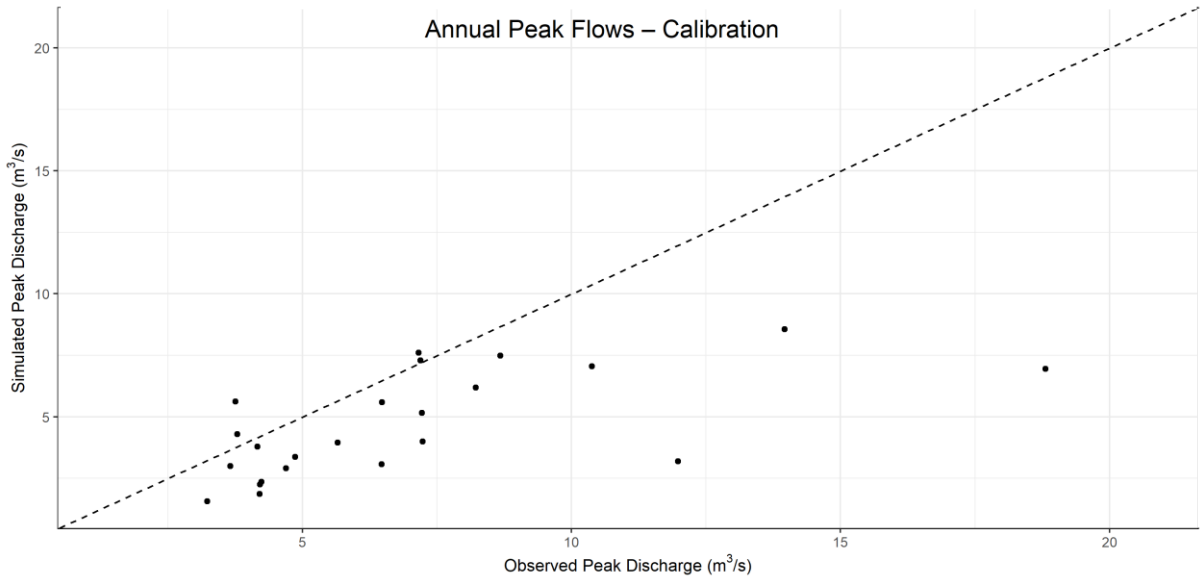

Figure 25. Scatter plot of observed vs. simulated annual peak flows (calibration period).

Figure 26 displays the monthly percent bias in simulated flow volumes relative to observations during the calibration period. The plot reveals a clear seasonal structure in model performance. Winter and early spring months (January–April) show consistent overestimation of discharge, with March exhibiting the highest positive bias. In contrast, summer months (July–August) are underestimated, suggesting challenges in simulating low-flow conditions during dry periods. Autumn shows mixed but generally positive biases. These patterns imply potential limitations in capturing evapotranspiration dynamics and snowmelt timing and highlight the importance of season-specific calibration adjustments.

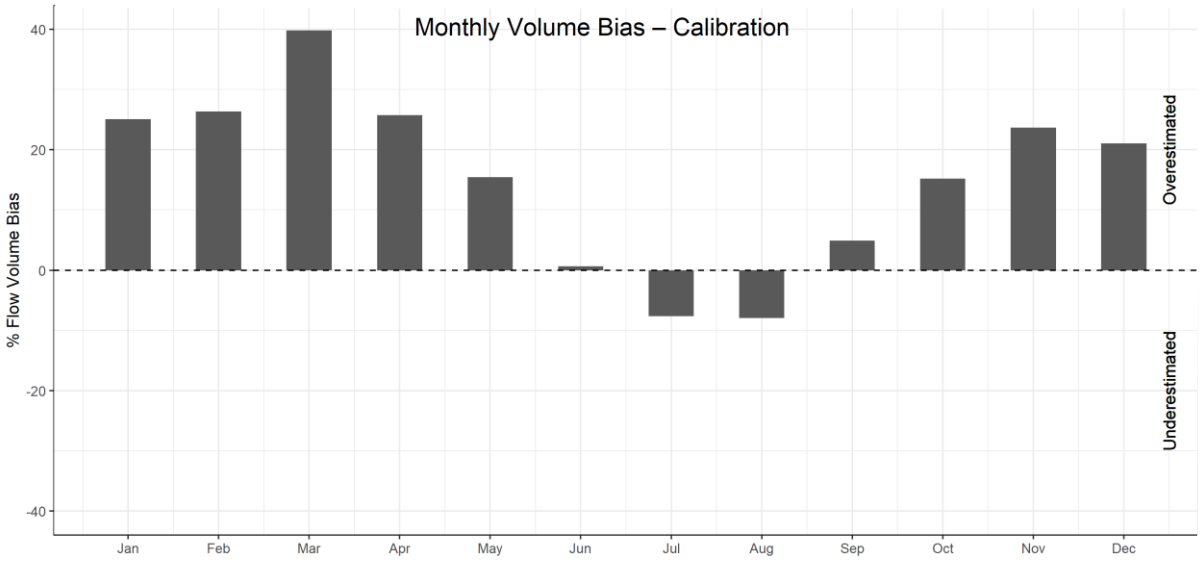

Figure 26. Monthly bias of simulated flow volumes relative to observations during calibration.

Figure 27 (p. 80) presents the hydrograph for the best calibration year (1988), where the model achieved a Nash–Sutcliffe Efficiency (NSE) of 0.838. The observed and simulated discharge series show strong agreement across the year, with good replication of peak timing, flow magnitudes, and seasonal variability. Most high-flow events are captured accurately, although

minor deviations occur in the intensity of some flood peaks. Recession flows and baseflow dynamics are well reproduced, indicating that the model effectively represents the dominant hydrological processes during the calibration phase. Overall, the results confirm a reliable simulation of intra-annual flow dynamics for the Eyach catchment.

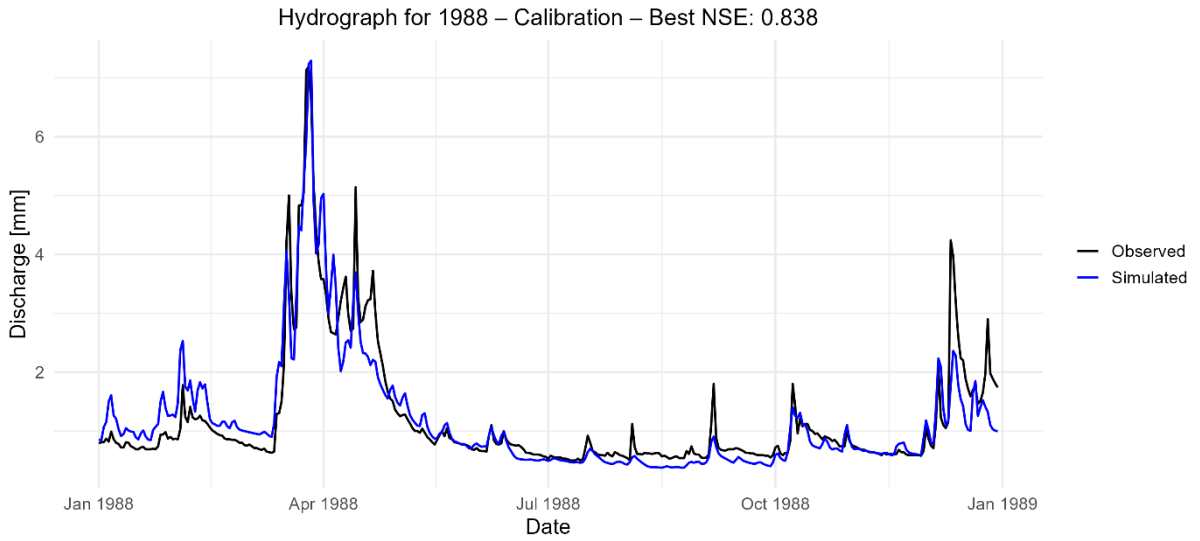

Figure 27. Hydrograph with the highest fit of simulated vs. observed streamflow during calibration

Validation

Cumulative discharge curves over the validation period (Figure 28) indicate a general underestimation of total flow volume**.** While the model captures the seasonal accumulation pattern reasonably well, the simulated cumulative volumes remain consistently below the observed values, particularly in the latter half of the period. This suggests a systematic underrepresentation of runoff generation or flow routing during validation, which may be influenced by parameter transferability or climatic shifts not captured during calibration.

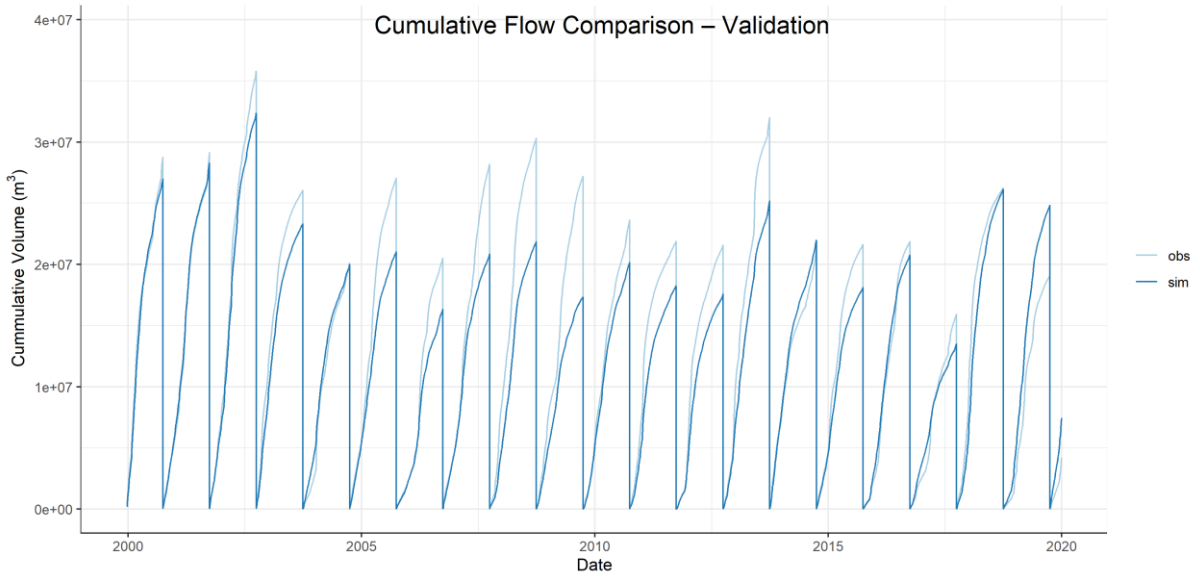

Figure 28. Cumulative observed vs. simulated discharge volumes (1975–2019) within validation.

Figure 29 compares observed and simulated peak discharges for each year of the validation period. Most data points fall below the 1:1 reference line, indicating a systematic underestimation of peak flows by the model. This suggests that during independent validation, the model tends to attenuate high-magnitude discharge events. Although the general trend of peak timing may be preserved, this pattern highlights limitations in capturing extreme runoff conditions without calibration constraints. Nonetheless, the representation remains informative for broader hydrologic assessments.

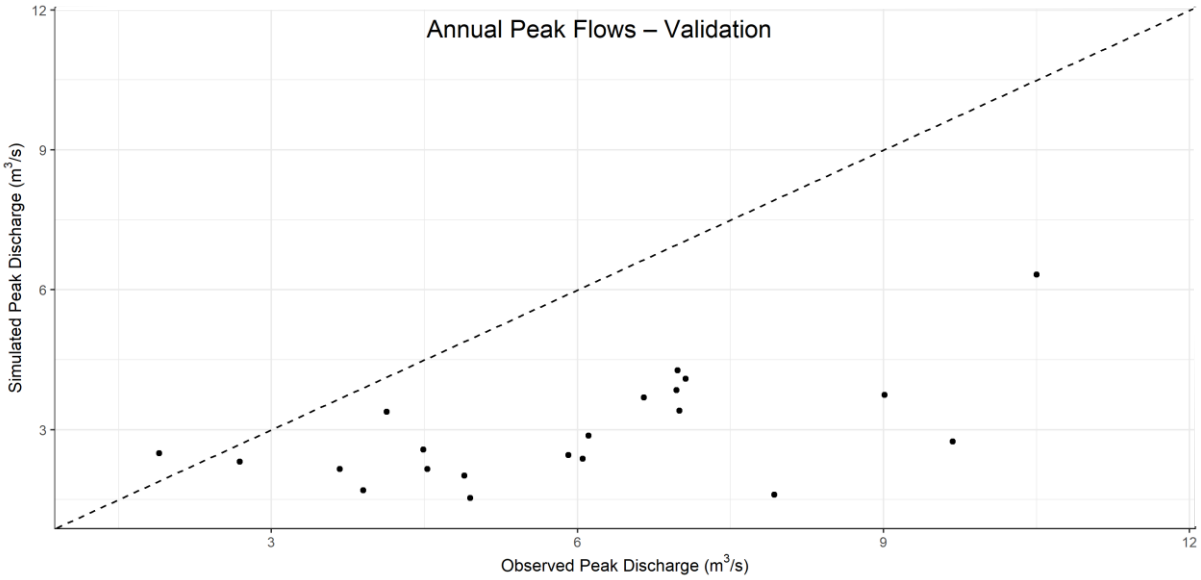

Figure 29. Scatter plot of observed vs. simulated annual peak flows (validation period).

Figure 30 (p. 82) shows the monthly percent bias in simulated discharge volumes for the validation period. The seasonal pattern is evident, with notable underestimation during late spring and summer months—especially in June—indicating difficulties in reproducing low-flow conditions. Slight overestimations occur in winter and late autumn, particularly in November. These trends suggest the model performs less reliably during dry periods and transitional seasons, possibly due to limitations in representing soil moisture and delayed runoff processes under validation conditions.

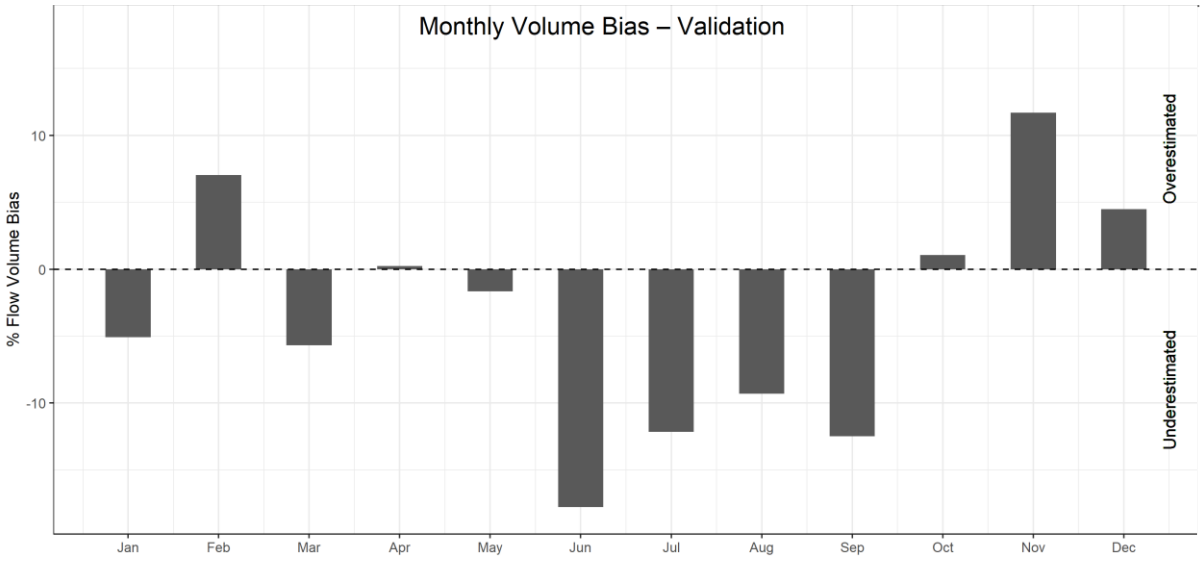

Figure 30. Monthly bias of simulated flow volumes relative to observations during validation.

Figure 31 displays the hydrograph for the best validation year (2001), achieving a Nash–Sutcliffe Efficiency (NSE) of 0.726. The model reproduces the overall flow dynamics well, including the timing of major peaks and recession limbs. However, some discrepancies are evident during high-flow periods, where simulated peaks tend to slightly underestimate observed discharge magnitudes. Baseflows and recession phases align more closely, supporting the model's robustness in capturing sustained runoff. Despite minor deviations in extreme events, the hydrograph indicates a solid validation performance under independent data conditions.

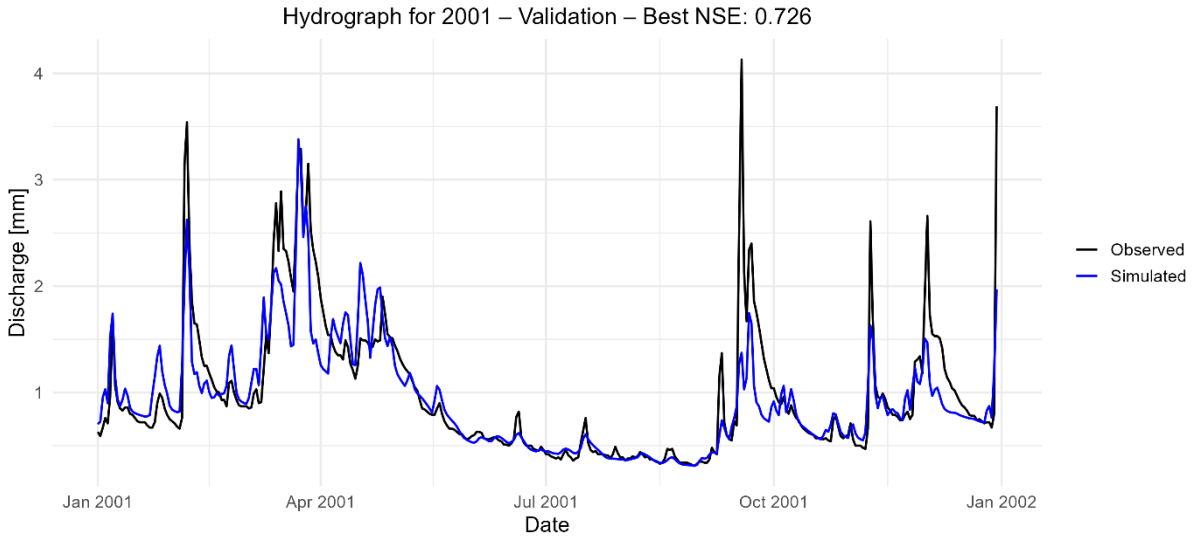

Figure 31. Hydrograph with the highest fit of simulated vs. observed streamflow during validation.

HBV-Light

The HBV-Light model was calibrated against daily discharge observations for the Eyach catchment over the period 1976–2019, with a one-year spin-up in 1975 to allow system stabilization. Overall, the model showed good predictive performance, with a Nash–Sutcliffe

Efficiency (NSE) of 0.66, Kling–Gupta Efficiency (KGE) of 0.78, and Coefficient of Determination (R^2) of 0.66, indicating a strong agreement with observed streamflow. The small percent bias (PBIAS) of –2 % further suggests only a slight underestimation of total flow volume (Table 13).

A total of 15,000 model runs were conducted using a global search based on the GAP optimization approach. Subsequently, an additional 15,000 model runs were carried out using the Powell local search method to refine the parameter estimates. This two-stage procedure ensured both a comprehensive exploration of the parameter space and targeted refinement, thereby minimizing equifinality and enhancing model robustness.

Table 13. Goodness-of-Fit Metrics for the Calibrated HBV-Light Model.

Metric	Value	Description
Nash–Sutcliffe Efficiency (NSE)	0.66	Measures relative predictive skill (ideal = 1)
Kling–Gupta Efficiency (KGE)	0.78	Balances correlation, bias, and variability
Coefficient of Determination (R^2)	0.66	Measures strength of linear relationship
Percent Bias (PBIAS)	–2 %	Indicates volume bias (negative = underestimation)

Cumulative flow volume analysis (Figure 32) indicates that the long-term water balance is well preserved, with minimal divergence between observed and simulated cumulative volumes. This outcome implies that the model reliably simulates total runoff generation and transport processes over multi-decadal periods.

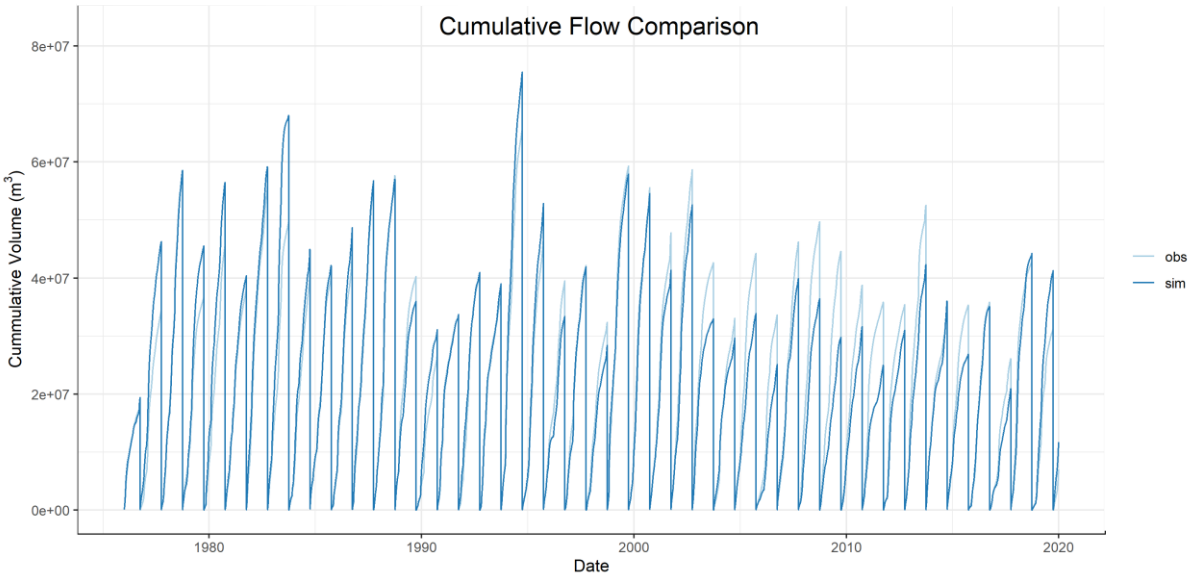

Figure 32. Cumulative observed vs. simulated discharge volumes (1976–2019).

Annual peak discharge comparison (Figure 33, p. 84) further highlights the model's limitations in capturing the full magnitude of extreme flow events. The 1:1 scatter plot shows a systematic underestimation of peak flows, particularly at higher magnitudes. This behaviour could stem from underrepresentation of snowmelt dynamics, rainfall-runoff intensity during extreme precipitation events, or inadequate routing of surface runoff. Nevertheless, the correlation

between simulated and observed peaks remains reasonably strong, confirming that the model responds correctly to the timing of high-flow events, even if peak magnitudes are attenuated.

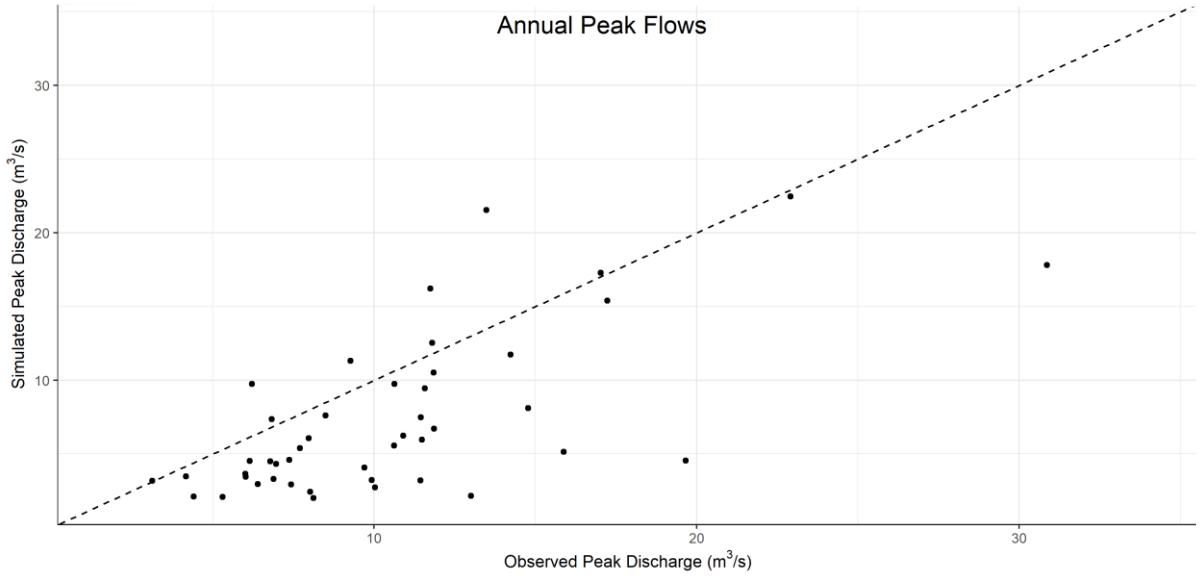

Figure 33. Scatter plot of observed vs. simulated annual peak flows.

Monthly performance was evaluated using flow volume bias (Figure 34). The model shows a tendency to underestimate streamflow from January to April, particularly in March, while moderate overestimations occur from June through November, peaking in August. These biases may reflect challenges in capturing hydrological processes such as snowmelt or evapotranspiration dynamics during different parts of the year.

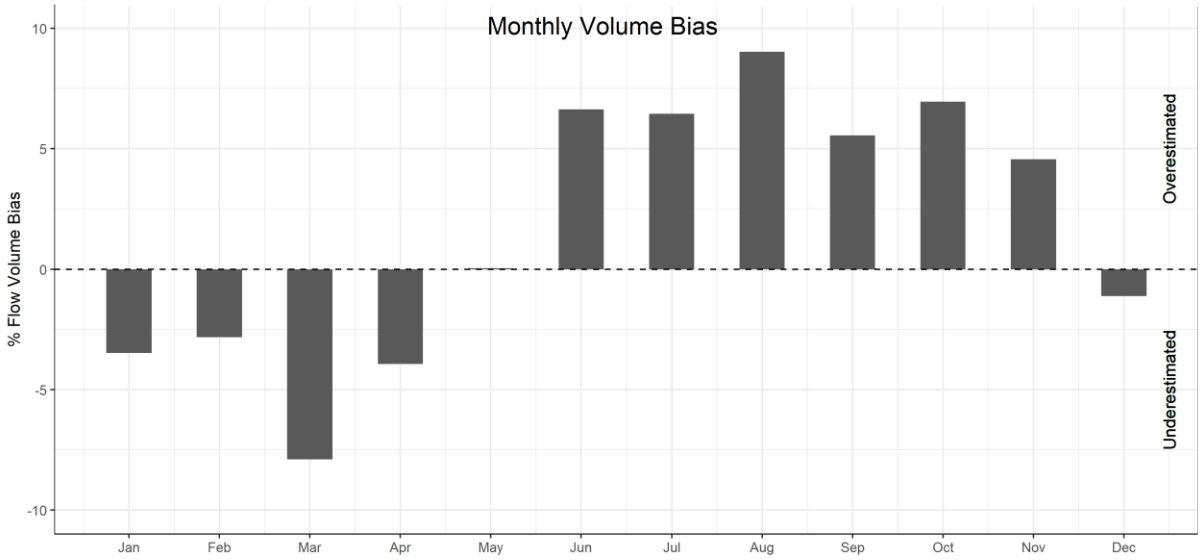

Figure 34. Monthly bias of simulated flow volumes relative to observations.

Of particular note is the analysis of annual model performance. By computing the NSE for each individual year, the year 1993 emerged as the best-performing period, with an annual NSE of 0.925. The hydrograph for 1993 (Figure 35, p. 85) shows a near-perfect match between

simulated and observed flows, both in terms of baseflow and peak discharge timing and magnitude. This result confirms that, under certain hydrological conditions, the model can reproduce the observed streamflow dynamics with high precision.

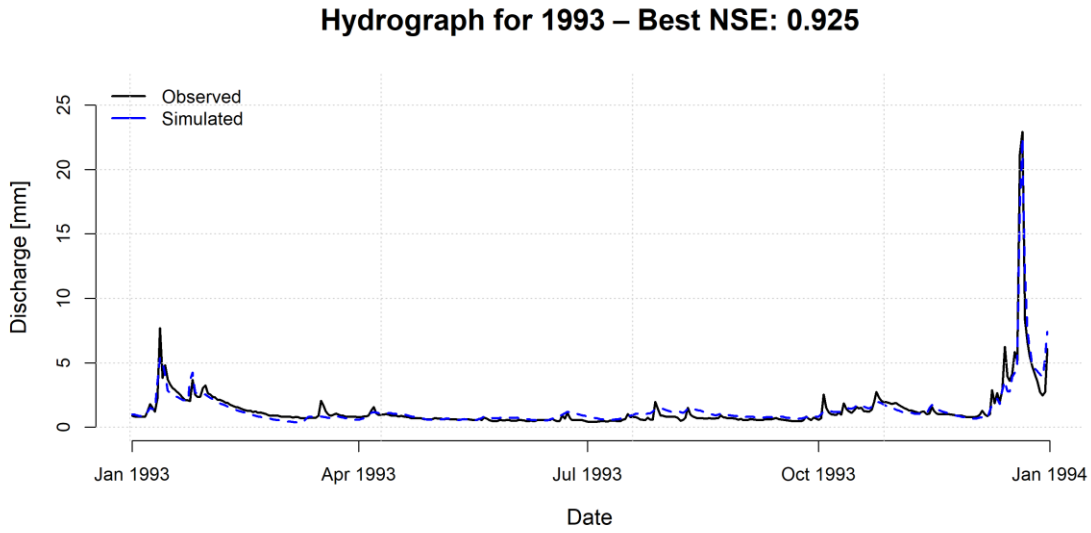

Figure 35. Hydrograph with the highest fit of simulated vs. observed streamflow during validation.

Overall, the evaluation demonstrates that the applied models are capable of simulating streamflow and key ecohydrological variables with reasonable fidelity across a range of hydrological and climatic conditions. While individual model limitations are evident—such as underestimation of peak flows or divergent evapotranspiration magnitudes—their performance aligns with expectations given their structural complexity and calibration strategy. Particularly, the models capture essential temporal dynamics and long-term trends, offering valuable insights into the hydrological functioning of the Eyach catchment.

Summarizing across models and components, several consistent patterns emerge: evapotranspiration exhibits high interannual variability, with a weak upward trend primarily during spring; soil moisture shows a robust, statistically significant decline, especially in spring and summer, pointing toward increasing hydroclimatic stress; and snow cover duration has clearly diminished over the past four decades, with all models confirming significant negative trends. Together, these multi-model results present a coherent and physically plausible picture of the catchment's hydrologic response to historical climate variability and change. Importantly, they highlight the necessity of accounting for model structural differences—particularly regarding vegetation, snow, and soil processes—when evaluating ecohydrological impacts under ongoing climate change.

Chapter 4

This chapter addresses Objective 5 of the study: evaluating how different forest compositions influence hydrological processes under changing climatic conditions. Building on earlier model results, it introduces a scenario-based application of the LWF-Brook90 (B90) model to explore the hydrological implications of tree species adaptation.

A key advantage of B90 is its ability to simulate species-specific vegetation dynamics by modifying physiological and phenological traits such as leaf area index (LAI), and phenology. This flexibility enables the modelling of realistic forest scenarios under identical climatic and soil conditions. While previous simulations focused on *Picea abies*—the dominant species in the Eyach catchment—this chapter includes *Fagus sylvatica* and *Quercus robur* to assess their contrasting water use strategies and potential contributions to hydrological resilience.

The simulations aim to quantify differences in evapotranspiration, soil moisture dynamics, vegetation period dynamics and snow cover resulting from alternative species configurations. By applying consistent climate forcing across all scenarios, the analysis isolates species effects and highlights the role of forest composition in shaping catchment-scale water balance.

These results offer critical insights for climate adaptation planning in forested catchments. As regions like the Black Forest experience increasing hydroclimatic stress, species selection becomes a strategic tool for sustaining ecosystem function and water availability. The findings underscore the value of integrating ecological and hydrological modelling to inform reforestation and forest management efforts in a changing climate (Keenan, 2015).

4. Tree Species Adaptation Modeling

4.1 Evapotranspiration

Figure 36 (p. 87) displays the annual total evapotranspiration (ETA) trends for *Fagus sylvatica*, *Quercus robur*, and *Picea abies*, simulated with the LWF-Brook90 model from 1975 to 2019 in the Eyach catchment. *Picea abies*, the only evergreen species, consistently exhibits higher annual ETA than the two deciduous species. This pattern reflects its continuous year-round transpiration, in contrast to the seasonally constrained water use of *Fagus* and *Quercus*.

All three species show declining ETA over the 45-year period, yet only the trend for *Picea abies* is statistically significant (Sen's slope: –3.28 mm/year, $p = 0.011$) (Table14, p. 87). The declines for *Fagus sylvatica* (–2.36 mm/year, $p = 0.059$) and *Quercus robur* (–2.26 mm/year, $p = 0.062$) are slightly weaker and not significant at the 0.05 level. Nevertheless, the consistent direction of these trends suggests a general reduction in forest water use, possibly linked to increasing atmospheric demand and soil moisture constraints under warming conditions.

Table 14. Mann–Kendall Trend Analysis of Annual Evapotranspiration for Three Tree Species (1975–2019)

Species	Season	Sen´s Slope	p-value
Fagus sylvatica	Annual	-2.35952899	0.05903
Picea abies	Annual	-3.27530139	**0.01129***
Quercus robur	Annual	-2.26443167	0.06170

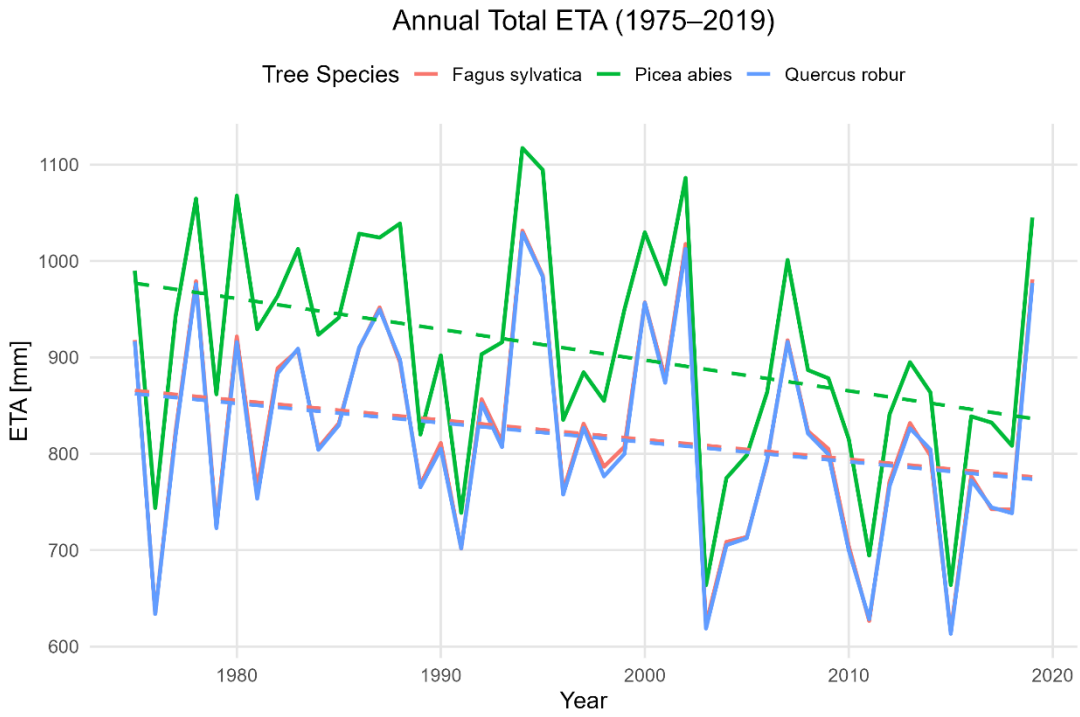

Figure 36. Annual total evapotranspiration (ETA) trends by species from 1975–2019 (LWF-Brook90 simulations, Eyach catchment).

Figure 37 (p. 88) complements these findings by comparing the species-wise distributions of annual ETA. *Picea abies* has the highest median and greatest interannual variability, confirming its higher and more climate-sensitive transpiration regime. In contrast, *Fagus sylvatica* and *Quercus robur* show lower medians and narrower ranges, reflecting their more conservative water use strategy.

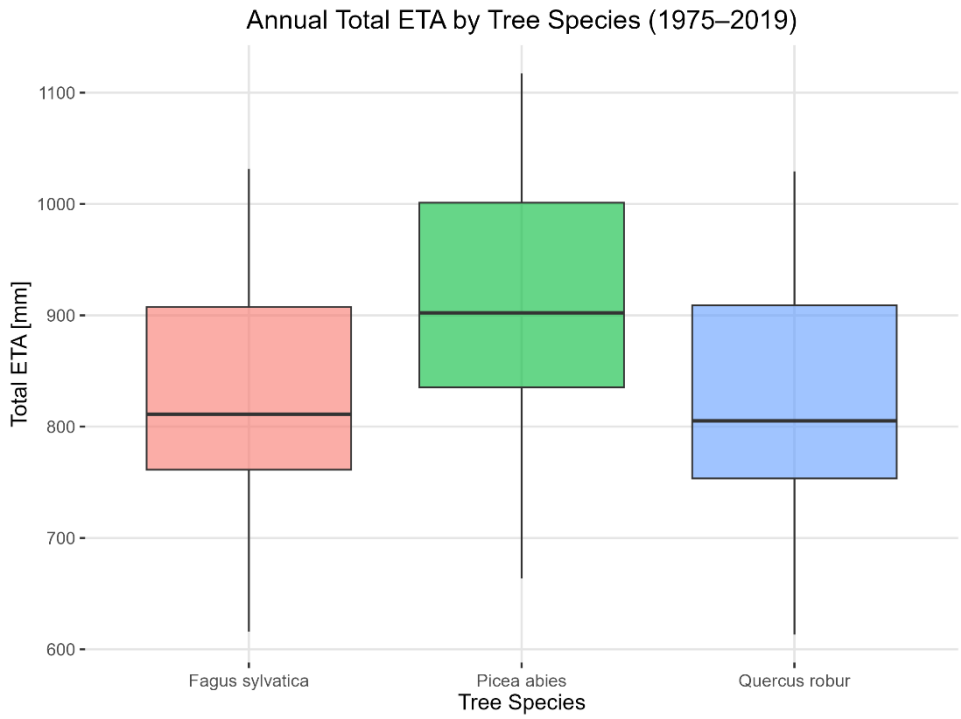

Figure 37. Distribution of total annual evapotranspiration by species (boxplots for Picea abies, Fagus sylvatica, Quercus robur, 1975–2019).

Seasonal Mann–Kendall trend analysis revealed no significant ETA trends for Fagus sylvatica or Quercus robur across any season ($p > 0.05$). However, Picea abies showed a significant decline in autumn ETA (Sen's slope: –0.77 mm/year, $p = 0.041$) (Table 15), despite rising autumn temperatures (see Section 3.1.1). This may reflect ecohydrological decoupling, where warming does not increase transpiration due to other limiting factors. While warmer autumns can delay photosynthetic decline in *Picea abies* Stinziano et al., (2015), this does not necessarily lead to higher water use under real-world moisture constraints. These interspecific differences in evapotranspiration are rooted in leaf habit and phenology. The evergreen canopy of *Picea* permits continuous evaporation and interception throughout the year, while the deciduous *Fagus* and *Quercus* restrict their transpiration to the growing season—a pattern broadly explained by the differing ecological strategies of evergreen and deciduous species (Givnish, 2002).

Table 15. Seasonal Sen's slopes and p-values for annual evapotranspiration (ETA) trends (1975–2019) simulated with LWF-Brook90.

Species	Season	Sen's Slope	p-value
Fagus sylvatica	Autumn	-0.597	0.168
Fagus sylvatica	Spring	-1.226	0.125
Fagus sylvatica	Summer	-0.795	0.323
Fagus sylvatica	Winter	+0.492	0.500
Picea abies	**Autumn**	**-0.772**	**0.041***
Picea abies	Spring	-1.230	0.077
Picea abies	Summer	-0.954	0.286
Picea abies	Winter	-0.147	0.703

Species	Season	Sen's Slope	p-value
Quercus robur	Autumn	-0.549	0.200
Quercus robur	Spring	-1.219	0.102
Quercus robur	Summer	-0.769	0.353
Quercus robur	Winter	+0.457	0.428

4.2 Soil Moisture

For all three species, annual soil moisture (SM) shows a statistically significant declining trend over the simulation period 1975–2019 (Table 16). The Mann–Kendall test reveals strong negative trends for all three tree species. These results underscore that, despite physiological and phenological differences, all species are affected by long-term drying under the given climatic conditions.

Table 16. Mann–Kendall trend statistics (Sen's slope and p-values) for seasonal and annual soil moisture (SM) in three tree species (1975–2019).

Species	Season	Sen´s Slope	p-value
Fagus sylvatica	**Annual**	**-0.32782854**	**0.00192871***
Picea abies	**Annual**	**-0.40001776**	**0.0006401***
Quercus robur	**Annual**	**-0.32614301**	**0.00206008***

Figures 38 and 39 (p. 90) illustrate interspecific differences in annual mean SM between *Fagus sylvatica*, *Quercus robur*, and *Picea abies* over the period 1975–2019. While absolute differences in SM are relatively small, both deciduous species consistently maintain slightly higher SM levels than the evergreen reference, *Picea abies*. This pattern is visible in the time series plot (Figure 40), where the *Fagus sylvatica* and *Quercus robur* lines tend to remain above those of *Picea abies*, especially in more recent decades. The declining trends are parallel across all species but start from marginally higher baselines for the deciduous species.

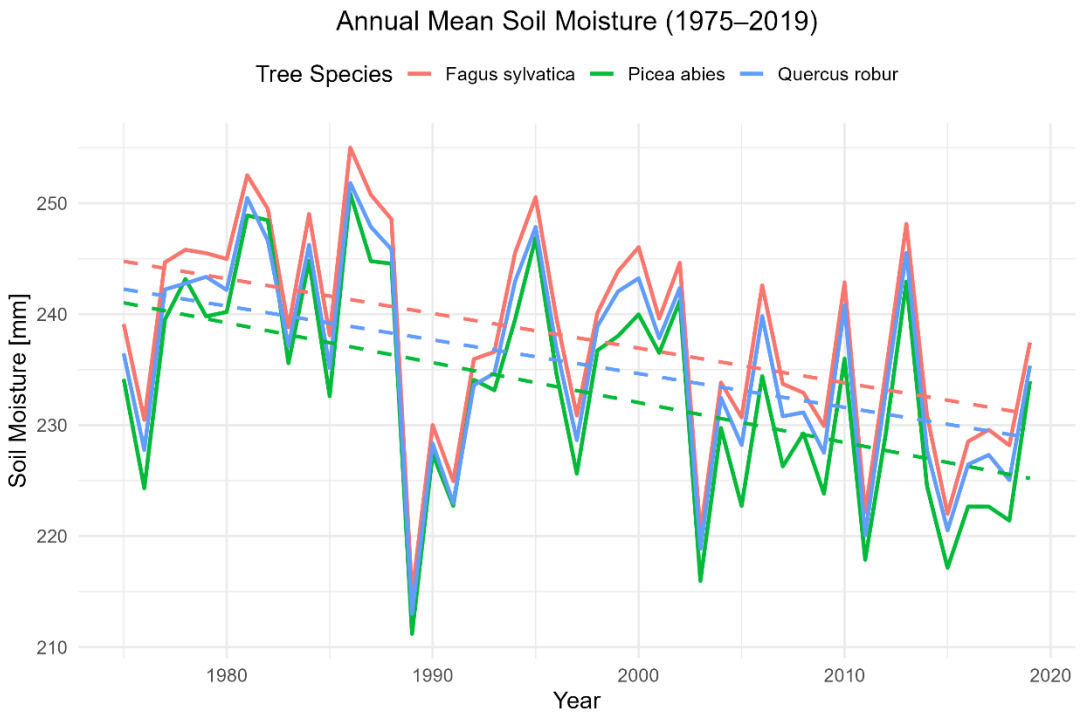

Figure 38. Annual mean soil moisture (1975–2019) simulated for Fagus sylvatica, Picea abies, and Quercus robur using the LWF-Brook90 model. Solid lines show yearly values; dashed lines indicate linear trends.

The boxplot (Figure 39) confirms this pattern statistically. Median SM values are highest for *Fagus sylvatica*, followed closely by *Quercus robur*, with *Picea abies* showing the lowest overall median. Variability is comparable among the three species, but the interquartile range for the deciduous species is slightly wider, suggesting a greater spread in annual SM conditions.

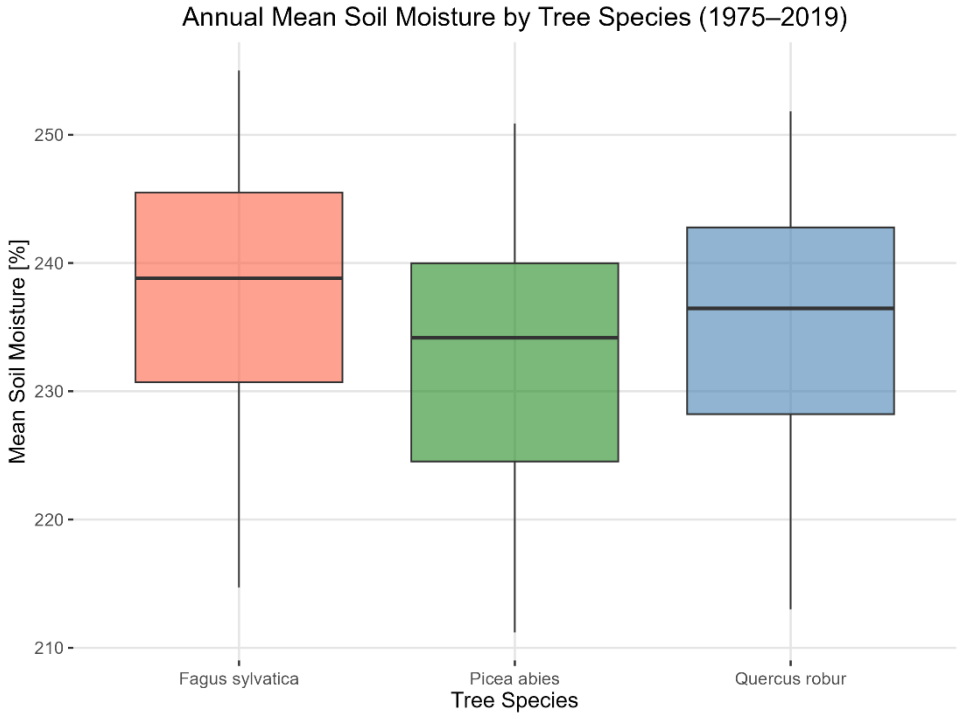

Figure 39. Distribution of annual soil moisture by species (boxplots for Picea abies, Fagus sylvatica, Quercus robur, 1975–2019)

These subtle but consistent differences support the interpretation that species with lower annual evapotranspiration—largely due to their deciduous leaf habit—may better preserve soil moisture over time (Bréda et al., 2006). Although all species exhibit a downward trend in absolute SM levels due to broader climatic drivers, the deciduous species appear to retain a modest hydrological advantage. This has potential implications for forest composition and management under future drought scenarios, where the ability to buffer soil moisture may enhance ecosystem resilience (Bréda et al., 2006; Teuling et al., 2010).

Seasonal trend analysis reveals statistically significant soil moisture (SM) declines in spring and winter across all three species (Table 17). The strongest drying trend is observed in *Picea abies* during spring followed by *Fagus sylvatica* and *Quercus robur* in winter. These results indicate that both early and late-season soil moisture availability has decreased markedly since 1975, particularly for the evergreen species. In contrast, summer and autumn trends are generally weaker and not statistically significant, suggesting that moisture dynamics in these seasons may be more buffered or more variable. Overall, the spring and winter SM declines likely reflect the combined effects of earlier onset of vegetation activity and reduced snow accumulation or retention (section 3.2).

Table 17. Seasonal Mann-Kendall trend results for soil moisture (1975–2019) by species. Statistically significant trends ($p < 0.05$) are marked with an asterisk (*).

Species	Season	Sen's Slope [mm/year]	p-value
Fagus sylvatica	**Spring**	–0.429	**0.0338 ***
Fagus sylvatica	Summer	–0.117	0.3231
Fagus sylvatica	Autumn	–0.286	0.1866
Fagus sylvatica	**Winter**	**–0.424**	**0.0184 ***
Picea abies	**Spring**	**–0.642**	**0.0056 ***
Picea abies	Summer	–0.132	0.2444
Picea abies	Autumn	–0.314	0.1450
Picea abies	**Winter**	**–0.404**	**0.0165 ***
Quercus robur	**Spring**	**–0.423**	**0.0409 ***
Quercus robur	Summer	–0.106	0.3630
Quercus robur	Autumn	–0.264	0.2289
Quercus robur	**Winter**	**–0.416**	**0.0174 ***

4.3 Snow Cover Days

All three simulated species show a statistically significant decline in winter snow cover duration (SCD) over the period 1975–2019, as summarized in Table 18. The evergreen conifer *Picea abies* exhibits the strongest negative trend, followed by *Quercus robur* and *Fagus*. These results confirm a consistent and significant loss of winter snow cover across forest types under changing climate conditions.

Table 18. Sen's slope and p-values for long-term trends in vegetation period duration (1975–2019) simulated by species.

Tree Species	Sen's Slope (days/year)	p-value
Fagus sylvatica	**–0.80**	**0.012 ***
Picea abies	**–1.00**	**0.011 ***
Quercus robur	**–0.82**	**0.012 ***

As illustrated in Figure 40, the temporal evolution of SCD shows a sharp decline from the 1980s onward across all species, with considerable interannual variability. While *Picea abies* generally maintains slightly higher SCD values, the observed trajectories for all species suggest convergence under warming winters (section 3.1.1) and reduced snowfall events.

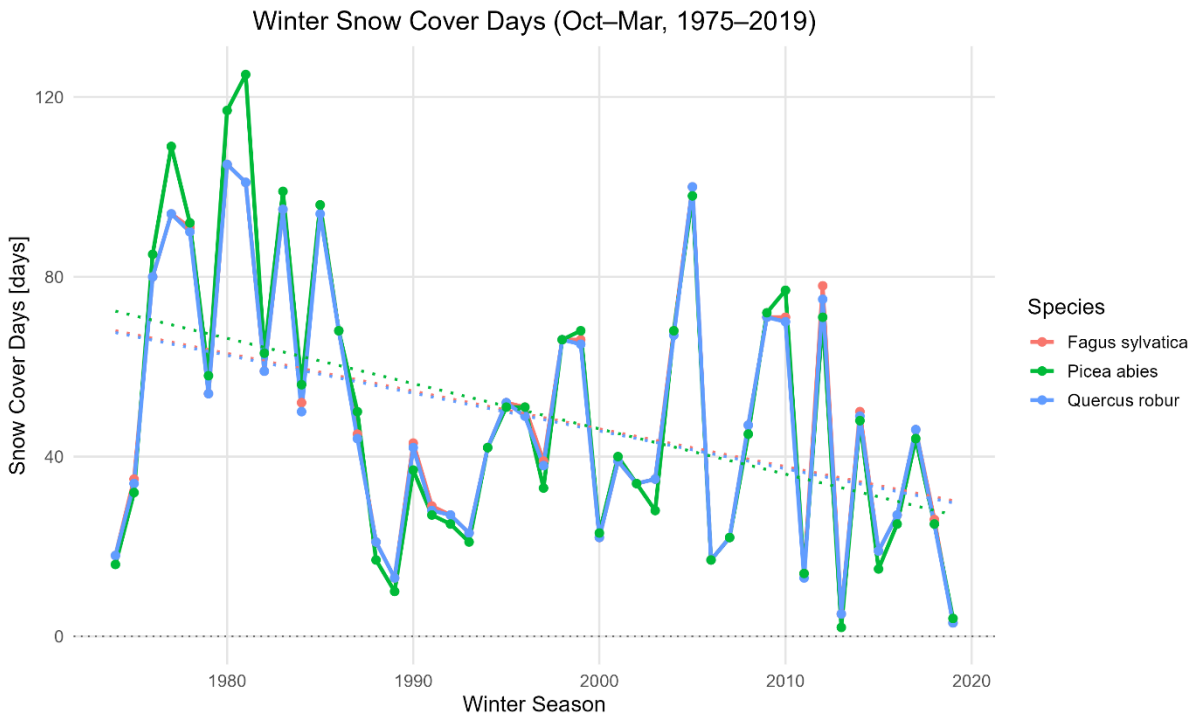

Figure 40. Temporal trends in winter snow cover duration (October–March) for three tree species (1975–2019).

The accompanying boxplot (Figure 41, p 93) indicates that *Fagus sylvatica* and *Quercus robur* maintain similar or only slightly lower median SCD values compared to *Picea abies*, despite their lower winter canopy cover. This suggests that species-specific canopy traits—such as reduced interception and shading in deciduous stands—may buffer SCD losses, particularly during leaf-off conditions and in sheltered sites where snow can accumulate beneath the canopy (Varhola et al., 2010).

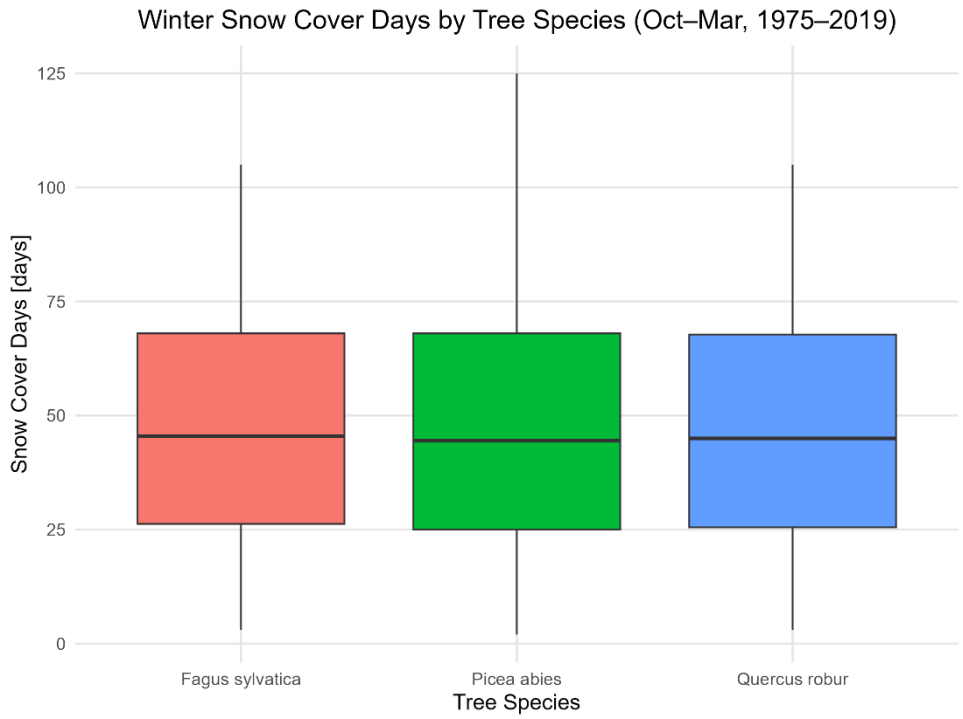

Figure 41. Distribution of winter snow cover duration (October–March, 1975–2019) for three tree species.

These findings suggest that while all forest types experience a clear reduction in winter snow cover under warming conditions, species-specific differences in SCD are relatively minor in this case. Nonetheless, small differences in canopy structure may still influence snow retention at the local scale (Varhola et al., 2010) and should be considered where forests differ markedly in structure or density. However, in this study, interspecies differences appear to play only a limited role in shaping broader snow dynamics.

4.4 Vegetation Period Dynamics – Start and End of Growing Season

The timing of the vegetation period shows pronounced species-specific patterns and clear climate-driven trends in the onset of the growing season, while the end remains comparatively stable. In comparison to the evergreen *Picea abies*, both *Fagus sylvatica* and *Quercus robur* demonstrate distinct phenological dynamics over the study period, with strong signals of advancement in spring leaf-out but no significant changes in autumn senescence.

Linear trend analysis confirms a significant advancement in the start of the vegetation period for both deciduous species (Table 19, p. 94). Sen's slope estimates indicate a mean shift of –0.42 days per year for *Fagus sylvatica* and –0.50 days per year for *Quercus robur*, corresponding to a total advance of 15–20 days since the mid-1970s. These trends are statistically robust, with p-values < 0.05. In contrast, no significant trends were detected in the end of the vegetation period for either species, indicating relatively stable senescence timing despite warming conditions.

Table 19. Long-Term Trends (1975–2019) in the Start of the Vegetation Period for Selected Tree Species.

Species	Period	Sen's Slope (days/year)	p-value
Fagus sylvatica	**Start**	**-0.42**	**1.62E-07**
Picea abies	**Start**	**-0.47**	**5.78E-06**
Quercus robur	**Start**	**-0.50**	**3.34E-05**

These patterns are further supported by comparative analyses of phenological differences to *Picea abies*. Figure 42 illustrates the temporal evolution of vegetation period start differences relative to Picea. Both *Fagus sylvatica* and *Quercus robur* consistently initiate their growing season earlier than *Picea abies*, with average differences ranging from 5 to 15 days. These offsets have gradually increased, suggesting a decoupling of phenological strategies under ongoing climate change. The increase in difference is paralleled by a rise in mean annual temperatures (dashed black line), further reinforcing temperature as a primary phenological driver.

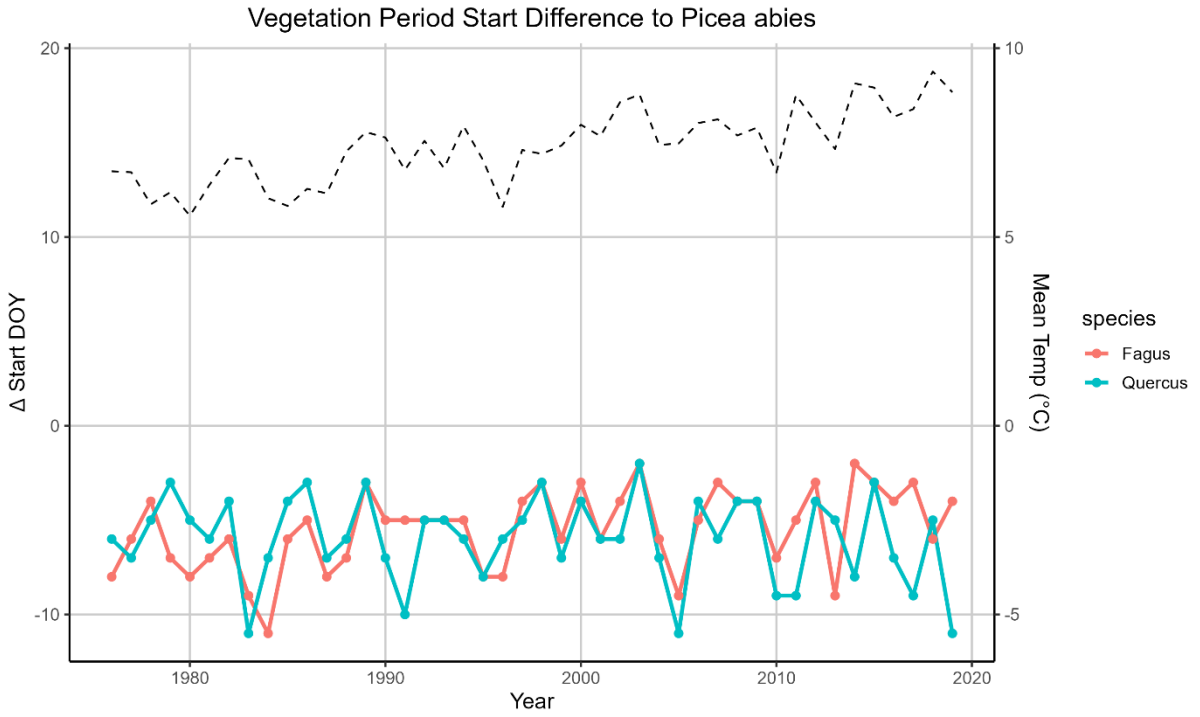

Figure 42. Annual Onset Difference of the Vegetation Period for Fagus sylvatica and Quercus robur relative to Picea abies (1975–2019).

Temperature sensitivity of spring phenology is confirmed through correlation analysis (Figures 43 & 44, p. 95). For *Fagus sylvatica*, start-of-season DOY declines by 0.42 days per °C increase, with a highly significant correlation ($p \approx 2e–09$). Similarly, *Quercus robur* exhibits a –0.50 days/°C relationship ($p \approx 4.2e–12$), marking it as the most temperature-sensitive species among those analysed.

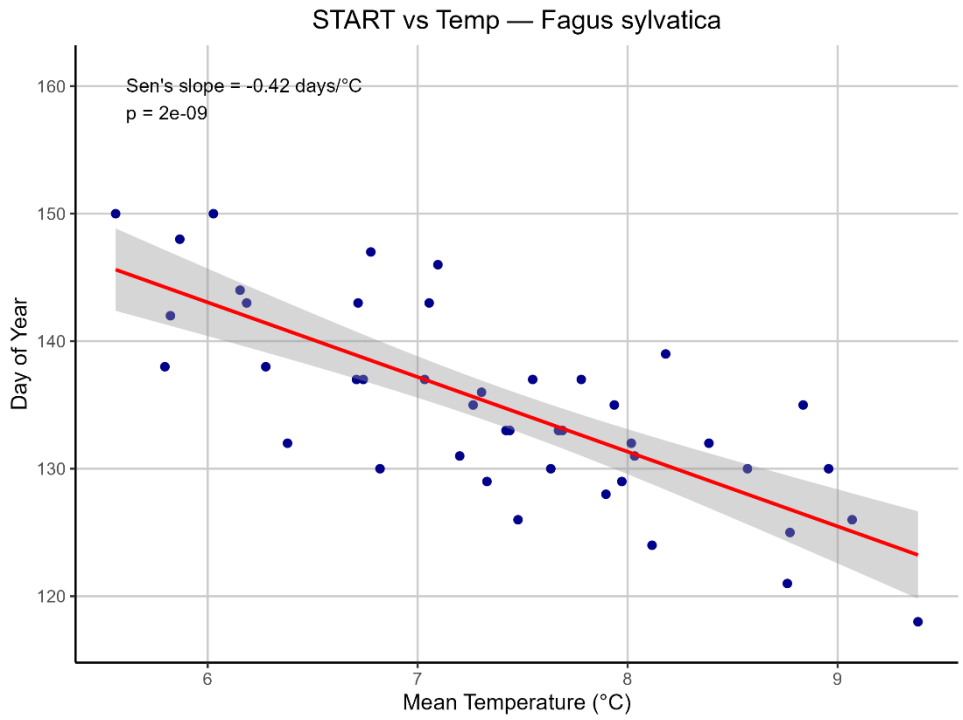

Figure 43. Scatter plot of mean spring temperature versus start of vegetation period (day of year, DOY) for Fagus sylvatica from 1975 to 2019. A linear regression line (red) with 95% confidence interval (grey shading) is shown.

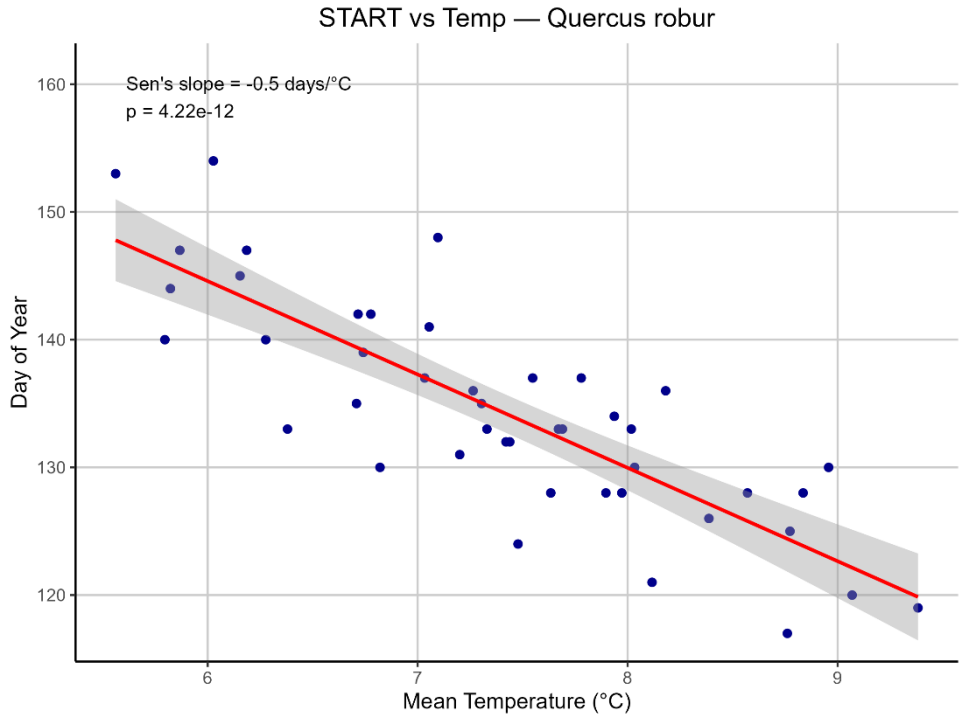

Figure 44. Scatter plot of mean spring temperature versus start of vegetation period (day of year, DOY) for Quercus robur from 1975 to 2019. A linear regression line (red) with 95% confidence interval (grey shading) is shown.

Importantly, while spring phenology tightly correlates with temperature, autumnal responses are more variable, with end-of-season dates showing weaker and statistically non-significant trends. This asymmetry suggests that the extension of the growing season in *Fagus sylvatica*

and *Quercus robur* is largely driven by earlier leaf-out, rather than delayed senescence. The absence of strong end-of-season trends may reflect additional regulatory mechanisms such as photoperiod sensitivity or species-specific physiological constraints on autumn phenology.
Together, these results support the conclusion that deciduous broadleaved species in temperate forests exhibit stronger phenological responses to warming than evergreen conifers. The earlier and more temperature-sensitive leaf-out patterns of *Fagus sylvatica* and *Quercus robur* suggest an adaptive capacity to exploit extended growing seasons under climate change, consistent with findings by Vitasse et al., (2011), who showed that canopy duration increased more strongly in deciduous than coniferous species, driven primarily by earlier spring onset. Similarly, Menzel and Fabian, (1999) reported a Europe-wide extension of the growing season by approximately 10 days since the 1960s, with spring advancement being more pronounced than autumn delay. These results underline the phenological plasticity of deciduous species in response to warming. Although longer-term ecological implications—such as frost risk or altered carbon allocation—remain subjects of further investigation, the current evidence indicates a clear species-specific advantage in phenological responsiveness for deciduous trees under ongoing climate change.

Chapter 5

In this chapter, future climate scenarios are explored to assess how changing climatic conditions may impact hydrological parameters and forest dynamics within the Eyach catchment. For this analysis, the CORDEX REMO 2009 dataset was used to model climate projections up to the year 2050 under different Representative Concentration Pathways (RCPs), reflecting varying levels of CO_2 emissions. These projections serve as the basis for evaluating potential changes in key hydrological variables such as evapotranspiration, soil moisture, and water availability.
To assess these changes, the TRAIN and LWF-Brook90 models were selected and applied. These two models were specifically chosen because they do not require discharge data as input—making them suitable for future scenario analysis, where such observed discharge data is inherently unavailable. This key advantage allows for the simulation of forward-looking scenarios without the need for calibration to measured streamflow, which is a limitation for other models.
The TRAIN model was driven by climate forcing data previously processed from the CORDEX REMO 2009 dataset, which included coordinate transformation, spatial resampling, and clipping to the Eyach catchment area. The LWF-Brook90 model was also driven by climate data from the CORDEX REMO 2009 dataset; however, instead of using gridded data as in TRAIN, the forcing variables were spatially averaged over the Eyach catchment to produce single time series inputs for the simulations. This ensured compatibility with the point-scale structure of LWF-Brook90 and enabled consistent comparison of future hydrological responses between the two models.
Both models were employed to explore how the catchment's water balance and forest-climate interactions might evolve by 2050 under the influence of climate change. In the sections that follow, the methodology for preparing the climate data for both models is explained, followed by a discussion of the simulated impacts under different future climate scenarios.

5. Future Climate Scenario Modelling

5.1 Future Climate Conditions

5.1.1 Temperature

Projected annual mean temperatures for the Eyach catchment show a clear divergence across emission scenarios over the near-term future (2020–2050). Under RCP2.6, annual temperatures remain relatively stable with no statistically significant trend, whereas RCP4.5 and especially RCP8.5 display clear warming trajectories (Figure 45, p 98). These patterns align with the increasing radiative forcing of each scenario, as also projected globally by the IPCC Sixth Assessment Report (2021), which indicates continued warming across all RCPs, with stronger increases under higher emissions.
Importantly, the modelled annual temperatures for all three scenarios already lie well above the 1981–2010 reference mean of 7.26 °C (indicated as a baseline in the plots), demonstrating a shift in average conditions relative to recent historical norms. The Sen's slope estimates and p-values from Mann-Kendall trend analysis (Table 20, p. 99) confirm the visual patterns: no

statistically significant change under RCP2.6, moderate but significant warming under RCP4.5, and the strongest and most statistically significant warming under RCP8.5.

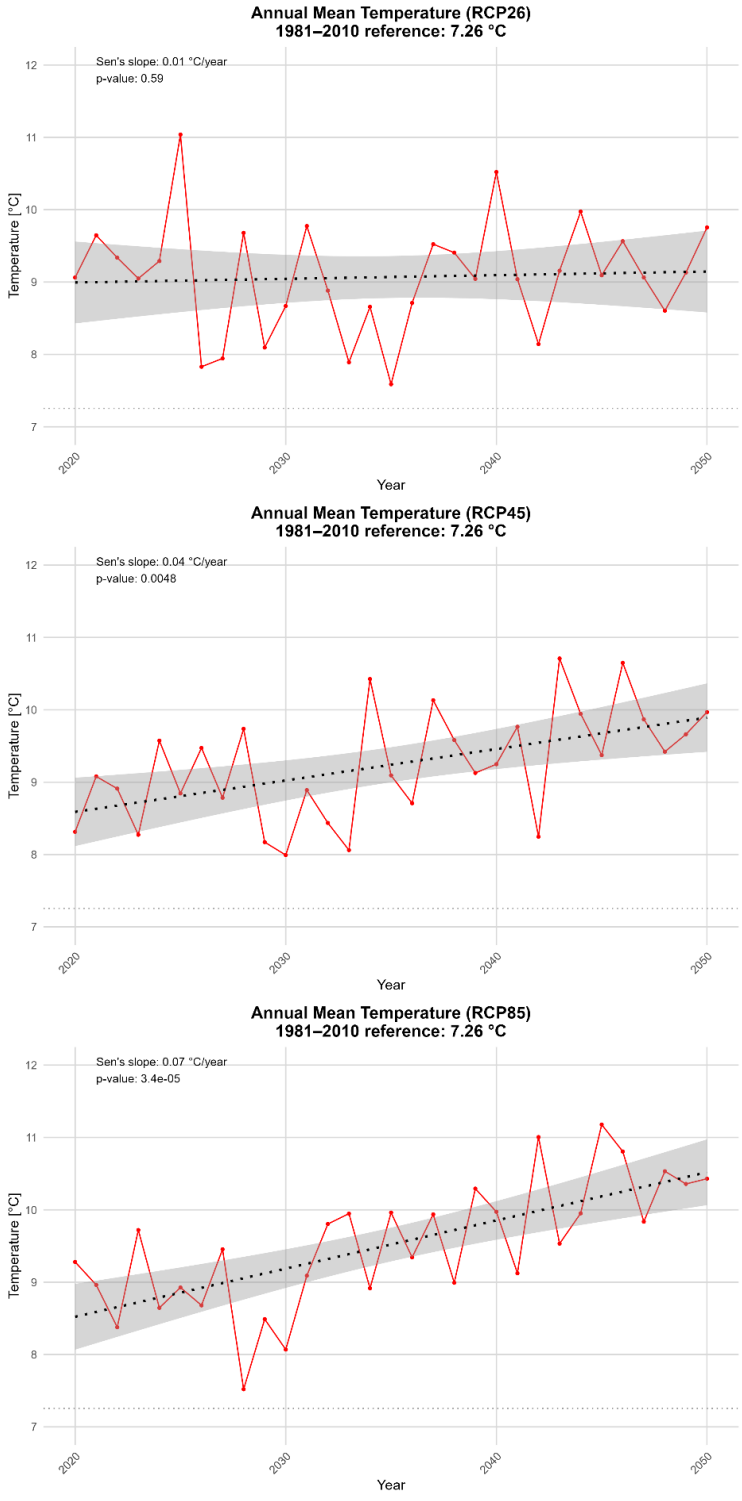

Figure 45. Annual mean air temperature time series for the Eyach catchment (2020–2050) under RCP2.6, RCP4.5, and RCP8.5 climate scenarios. Each panel shows a time series of projected annual temperatures (red line) with a fitted linear regression (dotted black line) and corresponding 95% confidence interval (grey shading). The 1981–2010 reference mean (7.26 °C) is indicated for context.

Table 20. Sen's slope and p-values for annual and seasonal air temperature trends (2020–2050) under RCP2.6, RCP4.5, and RCP8.5 scenarios. Statistically significant trends (p < 0.05) are marked with an asterisk (*).

Scenario	Aggregation	Season	Sen's Slope (°C/year)	p-value
RCP26	Annual	—	0.01	0.59
RCP26	Seasonal	Autumn	0.02	0.52
		Spring	0.01	0.76
		Summer	0.01	0.71
		Winter	0.00	0.97
RCP45	**Annual**	—	**0.04**	**0.0048***
RCP45	**Seasonal**	Autumn	0.02	0.28
		Spring	0.03	0.34
		Summer	**0.05**	**0.03***
		Winter	**0.07**	**0.016***
RCP85	**Annual**	—	**0.07**	**3.4e-05***
RCP85	**Seasonal**	**Autumn**	**0.05**	**0.013***
		Spring	**0.06**	**0.038***
		Summer	**0.08**	**0.00031***
		Winter	**0.09**	**0.0039***

Seasonal analyses reveal additional insights into the nature of warming (Table 20). The strongest seasonal warming is observed in summer, followed by winter, reflecting a robust and seasonally asymmetric response to higher radiative forcing. Under RCP8.5, all four seasons show statistically significant warming trends, with summer warming at +0.08 °C/year ($p = 0.00031$) and winter at +0.09 °C/year ($p = 0.0039$). In contrast, RCP2.6 shows no significant seasonal trends, while RCP4.5 exhibits moderate but significant increases in summer (+0.05 °C/year) and winter (+0.07 °C/year).

These trends highlight a clear pattern of seasonally uneven warming, with winter temperatures increasing more steeply than those in spring or autumn under higher-emission scenarios. This pattern aligns with global climate model projections by the Intergovernmental Panel On Climate Change (Ipcc),(2023a), which attribute disproportionate winter warming to feedback mechanisms such as reduced snow cover, enhanced atmospheric moisture, and increased longwave radiation in colder months.

5.1.2 Precipitation

Projected annual precipitation totals for the Eyach catchment from 2020 to 2050 reveal scenario-dependent differences (Figure 46, p. 100). Relative to the 1981–2010 reference mean of 1234.49 mm, all scenarios exhibit substantial interannual variability, which complicates the detection of clear long-term changes. Under RCP2.6, no meaningful trend is observed, and the Sen's slope estimate of –4.85 mm/year ($p = 0.26$) confirms the lack of statistical significance.

RCP4.5 and RCP8.5 both show weak upward trends in annual precipitation (Sen's slopes of +1.73 mm/year and +1.72 mm/year, respectively), but neither is statistically significant ($p = 0.138$ and $p = 0.215$, respectively). These observations are supported by the trend statistics in Table 21, underscoring the high year-to-year variability and limited directional signal in total annual precipitation over the near-term period.

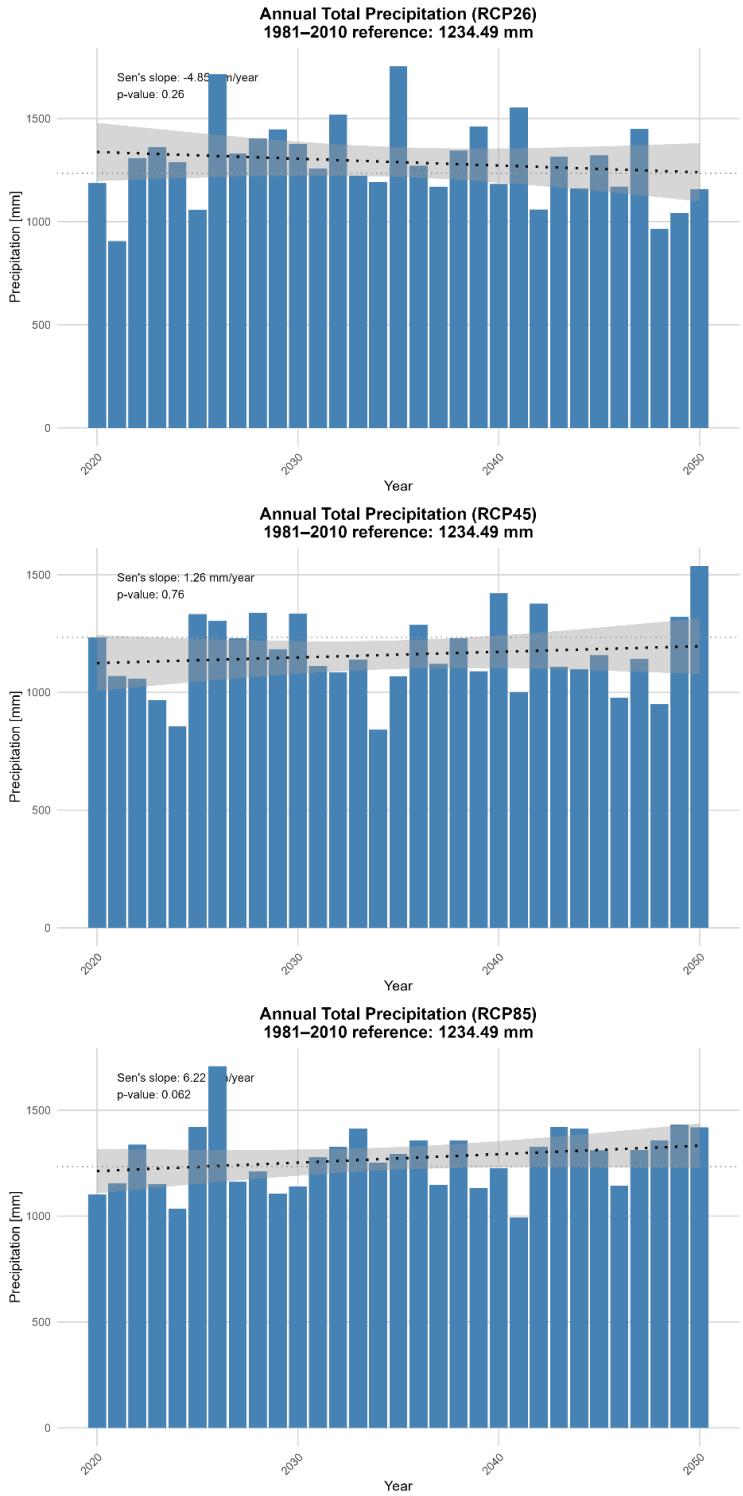

Figure 46. Annual total precipitation for the Eyach catchment from 2020 to 2050 under RCP2.6, RCP4.5, and RCP8.5 scenarios. Bars represent annual precipitation sums. The dotted black line shows a fitted linear regression with associated 95% confidence interval (grey shading). The 1981–2010 reference mean precipitation (1234.49 mm) is included for comparison.

Table 21. Sen's Slope and p-values for Annual and Seasonal Precipitation Trends (2020–2050).

Scenario	Aggregation	Season	Sen's Slope (mm/year)	p-value
RCP2.6	Annual	—	-4.85	0.262
RCP2.6	Seasonal	Autumn	-0.90	0.434
		Spring	-0.65	0.786
		Summer	-1.54	0.248
		Winter	-1.24	0.587
RCP4.5	Annual	—	1.73	0.138
RCP4.5	Seasonal	Autumn	-0.14	0.933
		Spring	3.16	0.099
		Summer	1.80	0.214
		Winter	-0.06	0.987
RCP8.5	Annual	—	1.72	0.215
RCP8.5	Seasonal	Autumn	0.88	0.533
		Spring	0.98	0.759
		Summer	1.23	0.662
		Winter	**3.27**	**0.026***

Seasonal trend patterns, however, offer more differentiated insights (Table 21). Under RCP2.6, none of the four seasons exhibit significant changes, though all show slight negative trends except winter, which displays a weak, non-significant increase. RCP4.5 shows a similar seasonal structure, with no statistically significant shifts, although spring emerges with the strongest positive trend (+3.16 mm/year), approaching significance ($p = 0.099$). Under RCP8.5, only winter shows a statistically significant increase in precipitation (+3.27 mm/year, $p = 0.026$), while the other seasons exhibit non-significant positive tendencies.

These patterns—particularly the recurring winter increases under both RCP4.5 and RCP8.5—are consistent with broader regional projections reported by Intergovernmental Panel On Climate Change (Ipcc), (2023a), which identify wintertime precipitation increases in Central Europe as a likely consequence of continued greenhouse gas emissions. This tendency is commonly attributed to changes in atmospheric circulation patterns and increased moisture availability during colder months.

5.1.3 Global Radiation

Projected annual mean global radiation across the Eyach catchment between 2020 and 2050 shows no consistent trends across RCP scenarios (Figure 47, p. 103). Compared to the 1981–2010 reference period, which exhibits an observed mean of 3220.96 W/m², projected values under RCP2.6, RCP4.5, and RCP8.5 are systematically lower. This discrepancy is likely attributable to the fact that, unlike temperature and precipitation, the radiation data used here were not bias-adjusted. The absence of bias correction introduces notable limitations to the accuracy of modelled surface fluxes—particularly in regions like the Eyach catchment where complex topography and high cloud variability amplify model uncertainties. Several studies

confirm the importance of bias correction for radiation variables and highlight the consequences of neglecting it. Dosio and Panitz, 2016 demonstrate that regional climate models, even at relatively high resolution, can propagate substantial biases in surface energy fluxes when boundary conditions from global climate models are not corrected. In particular, radiation variables are highly sensitive to biases in cloud cover and atmospheric composition, which are difficult to resolve in complex terrain such as that of the Eyach catchment. Lange, 2018 further show that non-bias-corrected radiation data can significantly underestimate surface energy availability in mountainous regions, resulting in misleading signals for hydrological and ecological modelling. Similarly, Laux et al., 2021 highlight that the lack of bias correction in solar radiation can distort agricultural indicators and ecosystem modelling by reducing both the magnitude and variability of radiation inputs. Collectively, these findings reinforce the interpretation that the low radiation values observed here are not necessarily reflective of actual climatic change but rather of uncorrected model artifacts.

In terms of projected trends, none of the scenarios exhibit statistically significant changes in annual global radiation. Under RCP2.6 and RCP4.5, values fluctuate interannually with no clear directional signal, while RCP8.5 shows a slight positive tendency that is also not significant (Table 22).

Table 22. Sen's Slope and p-values for Annual and Seasonal Global Radiation Trends (2020–2050).

Scenario	Aggregation	Season	Sen's Slope (W/m²/year)	p-value
RCP2.6	Annual	—	0.56	0.89
RCP2.6	Seasonal	Autumn	2.95	0.54
		Spring	-11.04	0.17
		Summer	3.81	0.61
		Winter	1.17	0.79
RCP4.5	Annual	—	-0.14	0.95
RCP4.5	Seasonal	Autumn	-0.40	0.97
		Spring	3.47	0.73
		Summer	0.76	0.95
		Winter	-4.23	0.08
RCP8.5	Annual	—	-0.54	0.89
RCP8.5	Seasonal	Autumn	2.32	0.50
		Spring	-0.38	0.92
		Summer	0.77	0.89
		Winter	-4.45	0.07

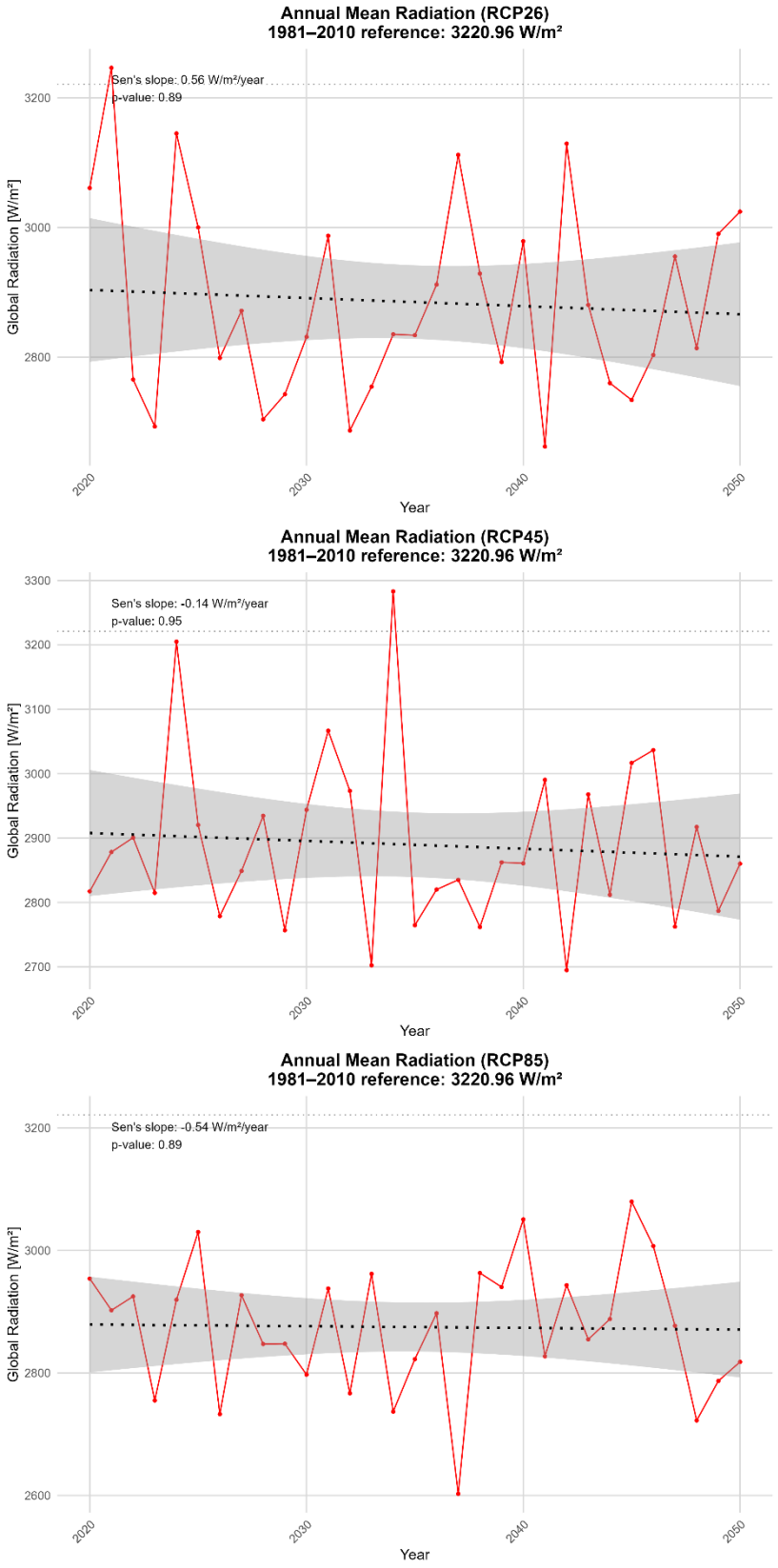

Figure 47. Annual mean global radiation for the Eyach catchment from 2020 to 2050 under RCP2.6, RCP4.5, and RCP8.5 scenarios. Red lines represent yearly values. The dotted black line shows the fitted linear regression with 95% confidence interval (grey shading). The 1981–2010 reference mean radiation (3220.96 W/m²) is shown for comparison..

Seasonal projections of global radiation over the Eyach catchment further reinforce the conclusion that clear trends are largely absent across all RCPs (Table 22, p. 102). Under

RCP2.6, no season exhibits statistically significant changes in mean surface radiation. Minor positive trends are observed in autumn (+2.95 W/m²/year, $p = 0.54$) and summer (+3.81 W/m²/year, $p = 0.61$), while spring shows a stronger—but still non-significant—decrease (–11.04 W/m²/year, $p = 0.17$). RCP4.5 shows mostly flat patterns, with small negative slopes in autumn and winter; the latter (–4.23 W/m²/year, $p = 0.08$) approaches significance but does not pass conventional thresholds. RCP8.5 displays a similarly scattered pattern of weak, non-significant trends, with a modest increase in autumn and slight declines in spring and winter. The strongest signal—a negative winter trend (–4.45 W/m²/year, $p = 0.07$)—remains just below statistical significance.

The overall absence of significant seasonal trends across all three scenarios highlights the low robustness of projected radiation changes in this region. This weak signal is likely compounded by the lack of bias correction in the modelled RG inputs, which are known to systematically underestimate observed values over the historical period (Boé et al., 2007; Dosio and Fischer, 2018). Consequently, any interpretation of radiation-related impacts based on these outputs should be made with caution. The apparent trends may reflect structural shortcomings in the underlying climate forcing data rather than meaningful physical shifts in future surface radiation. Future studies should therefore consider applying bias adjustment to radiation data before using them in downstream ecological or hydrological models or explicitly account for uncertainty when modelling RG-sensitive processes.

5.2 Future Hydrological Simulations

5.2.1 Evapotranspiration

The comparison of annual ETA trends under RCP 2.6, RCP 4.5, and RCP 8.5 (Figure 48, p. 106) shows that LWF-Brook90 consistently produces higher evapotranspiration estimates than the TRAIN model across all three Representative Concentration Pathways. However, the magnitude of difference between models is reduced compared to historical periods, indicating less divergence in model output under projected climate conditions (Chapter 3).

Importantly, results from the Mann-Kendall trend analysis (Table 23, p. 106) reveal that no statistically significant annual trends ($p > 0.05$) were found in either model, except for the TRAIN simulation under RCP 4.5, which shows a significant positive trend (+1.86 mm/year, $p = 0.021$). All other trends, including those under RCP 2.6 and RCP 8.5, were statistically non-significant. This supports the interpretation that ETA remains relatively stable throughout the mid-21st century in most cases.

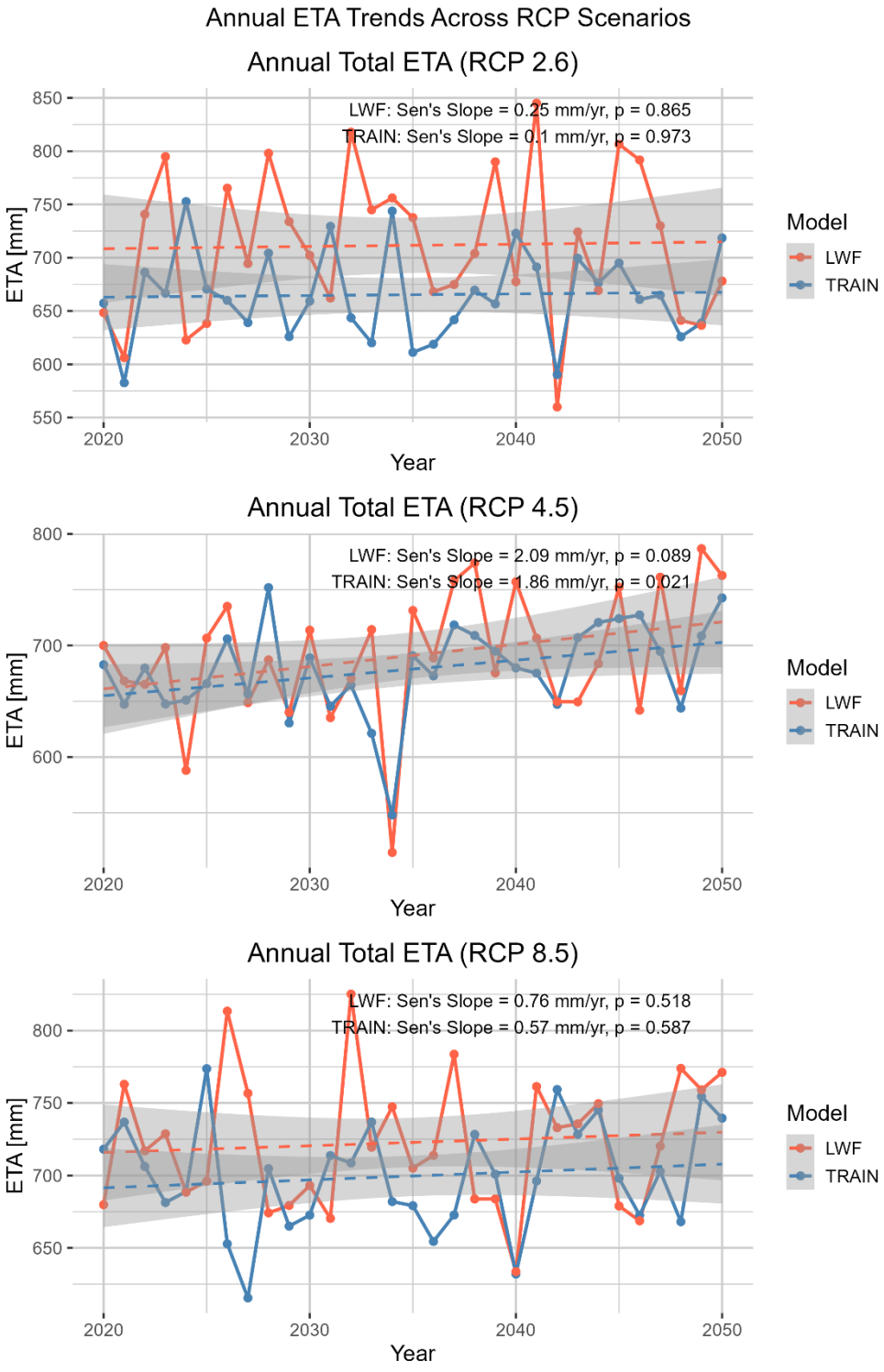

Figure 48. Annual total evapotranspiration (ETA) for the Eyach catchment from 2020 to 2050 under RCP2.6, RCP4.5, and RCP8.5 scenarios, simulated with the LWF-Brook90 (LWF) and TRAIN models. Solid lines show yearly values for each model. Dashed lines represent fitted linear regressions with associated 95% confidence intervals (grey shading). Sen's slope and p-values for each model and scenario are indicated within the panels.

Table 23. Annual Mann-Kendall Trend Results by Model and RCP Scenario (2020–2050).

Scenario	Model	Sen's Slope (mm/yr)	p-value
RCP 2.6	LWF-B90	0.25	0.865
RCP 2.6	TRAIN	0.57	0.386
RCP 4.5	LWF-B90	2.09	0.089
RCP 4.5	**TRAIN**	**1.86**	**0.021**
RCP 8.5	LWF-B90	0.76	0.518
RCP 8.5	TRAIN	0.57	0.587

This convergence between model outputs can likely be attributed to the moderated variability of future climate drivers, especially temperature, global radiation, and vapor pressure deficit (VPD). For instance, global radiation variability—a dominant control on ETA—is expected to decline in RCP-based projections. One possible explanation lies in the nature of the input climate data: the 2020–2050 forcing period shows lower overall variability and intensity than the historical baseline (1975–2019), potentially limiting the sensitivity range of both models. It is plausible that LWF-Brook90, being more responsive to high evaporative demand due to its vegetation-centric ETA formulation, exhibits less deviation under moderated climate inputs. This convergence in future projections suggests that model structural differences may matter more under extreme climate variability than under dampened forcing conditions.

Chan et al., (2022) noted that reduced radiative forcing results in diminished temperature variability. By analogy, if atmospheric drivers such as radiation, temperature, or vapor pressure deficit become less variable in future climate scenarios, structurally different hydrological models may likewise produce more similar ETA outputs—not because their sensitivities converge, but because external variability no longer triggers those sensitivities.

The boxplot comparison (Figure 49, p. 107) reinforces this interpretation. While LWF-B90 maintains a higher ETA median across all RCPs, the interquartile range is narrow and similar between models, suggesting reduced model divergence under future scenarios. Additionally, a weak upward trend in median ETA across RCP scenarios—from RCP 2.6 to RCP 8.5—is visible, particularly in the TRAIN simulations, potentially reflecting increased evaporative demand driven primarily by rising temperatures.

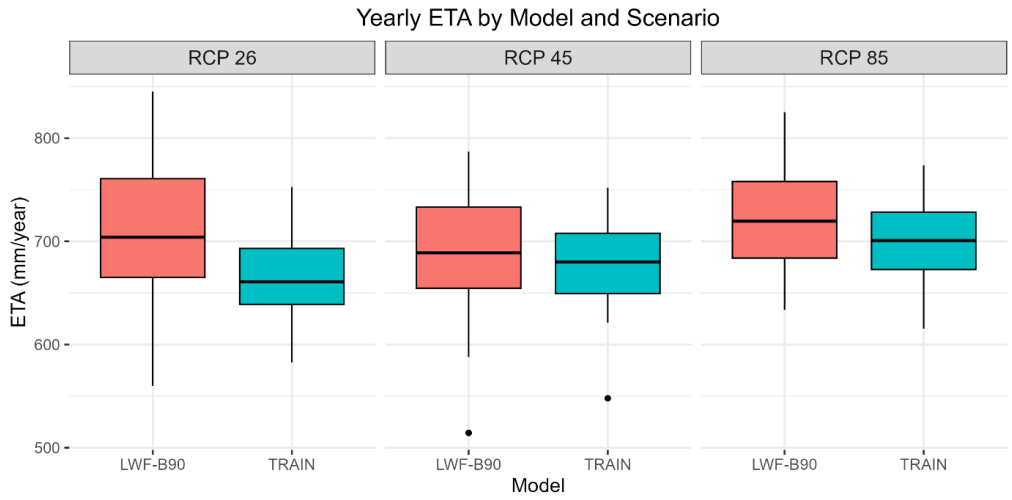

Figure 49. Distribution of annual evapotranspiration by model (boxplots) under RCP scenarios (2020–2050).

It should be noted that during the preparation of the RCP 2.6 simulation, the TRAIN model was inadvertently forced with global radiation data corresponding to RCP 4.5 rather than RCP 2.6. However, a subsequent comparative analysis of global radiation across RCP 2.6, RCP 4.5, and RCP 8.5 scenarios (Figure 50) revealed negligible differences in annual mean global radiation between scenarios.

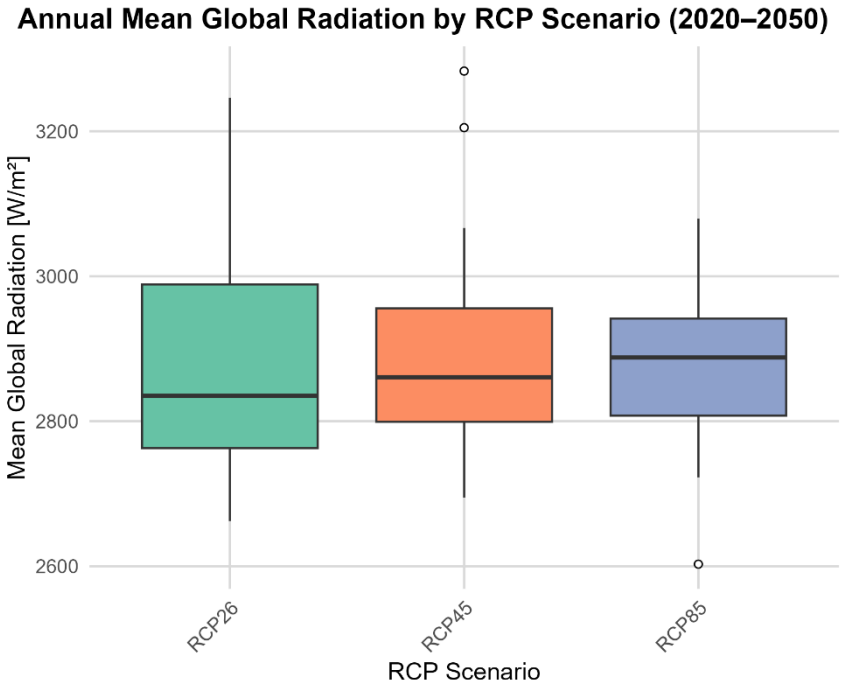

Figure 50. Annual mean global radiation under RCP 2.6, 4.5, 8.5 (2020–2050).

This minimal discrepancy justifies the continued use of the original ETA dataset for TRAIN RCP 2.6 in this study. Given that global radiation is a primary driver of ETA and considering the absence of a substantial bias between the RCP scenarios, a rerun was deemed unnecessary. The methodological decision to retain the existing simulation is therefore scientifically defensible and does not compromise the validity of the inter-model comparison.

Finally, the results of the seasonal Mann-Kendall test (see Appendix E, Table 42) reveal that while most seasonal ETA trends across models and RCP scenarios are not statistically significant ($p > 0.05$), significant positive trends do occur in winter. Specifically, ETA increases

significantly under RCP4.5 for both LWF-Brook90 ($p = 0.007$) and TRAIN ($p = 0.035$), and under RCP8.5 for LWF-Brook90 ($p = 0.012$). These cold-season increases may reflect future reductions in snowpack and the rise of patchy snow conditions, which have been shown to enhance winter evapotranspiration by increasing soil and vegetation exposure to atmospheric demand and enabling meltwater evaporation during brief thaw episodes—even in subfreezing conditions (Kraft and McNamara, 2022). Apart from these winter signals, all other seasonal changes remain statistically non-significant, suggesting that overall, ETA remains relatively stable across seasons and scenarios.

Figure 51 presents boxplots of annual evapotranspiration (ETA) for *Fagus sylvatica*, *Quercus robur*, and *Picea abies* under RCP2.6, RCP4.5, and RCP8.5 for the period 2020–2050, simulated using the LWF-Brook90 model. *Picea abies* consistently shows the highest ETA across all scenarios, reflecting its evergreen character and continuous transpiration (Granier et al., 2000) . In contrast, the deciduous species exhibit lower ETA due to limited growing season activity. Although median ETA values increase slightly from RCP2.6 to RCP8.5—especially for *Fagus sylvatica*—the overall species ranking remains unchanged. Variability within species also remains stable across scenarios, suggesting that physiological traits outweigh climatic effects in determining evapotranspiration behaviour (Allen et al., 1998; Granier et al., 2000).

Trends in ETA over time are generally weak and not statistically significant, with the exception of *Fagus sylvatica* under RCP4.5, which shows a significant increasing trend ($p = 0.049$). These results are summarized in Table 24 (p. 109)

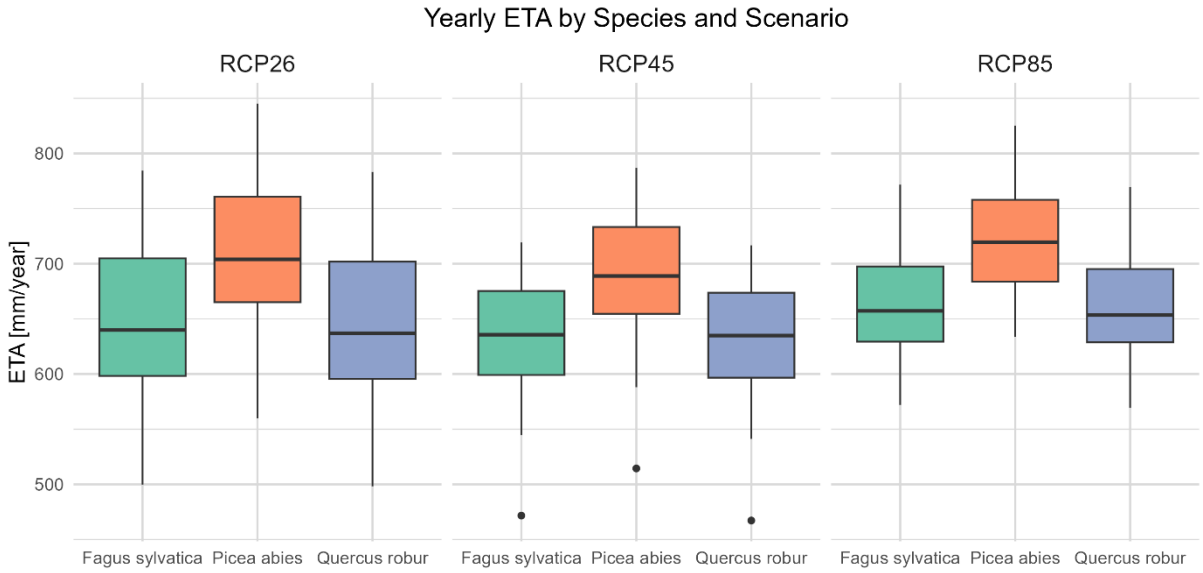

Figure 51. Distribution of annual evapotranspiration by species under RCP scenarios (2020–2050).

Table 24. Sen's Slope and p-values for ETA Trends (2020–2050) for Three different Tree Species.

RCP	Species	Sen's Slope (mm/year)	p-value
RCP2.6	*Fagus sylvatica*	0.371	0.7857
RCP2.6	*Picea abies*	0.252	0.8650
RCP2.6	*Quercus robur*	0.359	0.7597
RCP4.5	***Fagus sylvatica***	**2.427**	**0.0487***
RCP4.5	*Picea abies*	2.090	0.0892
RCP4.5	*Quercus robur*	2.298	0.0664
RCP8.5	*Fagus sylvatica*	0.893	0.5406
RCP8.5	*Picea abies*	0.760	0.5184
RCP8.5	*Quercus robur*	0.968	0.4966

Figure 52 (p. 110) further explores this by showing ETA differences between *Fagus sylvatica* / *Quercus robur* and *Picea abies*, along with mean differences and trend statistics. Both deciduous species maintain lower ETA than *Picea* throughout the 2020–2050 period, with typical differences of –30 to –80 mm/year. Simulated ΔETA values under all RCPs confirm that *Quercus robur* tends to show larger negative deviations than *Fagus sylvatica*, with some years—especially 2026, 2034, and 2044—exceeding –75 mm under RCP8.5. These consistent offsets reflect species specific water use strategies, such as more conservative stomatal regulation and lower canopy conductance in the deciduous species (Granier et al., 2000; Schume et al., 2004).

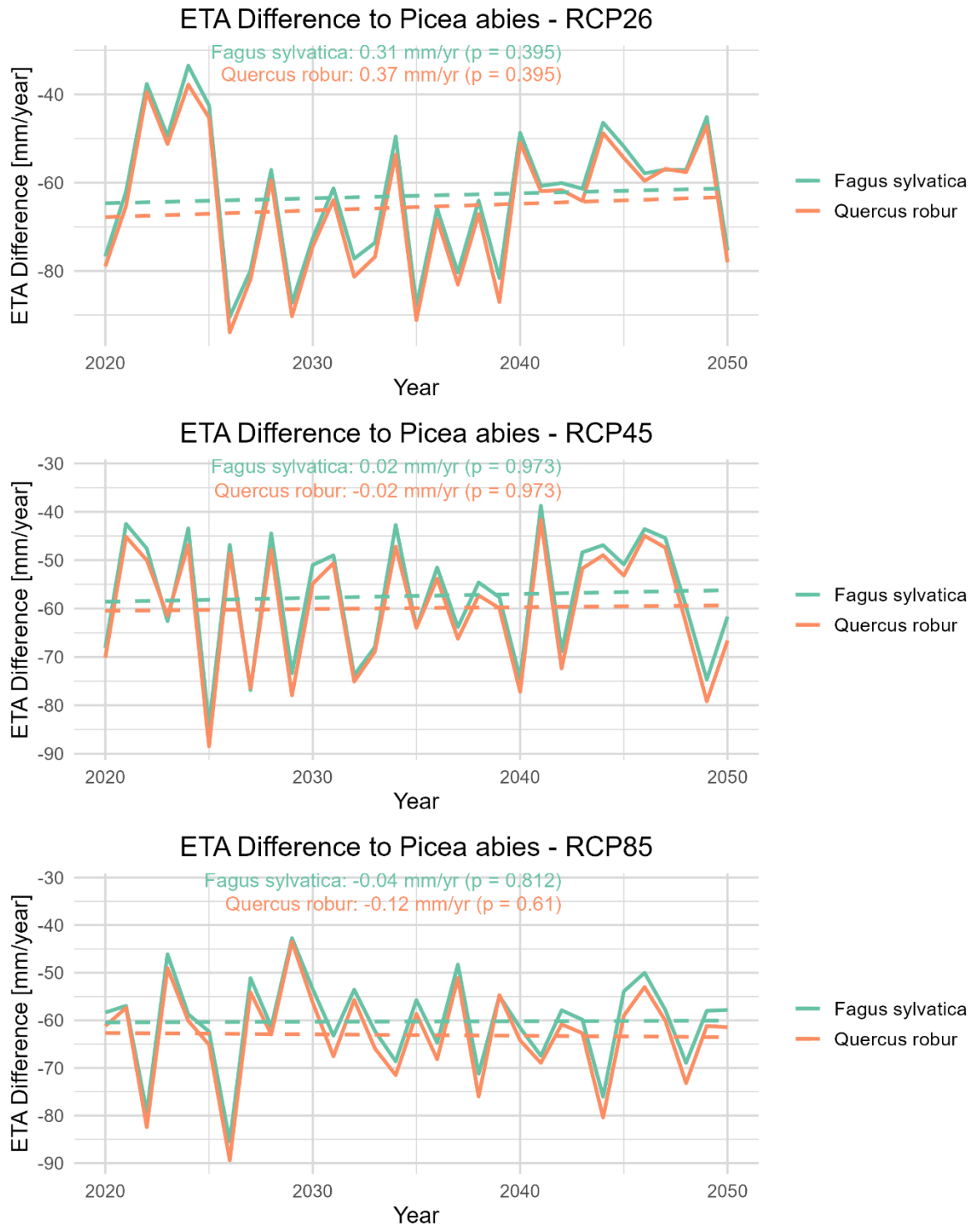

Figure 52. Annual evapotranspiration differences of Fagus sylvatica and Quercus robur relative to Picea abies under RCP scenarios (2020–2050).

Trend analysis reveals no statistically significant convergence or divergence between species across any of the RCP scenarios. All Sen's slopes are near zero, and p-values exceed 0.39 in all cases, confirming the absence of meaningful trends in species differences. The structural and physiological divergence—especially between evergreen and deciduous canopy traits—remains stable even under intensified radiative forcing, pointing to ecohydrological resilience and trait-governed differences in evapotranspiration. These findings highlight that while climate change may influence the overall magnitude of evapotranspiration, interspecific

differences are primarily governed by physiological and phenological traits—such as evergreen versus deciduous leaf habit, year-round canopy activity, and species-specific canopy conductance responses (Allen et al., 1998; Granier et al., 2000).

5.2.2 Soil Moisture

While future scenario ETA projections showed convergence between TRAIN and LWF-Brook90, soil moisture simulations exhibit a markedly larger and consistent divergence across all RCPs (Figure 53, p 112). This contrast can be explained by the different drivers and sensitivities of the two variables: ETA is closely coupled to meteorological forcing (e.g., temperature, radiation), and as such responds more uniformly when the 2020–2050 climate input series exhibits reduced interannual variability. In contrast, soil moisture is a memory-based state variable that integrates structural model behaviour over time.

As shown in Chapter 3, LWF-B90 consistently simulates higher soil moisture than other models, including TRAIN, which was attributed to its physically detailed multilayer soil profile, species-specific transpiration formulation, and explicit canopy interception processes (Orth et al., 2015; Saavedra et al., 2022). These structural features enhance water retention and limit evaporative loss, particularly under forested conditions. Even under dampened climatic forcing, these internal model mechanics persist and continue to influence outcomes, emphasizing that structural complexity—rather than only external drivers—governs model sensitivity in subsurface compartments.

The lack of a statistically significant trend in RCP 2.6 is consistent with the broader climate stability characteristic of this scenario Van Vuuren et al., (2011), suggesting that under sustained low-emission trajectories, soil moisture dynamics may remain within historical variability envelopes—though isolated dry years could still pose challenges for vegetation and hydrological function (Kirtman et al., 2013).

Under RCP 4.5, the response of soil moisture remains buffered, possibly due to compensating precipitation variability or the inertia of soil water storage mechanisms Rahmati et al., (2024). While no significant long-term trend was detected, some years—such as 2032 and 2048—showed notably lower soil moisture. These coincide with below-average precipitation and above-average temperatures (Figures 45, p. 98 and 46, p. 100), suggesting that interannual extremes in meteorological forcing can drive short-term subsurface water stress despite stable long-term means.

Under RCP 8.5, however, the divergence between LWF and TRAIN becomes especially apparent. Soil moisture shows a more pronounced decline in both models—particularly in TRAIN—despite relatively stable ETA. This is the only scenario where LWF-B90 shows a statistically significant annual drying trend (–0.16 mm/year, $p = 0.023$), while TRAIN remains non-significant, indicating that structural complexity does not necessarily buffer long-term drying. This highlights that, even in the absence of sharp increases in evaporative demand, subsurface water stores may decline, suggesting growing hydrological stress.

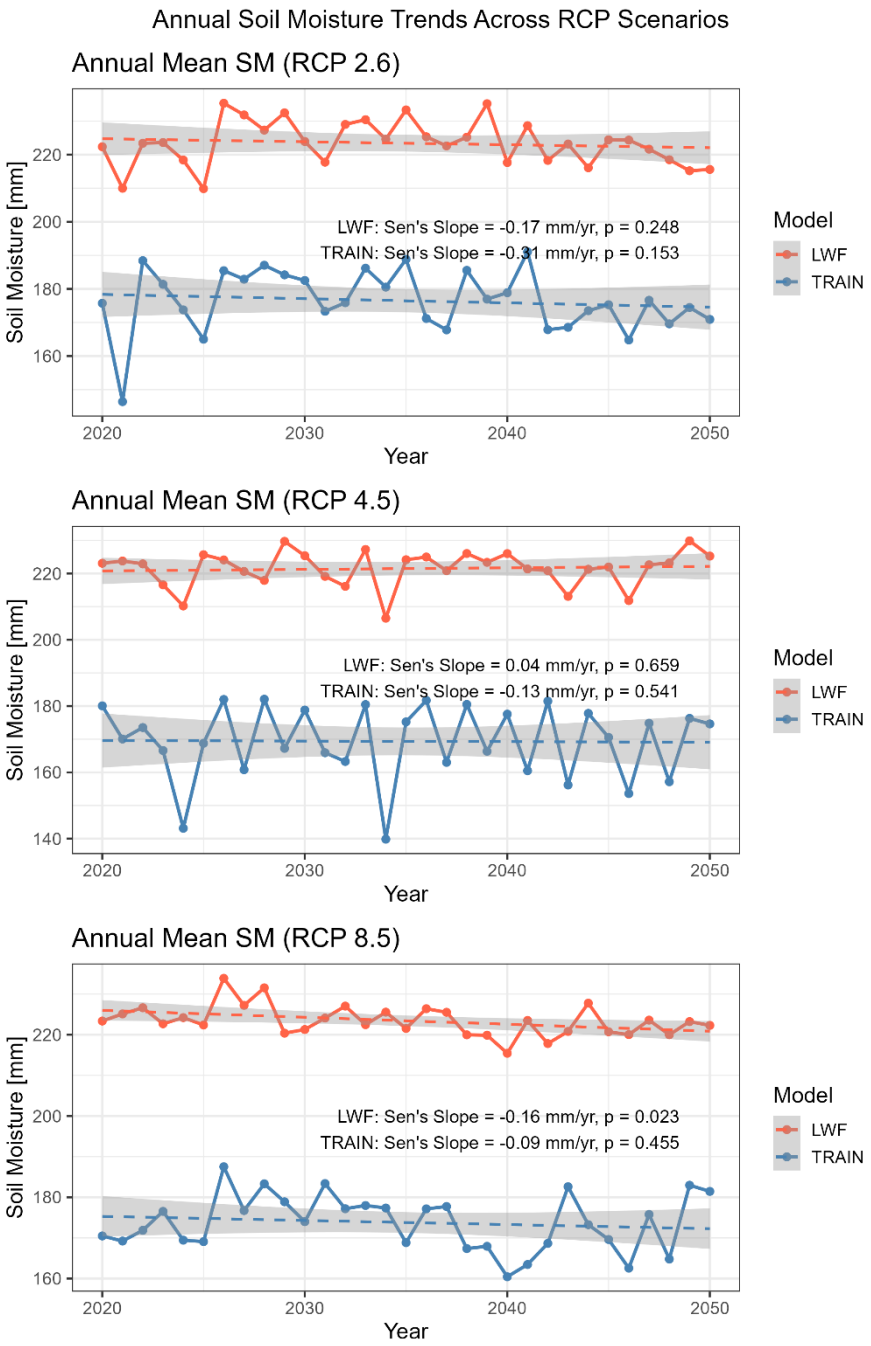

Figure 53. Annual soil moisture means for TRAIN and LWF-B90 under RCP scenarios (2020–2050).

This is clearly reflected in the boxplots (Figure 54, p. 113), where median soil moisture in LWF-B90 remains consistently ~40–50 mm higher than in TRAIN across all RCPs, with no signs of convergence. These differences illustrate the persistent role of model structure in shaping soil water dynamics, independent of external climate forcing scenarios. The interquartile ranges are narrower for LWF-B90 and show slightly less variability compared to TRAIN, which exhibits both lower medians and more frequent outliers—particularly under RCP 4.5.

This reinforces the broader interpretation that apparent inter-model agreement in one hydrological variable (like ETA) does not imply convergence across others, especially when those variables are governed by different structural layers and feedbacks. While climate input variability declines in future projections, structural contrasts between models—such as the empirical vs. process-based treatment of plant-soil interactions—continue to generate divergent

water balance outcomes, highlighting the importance of structural model evaluation when interpreting multi-model results under climate change scenarios.

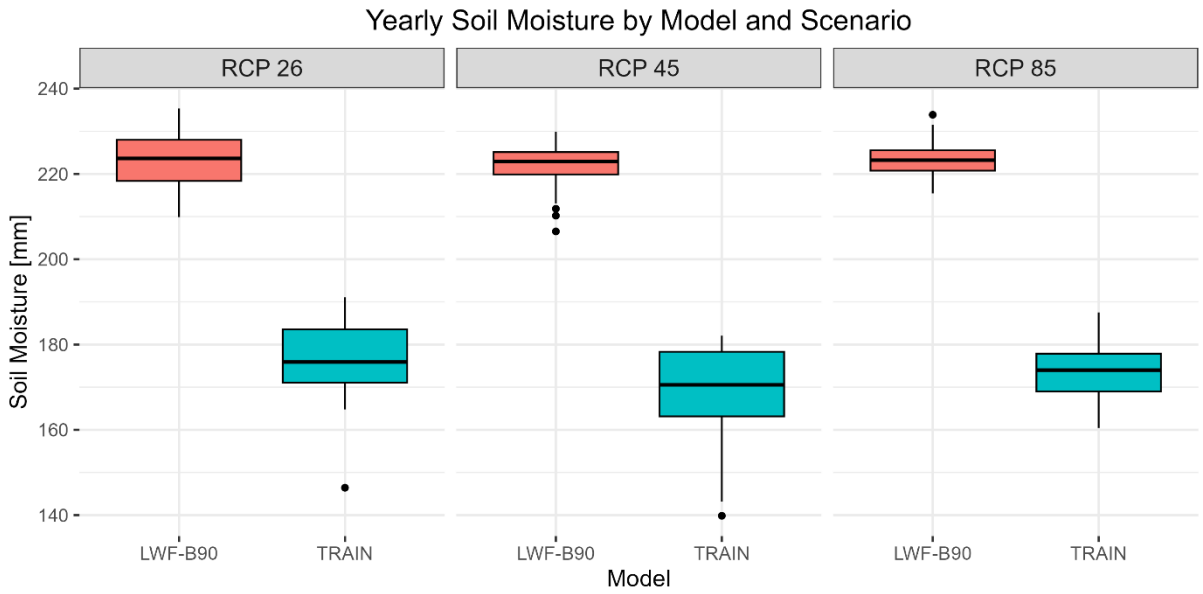

Figure 54. Distribution of annual soil moisture for TRAIN and LWF-B90 under RCP scenarios (2020–2050).

Seasonal analysis using the Mann-Kendall test (Appendix E, Table 43) revealed that no consistent statistically significant trends ($p > 0.05$) in seasonal soil moisture were found across models or scenarios. However, one exception occurred under RCP 8.5, where LWF-B90 showed a significant drying trend during summer (Sen's slope = –0.26 mm/year, $p = 0.049$), suggesting that peak evapotranspiration periods may experience increasing subsurface stress even in the absence of strong annual trends. Additionally, TRAIN under RCP 8.5 exhibited moderate negative slopes in summer and spring, although these were not statistically significant.

These findings emphasize that intra-annual dynamics may shift, particularly during critical ecological periods like summer, even when long-term annual averages remain relatively stable. Monitoring seasonal imbalances and short-term extremes may therefore be crucial for anticipating ecosystem stress under future climate conditions (Seneviratne et al., 2010; Teuling et al., 2010).

Figure 55 (p. 114) presents boxplots of simulated annual soil moisture for *Fagus sylvatica*, *Quercus robur*, and *Picea abies* under RCP2.6, RCP4.5, and RCP8.5 for the period 2020–2050, using the LWF-Brook90 model. Across all scenarios, *Fagus sylvatica* generally exhibits the highest median soil moisture, followed by *Quercus robur* and then *Picea abies*. This ordering contrasts with the evapotranspiration patterns discussed earlier, reflecting species-specific differences in water retention and usage. While variability within species remains relatively stable, *Picea abies* consistently shows lower central tendency and a greater occurrence of low-end outliers—particularly under RCP4.5 and RCP8.5.

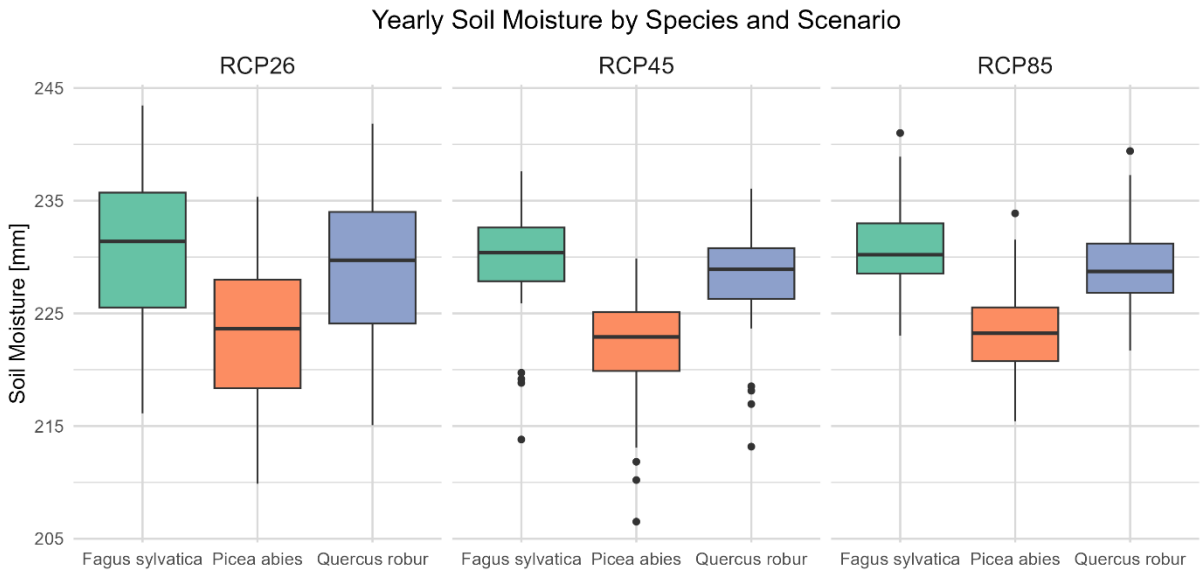

Figure 55. Distribution of annual soil moisture by species under RCP scenarios (2020–2050).

Figure 56 (p. 115) further explores this by showing the annual soil moisture differences between *Fagus sylvatica* / *Quercus robur* and *Picea abies*. Both deciduous species maintain consistently higher soil moisture than *Picea abies* across all scenarios, with average differences around 6–9 mm. This stable species ordering is consistent with earlier findings that attribute these differences to traits such as more conservative water use, deeper rooting systems, and differences in canopy interception (Kuželková et al., 2024; Schume et al., 2004). Although year-to-year variability is visible, *Fagus sylvatica* generally exhibits slightly higher soil moisture than *Quercus robur*, particularly in the early decades, likely reflecting lower water extraction rates and structural adaptations (Martinetti et al., 2025).

Trend analysis reveals that only under RCP2.6 are statistically significant increases observed in the SM gap—+0.04 mm/year for *Fagus sylvatica* ($p = 0.007$) and +0.03 mm/year for *Quercus robur* ($p = 0.045$)—suggesting an expanding divergence in species response under this low-emission pathway. Under RCP4.5 and RCP8.5, however, trends are weak or non-significant, and no directional convergence or divergence can be confirmed.

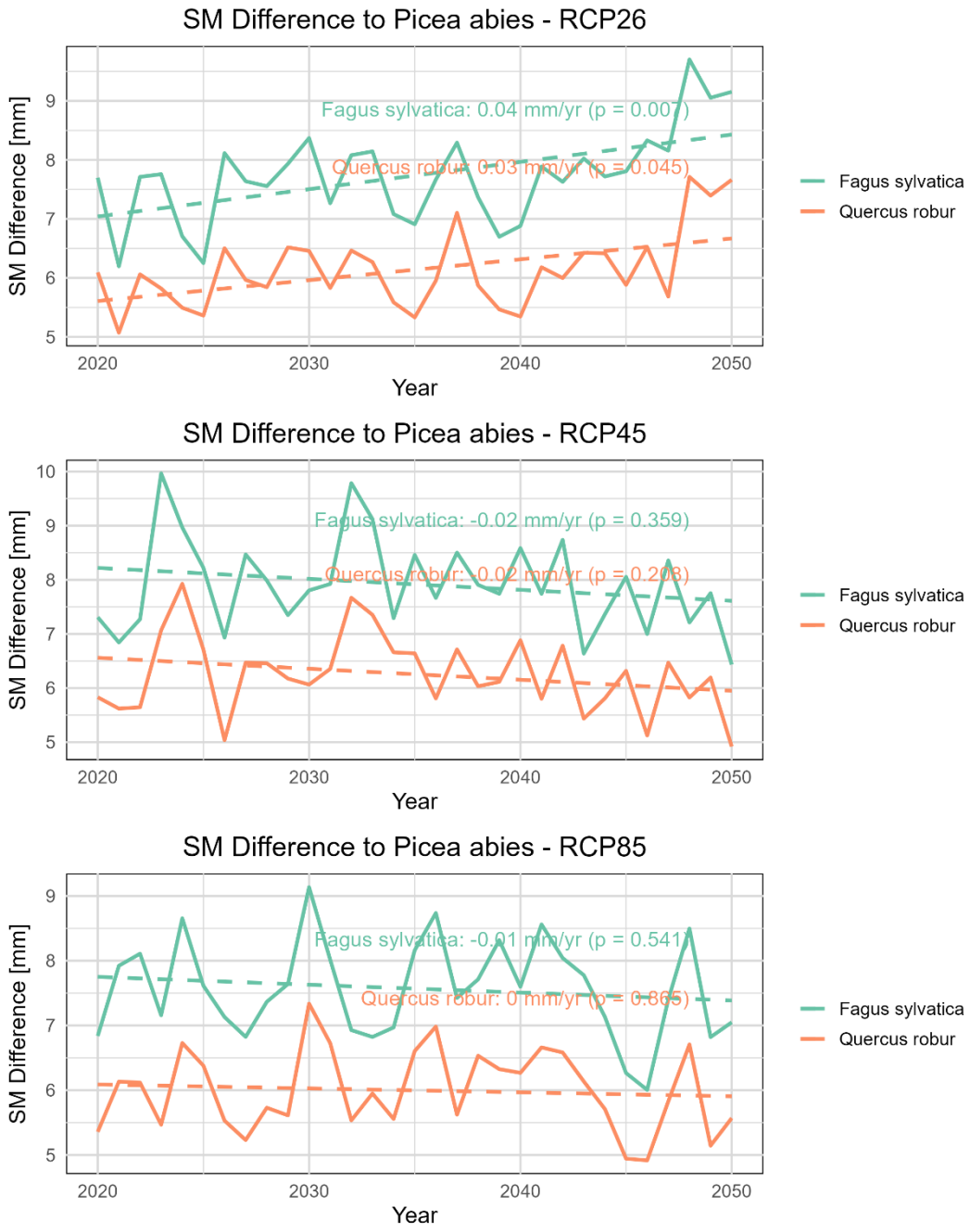

Figure 56. Annual soil moisture differences of Fagus sylvatica and Quercus robur relative to Picea abies under RCP scenarios (2020–2050).

Further, seasonal Mann-Kendall analysis revealed no significant trends in soil moisture for *Fagus sylvatica* or *Quercus robur* across any scenario. These findings suggest that species-specific physiological and structural traits—not just climatic drivers—shape soil moisture dynamics. The evergreen *Picea abies* exhibits more continuous water use and interception, whereas the deciduous species appear to retain more moisture on average. While future climate change may influence overall soil water availability, relative species differences are likely to persist, reflecting intrinsic ecohydrological strategies.

5.2.3 Vegetation Period Dynamics – Start and End of Growing Season of Three Tree Species under different RCP Scenarios

Figure 57 (p. 117) visualizes the start of the vegetation period (DOY) for Fagus sylvatica, Picea abies, and Quercus robur under RCP2.6, RCP4.5, and RCP8.5, alongside mean temperature trends for 2020–2050. All species show a tendency towards earlier onset (lower DOY) with rising temperature across scenarios, although none of the calculated Sen's slope trends reach statistical significance at $\alpha=0.05$. The progression of trends is summarized in Table 25.

Table 25. Sen's Slope (trend per year) and p-values for the start of the vegetation period under different RCPs.

Species	**RCP2.6 (Sen, p)**	**RCP4.5 (Sen, p)**	**RCP8.5 (Sen, p)**
Fagus sylvatica	-0.08, 0.633	-0.14, 0.129	-0.19, 0.143
Picea abies	-0.09, 0.645	-0.19, 0.195	-0.18, 0.213
Quercus robur	-0.07, 0.721	-0.19, 0.152	-0.12, 0.331

Notably, the absolute magnitude of trend becomes greater (more negative) from RCP2.6 to RCP8.5, reflecting the stronger temperature increase, but the trends remain statistically non-significant.

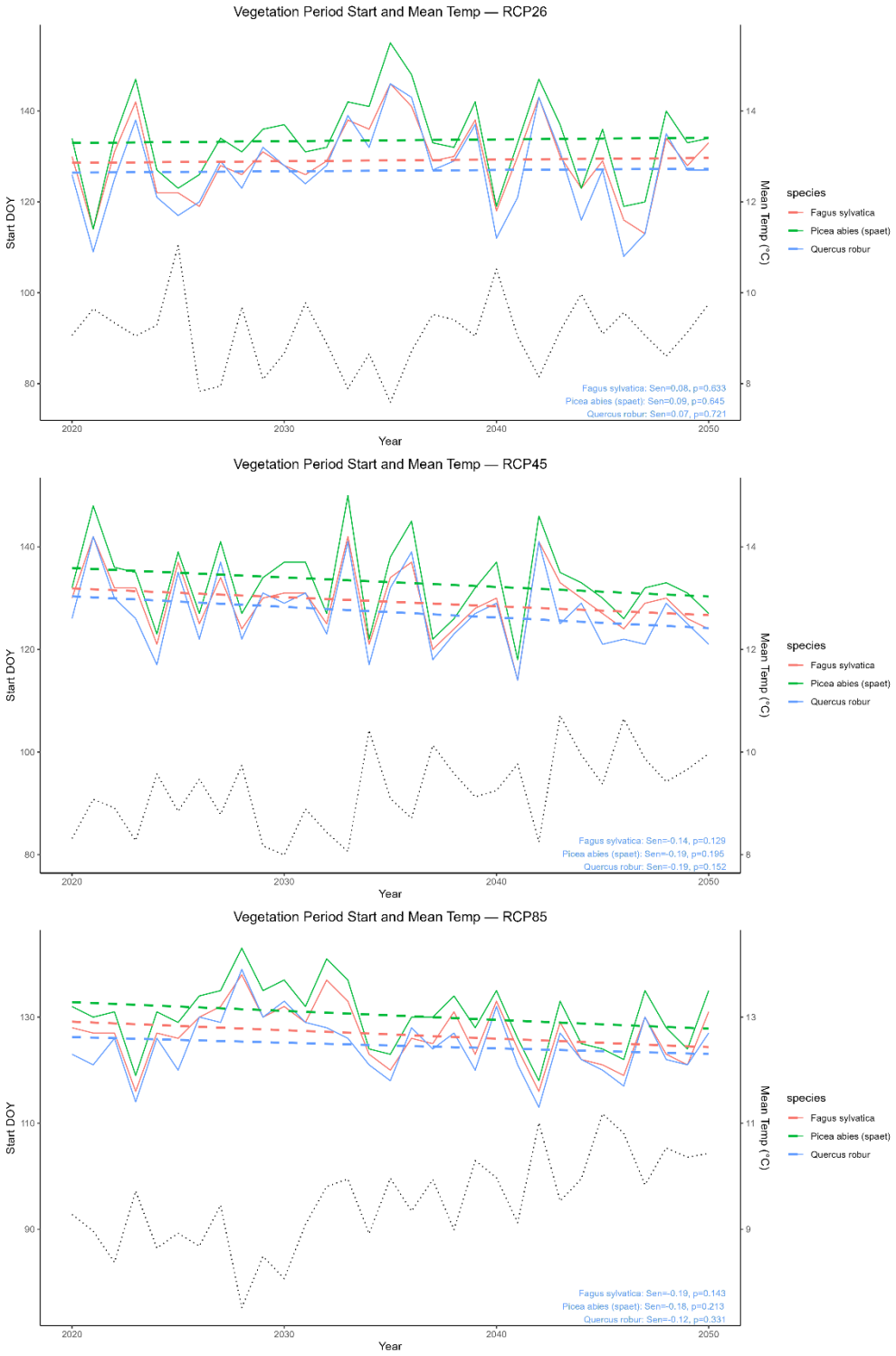

Figure 57. Start of vegetation period (DOY) by species under RCP scenarios relative to temperature (2020–2050).

Figures 58, 59 and 60 (p. 118) present the relationships between mean annual temperature and the start of the vegetation period (DOY) for *Fagus sylvatica*, *Picea abies*, and *Quercus robur* under RCP2.6, RCP4.5, and RCP8.5. In all scenarios, a consistent negative correlation is evident for each species, indicating that warmer years are associated with earlier onset of the vegetation period.

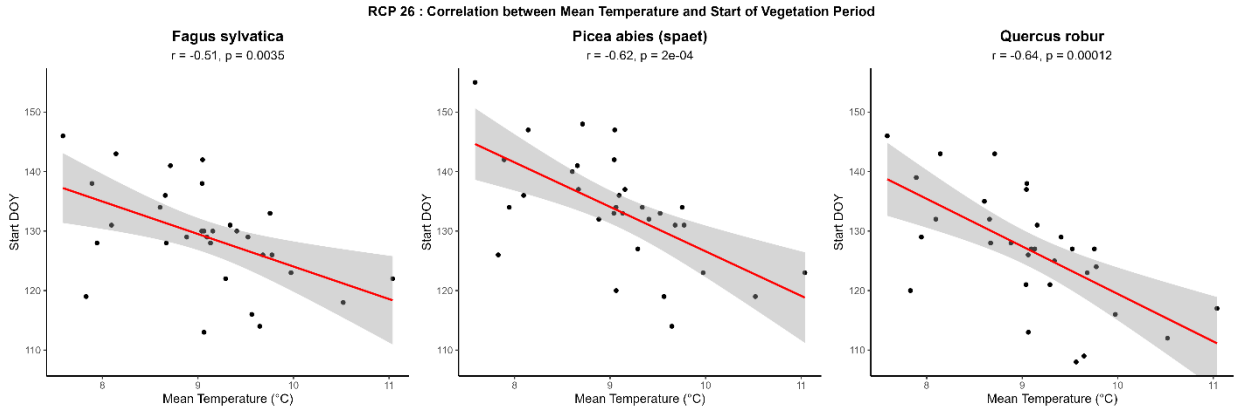

Figure 58. Scatter plots of mean annual temperature versus start of the vegetation period (day of year, DOY) for Fagus sylvatica, Picea abies (spaet), and Quercus robur under RCP2.6 (2020–2050). A linear regression line (red) and associated 95% confidence interval (grey shading) are shown for each species.

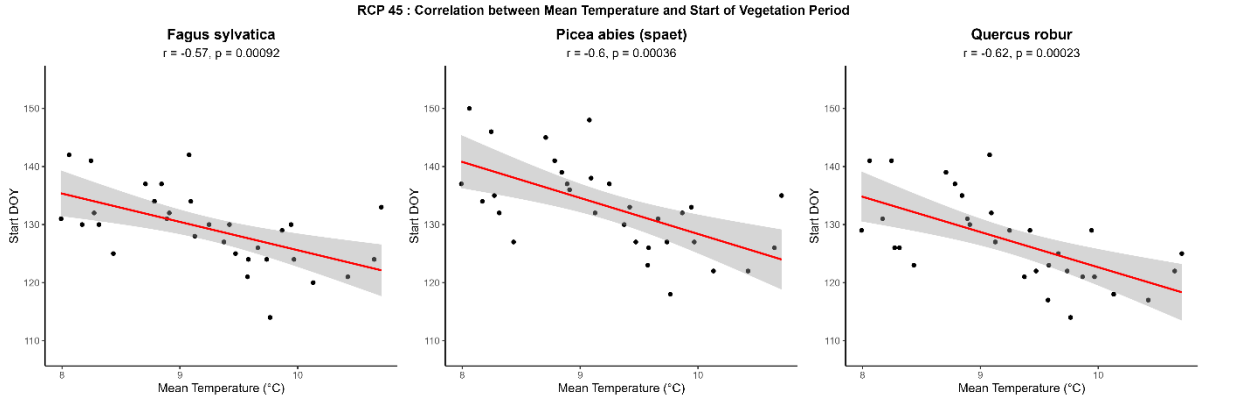

Figure 59. Scatter plots of mean annual temperature versus start of the vegetation period (day of year, DOY) for Fagus sylvatica, Picea abies (spaet), and Quercus robur under RCP4.5 (2020–2050). A linear regression line (red) and associated 95% confidence interval (grey shading) are shown for each species.

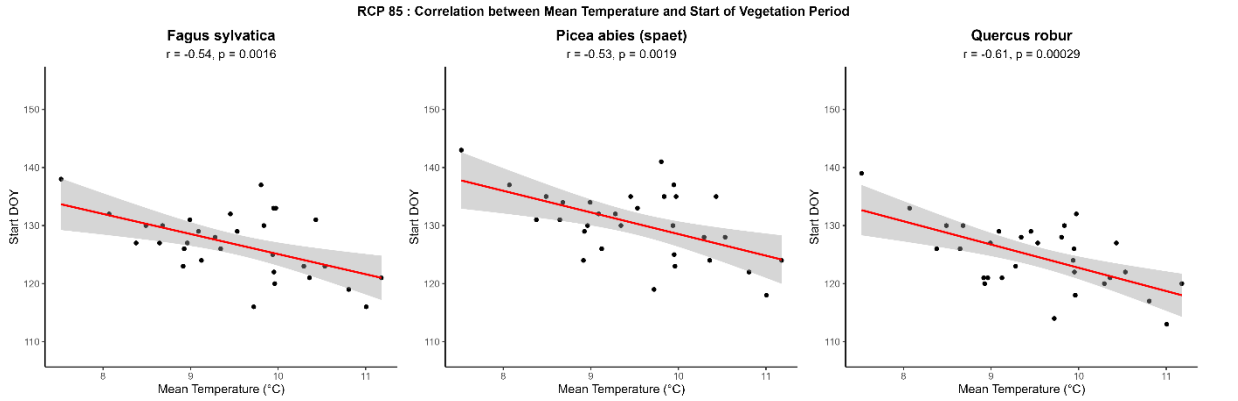

Figure 60. Scatter plots of mean annual temperature versus start of the vegetation period (day of year, DOY) for Fagus sylvatica, Picea abies (spaet), and Quercus robur under RCP8.5 (2020–2050). A linear regression line (red) and associated 95% confidence interval (grey shading) are shown for each species.

While the strength of the correlation is similar across RCPs (ranging from r = -0.30 to r = -0.42), statistical significance is only reached in isolated cases—most notably for *Picea abies* and *Quercus robur* under RCP2.6 and for *Quercus robur* under RCP4.5. In all other cases, the p-values are above 0.05, despite the clear warming signal in the temperature data. For example, under RCP8.5, despite the strongest and most significant warming trend (Sen's slope =

0.07 °C/year, p = 3.4e-5), the relationship between temperature and phenological onset remains non-significant for all species (all p > 0.06).

This apparent discrepancy is well-documented in the literature and arises from the much greater interannual variability in biological (phenological) data compared to temperature, as well as the influence of additional environmental drivers (e.g., chilling, photoperiod, drought) that can obscure temperature effects over short timeframes. In particular, late-successional conifers such as *Picea abies* exhibit high chilling and photoperiod requirements, which constrain earlier budburst and limit phenological shifts even under rapidly warming conditions (Körner and Basler, 2010; Laube et al., 2014; Richardson et al., 2013). In contrast, broadleaved species like *Fagus sylvatica* and *Quercus robur* display stronger temperature responsiveness and lower chilling thresholds, leading to consistently earlier spring phenology (Vitasse et al., 2011; Laube et al., 2014). This supports the observed interspecific differences in the timing of vegetation period onset under all RCP scenarios.

In summary, these results demonstrate the sensitivity of spring phenology to temperature, while also highlighting the challenges of detecting significant trends in ecological responses over limited timeframes, as is typical for near-term climate scenarios, where statistical power is constrained by high interannual variability and short observation periods (Richardson et al., 2013).

Regarding the end of the vegetation period, neither trends nor correlations with temperature are evident. This is consistent with the broader phenological literature: Menzel et al. (2006), Richardson et al. (2013), and Zohner and Renner, (2015) report that while spring events advance robustly with warming, autumn phenology (vegetation period end) shows little or inconsistent change due to the strong regulatory role of photoperiod.

These findings should also be interpreted with consideration of model limitations, such as the omission of rare but impactful events (e.g., late frost) and possible genetic adaptation, which may influence phenological responses in real-world conditions (Basler, 2016; Laube et al., 2014). Altogether, this underscores the importance of continued long-term monitoring, the use of new observation tools, and multi-species process-based modelling to understand and manage future changes in forest phenology and ecosystem function (Piao et al., 2019).

Chapter 6

6. Conclusion and Outlook

This dissertation investigated long-term climatic and hydrological dynamics in the Eyach catchment—a 52 km² forested watershed in Germany's Black Forest—over the period 1975–2019. Using a multi-model framework (TRAIN, HBV-Light, LWF-Brook90, and Raven-HMETS), the study simulated key water balance components (evapotranspiration, soil moisture, snow processes, and discharge), examined species-specific vegetation effects, and projected future climate-hydrology interactions under RCP scenarios. Chapter 6 synthesizes the main findings, contextualizes them within broader climate and ecological processes, and reflects on their implications for future research and forest management.

6.1 Summary of Achievements and Climate-Hydrology Insights

Analyses of historical climate data for the Eyach catchment confirmed a clear warming trend in recent decades, accompanied by increasing solar radiation, while long-term precipitation showed no significant overall change. These findings align with broader observations in Central Europe: the region has warmed about twice as fast as the global average since the 1980 (Schumacher et al., 2024) due in part to declining aerosol pollution that has brightened the atmosphere (increased solar irradiance) and amplified greenhouse warming (Schumacher et al., 2024). Meanwhile, precipitation changes have been modest and seasonally variable, with no robust long-term trend in annual totals over Central Europe (Kovats et al., 2014). This backdrop of anthropogenic greenhouse warming and post-1980s "surface brightening" Schumacher et al., (2024) provides important context for the catchment's hydrological changes.

Using a multi-model framework (TRAIN, HBV-Light, LWF-Brook90, and Raven-HMETS), this study captured pronounced interannual variability in soil moisture and evapotranspiration, reflecting the complex interplay between climatic forcing and land-cover heterogeneity. The results underscore that both climate drivers and vegetation characteristics govern hydrological responses.

Seasonal trend analysis further revealed that evapotranspiration significantly increased during both spring and winter in the TRAIN model. These changes are consistent with observed trends toward earlier vegetation activity and reduced snow cover in the catchment, supporting the interpretation that both phenological shifts and cold-season dynamics are influencing land–atmosphere exchange (Kraft and McNamara, 2022). Importantly, future scenario simulations also show significant winter ETA increases under RCP4.5 and RCP8.5 in both TRAIN and LWF-Brook90, reinforcing the expectation that reduced snowpack and more frequent thaw conditions will enhance cold-season evapotranspiration under continued warming - even as annual totals begin to plateau due to growing water limitations during the summer months.

For instance, under RCP8.5, increasing temperatures combined with largely stable precipitation led to a significant decline in soil moisture, particularly in LWF-Brook90 outputs. Evapotranspiration rates plateaued despite warming, indicating a shift from energy to water limitation. These model-based findings confirm that warming alone, even without substantial precipitation decline, can cause hydroclimatic drying. Additionally, the vegetation-specific

simulations demonstrated that *Quercus robur* and *Fagus sylvatica* retained more soil moisture than *Picea abies*, underscoring the influence of rooting traits and transpiration efficiency. This quantifiable species-driven difference illustrates how vegetation composition can buffer or exacerbate future drought impacts.

The successful implementation of three different hydrological models – the semi-distributed TRAIN, the species-specific LWF-Brook90, and the conceptual Raven – was a key achievement of this work. Each model credibly reproduced observed patterns while offering unique insights. Notably, LWF-Brook90 excelled in differentiating hydrological fluxes by tree species, and Raven provided reliable simulations of discharge dynamics under changing climate inputs. Together, these models enabled cross-validation of results and strengthened confidence in the findings. In summary, the study achieved its objectives by providing a multi-faceted understanding of how climate change has already altered – and will likely continue to alter – the water balance in a densely forested watershed.

6.2 Model Evaluation and Intercomparison

The multi-model intercomparison revealed that although all models captured the general seasonal and interannual trends of key hydrological fluxes, their sensitivities to climate inputs and internal process representations differed significantly. Raven-HMETS, for example, showed strong performance in simulating streamflow and runoff peaks, while LWF-Brook90 provided more nuanced insight into soil moisture and evapotranspiration differences across tree species. Model validation against multiple observational datasets—ERA5 and GLEAM for evapotranspiration, ERA5 for soil moisture, and direct field observations for snow cover—demonstrated varying levels of agreement.

The observed performance differences in evapotranspiration (ETA) and soil moisture (SM) can be traced to model structural characteristics. LWF-Brook90 incorporates detailed vegetation representation and physically based soil processes, producing higher ETA and SM values, especially under dense canopy cover. HBV-Light, by contrast, offers a more parsimonious conceptual approach with limited process detail, leading to lower simulated ETA but a surprisingly good match to ERA5-derived SM. TRAIN's SVAT framework with explicit energy balance and canopy dynamics yielded intermediate ETA values in good agreement with observational benchmarks. Raven-HMETS displayed wider variability in both fluxes, consistent with its modular, semi-distributed structure that requires careful configuration to avoid internal inconsistencies.

With the inclusion of snow validation, further differences in model behaviour emerged. All models implemented a degree-day snow routine with identical meteorological forcing, yet their snow cover day (SCD) outputs diverged significantly. When benchmarked against observational data from Wolfgang Roos (1975–1985 and 2013–2019), Raven-HMETS delivered the best performance, simulating a median SCD near 90 days and achieving the lowest RMSE and bias (Table 24). HBV-Light and LWF-B90 moderately underestimated snow duration (medians ~55 and 45 days, respectively) but retained strong correlations with observations (~0.76). TRAIN, in its catchment-aggregated configuration, produced the shortest snow duration (median ~30 days) and exhibited the largest bias. A high-elevation grid cell extracted from the TRAIN model improved agreement somewhat but still underestimated observed SCDs by over 50 days on average.

These results underscore the importance of structural features—beyond the shared snow routine—in shaping snow model performance. Although all models apply a comparable degree-day method, their spatial representation, air temperature handling, vegetation shading, and snowmelt refreezing routines influence the frequency and persistence of simulated snow cover. For instance, Raven-HMETS includes a refreezing component that may contribute to improved snow retention, while LWF-B90 lacks explicit refreezing but benefits from multi-layer soil and canopy dynamics.

Overall, the intercomparison confirms that even with similar external forcing and snow schemes, the internal architecture of each model significantly affects outputs—not only for evapotranspiration and soil moisture but also for snow (see Appendix F for an overview table summarizing the key features of each model, Table 44). These findings reinforce the necessity of multi-variable validation and highlight the limitations of relying solely on discharge calibration. Importantly, they demonstrate that structural differences persist even under harmonized inputs and parameter tuning, and that model performance varies by variable and application context.

In summary, while all models reproduced general trends, no single model excelled across all hydrological variables. TRAIN and LWF-Brook90 performed strongly for ETA and vegetation-related fluxes; HBV-Light proved efficient for soil moisture; and Raven-HMETS achieved the best agreement in snow dynamics and runoff peaks. These distinctions illustrate that model choice must be aligned with the specific research or management objective. In practice, a multi-model ensemble—as employed in this study—offers the most reliable path forward, providing both cross-validation and a deeper understanding of uncertainty in simulated hydrological behaviour.

6.3 Vegetation Dynamics and Species Sensitivity

A novel aspect of this work was the exploration of species-specific hydrological behaviour using the LWF-Brook90 model. The simulations revealed clear and statistically significant differences among *Picea abies*, *Fagus sylvatica* and *Quercus robur* in terms of water use and soil moisture retention. The deciduous broadleaf species (beech and oak) maintained higher soil moisture levels and exhibited lower evapotranspiration rates compared to the evergreen conifer (spruce) under the same atmospheric conditions. These patterns were consistent across years and indicate that forests dominated by deciduous trees may buffer climatic water stress more effectively than conifer-dominated stands. This finding is supported by other studies. For example, a recent field study in Germany found that pure Douglas-fir (an isohydric, evergreen conifer) consumed over twice as much water as pure beech in a wet year, and even in a drought year the conifers' total stand transpiration remained higher than that of beech despite cutbacks, leading to faster soil moisture depletion under the conifers (Paligi et al., 2025). By contrast, beech (an anisohydric deciduous species) was able to sustain its water use and even slightly increase transpiration in the dry year as vapor-pressure deficits rose, indicating a capacity to use available soil moisture without exhausting it (Paligi et al., 2025).

These results echo findings from tree-ring analyses of drought response. In pure stands, spruce tends to suffer the greatest growth reductions (lowest drought resistance), while beech and oak exhibit more robust responses. Notably, beech benefits when grown with oak in mixed stands, likely due to complementary water use strategies and hydraulic lift from the deeper-rooted oak

(Pretzsch et al., 2013). This pattern is reinforced by experimental results from Pretzsch et al., (2014), who demonstrated that spruce–beech mixtures under controlled drought conditions exhibited enhanced stability. Their findings point to ecophysiological complementarity—such as differences in rooting depth, stomatal behaviour, and hydraulic redistribution—as a key mechanism for improved stand resilience. In essence, the conservative water use strategies of deciduous species during dry periods enhance soil moisture retention relative to evergreens, which continue transpiring throughout the year.

Analysis of vegetation period (phenology) further highlighted interspecific differences in the timing of leaf-out and senescence. Results showed that deciduous species demonstrate more flexibility in the start and end of the growing season compared to spruce. This aligns with physiological studies showing that many deciduous trees use photoperiod cues to avoid premature leaf-out and thereby reduce the risk of late frost damage. For example, under artificially shortened daylengths, budburst in *Fagus sylvatica* can be delayed by over 40 days, whereas *Picea abies* is largely unaffected by photoperiod (Zohner and Renner, 2015). This photoperiod sensitivity enables beech and oak to delay budburst during unseasonal warm spells, maintaining resilience against frost. By contrast, the daylength-independent strategy of spruce allows it to respond rapidly to warming, increasing the risk of frost damage (Zohner and Renner, 2015). The implication is that *Fagus sylvatica* and *Quercus robur* may be better adapted to future climate variability, combining phenological plasticity with conservative water use, whereas spruce's fixed growth rhythm and higher water consumption make it more vulnerable to warming-induced water stress.

These insights are not merely theoretical—they have tangible implications for forest management. Promoting species with lower water use and greater drought tolerance, such as beech and oak, could enhance forest hydrological resilience under climate change, especially in regions facing high drought risk and limited adaptive capacity (Lindner et al., 2010). Dendroecological studies further confirm that *Picea abies* is significantly more drought-sensitive than beech or fir, while *Fagus sylvatica* shows superior resilience and tolerance to repeated drought events across diverse sites in southern Germany and the Alpine region (Zang et al., 2014). These findings support adaptive strategies that prioritize structurally and physiologically resilient species to buffer against increasing hydroclimatic extremes.

While the species differed markedly in water use and phenological sensitivity, modelled results showed no substantial interspecific differences in winter snow cover duration, despite clear overall declining trends. This suggests that, in this temperate forest context, canopy-mediated snow processes may be less species-dependent. However, further research in more structurally divergent stands or snow-dominated regions could better illuminate species effects on snowpack accumulation, retention, and melt-driven runoff—especially where variations in canopy density, interception capacity, and spatial forest structure play a larger role (Varhola et al., 2010). Where detailed, site-specific parameterization is available, simulations may better capture subtle but ecologically relevant species differences in snow-related hydrological processes.

6.4 Future Climate Scenarios

Looking ahead, scenario simulations for the period 2020–2050 under low (RCP 2.6), medium (RCP 4.5), and high (RCP 8.5) greenhouse gas forcing provide a forward view of potential hydrological shifts. Under the most extreme scenario (RCP 8.5), a noticeable decline in average soil moisture is projected, even though evapotranspiration does not rise dramatically. In fact, under RCP 8.5 conditions, evapotranspiration increases remain modest despite significantly warmer temperatures—reinforcing the notion that limited soil moisture availability constrains evaporative losses. This projection aligns with IPCC assessments that high levels of warming are very likely to reduce soil moisture in many regions, not only due to changes in precipitation but also as a result of increased evaporative demand from a warmer atmosphere (Intergovernmental Panel On Climate Change (Ipcc), 2023a). Even in the absence of substantial reductions in total precipitation, elevated temperatures and vapor-pressure deficits under RCP 8.5 are expected to lead to drier soils, as any additional rainfall is insufficient to offset the intensified atmospheric demand. Beyond a certain point, further warming yields little additional evapotranspiration, as the availability of soil water becomes the limiting factor (Intergovernmental Panel On Climate Change (Ipcc), 2023b).

Crucially, the results indicate that rising temperatures do not uniformly translate into increasing evapotranspiration. In the high-emission scenario RCP8.5, evapotranspiration simulated by both LWF-Brook90 and TRAIN tends to plateau or increase only modestly, while soil moisture shows a significant declining trend. This behaviour suggests that as soils dry, further increases in evapotranspiration are limited—even in the presence of elevated atmospheric demand. In other words, once soil water becomes scarce, additional heat energy cannot drive proportional increases in evaporation. This decoupling is well-documented in land–climate feedback literature, where drying soils weaken evaporative cooling and reinforce heat extremes (Seneviratne et al., 2010). Simulations support this mechanism: while warming continues under RCP8.5, LWF-Brook90 shows significantly reduced soil moisture, with evapotranspiration becoming increasingly water-limited—particularly in summer.

This dynamic highlights the importance of considering both water supply (i.e., soil moisture) and atmospheric demand in climate impact assessments. The finding that evapotranspiration flattens while temperatures rise is consistent with broader land–atmosphere feedback literature, which emphasizes that enhanced evaporative demand can itself exacerbate drought by accelerating soil moisture depletion (Intergovernmental Panel On Climate Change (Ipcc), 2023b). Observational studies further show that under such dry and hot conditions, vegetation becomes increasingly water-limited, leading to suppressed evapotranspiration and reinforced local warming (Teuling et al., 2010).

From a practical standpoint, this implies that under intense warming scenarios like RCP8.5, ecosystems may become increasingly water-limited, leading to diminishing evaporative responses despite rising temperatures. Such conditions are conducive to what are now termed "hotter droughts"—compound extremes of high temperature and low soil moisture that impair vegetation function. There is growing evidence that these events have already contributed to widespread tree mortality (Allen et al., 2010; Anderegg et al., 2013) and forest vulnerability is projected to increase, even in regions not typically considered water-limited.

This outcome raises serious concerns about long-term plant water availability. If soils dry earlier or more severely during the growing season—as suggested by my LWF-Brook90

simulations—forest ecosystems may experience chronic water stress, impairing tree growth and survival. Models currently struggle to represent these dynamics accurately, especially under drought stress, as demonstrated in global evaporation model evaluations (Miralles et al., 2016). The observed divergence in evapotranspiration behaviour across products like GLEAM, PT-JPL, and PM-MOD highlights the challenges of capturing evaporative responses under water-limited conditions. These discrepancies become particularly pronounced during droughts, when model assumptions about partitioning between transpiration, soil evaporation, and interception loss lead to substantial differences. Such structural limitations imply that projections of vegetation water use under climate change must be interpreted with caution—especially in regions prone to "hotter droughts" and prolonged moisture deficits (Allen et al., 2010; Anderegg et al., 2013).

In the more moderate scenario (RCP 4.5), these trends appear less pronounced but still indicate shifts in water partitioning—e.g., slightly higher evapotranspiration and mildly reduced soil moisture by mid-century. Under RCP 2.6, changes remain minimal, reflecting a future in which climate forcing stabilizes at a relatively low level.

Importantly, the scenario analysis suggests that forest composition will become an even more critical factor under future climate conditions. Species-specific responses indicate that catchments dominated by oak or beech may retain soil water more effectively in summer than those dominated by spruce. These differences have implications for adaptive forestry. Recent research on climate adaptation in forest systems has emphasized that mixed-species stands or those dominated by deep-rooted, drought-tolerant species can enhance ecosystem resilience and water sustainability under climate change (Pretzsch et al., 2013). Projections from the LWF-Brook90 simulations support this: under identical climate conditions, stands composed of *Quercus robur* or *Fagus* sylvatica maintain higher soil moisture than stands dominated by *Picea abies*, suggesting an improved buffering capacity against warmer and drier conditions. This insight may inform forest management and reforestation strategies by advocating for tree species that offer hydrological advantages in projected future climates.

Moreover, the model intercomparison (cf. Section 6.3) revealed that while future ETA projections across RCPs showed narrowing differences between TRAIN and LWF-Brook90, soil moisture responses remained strongly divergent. This suggests that ETA is more tightly constrained by the external climate forcing, whereas soil moisture integrates structural features such as canopy interception, soil layering, and rooting depth. As previously shown (Chapter 4.2.2), LWF-Brook90 simulates consistently higher soil moisture due to its physically based soil and vegetation processes (Orth et al., 2015; Saavedra et al., 2022). These differences persist even under dampened forcing, implying that model architecture—not just input variability—shapes hydrological response. Consequently, hydrological model selection for future impact assessments must be guided by the variable of interest and the structural strengths of the chosen model.

While projections under RCP 2.6 suggest manageable shifts in hydrological balance, RCP 8.5 scenarios imply significant moisture deficits during key vegetation periods. This wide range should inform adaptive scenario planning in forestry operations, including strategic thinning, afforestation planning, and water retention strategies.

Overall, the scenario results portray a future in which water is likely to become a limiting resource during parts of the year. In this context, species selection and forest management are

expected to play a pivotal role in mitigating the impacts of climate change on catchment hydrology.

6.5 Final Reflections and Outlook

In conclusion, this research demonstrates the value of a multi-model, ecologically nuanced approach in assessing forest hydrology under climate change. The integration of multiple models and the comparison of their outcomes provided a more robust and comprehensive understanding than could be achieved by relying on a single model.

Furthermore, this study affirms that model calibration is not merely a technical step but a critical part of achieving reliable hydrological simulation. As emphasized by Refsgaard and Storm (1996), uncertainties in hydrological modelling stem from multiple sources—ranging from errors in input and observation data to limitations in parameter values and model structure. Calibration serves to mitigate these uncertainties by adjusting model parameters until simulated outputs align with observed data within acceptable error bounds. Even models that share identical process routines can yield significantly different results if left uncalibrated, particularly when applied in new geographic contexts. Therefore, careful site-specific calibration is essential whenever a model is newly applied, especially in complex terrains like forested mountain catchments. This is consistent with findings by Mendoza et al., (2015), who demonstrated that inter-model differences in hydrological response can exceed the projected climate signal itself—particularly for evapotranspiration and snowpack—and that calibration, while important, does not eliminate structural divergence.

The convergence of evidence across models increases confidence in several key conclusions: significant warming has already affected the catchment's water balance; soil moisture dynamics are as important as rainfall in determining evaporation rates; and vegetation composition critically mediates hydrological outcomes. These findings are consistent with broader literature. For instance, Seneviratne et al. (2010) emphasized the central role of soil moisture in controlling transpiration and temperature feedbacks at multiple scales, while Mueller and Seneviratne, (2012) demonstrated that precipitation deficits strongly increase the likelihood of hot days through soil moisture–temperature coupling. Similarly, Anderegg et al. (2013) documented how drought-induced tree mortality poses increasing risks to forest functioning under warming, underlining the ecological consequences of evaporative constraints. Finally, Pretzsch et al., (2013) showed that species composition—especially in mixed stands—affects drought resilience, with beech–oak mixtures exhibiting higher resistance under water stress. Together, these studies reinforce the mechanistic understanding that underpins my simulation-based conclusions and highlight their relevance for anticipating forest hydrological responses under climate change.

Looking forward, there are several avenues to extend and deepen this work. Temporal extension is one clear need: future studies should push the simulation horizon beyond 2050 (e.g. to 2100) to capture longer-term trends and potential non-linear climate–vegetation feedbacks. Recent work even advocates extending climate projections beyond 2100 to support long-term planning in forestry, water, and infrastructure sectors (Easterling, 2024). Likewise, exploring a wider range of climate scenarios—including updated pathways or downscaled regional projections—would help to better bracket uncertainties, as emphasized by Moss et al., (2010), who advocate

for a more flexible and iterative scenario framework that captures evolving socio-economic and climatic complexities.

Equally, careful selection and correction of climate model inputs is crucial for ensuring meaningful hydrological projections. As highlighted by Laux et al., (2021), impact studies that use raw or only singly corrected climate data may propagate substantial errors into downstream models, sometimes exceeding uncertainties from the climate models themselves. For future simulations, applying robust bias correction methods—or even ensembles thereof—is essential to reduce input-induced uncertainty, particularly for temperature and precipitation.

Another priority is the closer integration of ecophysiological processes into the modelling framework—for example, incorporating field observations of tree physiology (such as stomatal behaviour or drought-induced tree mortality thresholds) would improve model realism. This is supported by McDowell et al., (2013), who showed that including mechanistic processes such as hydraulic failure and carbon starvation improves model predictive power, and by Fatichi et al., (2016), who emphasized that models simulating stomatal and hydraulic behaviour offer superior realism under climatic stress.

Better representation of forest disturbances (e.g., pest outbreaks, wildfires), dynamic land cover changes (such as succession or silvicultural management), rooting depth distributions, and CO_2-fertilization effects on transpiration is essential to reflect the complex and dynamic nature of forest–climate interactions. Elevated CO_2 levels can alter stomatal behaviour, carbon allocation, and rooting profiles, with direct implications for transpiration and soil water dynamics (Fatichi et al., 2016). Likewise, land use and stand development influence vegetation structure and composition, which in turn modulate evapotranspiration and interception processes. Omitting such factors may lead to a misrepresentation of vegetation–hydrology feedbacks (Bonan and Doney, 2018). Coupling hydrological models with forest growth and carbon cycle models is therefore a promising strategy to achieve more holistic climate impact assessments, as it allows the simulation of interactions between water stress, tree growth, and carbon sequestration (Fatichi et al., 2016; Makela et al., 2000).

By addressing these aspects, future research can build on the foundation laid by this dissertation. Future work should also explore coupling such models with socio-economic scenarios to guide regional forestry policy under uncertainty. This is consistent with the scenario framework proposed by Moss et al., (2010b), who emphasized the importance of integrating climate projections with socio-economic pathways to better capture the interactions between environmental change, policy choices, and societal responses. In parallel, the integration of stakeholder feedback with multi-model outcomes could greatly enhance the relevance and adoption of climate-resilient forest management practices. Participatory scenario development, as outlined by Reed et al., (2013), offers a structured approach for incorporating both scientific and local knowledge into scenario processes, resulting in more robust, place-based strategies for adaptation. Moreover, the modelling framework applied here is transferable to other temperate and boreal forest regions facing similar climatic pressures, enabling broader applicability across Europe and beyond.

The ultimate goal is to provide knowledge that guides sustainable water and forest management – helping stakeholders to prepare for and adapt to intensifying climate pressures in the coming decades.

In sum, the findings of this study provide a scientific basis for informed management, and they underscore the importance of continuing interdisciplinary, multi-model research to support climate resilience in forested catchments.

References

Allen, C.D., Macalady, A.K., Chenchouni, H., Bachelet, D., McDowell, N., Vennetier, M., Kitzberger, T., Rigling, A., Breshears, D.D., Hogg, E.H. (Ted), Gonzalez, P., Fensham, R., Zhang, Z., Castro, J., Demidova, N., Lim, J.-H., Allard, G., Running, S.W., Semerci, A., Cobb, N., 2010. A global overview of drought and heat-induced tree mortality reveals emerging climate change risks for forests. For. Ecol. Manag. 259, 660–684. https://doi.org/10.1016/j.foreco.2009.09.001

Allen, R.G., Pereira, L.S., Raes, D., Smith, M., 1998. Crop evapotranspiration - Guidelines for computing crop water requirements - FAO Irrigation and drainage paper 56.

Anderegg, W.R.L., Kane, J.M., Anderegg, L.D.L., 2013. Consequences of widespread tree mortality triggered by drought and temperature stress. Nat. Clim. Change 3, 30–36. https://doi.org/10.1038/nclimate1635

Andréassian, V., 2004. Waters and forests: from historical controversy to scientific debate. J. Hydrol. 291, 1–27. https://doi.org/10.1016/j.jhydrol.2003.12.015

Basler, D., 2016. Evaluating phenological models for the prediction of leaf-out dates in six temperate tree species across central Europe. Agric. For. Meteorol. 217, 10–21. https://doi.org/10.1016/j.agrformet.2015.11.007

Battuvshin, G., Menzel, L., 2022. Adjusting line quantum sensing to improve leaf area index measurements and estimations in forests. MethodsX 9, 101805. https://doi.org/10.1016/j.mex.2022.101805

Bauwe, A., Criegee, C., Glatzel, S., Lennartz, B., 2012. Model-based analysis of the spatial variability and long-term trends of soil drought at Scots pine stands in northeastern Germany. Eur. J. For. Res. 131, 1013–1024. https://doi.org/10.1007/s10342-011-0573-6

Beniston, M., Stephenson, D.B., Christensen, O.B., Ferro, C.A.T., Frei, C., Goyette, S., Halsnaes, K., Holt, T., Jylhä, K., Koffi, B., Palutikof, J., Schöll, R., Semmler, T., Woth, K., 2007. Future extreme events in European climate: an exploration of regional climate model projections. Clim. Change 81, 71–95. https://doi.org/10.1007/s10584-006-9226-z

Bergström, S., 1976. Development and Application of a Conceptual Runoff Model for Scandinavian Catchments.

Bergström, S., 1992: The HBV Model: Its Structure and Applications, Swedish Meteorological and Hydrological Institute (SMHI), Hydrology, Norrk¨oping, 35 pp.

Beven, K.J., Clarke, R.T., 1986. On the Variation of Infiltration Into a Homogeneous Soil Matrix Containing a Population of Macropores. Water Resour. Res. 22, 383–388. https://doi.org/10.1029/wr022i003p00383

Boé, J., Terray, L., Habets, F., Martin, E., 2007. Statistical and dynamical downscaling of the Seine basin climate for hydro-meteorological studies. Int. J. Climatol. 27, 1643–1655. https://doi.org/10.1002/joc.1602

Bonan, G.B., Doney, S.C., 2018. Climate, ecosystems, and planetary futures: The challenge to predict life in Earth system models. Science 359. https://doi.org/10.1126/science.aam8328

Bréda, N., Huc, R., Granier, A., Dreyer, E., 2006. Temperate forest trees and stands under severe drought: a review of ecophysiological responses, adaptation processes and long-term consequences. Ann. For. Sci. 63, 625–644. https://doi.org/10.1051/forest:2006042

Brocca, L., Ciabatta, L., Massari, C., Camici, S., Tarpanelli, A., 2017. Soil Moisture for Hydrological Applications: Open Questions and New Opportunities. Water 9, 140. https://doi.org/10.3390/w9020140

Bruijnzeel, L.A., 2004. Hydrological functions of tropical forests: not seeing the soil for the trees? Agric. Ecosyst. Environ. 104, 185–228. https://doi.org/10.1016/j.agee.2004.01.015

Calvin, K., Dasgupta, D., Krinner, G., Mukherji, A., Thorne, P.W., Trisos, C., Romero, J., Aldunce, P., Barrett, K., Blanco, G., Cheung, W.W.L., Connors, S., Denton, F., Diongue-Niang, A., Dodman, D., Garschagen, M., Geden, O., Hayward, B., Jones, C., Jotzo, F., Krug, T., Lasco, R., Lee, Y.-Y., Masson-Delmotte, V., Meinshausen, M., Mintenbeck, K., Mokssit, A., Otto, F.E.L., Pathak, M., Pirani, A., Poloczanska, E., Pörtner, H.-O., Revi, A., Roberts, D.C., Roy, J., Ruane, A.C., Skea, J., Shukla, P.R., Slade, R., Slangen, A., Sokona, Y., Sörensson, A.A., Tignor, M., Van Vuuren, D., Wei, Y.-M., Winkler, H., Zhai, P., Zommers, Z., Hourcade, J.-C., Johnson, F.X., Pachauri, S., Simpson, N.P., Singh, C., Thomas, A., Totin, E., Arias, P., Bustamante, M., Elgizouli, I., Flato, G., Howden, M., Méndez-Vallejo, C., Pereira, J.J., Pichs-Madruga, R., Rose, S.K., Saheb, Y., Sánchez Rodríguez, R., Ürge-Vorsatz, D., Xiao, C., Yassaa, N., Alegría, A., Armour, K., Bednar-Friedl, B., Blok, K., Cissé, G., Dentener, F., Eriksen, S., Fischer, E., Garner, G., Guivarch, C., Haasnoot, M., Hansen, G., Hauser, M., Hawkins, E., Hermans, T., Kopp, R., Leprince-Ringuet, N., Lewis, J., Ley, D., Ludden, C., Niamir, L., Nicholls, Z., Some, S., Szopa, S., Trewin, B., Van Der Wijst, K.-I., Winter, G., Witting, M., Birt, A., Ha, M., Romero, J., Kim, J., Haites, E.F., Jung, Y., Stavins, R., Birt, A., Ha, M., Orendain, D.J.A., Ignon, L., Park, S., Park, Y., Reisinger, A., Cammaramo, D., Fischlin, A., Fuglestvedt, J.S., Hansen, G., Ludden, C., Masson-Delmotte, V., Matthews, J.B.R., Mintenbeck, K., Pirani, A., Poloczanska, E., Leprince-Ringuet, N., Péan, C., 2023. IPCC, 2023: Climate Change 2023: Synthesis Report. Contribution of Working Groups I, II and III to the Sixth Assessment Report of the Intergovernmental Panel on Climate Change [Core Writing Team, H. Lee and J. Romero (eds.)]. IPCC, Geneva, Switzerland. Intergovernmental Panel on Climate Change (IPCC). https://doi.org/10.59327/IPCC/AR6-9789291691647

Chai, T., Draxler, R.R., 2014. Root mean square error (RMSE) or mean absolute error (MAE)? – Arguments against avoiding RMSE in the literature. Geosci. Model Dev. 7, 1247–1250. https://doi.org/10.5194/gmd-7-1247-2014

Chan, D., Rigden, A., Proctor, J., Chan, P.W., Huybers, P., 2022. Differences in Radiative Forcing, Not Sensitivity, Explain Differences in Summertime Land Temperature Variance Change Between CMIP5 and CMIP6. Earths Future 10. https://doi.org/10.1029/2021ef002402

Chernos, M., Green, K., MacDonald, R., 2023. Hydrological Modelling to Inform Forest Management: Moving Beyond Equivalent Clearcut Area. Conflu. J. Watershed Sci. Manag. 6. https://doi.org/10.22230/jwsm.2023v6n1a47

Chernos, M., MacDonald, R., Craig, J., 2017. Efficient Semi-Distributed Hydrological Modelling Workflow for Simulating Streamflow and Characterizing Hydrologic Processes. Conflu. J. Watershed Sci. Manag. 1. https://doi.org/10.22230/jwsm.2018v1n3a6

Chlumsky, R., Mai, J., Craig, J.R., Tolson, B.A., 2021. Simultaneous Calibration of Hydrologic Model Structure and Parameters Using a Blended Model. Water Resour. Res. 57, e2020WR029229. https://doi.org/10.1029/2020WR029229

Copernicus Climate Change Service, Climate Data Store, (2019): CORDEX regional climate

model data on single levels. Copernicus Climate Change Service (C3S) Climate Data Store (CDS). DOI: 10.24381/cds.bc91edc3 , Accessed over: https://esgf-metagrid.cloud.dkrz.de/search/cordex-dkrz/, (Last Accessed on 19-5-2025)

Copernicus Climate Change Service, Climate Data Store, (2024): ERA5 Land post-processed daily statistics from 1950 to present. Copernicus Climate Change Service (C3S) Climate Data Store (CDS), DOI: https://doi.org/10.24381/cds.e9c9c792, Accessed over Google Earth Engine Code Editor. Daily Aggregates: https://developers.google.com/earthengine/datasets/catalog/ECMWF_ERA5_LAND_DAILY_AGGR?hl=de#bands (Accessed on 5-5-2025)

CORINE Land Cover, 2018. European Union's Copernicus Land Monitoring Service information. https://land.copernicus.eu/en/products/corine-land-cover/clc2018?tab=download, https://doi.org/10.2909/71c95a07-e296-44fc-b22b-415f42acfdf0. Last accessed on July 2024.

Craig, J.R., Brown, G., Chlumsky, R., Jenkinson, R.W., Jost, G., Lee, K., Mai, J., Serrer, M., Sgro, N., Shafii, M., Snowdon, A.P., Tolson, B.A., 2020. Flexible watershed simulation with the Raven hydrological modelling framework. Environ. Model. Softw. 129, 104728. https://doi.org/10.1016/j.envsoft.2020.104728

Darcy, H.; 1856. Les Fontaines Publiques de La Ville de Dijon : Exposition et Application Des Principes a Suivre et Des Formules a Employer Dans Les Questions de Distribution d'Eau : Ouvrage Terminé Par Un Appendice Relatif Aux Fournitures d'Eau de Plusierus Villes ... Paris: Victor Dalmont, éditeur.

Dingman, S., 2002. Physical Hydrology. Waveland Press Inc.

Dingman, S. Lawrence. 2015. Physical Hydrology. 3rd ed. Long Grove, IL: Waveland Press.

Dobler, L., Gerlach, N., and Hinterding, A., 2004: INTERMET– Inter polation stündlicher und tagesbasierter meteorologischer Param eter, Federal state office for the environment of Rhineland Palati nate, Mainz, Germany, technical report, (in German).

Dong, J., Zhu, Y., Jia, X., Shao, M., Han, X., Qiao, J., Bai, C., Tang, X., 2022. Nation-scale reference evapotranspiration estimation by using deep learning and classical machine learning models in China. J. Hydrol. 604, 127207. https://doi.org/10.1016/j.jhydrol.2021.127207

Dosio, A., Fischer, E.M., 2018. Will Half a Degree Make a Difference? Robust Projections of Indices of Mean and Extreme Climate in Europe Under 1.5°C, 2°C, and 3°C Global Warming. Geophys. Res. Lett. 45, 935–944. https://doi.org/10.1002/2017gl076222

Dosio, A., Panitz, H.-J., 2016. Climate change projections for CORDEX-Africa with COSMO-CLM regional climate model and differences with the driving global climate models. Clim. Dyn. 46, 1599–1625. https://doi.org/10.1007/s00382-015-2664-4

DWD (German Weather Serivce): Dokumentation Bodenfeuchte, German Weather Service (DWD), Offenbach, Germany, regular documentation, 2018 (in German).

DWD (German Weather Service): Climate Data Center; used are grids and observation for Germany, available at: ftp://opendata. dwd.de/climate_environment/CDC/, last access: 1 July 2019.

Easterling, D.R., 2024. Long-term planning requires climate projections beyond 2100. Nat. Clim. Change.

Ellison, D., Morris, C.E., Locatelli, B., Sheil, D., Cohen, J., Murdiyarso, D., Gutierrez, V., Noordwijk, M.V., Creed, I.F., Pokorny, J., Gaveau, D., Spracklen, D.V., Tobella, A.B., Ilstedt, U., Teuling, A.J., Gebrehiwot, S.G., Sands, D.C., Muys, B., Verbist, B., Springgay, E., Sugandi, Y., Sullivan, C.A., 2017. Trees, forests and water: Cool insights for a hot world. Glob. Environ. Change 43, 51–61. https://doi.org/10.1016/j.gloenvcha.2017.01.002

Farthing, M.W., Ogden, F.L., 2017. Numerical Solution of Richards' Equation: A Review of Advances and Challenges. Soil Sci. Soc. Am. J. 81, 1257–1269. https://doi.org/10.2136/sssaj2017.02.0058
Fatichi, S., Pappas, C., Ivanov, V.Y., 2016. Modeling plant–water interactions: an ecohydrological overview from the cell to the global scale. WIREs Water 3, 327–368. https://doi.org/10.1002/wat2.1125
Federer, C.A., 1995, BROOK90: A simulation model for evaporation, soil water, and streamflow, Version 3.1. Gen. Tech. Rep. NE-141. U.S. Department of Agriculture, Forest Service, Northeastern Forest Experiment Station, Durham, NH, USA.
Federer, C.A., Vörösmarty, C., Fekete, B., 2003. Sensitivity of Annual Evaporation to Soil and Root Properties in Two Models of Contrasting Complexity. J. Hydrometeorol. 4, 1276–1290. https://doi.org/10.1175/1525-7541(2003)004<1276:SOAETS>2.0.CO;2
Feldmann, H., Früh, B., Schädler, G., Panitz, H.-J., Keuler, K., Jacob, D., Lorenz, P., 2008. Evaluation of the precipitation for South-western Germany from high resolution simulations with regional climate models. Meteorol. Z. 17, 455–465. https://doi.org/10.1127/0941-2948/2008/0295
Feng, H., 2016. Individual contributions of climate and vegetation change to soil moisture trends across multiple spatial scales. Sci. Rep. 6, 32782. https://doi.org/10.1038/srep32782
Food and Agriculture Organization of the United Nations (Ed.), 1998. Crop evapotranspiration: guidelines for computing crop water requirements, FAO irrigation and drainage paper. Food and Agriculture Organization of the United Nations, Rome.
Germer, S., Kaiser, K., Bens, O., Hüttl, R.F., n.d. Water Balance Changes and Responses of Ecosystems and Society in the Berlin-Brandenburg Region – a Review.
Giese, M., Müller, C., Vi, F., n.d. Entwicklung und GIS gestützte Parametrisierung eines Niederschlag-Abfluss-Modells zur Abschätzung der Auswirkung dezentraler Hochwasserschutzmaßnahmen auf die Abflussganglinie eines mesoskaligen Einzugsgebietes der Eifel.
Givnish, T., 2002. Adaptive significance of evergreen vs. deciduous leaves: solving the triple paradox. Silva Fenn. 36. https://doi.org/10.14214/sf.535
Gleick, P.H., 1986. Methods for evaluating the regional hydrologic impacts of global climatic changes. J. Hydrol. 88, 97–116. https://doi.org/10.1016/0022-1694(86)90199-X
Goodbrand, A., Anderson, A., Devito, K., Silins, U., 2022. Untangling harvest-streamflow responses in foothills conifer forests: Nexus of teleconnections, summer-dominated precipitation, and storage. Hydrol. Process. 36, e14479. https://doi.org/10.1002/hyp.14479
Granier, A., Loustau, D., Br□da, N., 2000. A generic model of forest canopy conductance dependent on climate, soil water availability and leaf area index. Ann. For. Sci. 57, 755–765. https://doi.org/10.1051/forest:2000158
Gray, V., 2007. Climate Change 2007: The Physical Science Basis Summary for Policymakers. Energy Environ. 18, 433–440. https://doi.org/10.1260/095830507781076194
Green, J., 2002. Study of the Potential Impacts on Water Resources.
Groh, J., Puhlmann, H., 2013. Kalibrierung eines Bodenwasserhaushaltsmodells mit einer kombinierten Zielfunktion für die Optimierung der Wasserretentionskurve.
Gupta Hoshin Vijai, Sorooshian Soroosh, Yapo Patrice Ogou, 1999. Status of Automatic Calibration for Hydrologic Models: Comparison with Multilevel Expert Calibration. J. Hydrol. Eng. 4, 135–143. https://doi.org/10.1061/(ASCE)1084-0699(1999)4:2(135)
Hamed, K.H., Ramachandra Rao, A., 1998. A modified Mann-Kendall trend test for autocorrelated data. J. Hydrol. 204, 182–196. https://doi.org/10.1016/S0022-1694(97)00125-X

Hammel, K., Kennel, M., 2001. Charakterisierung und Analyse der Wasserverfügbarkeit und des Wasserhaushalts von Waldstandorten in Bayern mit dem Simulationsmodell BROOK90, Forstliche Forschungsberichte München. Frank, München.
Han, L., Menzel, L., 2022. Hydrological variability in southern Siberia and the role of permafrost degradation. J. Hydrol. 604, 127203. https://doi.org/10.1016/j.jhydrol.2021.127203
Hanna, E., Cappelen, J., Fettweis, X., Mernild, S.H., Mote, T.L., Mottram, R., Steffen, K., Ballinger, T.J., Hall, R.J., 2021. Greenland surface air temperature changes from 1981 to 2019 and implications for ice-sheet melt and mass-balance change. Int. J. Climatol. 41. https://doi.org/10.1002/joc.6771
Haverkamp, R., Vauclin, M., 1979. A note on estimating finite difference interblock hydraulic conductivity values for transient unsaturated flow problems. Water Resour. Res. 15, 181–187. https://doi.org/10.1029/wr015i001p00181
Hengl, T., Mendes De Jesus, J., Heuvelink, G.B.M., Ruiperez Gonzalez, M., Kilibarda, M., Blagotić, A., Shangguan, W., Wright, M.N., Geng, X., Bauer-Marschallinger, B., Guevara, M.A., Vargas, R., MacMillan, R.A., Batjes, N.H., Leenaars, J.G.B., Ribeiro, E., Wheeler, I., Mantel, S., Kempen, B., 2017. SoilGrids250m: Global gridded soil information based on machine learning. PLOS ONE 12, e0169748. https://doi.org/10.1371/journal.pone.0169748
Hock, R., 2003. Temperature index melt modelling in mountain areas. J. Hydrol. 282, 104–115. https://doi.org/10.1016/S0022-1694(03)00257-9
Hörmann, G., 1996. Speichermodell Bodenwasserhaushalt.
Intergouvernemental panel on climate change (Ed.), 2007. Climate change 2007: the physical science basis. Cambridge university press, Cambridge.
Intergovernmental Panel On Climate Change (Ipcc), 2023a. Climate Change 2021 – The Physical Science Basis: Working Group I Contribution to the Sixth Assessment Report of the Intergovernmental Panel on Climate Change, 1st ed. Cambridge University Press. https://doi.org/10.1017/9781009157896
Intergovernmental Panel On Climate Change (Ipcc), 2023b. Climate Change 2021 – The Physical Science Basis: Working Group I Contribution to the Sixth Assessment Report of the Intergovernmental Panel on Climate Change, 1st ed. Cambridge University Press. https://doi.org/10.1017/9781009157896
Jacob, D., Elizalde, A., Haensler, A., Hagemann, S., Kumar, P., Podzun, R., Rechid, D., Remedio, A. R., Saeed, F., Sieck, K., Teichmann, C., & Wilhelm, C.,2012. Assessing the Transferability of the Regional Climate Model REMO to Different COordinated Regional Climate Downscaling EXperiment (CORDEX) Regions. *Atmosphere*, *3*(1), 181-199. https://doi.org/10.3390/atmos3010181
Jenicek, M., Seibert, J., Staudinger, M., 2018. Modeling of Future Changes in Seasonal Snowpack and Impacts on Summer Low Flows in Alpine Catchments. Water Resour. Res. 54, 538–556. https://doi.org/10.1002/2017WR021648
Jones, J. A., Wei, X., Archer, E., Bishop, K., Blanco, J. A., Ellison, D., Gush, M. B., McNulty, S. G., van Noordwijk, M., & Creed, I. F., 2020. Forest–water interactions under global change. In D. F. Levia, D. Carlyle-Moses, & T. Tanaka (Eds.), Forest-Water Interactions: Ecological Studies (Vol. 240, pp. 589–611). Springer. https://doi.org/10.1007/978-3-030-26086-6_24
Keenan, R.J., 2015. Climate change impacts and adaptation in forest management: a review. Ann. For. Sci. 72, 145–167. https://doi.org/10.1007/s13595-014-0446-5
Khaine, I., Woo, S.Y., 2015. An overview of interrelationship between climate change and forests. For. Sci. Technol. 11, 11–18. https://doi.org/10.1080/21580103.2014.932718
Kirtman, B., Power, S. B., Adedoyin, J. A., Boer, G. J., Bojariu, R., Camilloni, I., ... &

Zhou, T., 2013. Near-term climate change: Projections and predictability. In T. F. Stocker, D. Qin, G.-K. Plattner, M. Tignor, S. K. Allen, J. Boschung, ... & P. M. Midgley (Eds.), Climate Change 2013: The Physical Science Basis. Contribution of Working Group I to the Fifth Assessment Report of the Intergovernmental Panel on Climate Change (pp. 953–1028). Cambridge University Press.

Konz, M., Seibert, J., 2010. On the value of glacier mass balances for hydrological model calibration. J. Hydrol. 385, 238–246. https://doi.org/10.1016/j.jhydrol.2010.02.025

Körner, C., Basler, D., 2010. Phenology Under Global Warming. Science 327, 1461–1462. https://doi.org/10.1126/science.1186473

Koudahe, K., Kayode, A.J., Samson, A.O., Adebola, A.A., Djaman, K., 2017. Trend Analysis in Standardized Precipitation Index and Standardized Anomaly Index in the Context of Climate Change in Southern Togo. Atmospheric Clim. Sci. 07, 401–423. https://doi.org/10.4236/acs.2017.74030

Kour, R., Patel, N., Krishna, A.P., 2016. Climate and hydrological models to assess the impact of climate change on hydrological regime: a review. Arab. J. Geosci. 9, 544. https://doi.org/10.1007/s12517-016-2561-0

Kovats, R.S., R. Valentini, L.M. Bouwer, E. Georgopoulou, D. Jacob, E. Martin, M. Rounsevell, and J.-F. Soussana., 2014: Europe. In: Climate Change 2014: Impacts, Adaptation, and Vulnerability. Part B: Regional Aspects. Contribution of Working Group II to the Fifth Assessment Report of the Intergovernmental Panel on Climate Change [Barros, V.R., C.B. Field, D.J. Dokken, M.D. Mastrandrea, K.J. Mach, T.E. Bilir, M. Chatterjee, K.L. Ebi, Y.O. Estrada, R.C. Genova, B. Girma, E.S. Kissel, A.N. Levy, S. MacCracken, P.R. Mastrandrea, and L.L. White (eds.)]. Cambridge University Press, Cambridge, United Kingdom and New York, NY, USA, pp. 1267-1326.

Kraft, M., McNamara, J.P., 2022. Evapotranspiration across the rain–snow transition in a semi-arid watershed. Hydrol. Process. 36. https://doi.org/10.1002/hyp.14519

Krause, P., Boyle, D.P., Bäse, F., 2005. Comparison of different efficiency criteria for hydrological model assessment. Adv. Geosci. 5, 89–97. https://doi.org/10.5194/adgeo-5-89-2005

Kurzweil, J.R., Metlen, K., Abdi, R., Strahan, R., Hogue, T.S., 2021. Surface water runoff response to forest management: Low-intensity forest restoration does not increase surface water yields. For. Ecol. Manag. 496, 119387. https://doi.org/10.1016/j.foreco.2021.119387

Kuželková, M., Jačka, L., Kovář, M., Hradilek, V., Máca, P., 2024. Tree trait-mediated differences in soil moisture regimes: a comparative study of beech, spruce, and larch in a drought-prone area of Central Europe. Eur. J. For. Res. 143, 319–332. https://doi.org/10.1007/s10342-023-01628-y

Lamacova, A., Vlnas, R., Kram, P., 2022. Interception loss as an underestimated component of evapotranspiration modelling in a forested catchment. https://doi.org/10.5194/iahs2022-724

Lange, S., 2018. Bias correction of surface downwelling longwave and shortwave radiation for the EWEMBI dataset. Earth Syst. Dyn. 9, 627–645. https://doi.org/10.5194/esd-9-627-2018

Laube, J., Sparks, T.H., Estrella, N., Höfler, J., Ankerst, D.P., Menzel, A., 2014. Chilling outweighs photoperiod in preventing precocious spring development. Glob. Change Biol. 20, 170–182. https://doi.org/10.1111/gcb.12360

Laux, P., Rötter, R.P., Webber, H., Dieng, D., Rahimi, J., Wei, J., Faye, B., Srivastava, A.K., Bliefernicht, J., Adeyeri, O., Arnault, J., Kunstmann, H., 2021. To bias correct or not to bias correct? An agricultural impact modelers' perspective on regional climate model data. Agric. For. Meteorol. 304–305, 108406. https://doi.org/10.1016/j.agrformet.2021.108406

LGRB (Federal State Office for Geology Resources and Mining): Soil maps for Baden-Württemberg (BK50), available at: https: //lgrb-bw.de/bodenkunde, last access: 1 July 2019

Lindner, M., Maroschek, M., Netherer, S., Kremer, A., Barbati, A., Garcia-Gonzalo, J., Seidl, R., Delzon, S., Corona, P., Kolström, M., Lexer, M.J., Marchetti, M., 2010. Climate change impacts, adaptive capacity, and vulnerability of European forest ecosystems. For. Ecol. Manag. 259, 698–709. https://doi.org/10.1016/j.foreco.2009.09.023

Lindström, G., Johansson, B., Persson, M., Gardelin, M., Bergström, S., 1997. Development and test of the distributed HBV-96 hydrological model. J. Hydrol. 201, 272–288. https://doi.org/10.1016/s0022-1694(97)00041-3

Lucas-Borja, M.E., Fernández, C., Plaza-Alvarez, P.A., Carrà, B.G., Zema, D.A., 2022. Variability of soil properties with fire severity in pine forests and reforested areas under Mediterranean conditions. J. Hydrol. Hydromech. 70, 462–474. https://doi.org/10.2478/johh-2022-0028

Ludemann, T., 2014. Standorte, natürliche Vegetation und anthropogene Veränderung* The Forests of the Northern Black Forest, SW-Germany.

Makela, A., Landsberg, J., Ek, A.R., Burk, T.E., Ter-Mikaelian, M., Agren, G.I., Oliver, C.D., Puttonen, P., 2000. Process-based models for forest ecosystem management: current state of the art and challenges for practical implementation. Tree Physiol. 20, 289–298. https://doi.org/10.1093/treephys/20.5-6.289

Mann, H.B., 1945. Nonparametric Tests Against Trend. Econometrica 13, 245–259. https://doi.org/10.2307/1907187

Martel, J.-L., Demeester, K., Brissette, F.O., Poulin, A., Arsenault, R., 2017. HMETS—A Simple and Efficient Hydrology Model for Teaching Hydrological Modelling, Flow Forecasting and Climate Change Impacts.

Martinetti, S., Molnar, P., Carminati, A., Floriancic, M.G., 2025. Contrasting the soil–plant hydraulics of beech and spruce by linking root water uptake to transpiration dynamics. Tree Physiol. 45, tpae158. https://doi.org/10.1093/treephys/tpae158

Matott, L.S., 2017. OSTRICH – an Optimization Software Tool, Documentation and User's Guide, Version 17.12.19. 79 pages, University at Buffalo Center for Computational Research, http://www.civil.uwaterloo.ca/envmodelling/Ostrich.html.

McDowell, N.G., Fisher, R.A., Xu, C., Domec, J.C., Hölttä, T., Mackay, D.S., Sperry, J.S., Boutz, A., Dickman, L., Gehres, N., Limousin, J.M., Macalady, A., Martínez-Vilalta, J., Mencuccini, M., Plaut, J.A., Ogée, J., Pangle, R.E., Rasse, D.P., Ryan, M.G., Sevanto, S., Waring, R.H., Williams, A.P., Yepez, E.A., Pockman, W.T., 2013. Evaluating theories of drought-induced vegetation mortality using a multimodel–experiment framework. New Phytol. 200, 304–321. https://doi.org/10.1111/nph.12465

Mendoza, P.A., Clark, M.P., Mizukami, N., Newman, A.J., Barlage, M., Gutmann, E.D., Rasmussen, R.M., Rajagopalan, B., Brekke, L.D., Arnold, J.R., 2015. Effects of Hydrologic Model Choice and Calibration on the Portrayal of Climate Change Impacts. J. Hydrometeorol. 16, 762–780. https://doi.org/10.1175/jhm-d-14-0104.1

Menzel, A., 1997. Phänologie von Waldbäumen unter sich ändernden Klimabedingungen: Auswertung der Beobachtungen in den internationalen phänologischen Gärten und Möglichkeiten der Modellierung von Phänodaten, Forstliche Forschungsberichte München. Lehrstuhl für Bioklimatologie und Immissionsforschung der Univ. München.

Menzel, A., Fabian, P., 1999. Growing season extended in Europe. Nature 397, 659–659. https://doi.org/10.1038/17709

Menzel, A., Sparks, T.H., Estrella, N., Koch, E., Aasa, A., Ahas, R., Alm-Kübler, K., Bissolli, P., Braslavská, O., Briede, A., Chmielewski, F.M., Crepinsek, Z., Curnel, Y., Dahl, Å., Defila, C., Donnelly, A., Filella, Y., Jatczak, K., Måge, F., Mestre, A., Nordli, Ø.,

Peñuelas, J., Pirinen, P., Remišová, V., Scheifinger, H., Striz, M., Susnik, A., Van Vliet, A.J.H., Wielgolaski, F., Zach, S., Zust, A., 2006. European phenological response to climate change matches the warming pattern. Glob. Change Biol. 12, 1969–1976. https://doi.org/10.1111/j.1365-2486.2006.01193.x
Menzel, L., 1999. Flächenhafte Modellierung der Evapotranspiration mit TRAIN.
Menzel, L., 1996. Modellierung der Evapotranspiration im System Boden-Pflanze-Atmosphäre.
Menzel, L., Lang, H., 2005. Spatial Heterogeneity of Snow Conditions and Evapotranspiration in the Swiss Alps, in: Huber, U.M., Bugmann, H.K.M., Reasoner, M.A. (Eds.), Global Change and Mountain Regions, Advances in Global Change Research. Springer Netherlands, Dordrecht, pp. 275–282. https://doi.org/10.1007/1-4020-3508-X_28
Menzel, L., Rötzer, T., 2007. SVAT-Modelle und deren Anwendung.
Menzel, L., 2013. Land-use classification scheme in TRAIN – Applied code numbers
Milly, P.C.D., Betancourt, J., Falkenmark, M., Hirsch, R.M., Kundzewicz, Z.W., Lettenmaier, D.P., Stouffer, R.J., 2008. Stationarity Is Dead: Whither Water Management? Science 319, 573–574. https://doi.org/10.1126/science.1151915
Miralles, D.G., Bonte, O., Koppa, A., Baez-Villanueva, O.M., Tronquo, E., Zhong, F., Beck, H.E., Hulsman, P., Dorigo, W., Verhoest, N.E.C., Haghdoost, S., 2025. GLEAM4: global land evaporation and soil moisture dataset at 0.1° resolution from 1980 to near present. Sci. Data 12, 416. https://doi.org/10.1038/s41597-025-04610-y
Miralles, D.G., Jiménez, C., Jung, M., Michel, D., Ershadi, A., McCabe, M.F., Hirschi, M., Martens, B., Dolman, A.J., Fisher, J.B., Mu, Q., Seneviratne, S.I., Wood, E.F., Fernández-Prieto, D., 2016. The WACMOS-ET project – Part 2: Evaluation of global terrestrial evaporation data sets. Hydrol. Earth Syst. Sci. 20, 823–842. https://doi.org/10.5194/hess-20-823-2016
Mondal, S., Mishra, A., 2024. Quantifying the Precipitation, Evapotranspiration, and Soil Moisture Network's Interaction Over Global Land Surface Hydrological Cycle. Water Resour. Res. 60, e2023WR034861. https://doi.org/10.1029/2023WR034861
Monteith, J., 1965. The state and movement of water in living organisms. Academic Press Inc., New York. volume 17. chapter Evaporation and environment. pp. 205–234.
Monteith, J.L., Unsworth, M.H., 2013. Principles of environmental physics: plants, animals, and the atmosphere, 4th edition. ed. Elsevier/Academic Press, Amsterdam Boston.
Morales-Santos, A., Köhler, M., Fleck, S., Scheler, B., Wagner, M., Meesenburg, H., 2025. Modelling water balance components in a temperate forest in Germany: A comparative analysis of pine, oak, and beech. https://doi.org/10.5194/egusphere-egu24-17088
Moss, R.H., Edmonds, J.A., Hibbard, K.A., Manning, M.R., Rose, S.K., Van Vuuren, D.P., Carter, T.R., Emori, S., Kainuma, M., Kram, T., Meehl, G.A., Mitchell, J.F.B., Nakicenovic, N., Riahi, K., Smith, S.J., Stouffer, R.J., Thomson, A.M., Weyant, J.P., Wilbanks, T.J., 2010a. The next generation of scenarios for climate change research and assessment. Nature 463, 747–756. https://doi.org/10.1038/nature08823
Moss, R.H., Edmonds, J.A., Hibbard, K.A., Manning, M.R., Rose, S.K., Van Vuuren, D.P., Carter, T.R., Emori, S., Kainuma, M., Kram, T., Meehl, G.A., Mitchell, J.F.B., Nakicenovic, N., Riahi, K., Smith, S.J., Stouffer, R.J., Thomson, A.M., Weyant, J.P., Wilbanks, T.J., 2010b. The next generation of scenarios for climate change research and assessment. Nature 463, 747–756. https://doi.org/10.1038/nature08823
Mualem, Y., 1976. A new model for predicting the hydraulic conductivity of unsaturated porous media. Water Resour. Res. 12, 513–522. https://doi.org/10.1029/wr012i003p00513

Muauz, A., Berehanu, B., Bedru, H., 2024. Utilizing the HBV-Light semi-distributed conceptual hydrological model to estimate groundwater recharge in the upstream part of the Awash River basin, Ethiopia. J. Hydrol. Reg. Stud. 56, 102018. https://doi.org/10.1016/j.ejrh.2024.102018

Mueller, B., Seneviratne, S.I., 2012. Hot days induced by precipitation deficits at the global scale. Proc. Natl. Acad. Sci. 109, 12398–12403. https://doi.org/10.1073/pnas.1204330109

Muñoz Sabater, J., 2019: ERA5-Land hourly data from 1950 to present. Copernicus Climate Change Service (C3S) Climate Data Store (CDS). DOI: 10.24381/cds.e2161bac, Accessed over Google Earth Engine Code Editor. Daily Aggregates: https://developers.google.com/earthengine/datasets/catalog/ECMWF_ERA5_LAND_DAILY_AGGR?hl=de , Accessed 5-4-2025

Murray, F.W., 1967. On the Computation of Saturation Vapor Pressure. J. Appl. Meteorol. 6, 203–204. https://doi.org/10.1175/1520-0450(1967)006<0203:OTCOSV>2.0.CO;2

Nash, J.E., Sutcliffe, J.V., 1970. River flow forecasting through conceptual models part I — A discussion of principles. J. Hydrol. 10, 282–290. https://doi.org/10.1016/0022-1694(70)90255-6

Orth, R., Staudinger, M., Seneviratne, S.I., Seibert, J., Zappa, M., 2015. Does model performance improve with complexity? A case study with three hydrological models. J. Hydrol. 523, 147–159. https://doi.org/10.1016/j.jhydrol.2015.01.044

Pachauri, R.K., Mayer, L., Intergovernmental Panel on Climate Change (Eds.), 2015. Climate change 2014: synthesis report. Intergovernmental Panel on Climate Change, Geneva, Switzerland.

Paligi, S.S., Link, R.M., Hackmann, C.A., Coners, H., Leuschner, C., 2025. Water consumption of beech, spruce and Douglas fir in pure and mixed stands in a wet and a dry year – Testing predictions of the iso/anisohydry concept. Sci. Total Environ. 970, 178948. https://doi.org/10.1016/j.scitotenv.2025.178948

Parmesan, C., Yohe, G., 2003. A globally coherent fingerprint of climate change impacts across natural systems. Nature 421, 37–42. https://doi.org/10.1038/nature01286

Pfeifroth, U., Trentmann, J., Hollmann, R., Selbach, N., Wer scheck, M., and Meirink, J. F.: ICDR SEVIRI Radiation– based on SARAH-2 methods, Satellite Application Facility on Cli mate Monitoring, available at: https://wui.cmsaf.eu/safira/action/viewICDRDetails?acronym=SARAH_V002_ICDR.

Piao, S., Liu, Q., Chen, A., Janssens, I.A., Fu, Y., Dai, J., Liu, L., Lian, X., Shen, M., Zhu, X., 2019. Plant phenology and global climate change: Current progresses and challenges. Glob. Change Biol. 25, 1922–1940. https://doi.org/10.1111/gcb.14619

Pretzsch, H., Rötzer, T., Matyssek, R., Grams, T.E.E., Häberle, K.-H., Pritsch, K., Kerner, R., Munch, J.-C., 2014. Mixed Norway spruce (Picea abies [L.] Karst) and European beech (Fagus sylvatica [L.]) stands under drought: from reaction pattern to mechanism. Trees 28, 1305–1321. https://doi.org/10.1007/s00468-014-1035-9

Pretzsch, H., Schütze, G., Uhl, E., 2013. Resistance of European tree species to drought stress in mixed *versus* pure forests: evidence of stress release by inter-specific facilitation. Plant Biol. 15, 483–495. https://doi.org/10.1111/j.1438-8677.2012.00670.x

Rahmati, M., Amelung, W., Brogi, C., Dari, J., Flammini, A., Bogena, H., Brocca, L., Chen, H., Groh, J., Koster, R.D., McColl, K.A., Montzka, C., Moradi, S., Rahi, A., Sharghi S., F., Vereecken, H., 2024. Soil Moisture Memory: State-Of-The-Art and the Way Forward. Rev. Geophys. 62, e2023RG000828. https://doi.org/10.1029/2023RG000828

Rauthe, M., Steiner, H., Riediger, U., Mazurkiewicz, A., Gratzki, A., 2013. A Central European precipitation climatology Part I: Generation and validation of a high-

resolution gridded daily data set (HYRAS). Meteorol. Z. 22, 235–256. https://doi.org/10.1127/0941-2948/2013/0436
Reed, M.S., Kenter, J., Bonn, A., Broad, K., Burt, T.P., Fazey, I.R., Fraser, E.D.G., Hubacek, K., Nainggolan, D., Quinn, C.H., Stringer, L.C., Ravera, F., 2013. Participatory scenario development for environmental management: A methodological framework illustrated with experience from the UK uplands. J. Environ. Manage. 128, 345–362. https://doi.org/10.1016/j.jenvman.2013.05.016
Refsgaard, J.C., & Storm, B., 1996. Construction, calibration and validation of hydrological models. In M.B. Abbott & J.C. Refsgaard (Eds.), Distributed Hydrological Modelling (pp. 41–54). Kluwer Academic Publishers.
Reyer, C.P.O., Brouwers, N., Rammig, A., Brook, B.W., Epila, J., Grant, R.F., Holmgren, M., Langerwisch, F., Leuzinger, S., Lucht, W., Medlyn, B., Pfeifer, M., Steinkamp, J., Vanderwel, M.C., Verbeeck, H., Villela, D.M., 2015. Forest resilience and tipping points at different spatio-temporal scales: approaches and challenges. J. Ecol. 103, 5–15. https://doi.org/10.1111/1365-2745.12337
Richards, L.A., 1931. Capillary conduction of liquids through porous mediums. Physics, 1(5), pp.318–333. https://doi.org/10.1063/1.1745010
Richardson, A.D., Keenan, T.F., Migliavacca, M., Ryu, Y., Sonnentag, O., Toomey, M., 2013. Climate change, phenology, and phenological control of vegetation feedbacks to the climate system. Agric. For. Meteorol. 169, 156–173. https://doi.org/10.1016/j.agrformet.2012.09.012
Rosenzweig, C., Casassa, G., Karoly, D.J., Imeson, A., Liu, C., Menzel, A., Rawlins, S., Root, T.L., Seguin, B., Tryjanowski, P., 2007. Assessment of observed changes and responses in natural and managed systems. https://doi.org/10.5167/UZH-33180
Saavedra, D., Mendoza, P.A., Addor, N., Llauca, H., Vargas, X., 2022. A multi-objective approach to select hydrological models and constrain structural uncertainties for climate impact assessments. Hydrol. Process. 36, e14446. https://doi.org/10.1002/hyp.14446
Schäfer, C., Fäth, J., Kneisel, C., Baumhauer, R., Ullmann, T., 2023. Multidimensional hydrological modeling of a forested catchment in a German low mountain range using a modular runoff and water balance model. Front. For. Glob. Change 6, 1186304. https://doi.org/10.3389/ffgc.2023.1186304
Schmidt-Walter, P., Trotsiuk, V., Hammel, K., Kennel, M., Federer, A., Hohenbrink, T., Hetkamp, G., 2021. LWFBrook90R: Simulate Evapotranspiration and Soil Moisture with the SVAT Model LWF-Brook90. CRAN: Contributed Packages. https://doi.org/10.32614/cran.package.lwfbrook90r
Schmidt-Walter, P., Trotsiuk, V., Meusburger, K., Zacios, M., Meesenburg, H., 2020. Advancing simulations of water fluxes, soil moisture and drought stress by using the LWF-Brook90 hydrological model in R. Agric. For. Meteorol. 291, 108023. https://doi.org/10.1016/j.agrformet.2020.108023
Schumacher, D.L., Singh, J., Hauser, M., Fischer, E.M., Wild, M., Seneviratne, S.I., 2024. Exacerbated summer European warming not captured by climate models neglecting long-term aerosol changes. Commun. Earth Environ. 5, 182. https://doi.org/10.1038/s43247-024-01332-8
Schume, H., Jost, G., Hager, H., 2004. Soil water depletion and recharge patterns in mixed and pure forest stands of European beech and Norway spruce. J. Hydrol. 289, 258–274. https://doi.org/10.1016/j.jhydrol.2003.11.036
Scott, D.F., Bruijnzeel, L.A., Vertessy, R.A., Calder, I.R., 2004. HYDROLOGY | Impacts of Forest Plantations on Streamflow, in: Encyclopedia of Forest Sciences. Elsevier, pp. 367–377. https://doi.org/10.1016/B0-12-145160-7/00272-6

Seibert, J., 2000. Multi-criteria calibration of a conceptual runoff model using a genetic algorithm. Hydrol. Earth Syst. Sci. 4, 215–224. https://doi.org/10.5194/hess-4-215-2000
Seibert, J., McDonnell, J.J., 2010. Land-cover impacts on streamflow: a change-detection modelling approach that incorporates parameter uncertainty. Hydrol. Sci. J. 55, 316–332. https://doi.org/10.1080/02626661003683264
Seibert, J., Vis, M.J.P., 2012. Teaching hydrological modeling with a user-friendly catchment-runoff-model software package. Hydrol. Earth Syst. Sci. 16, 3315–3325. https://doi.org/10.5194/hess-16-3315-2012
Sen, P.K., 1968. Estimates of the Regression Coefficient Based on Kendall's Tau. J. Am. Stat. Assoc. 63, 1379–1389. https://doi.org/10.1080/01621459.1968.10480934
Seneviratne, S.I., Corti, T., Davin, E.L., Hirschi, M., Jaeger, E.B., Lehner, I., Orlowsky, B., Teuling, A.J., 2010. Investigating soil moisture–climate interactions in a changing climate: A review. Earth-Sci. Rev. 99, 125–161. https://doi.org/10.1016/j.earscirev.2010.02.004
Shuttleworth, W.J., Wallace, J.S., 1985. Evaporation from sparse crops-an energy combination theory. Q. J. R. Meteorol. Soc. 111, 839–855. https://doi.org/10.1002/qj.49711146910
Spinoni, J., Naumann, G., Vogt, J., Barbosa, P., 2015. European drought climatologies and trends based on a multi-indicator approach. Glob. Planet. Change 127, 50–57. https://doi.org/10.1016/j.gloplacha.2015.01.012
Stinziano, J.R., Hüner, N.P.A., Way, D.A., 2015. Warming delays autumn declines in photosynthetic capacity in a boreal conifer, Norway spruce (*Picea abies*). Tree Physiol. 35, 1303–1313. https://doi.org/10.1093/treephys/tpv118
Stork, M., Menzel, L., 2016. Analysis and simulation of the water and energy balance of intense agriculture in the Upper Rhine valley, south-west Germany. Environ. Earth Sci. 75, 1166. https://doi.org/10.1007/s12665-016-5980-z
SONNY LiDAR DIGITAL TERRAIN MODELS of EUROPE, Germany DTM50, https://sonny.4lima.de/, Last Accessed: July 2025
Sunderlin, W.D., Dewi, S., Puntodewo, A., Müller, D., Angelsen, A., Epprecht, M., 2008. Why Forests Are Important for Global Poverty Alleviation: a Spatial Explanation. Ecol. Soc. 13, art24. https://doi.org/10.5751/ES-02590-130224
Taheri, M., Ranjram, M., Craig, J.R., 2023. An Upscaled Model of Fill-And-Spill Hydrological Response. Water Resour. Res. 59, e2022WR033494. https://doi.org/10.1029/2022WR033494
Teuling, A.J., Seneviratne, S.I., Stöckli, R., Reichstein, M., Moors, E., Ciais, P., Luyssaert, S., Van Den Hurk, B., Ammann, C., Bernhofer, C., Dellwik, E., Gianelle, D., Gielen, B., Grünwald, T., Klumpp, K., Montagnani, L., Moureaux, C., Sottocornola, M., Wohlfahrt, G., 2010a. Contrasting response of European forest and grassland energy exchange to heatwaves. Nat. Geosci. 3, 722–727. https://doi.org/10.1038/ngeo950
Tijdeman, E., Menzel, L., 2021. The development and persistence of soil moisture stress during drought across southwestern Germany. Hydrol. Earth Syst. Sci. 25, 2009–2025. https://doi.org/10.5194/hess-25-2009-2021
Toledo, M., Poorter, L., Peña-Claros, M., Alarcón, A., Balcázar, J., Leaño, C., Licona, J.C., Llanque, O., Vroomans, V., Zuidema, P., Bongers, F., 2011. Climate is a stronger driver of tree and forest growth rates than soil and disturbance. J. Ecol. 99, 254–264. https://doi.org/10.1111/j.1365-2745.2010.01741.x
Tolson, B. A., & Shoemaker, C. A., 2007. Dynamically dimensioned search algorithm for computationally efficient watershed model calibration. Water Resources Research, 43(1), W01413. https://doi.org/10.1029/2005WR004723

Törnros, T., Menzel, L., 2010. Heading for knowledge in a data scarce river basin: Kharaa, Mongolia.
Uhlenbrook, S., Seibert, J., Leibundgut, C., Rodhe, A., 1999. Prediction uncertainty of conceptual rainfall-runoff models caused by problems in identifying model parameters and structure. Hydrol. Sci. J. 44, 779–797. https://doi.org/10.1080/02626669909492273
Usman, M., Ndehedehe, C.E., Farah, H., Ahmad, B., Wong, Y., Adeyeri, O.E., 2022. Application of a Conceptual Hydrological Model for Streamflow Prediction Using Multi-Source Precipitation Products in a Semi-Arid River Basin. Water 14, 1260. https://doi.org/10.3390/w14081260
Van Genuchten, M.Th., 1980. A Closed-form Equation for Predicting the Hydraulic Conductivity of Unsaturated Soils. Soil Sci. Soc. Am. J. 44, 892–898. https://doi.org/10.2136/sssaj1980.03615995004400050002x
Van Vuuren, D.P., Edmonds, J., Kainuma, M., Riahi, K., Thomson, A., Hibbard, K., Hurtt, G.C., Kram, T., Krey, V., Lamarque, J.-F., Masui, T., Meinshausen, M., Nakicenovic, N., Smith, S.J., Rose, S.K., 2011. The representative concentration pathways: an overview. Clim. Change 109, 5–31. https://doi.org/10.1007/s10584-011-0148-z
Varhola, A., Coops, N.C., Weiler, M., Moore, R.D., 2010. Forest canopy effects on snow accumulation and ablation: An integrative review of empirical results. J. Hydrol. 392, 219–233. https://doi.org/10.1016/j.jhydrol.2010.08.009
Vidmar, A., Brilly, M., Sapač, K., Kryžanowski, A., 2020. Efficient Calibration of a Conceptual Hydrological Model Based on the Enhanced Gauss–Levenberg–Marquardt Procedure. Appl. Sci. 10, 3841. https://doi.org/10.3390/app10113841
Vitasse, Y., François, C., Delpierre, N., Dufrêne, E., Kremer, A., Chuine, I., Delzon, S., 2011. Assessing the effects of climate change on the phenology of European temperate trees. Agric. For. Meteorol. 151, 969–980. https://doi.org/10.1016/j.agrformet.2011.03.003
Von Wilpert, K. ,1990. Die Jahrringstruktur von Fichten in Abhängigkeit vom Bodenwasserhaushalt auf Pseudogley und Parabraunerde: Ein Methodenkonzept zur Erfassung standortsspezifischer Wasserstreßdisposition. Freiburg: Freiburger Bodenkundliche Abhandlungen.
Vorobevskii, I., Kronenberg, R., Bernhofer, C., 2020. Global BROOK90 R Package: An Automatic Framework to Simulate the Water Balance at Any Location. Water 12, 2037. https://doi.org/10.3390/w12072037
Vorobevskii, I., Luong, T.T., Kronenberg, R., Grünwald, T., Bernhofer, C., 2022. Modelling evaporation with local, regional and global BROOK90 frameworks: importance of parameterization and forcing. Hydrol. Earth Syst. Sci. 26, 3177–3239. https://doi.org/10.5194/hess-26-3177-2022
Vorobevskii, I., Luong, T.T., Kronenberg, R., Petzold, R., 2024. High-resolution operational soil moisture monitoring for forests in central Germany. Hydrol. Earth Syst. Sci. 28, 3567–3595. https://doi.org/10.5194/hess-28-3567-2024
Wang, L., She, D., Yang, Y., Meng, L., Xia, J., 2025. Direct and indirect effects of spring phenology on forest transpiration. Agric. For. Meteorol. 372, 110661. https://doi.org/10.1016/j.agrformet.2025.110661
Wang, M., Menzel, L., Jiang, S., Ren, L., Xu, C.-Y., Cui, H., 2023. Evaluation of flash drought under the impact of heat wave events in southwestern Germany. Sci. Total Environ. 904, 166815. https://doi.org/10.1016/j.scitotenv.2023.166815
Weis, W., Ahrends, B., Böhner, J., Falk, W., Fleck, S., Habel, R., Klemmt, H.-J., Meesenburg, H., Müller, A.-C., Puhlmann, H., Wehberg, J.-A., Wellpott, A., Wolf, T., 2023. Standortsfaktor Wasserhaushalt im Klimawandel (WHH-KW): Abschlussveröffentlichung zum Forschungsprojekt, Teilprojekte 01, 02, 03, 04,

Forstliche Forschungsberichte München. Zentrum Wald Forst Holz Weihenstephan, Freising.
Weiskopf, S.R., Rubenstein, M.A., Crozier, L.G., Gaichas, S., Griffis, R., Halofsky, J.E., Hyde, K.J.W., Morelli, T.L., Morisette, J.T., Muñoz, R.C., Pershing, A.J., Peterson, D.L., Poudel, R., Staudinger, M.D., Sutton-Grier, A.E., Thompson, L., Vose, J., Weltzin, J.F., Whyte, K.P., 2020. Climate change effects on biodiversity, ecosystems, ecosystem services, and natural resource management in the United States. Sci. Total Environ. 733, 137782. https://doi.org/10.1016/j.scitotenv.2020.137782
Wild, M., 2009. Global dimming and brightening: A review. J. Geophys. Res. Atmospheres 114, 2008JD011470. https://doi.org/10.1029/2008JD011470
Wimmer, F., Schlaffer, S., Aus Der Beek, T., Menzel, L., 2009. Distributed modelling of climate change impacts on snow sublimation in Northern Mongolia. Adv. Geosci. 21, 117–124. https://doi.org/10.5194/adgeo-21-117-2009
World Meteorological Organization (WMO)., 2017. WMO guidelines on the calculation of climate normals (WMO-No. 1203). Geneva, Switzerland: World Meteorological Organization.
Xu, C.-Y., 2000. Climate Change and Hydrologic Models: A Review of Existing Gaps and Recent Research Developments.
Xu, Z., Man, X., Cai, T., Shang, Y., 2022. How Potential Evapotranspiration Regulates the Response of Canopy Transpiration to Soil Moisture and Leaf Area Index of the Boreal Larch Forest in China. Forests 13, 571. https://doi.org/10.3390/f13040571
Zampieri, M., D'Andrea, F., Vautard, R., Ciais, P., De Noblet-Ducoudré, N., Yiou, P., 2009. Hot European Summers and the Role of Soil Moisture in the Propagation of Mediterranean Drought. J. Clim. 22, 4747–4758. https://doi.org/10.1175/2009JCLI2568.1
Zang, C., Hartl-Meier, C., Dittmar, C., Rothe, A., Menzel, A., 2014. Patterns of drought tolerance in major European temperate forest trees: climatic drivers and levels of variability. Glob. Change Biol. 20, 3767–3779. https://doi.org/10.1111/gcb.12637
Zema, D.A., Carrà, B.G., Lucas-Borja, M.E., 2022. Exploring and Modeling the Short-Term Influence of Soil Properties and Covers on Hydrology of Mediterranean Forests after Prescribed Fire and Mulching. Hydrology 9, 21. https://doi.org/10.3390/hydrology9020021
Zhang, M., Liu, N., Harper, R., Li, Q., Liu, K., Wei, X., Ning, D., Hou, Y., Liu, S., 2017. A global review on hydrological responses to forest change across multiple spatial scales: Importance of scale, climate, forest type and hydrological regime. J. Hydrol. 546, 44–59. https://doi.org/10.1016/j.jhydrol.2016.12.040
Zhou, S., Williams, A.P., Berg, A.M., Cook, B.I., Zhang, Y., Hagemann, S., Lorenz, R., Seneviratne, S.I., Gentine, P., 2019. Land–atmosphere feedbacks exacerbate concurrent soil drought and atmospheric aridity. Proc. Natl. Acad. Sci. 116, 18848–18853. https://doi.org/10.1073/pnas.1904955116
Zohner, C.M., Renner, S.S., 2015. Perception of photoperiod in individual buds of mature trees regulates leaf-out. New Phytol. 208, 1023–1030. https://doi.org/10.1111/nph.13510

Appendix A – RAVEN-HMETS

Raven-HMETS Configuration

RVI- FILE:

```
# ------------------------------------------------------------
# Raven Template Input File
# UBC Watershed Model v5 Emulation
# ------------------------------------------------------------
:RunName Raven_HMETS
:StartDate 1974-12-31  24:00:00
:EndDate 2020-01-01 00:00:00
:TimeStep 1.0
:Method                  ORDERED_SERIES
:SoilModel               SOIL_MULTILAYER 3
:Interpolation           INTERP_NEAREST_NEIGHBOR
:Evaporation             PET_PENMAN_MONTEITH
:RainSnowFraction        RAINSNOW_DINGMAN
:PotentialMeltMethod     POTMELT_HMETS
:Routing                 ROUTE_NONE
:CatchmentRoute          ROUTE_DUMP
:OroTempCorrect          OROCORR_HBV
:OroPrecipCorrect        OROCORR_HBV
:WindspeedMethod         WINDVEL_DATA
:RelativeHumidityMethod RELHUM_DATA
:SWRadiationMethod       SW_RAD_DATA
:PrecipIceptFract        PRECIP_ICEPT_USER
:HydrologicProcesses
:SnowBalance             SNOBAL_HMETS     MULTIPLE          MULTIPLE
:Precipitation           RAVEN_DEFAULT    ATMOS_PRECIP      MULTIPLE
:Infiltration            INF_HMETS        PONDED_WATER      MULTIPLE
:Overflow                OVERFLOW_RAVEN SOIL[0]             CONVOLUTION[1]
:Overflow                OVERFLOW_RAVEN SOIL[1]             CONVOLUTION[1]
:Baseflow                BASE_LINEAR      SOIL[0]    SURFACE_WATER #interflow
:Baseflow                BASE_LINEAR      SOIL[1]    SURFACE_WATER
:Baseflow                BASE_LINEAR      SOIL[2]    SURFACE_WATER
:Percolation             PERC_LINEAR      SOIL[0]    SOIL[1] #recharge
:Percolation             PERC_LINEAR      SOIL[1]    SOIL[2] #recharge
:SoilEvaporation         SOILEVAP_ALL     SOIL[0]        ATMOSPHERE #AET
:CanopyEvaporation       CANEVP_ALL       CANOPY         ATMOSPHERE
:CanopySnowEvap          CANEVP_ALL       CANOPY_SNOW    ATMOSPHERE
:Convolve                CONVOL_GAMMA     CONVOLUTION[0] SURFACE_WATER
#surf. runoff
:Convolve                CONVOL_GAMMA_2 CONVOLUTION[1] SURFACE_WATER
#delay. runoff
:EndHydrologicProcesses
# write metrics to Diagnostics.csv for each set of observations
:EvaluationPeriod WARMUP 1975-01-01 1977-12-31
:EvaluationPeriod CALIBRATION 1978-01-01 1999-12-31
:EvaluationPeriod VALIDATION 2000-01-01 2020-01-01
:EvaluationMetrics NASH_SUTCLIFFE RMSE PCT_BIAS
```

create rvp template - will give you some guidance on building the file
your soil classes etc will need to be built
:WriteMassBalanceFile
#:WriteEnergyStorage
#Outout options
:CustomOutput DAILY AVERAGE SNOW ENTIRE_WATERSHED
:CustomOutput DAILY AVERAGE SNOW BY_HRU
:CustomOutput DAILY AVERAGE SOIL[0] ENTIRE_WATERSHED
:CustomOutput DAILY AVERAGE SOIL[1] ENTIRE_WATERSHED
:CustomOutput DAILY AVERAGE SOIL[2] ENTIRE_WATERSHED
#output options / creates only template file -> turn off when wanting to update
#:CreateRVPTemplate
#:SilentMode #supresses printing of time steps

RVP-FILE:

:SoilClasses
:Attributes ,%SAND,%CLAY,%SILT
:Units , none, none, none
L1 , 60,25,15,
L2 , 75,10,15,
L3 , 92,5,3,
:EndSoilClasses
:SoilProfiles
pbraunerde1, 3, L1,0.6,L2,0.2,L3,0.2
pbraunerde2, 3, L1,0.6,L2,0.2,L3,0.2
pbraunerde3, 3, L1,0.6,L2,0.2,L3,0.2
pbraunerde4, 3, L1,0.6,L2,0.2,L3,0.2
pbraunerde5, 3, L1,0.6,L2,0.2,L3,0.2
:EndSoilProfiles
#--
Global Parameters
#--
:GlobalParameter AVG_ANNUAL_RUNOFF 550
:GlobalParameter RAINSNOW_TEMP 1.898690E-02
:GlobalParameter ADIABATIC_LAPSE 8.171399E-01
:GlobalParameter SNOW_SWI_MIN 4.085386E-02
:GlobalParameter SNOW_SWI_MAX 6.905615E-02
:GlobalParameter SWI_REDUCT_COEFF 7.919832E-02
:GlobalParameter SNOW_SWI 5.738645E-02
:GlobalParameter TOC_MULTIPLIER 5.575134E-01
note: required soil parameters were missing, added block down below.
###
#--
Soil Parameters
#--
:SoilParameterList
:Parameters,POROSITY,PERC_COEFF,PET_CORRECTION,BASEFLOW_COEFF,ALBEDO_WET,ALBEDO_DRY
:Units, -, 1/d, -, 1/d
L1 ,3.284978E-01,1.813445E-02,1.0,3.598535E-03,4.993875E-01,4.995370E-01

L2 ,5.878274E-01,5.955563E-01,1.0,6.815431E-01,1.905242E-01,1.618469E-01
L3 ,7.992383E-01,5.104572E-01,1.0,6.009793E-03,2.763727E-01,3.423951E-01
:EndSoilParameterList
:LandUseClasses
:Attributes ,IMPERMEABLE_FRAC, FOREST_COVERAGE
:Units , frac, frac,
CONIFER, 4.617224E-03, 9.995692E-01
MIX, 2.225273E-03, 9.992464E-01
:EndLandUseClasses
:VegetationClasses
:Attributes , MAX_HT,MAX_LAI,MAX_LEAF_COND
:Units , m, none, mm/s
CONIFER_FOREST, 2.902075E+01, 1.999538E+00, 5.888903E+00
MIXED, 2.989950E+01, 2.039088E+00, 5.641170E+00
:EndVegetationClasses
:LandUseParameterList
:Parameters, MIN_MELT_FACTOR, MAX_MELT_FACTOR,DD_MELT_TEMP,DD_AGGRADATION,REFREEZE_FACTOR, REFREEZE_EXP, DD_REFREEZE_TEMP,HMETS_RUNOFF_COEFF,GAMMA_SHAPE, GAMMA_SCALE, GAMMA_SHAPE2, GAMMA_SCALE2, FOREST_SPARSENESS, ROUGHNESS
:Units, mm/d/C, mm/d/C, C, 1/mmmm/d/C, -, C, -,
CONIFER, 2.478336E+00, 2.614411E+00, 0.000000E+00, 1.000000E-01, 2.753368E-02, 5.000000E-01, 0.000000E+00, 3.221125E-01, 3.945433E+00, 5.290041E+00, 3.628769E+00, 1.452833E+01, 1.009599E-03, 5.963595E+00
MIX, 2.276506E+00, 2.870362E+00, 0.000000E+00, 1.000000E-01, 8.872944E-01, 5.000000E-01, 0.000000E+00, 3.346624E-01, 2.831749E+00, 1.834402E+00, 4.540983E+00, 1.433705E-01, 2.297683E-01, 8.032219E+00
:EndLandUseParameterList
:VegetationParameterList
:Parameters, RAIN_ICEPT_PCT, SNOW_ICEPT_PCT,MAX_CAPACITY,MAX_SNOW_CAPACITY,ALBEDO,SVF_EXTINCTION,SAI_HT_RATIO
:Units, -, -,
CONIFER_FOREST, 1.965624E-01, 1.992003E01 , 6.231972E+00, 1.347514E+02, 8.041413E-01, 0.5, 3.372508E+00
MIXED, 1.996482E-01, 1.769942E-01, 9.499432E+01 , 4.781150E+01, 8.275477E-01, 0.5, 1.529870E-01
:EndVegetationParameterList
:SeasonalRelativeLAI
CONIFER_FOREST, 1.0, 1.0, 1.0, 1.0, 1.0, 1.0, 1.0, 1.0, 1.0, 1.0, 1.0, 1.0
MIXED, 0.6, 0.6, 0.6, 0.7, 1.0, 1.0, 1.0, 1.0, 0.9, 0.7, 0.6, 0.6
:EndSeasonalRelativeLAI
:SeasonalRelativeHeight
CONIFER_FOREST, 1.0, 1.0, 1.0, 1.0, 1.0, 1.0, 1.0, 1.0, 1.0, 1.0, 1.0, 1.0
MIXED, 1.0, 1.0, 1.0, 1.0, 1.0, 1.0, 1.0, 1.0, 1.0, 1.0, 1.0, 1.0
:EndSeasonalRelativeHeight

RVC-FILE:

```
:UniformInitialConditions SOIL[0] 8.499925E+01
:UniformInitialConditions SOIL[1] 2.298376E+02
:UniformInitialConditions SOIL[2] 7.619323E+01
```

RVH-FILE

```
##########################################################################
:FileType rvh ASCII Raven 2.5
:WrittenBy        Leonard Kölsch-Kurtz
:CreationDate     Aug 2021
# Eyach
#-------------------------------------------------------------------
#
:SubBasins
  :Attributes,        NAME,
DOWNSTREAM_ID,PROFILE,REACH_LENGTH,GAUGED
  :Units    ,         none,         none,         none,      km,      none
  10,                 Brotenaubach,     13,          NONE,    _AUTO,       1
  11,                 Duerreychbach,    13,          NONE,    _AUTO,       0
  12,                 Mannenbaechle,    14,          NONE,    _AUTO,       0
  13,                 Obereyach,        14,          NONE,    _AUTO,       0
  14,                 Unteryach,        -1,          NONE,    _AUTO,       1
:EndSubBasins
# note: lat and long needed to be fixed below, should be in range of (-90<lat<90; -
180<lon<180) (not in projected or local coordinates)
:HRUs
  :Attributes,  AREA, ELEVATION, LATITUDE,     LONGITUDE,
BASIN_ID,LAND_USE_CLASS, VEG_CLASS,      SOIL_PROFILE,
AQUIFER_PROFILE, TERRAIN_CLASS, SLOPE, ASPECT
  :Units    ,   km2, m,         deg,          deg,          none,    none,          none,          none,
none,          none,          deg,   deg
1,            15.2,826.2,      48.7344384100,8.4682610228, 10,       CONIFER,
CONIFER_FOREST,braunerde5,          [NONE],          [NONE],          10.01, 178.02
2,            7.2 ,830.6,      48.74954,     8.45278,      11,       CONIFER,
CONIFER_FOREST,braunerde4,          [NONE],          [NONE],          11.9,  109.03
3,            5.5 ,694,        48.78664,     8.49293,      12,       CONIFER,
CONIFER_FOREST,braunerde1,          [NONE],          [NONE],          6.9,   120
4,            9.5 ,682,        48.7708293150,8.5028765311, 13,       CONIFER,
CONIFER_FOREST,braunerde3,          [NONE],          [NONE],          13.8,  185.6
5,            15.4,602.1,      48.7971881790,8.5439151180, 14,       MIX,           MIXED,
braunerde2,         [NONE],          [NONE],          12.3,  190
:EndHRUs
```

RVT-FILE:

```
########################
#METEOROLOGICAL DATA
```

```
########################
:Gauge Eyach
  :Latitude 48.7344384100
  :Longitude 8.4682610228
  :Elevation 555
:RainCorrection 9.001543E-01
:SnowCorrection 9.001305E-01
:RedirectToFile BW6BroNT.rvt
:RedirectToFile BW6BroRELH.rvt
:RedirectToFile BW6BroWIND.rvt
:RedirectToFile BW6BroRAD.rvt
:EndGauge
```

```
########################
#STREAM GAUGES
########################
:RedirectToFile BW6Observed.rvt  #Eyach
:RedirectToFile BW6Observed_2.rvt #Brotenaubach
```

Input Parameters Raven-HMETS:

Table 26. Soil Classes

Layer	%SAND	%CLAY	%SILT
L1	60	25	15
L2	75	10	15
L3	92	5	3

Table 27. Soil Profiles

Profile	Num Layers	Layer 1	Thickness 1	Layer 2	Thickness 2	Layer 3	Thickness 3
braunerde1	3	L1	0.6	L2	0.2	L3	0.2
braunerde2	3	L1	0.6	L2	0.2	L3	0.2
braunerde3	3	L1	0.6	L2	0.2	L3	0.2
braunerde4	3	L1	0.6	L2	0.2	L3	0.2
braunerde5	3	L1	0.6	L2	0.2	L3	0.2

Table 28. Soil Parameters

Parameter	L1	L2	L3
POROSITY	0.328498	0.587827	0.799238
PERC_COEFF (1/d)	0.018134	0.595556	0.510457
PET_CORRECTION	1.0	1.0	1.0
BASEFLOW_COEFF (1/d)	0.003599	0.681543	0.006010
ALBEDO_WET	0.499388	0.190524	0.276373
ALBEDO_DRY	0.499537	0.161847	0.342395

Table 29. Land Use Classes

Land Use	IMPERMEABLE_FRAC	FOREST_COVERAGE
CONIFER	0.004617	0.999569
MIX	0.002225	0.999246

Table 30. Vegetation Classes

Vegetation	MAX_HT (m)	MAX_LAI (m3/m3)	MAX_LEAF_COND (mm/s)
CONIFER_FOREST	29.02075	1.999538	5.888903
MIXED	29.8995	2.039088	5.641170

Table 31. Land Use Parameters

Parameter	CONIFER	MIX
MIN_MELT_FACTOR (mm/d/ ◦C)	2.478336	2.276506
MAX_MELT_FACTOR (mm/d/ ◦C)	2.614411	2.870362
DD_MELT_TEMP (°C)	0.0	0.0
DD_AGGRADATION (1/mm)	0.1	0.1
REFREEZE_FACTOR (mm/d/ ◦C)	0.027534	0.887294

Parameter	CONIFER	MIX
REFREEZE_EXP	0.5	0.5
DD_REFREEZE_TEMP (°C)	0.0	0.0
HMETS_RUNOFF_COEFF	0.322113	0.334662
GAMMA_SHAPE	3.945433	2.831749
GAMMA_SCALE	5.290041	1.834402
GAMMA_SHAPE2	3.628769	4.540983
GAMMA_SCALE2	14.52833	0.143371
FOREST_SPARSENESS	0.001010	0.229768
ROUGHNESS (m)	5.963595	8.032219

Table 32. Vegetation Parameters

Parameter	CONIFER_FOREST	MIXED
RAIN_ICEPT_PCT	0.196562	0.199648
SNOW_ICEPT_PCT	19.92003	0.176994
MAX_CAPACITY (mm)	6.231972	94.99432
MAX_SNOW_CAPACITY (mm)	134.7514	47.8115
ALBEDO	0.8041	0.8275
SVF_EXTINCTION	0.5	0.5
SAI_HT_RATIO (m2/m3)	3.372508	0.152987

Table 33. Uniformal Initial Conditions

Soil Layer	Initial SWI (Soil Water)
SOIL[0]	84.99925
SOIL[1]	229.8376
SOIL[2]	76.19323

Table 34. Correction Factors

Type	Value
RainCorrection	0.9001543
SnowCorrection	0.9001305

OSTRICH-CALIBRATION

OSTIN-FILE:

ProgramType DDS
ObjectiveFunction GCOP
ModelExecutable Ost-RAVEN.bat
PreserveBestModel save_best.bat
#ModelSubdir model
BeginExtraDirs
#model
EndExtraDirs
BeginFilePairs
BW6.rvp.tpl; model/BW6.rvp
BW6.rvt.tpl; model/BW6.rvt
BW6.rvc.tpl; model/BW6.rvc
EndFilePairs
#Parameter/DV Specification
BeginParams
#name init.
%par1% random 0.3 0.8 none none none #Porosity
%par2% random 0 1 none none none #Perccoeff
%par4% random 0 1 none none none #Baseflowcoeff
%par5% random 0.3 0.8 none none none #Porosity
%par6% random 0 1 none none none #Perccoeff
%par8% random 0 1 none none none #Baseflowcoeff
%par9% random 0.3 0.8 none none none #Porosity
%par10% random 0 1 none none none #Perccoeff
%par12% random 0 1 none none none #Baseflowcoeff
%par17% random 29 31 none none none #max_tree
%par18% random 1 4 none none none #LAI
%par19% random 1 6 none none none #leaf_cond
%par20% random 29 31 none none none #max_tree_mixed
%par21% random 3 6 none none none #LAI_mixed
%par22% random 1 6 none none none #leaf_cond_mixed
%par23% random 2 2.5 none none none #min_melt
%par24% random 2.5 3.5 none none none #max_melt
%par25% random 0 0 none none none #DD_melt_temp_CONIFER
%par26% random 0.1 0.1 none none none #DD_AGGRADATION_CONIFER
%par27% random 0 3 none none none #refreeze_CONIFER_CONIFER
%par28% random 0.5 0.5 none none none #REFREEZE_EXP_CONIFER
%par29% random 0 0 none none none #ddrefreeze_CONIFER
%par30% random 0.3 0.99 none none none #HMETS_RUNOFF_COEFF
%par31% random 0.5 5 none none none #GAMMA_SHAPE

%par32% random 0 20 none none none #GAMMA_SCALE
%par33% random 0.5 5 none none none #GAMMA_SHAPE2
%par34% random 0 20 none none none #GAMMA_SCALE2
%par35% random 0.02 0.2 none none none #rain_icpt_conifer
%par36% random 0.02 0.2 none none none #snow_icpt_conifer
%par37% random 0.02 0.2 none none none #rain_icpt_mixed
%par38% random 0.02 0.2 none none none #snow_icpt_mixed
%par39% random 0 1 none none none #Rainsnow_temp
%par40% random 0 1 none none none #Adiabatic_lapse
%par41% random 0.04 0.05 none none none #SNOW_SWI_MIN
%par42% random 0.05 0.15 none none none #SNOW_SWI_MAX
%par43% random 0 0.1 none none none #SWI_REDUCT_COEFF
%par44% random 0.04 0.07 none none none #SNOW_SWI
%par48% random 1 200 none none none #maxcapacity_forest
%par49% random 1 200 none none none #maxcapacity_forest_snow
%par50% random 1 200 none none none #maxcapacity_forest_mixed
%par51% random 1 200 none none none #maxcapacity_forest_snow_mixed
%par52% random 0 0.5 none none none #albedo_wet
%par53% random 0 0.5 none none none #albedo_dry
%par54% random 0 0.5 none none none #albedo_wet
%par55% random 0 0.5 none none none #albedo_dry
%par56% random 0 0.5 none none none #albedo_wet
%par57% random 0 0.5 none none none #albedo_dry
%par60% random 0.8 1.5 none none none #Albedo_coni
%par61% random 0.8 1.5 none none none #Albedo_mixed
%par62% random 1.5 2.0 none none none #min_melt
%par63% random 2.5 3.5 none none none #max_melt
%par65% random 0.1 0.1 none none none #DD_AGGRADATION_MIX
%par66% random 0 3 none none none #refreeze_MIX
%par67% random 0.5 0.5 none none none #REFREEZE_EXP_MIX
%par68% random 0 0 none none none #ddrefreeze_MIX
%par69% random 0.3 0.99 none none none #HMETS_RUNOFF_COEFF
%par70% random 0.5 5 none none none #GAMMA_SHAPE
%par71% random 0 20 none none none #GAMMA_SCALE
%par72% random 0.5 5 none none none #GAMMA_SHAPE2
%par73% random 0 20 none none none #GAMMA_SCALE2
%par74% random 0 10 none none none #SAI
%par75% random 0 10 none none none #SAI
%par76% random 0 2 none none none #TOC
%par77% random 0.9 1.1 none none none #RC
%par78% random 0.9 1.1 none none none #SC
%par79% random 0.5 1.0 none none none #CoverageCONIFER
%par80% random 0.5 1.0 none none none #CoverageMIX
%par81% random 0 300 none none none #InitialSOIL0
%par82% random 0 300 none none none #InitialSOIL1
%par83% random 0 300 none none none #InitialSOIL2
%par84% random 0.0 1.0 none none none #impermfractionconifer
%par85% random 0.0 1.0 none none none #impermfractionmix
%par86% random 0.0 0.99 none none none #forestsparsenessconifer
%par87% random 0.0 0.99 none none none #forestsparsenessmix
%par88% random 0.0 10.0 none none none #rougnessconifer

```
%par89% random 0.0 10.0 none none none #rougnessmix
EndParams
BeginResponseVars
 #name          filename                                        keyword          line     col
        token
 DIAG_NASH_SUTCLIFFE      ./model/out/Raven_HMETS_Diagnostics.csv ;OST_NULL
        3       3       ','
 DIAG_NASH_SUTCLIFFE_2  ./model/out/Raven_HMETS_Diagnostics.csv ;OST_NULL
        4       3       ','
EndResponseVars
BeginTiedRespVars
 NegNS 1 DIAG_NASH_SUTCLIFFE wsum -1.0
 NegNS2 1 DIAG_NASH_SUTCLIFFE_2 wsum -1.0
 SumNS 2 NegNS NegNS2 wsum 1.0 1.0
EndTiedRespVars
BeginGCOP
 CostFunction SumNS
 PenaltyFunction APM
EndGCOP
BeginConstraints
        # not needed when no constraints, but PenaltyFunction statement above is required
        # name    type    penalty   lwr   upr   resp.var
EndConstraints
# Randomsed control added
RandomSeed 20041992
#Algorithm should be last in this file:
BeginDDSAlg
        PerturbationValue 0.2
        MaxIterations 5000
        UseRandomParamValues
      # UseInitialParamValues
        # Note: above intializes DDS to parameter values IN the initial
        #       model input files IF 'extract' option used in BeginParams
        #       block (column 'init')
EndDDSAlg
```

RVP - Template File for Calibration

```
:SoilClasses
:Attributes ,%SAND,%CLAY,%SILT
:Units , none, none, none
L1     , 70,15,15,
L2     , 65,20,15,
L3     , 60,20,20,
:EndSoilClasses
:SoilProfiles
pbraunerde1, 3,      L1,0.1,L2,0.4,L3,0.5
pbraunerde2, 3,      L1,0.1,L2,0.4,L3,0.5
pbraunerde3, 3,      L1,0.1,L2,0.4,L3,0.5
pbraunerde4, 3,      L1,0.1,L2,0.4,L3,0.5
pbraunerde5, 3,      L1,0.1,L2,0.4,L3,0.5
```

:EndSoilProfiles
#--
Global Parameters
#--
:GlobalParameter AVG_ANNUAL_RUNOFF 250
:GlobalParameter RAINSNOW_TEMP %par39%
:GlobalParameter ADIABATIC_LAPSE %par40%
:GlobalParameter SNOW_SWI_MIN %par41%
:GlobalParameter SNOW_SWI_MAX %par42%
:GlobalParameter SWI_REDUCT_COEFF %par43%
:GlobalParameter SNOW_SWI %par44%
:GlobalParameter TOC_MULTIPLIER %par76%

note: required soil parameters were missing, added block down below.
###
#--
Soil Parameters
#--
:SoilParameterList
:Parameters, POROSITY, PERC_COEFF, PET_CORRECTION, BASEFLOW_COEFF,ALBEDO_WET,ALBEDO_DRY
:Units, -, 1/d, -, 1/d
L1 ,%par1%,%par2%,1.0,%par4%,%par52%,%par53%
L2 ,%par5%,%par6%,1.0,%par8%,%par54%,%par55%
L3 ,%par9%,%par10%,1.0,%par12%,%par56%,%par57%
:EndSoilParameterList
:LandUseClasses
:Attributes ,IMPERMEABLE_FRAC, FOREST_COVERAGE
:Units , frac, frac,
CONIFER, %par84%, 0.9
MIX, %par85%, 0.9
:EndLandUseClasses
:VegetationClasses
:Attributes , MAX_HT,MAX_LAI,MAX_LEAF_COND
:Units , m, none, mm/s
CONIFER_FOREST, %par17%, %par18%, %par19%
MIXED, %par20%, %par21%, %par22%
:EndVegetationClasses
:LandUseParameterList
:Parameters, MIN_MELT_FACTOR, MAX_MELT_FACTOR, DD_MELT_TEMP, DD_AGGRADATION, REFREEZE_FACTOR, REFREEZE_EXP, DD_REFREEZE_TEMP, HMETS_RUNOFF_COEFF,GAMMA_SHAPE, GAMMA_SCALE, GAMMA_SHAPE2, GAMMA_SCALE2, FOREST_SPARSENESS, ROUGHNESS
:Units, mm/d/C, mm/d/C, C, 1/mm, mm/d/C, -, C, -,
CONIFER, %par23%, %par24%, %par25%, %par26%, %par27%, %par28%, %par29%, %par30%, %par31%, %par32%, %par33%, %par34%, %par86%, %par88%

MIX, %par62%, %par63%, %par64%, %par65%, %par66%, %par67%, %par68%, %par69%, %par70%, %par71%, %par72%, %par73%, %par87%, %par89%

:EndLandUseParameterList

:VegetationParameterList

:Parameters, RAIN_ICEPT_PCT, SNOW_ICEPT_PCT,MAX_CAPACITY,MAX_SNOW_CAPACITY,ALBEDO,SVF_EXTINCTION,SAI_HT_RATIO

:Units, -, -,

CONIFER_FOREST, %par35% , %par36%, %par48%, %par49%, %par60%, 0.5, %par74%

MIXED, %par37%, %par38%, %par50%, %par51%, %par61%, 0.5, %par75%

:EndVegetationParameterList

:SeasonalRelativeLAI

CONIFER_FOREST, 1.0, 1.0, 1.0, 1.0, 1.0, 1.0, 1.0, 1.0, 1.0, 1.0, 1.0, 1.0

MIXED, 0.6, 0.6, 0.6, 0.7, 1.0, 1.0, 1.0, 1.0, 0.9, 0.7, 0.6, 0.6

:EndSeasonalRelativeLAI

:SeasonalRelativeHeight

CONIFER_FOREST, 1.0, 1.0, 1.0, 1.0, 1.0, 1.0, 1.0, 1.0, 1.0, 1.0, 1.0, 1.0

MIXED, 1.0, 1.0, 1.0, 1.0, 1.0, 1.0, 1.0, 1.0, 1.0, 1.0, 1.0, 1.0

:EndSeasonalRelativeHeight

RVC - Template File for Calibration

:UniformInitialConditions SOIL[0] %par81%
:UniformInitialConditions SOIL[1] %par82%
:UniformInitialConditions SOIL[2] %par83%

RVT - Template File for Calibration

```
#########################
#METEOROLOGICAL DATA
#########################
:Gauge Brotenaubach
  :Latitude 48.7344384100
  :Longitude 8.4682610228
  :Elevation 555
:RainCorrection  %par77%
:SnowCorrection %par78%
:RedirectToFile BW6BroNT.rvt
:RedirectToFile BW6BroRELH.rvt
:RedirectToFile BW6BroWIND.rvt
:RedirectToFile BW6BroRAD.rvt
:EndGauge



#########################
#STREAM GAUGES
#########################
:RedirectToFile BW6Observed.rvt
:RedirectToFile BW6Observed_2.rvt
```

Appendix B – LWF-B90

Table 35. General Site Parameters for LWF-Brook90 – Weis et al. (2023)

Parameter	Description	Unit	Value
ASPECT	Aspect (from North through East)	degree	
DSLOPE	Slope angle for calculating lateral subsurface flow	degree	
ESLOPE	Slope angle for calculating evapotranspiration and snowmelt	degree	
LENGTH	Slope length for calculating lateral subsurface flow	m	100
NLAYER	Number of soil layers to be simulated	–	
NMAT	Number of soil material types (physically defined substrates/horizons)	–	

Table 36. General Parameters for LWF-Brook90 – Weis et al. (2023)

Parameter	Description	Unit	Value
BYPAR	Macropore flow allowed (1) or not (0)	–	0
C1	Intercept (radiation vs. sunshine duration)	–	0.25
C2	Slope (radiation vs. sunshine duration)	–	0.5
C3	Cloud correction	–	0.2
CCFAC	Energy needed to warm snowpack to 0°C	MJ m^2 d^{-1} K^{-1}	0.3
CS	Ratio of stem area index to stand height	m	0.035
CZR	Roughness/height ratio (rough closed canopy)	–	0.05
CZS	Roughness/height ratio (smooth closed canopy)	–	0.13
DPSIMX	Max vertical potential difference	kPa	0.01
DRAIN	Fraction of matrix flow from lowest soil layer to groundwater	–	1
DSWMAX	Max soil moisture change rate	%	0.5
DTIMAX	Max iteration time step	d^{-1}	0.5
FETCH	Wind fetch length at weather station	m	5000
FXYLEM	Xylem conductivity	mm d^{-1} MPa^{-1}	0.5
GRDMLT	Snow melt rate at soil-snow interface	mm d^{-1}	0.35
GSC	Groundwater outflow rate	–	0
GSP	Groundwater discharge to seepage (vs. stream)	–	0
HR	Height above which CZR applies	m	10
HS	Height below which CZS applies	m	1
ILAYER	Infiltration distribution layers if INFEXP > 0	–	1
IMODEL	pF/ku model: 0=Clapp/Hornberger, 1=Mualem/van Genuchten	–	1
IMPERV	Impermeable surface fraction	–	0
INFEXP	Infiltration exponent	–	0
INTR	Initial rain interception	mm	0

Parameter	Description	Unit	Value
INTS	Initial snow interception	mm	0
KSNVP	Correction factor for snow evaporation	–	0.3
LAIMLT	Snow melt dependence on LAI	–	0.2
LPC	Minimum LAI for closed canopy	$m^2\ m^{-2}$	4
MAXLQF	Max liquid water fraction in snow	$mm\ d^{-1}$	0.05
MELFAC	Degree-day melt factor (open land)	$MJ\ m^{-2}\ d^{-1}\ K^{-1}$	1.5
NN	Extinction coefficient (wind/eddy diffusivity)	–	2.5
NOOUTF	Root-to-soil outflow allowed (0=yes, 1=no)	–	1
QFFC	Quickflow fraction at field capacity	–	0
QFPAR	Water content fraction for full quickflow	–	1
QLAYER	Layers for wetness calculation in source area	–	0
RM	Max shortwave radiation on leaf	$W\ m^{-2}$	1000
RSSA	Soil evaporation resistance at field capacity	$s\ m^{-1}$	100
RSSB	Exponent for soil evap resistance vs. potential	–	1
RSTEMP	Snow-rain transition base temperature	°C	-0.5
SAIMLT	Snow melt dependence on SAI	–	0.5
SNODEN	Snow density	$mm\ mm^{-1}$	0.3
WNDRAT	Night/day wind speed ratio	–	0.3
Z0G	Surface roughness height	m	0.02
Z0S	Snow surface roughness length	m	0.001
Z0W	Weather station roughness	m	0.005
ZMINH	Reference height above canopy	m	2
ZW	Wind measurement height	m	10
inirlen	Initial root length per soil surface	$m\ m^{-2}$	10
inirdep	Initial rooting depth	m	0.25
rgrorate	Vertical root growth rate	$m\ a^{-1}$	0.033
rgroper	Period of net root growth	a	0

Table 37. Species-Specific Parameters for LWF-Brook90 - Weis et al. (2023)

Parameter	Description	Unit	Beech	Oak	Spruce	Pine	Douglas-fir
ALB	Albedo without snow	–	0.21	0.21	0.13	0.13	0.13
ALBSN	Albedo with snow on ground	–	0.47	0.47	0.34	0.34	0.34
CINTRL	Interception capacity (rain) per LAI unit	mm	0.6	0.7	0.4	1.0	0.4
CINTRS	Interception capacity (rain) per SAI unit	mm	0.5	1.0	0.2	1.0	0.2
CINTSL	Interception capacity (snow) per LAI unit	mm	2.4	2.8	1.6	4.0	1.6
CINTSS	Interception capacity (snow) per SAI unit	mm	2.0	4.0	0.8	4.0	0.8

Parameter	Description	Unit	Beech	Oak	Spruce	Pine	Douglas-fir
CR	Light extinction coefficient in canopy	–	0.59	0.59	0.45	0.45	0.45
CVPD	Vapour pressure deficit for half stomatal conductance	kPa	2	2	2	2	2
FRINTL	Rain interception fraction per LAI unit	–	0.08	0.10	0.08	0.13	0.12
FRINTS	Rain interception fraction per SAI unit	–	0.08	0.10	0.08	0.13	0.20
FSINTL	Snow interception fraction per LAI unit	–	0.08	0.10	0.08	0.13	0.08
FSINTS	Snow interception fraction per SAI unit	–	0.40	0.50	0.10	0.30	0.10
GLMAX	Max leaf conductance (open stomata) per proj. leaf area	$m\ s^{-1}$	0.006	0.007	0.0035	0.0045	0.0025
GLMIN	Leaf conductance (closed stomata) per LAI	$m\ s^{-1}$	0.0002	0.0003	0.0001	0.0002	0.0001
LAI	Max leaf area index	$m^2\ m^{-2}$	6	4.5	7	3.5	6
LAIWinter	Leaf area index in dormant season	$m^2\ m^{-2}$	0	0	5.6	1.75	4.8
LWIDTH	Leaf width	m	0.04	0.05	0.001	0.001	0.001
MXKPL	Max tree water conductivity	$mm\ d^{-1}\ MPa^{-1}$	8	8	8	8	8
MXRTLN	Max fine root length per area	$m\ m^{-2}$	3200	3200	3000	3000	3000
PSICR	Critical leaf water potential	MPa	–2	–2.5	–2	–2.5	–2.5
R5	Radiation threshold for half stomatal conductance	$W\ m^{-2}$	100	100	100	100	100
RHOTP	Ratio total/projected leaf area	–	2	2	2.6	2.6	2.6
RTRAD	Avg. fine root radius	mm	0.25	0.25	0.25	0.25	0.25
SAI	Stem/branch surface area index (leafless)	$m^2\ m^{-2}$	1	0.9	2	0.8	0.8
SLA	Specific leaf area	$m^2\ kg^{-1}$	20	15	3.5	4	5
T1	Min temp. for stomatal opening	°C	10	10	10	10	10
T2	Max temp. for stomatal opening	°C	30	30	30	30	30
TH	Max temp. for closed stomata	°C	40	40	40	40	40
TL	Min temp. for closed stomata	°C	0	0	0	0	0
tbcd	Cold-day threshold (Menzel, 1997)	°C	9	9	9	9	9
tbtt	Heat trigger threshold (Menzel, 1997)	°C	6	4	4	5	4
a	Model constant (Menzel, 1997)	–	1921.8	1747.9	1848.1	1394.5	1848.1

Parameter	Description	Unit	Beech	Oak	Spruce	Pine	Douglas-fir
b	Model constant (Menzel, 1997)	–	–348.1	–298.4	–317.0	–222.7	–316.97
durld	Duration of leaf unfolding	d	28	28	28	28	28
doylf	Last DOY for leaf coloring (Wilpert, 1990)	DOY	279	279	279	279	279
tblf	Temp. threshold for leaf coloring (Wilpert, 1990)	°C	10	10	10	10	10
durlf	Duration of leaf fall	d	56	56	56	56	56
height	Stand height	m	34	26	36	30	40
age	Stand age	years	100	100	100	100	100
rootdepth	Max rooting depth	cm	160	200	120	200	160
beta	Beta (fine root distribution, Gale & Grigal, 1987)	–	0.966	0.966	0.976	0.976	0.976
humus	Min organic layer thickness	cm	3.0	4.0	5.0	6.0	4.0

Table 38. General Site and Model Parameters for LWF-Brook90 used in this Study – R Version

Parameter	Description	Unit	Value
c1	Intercept for solar radiation vs. sunshine duration	-	0.25
c2	Slope for solar radiation vs. sunshine duration	-	0.5
c3	Cloud correction factor	-	0.2
ccfac	Energy to warm snowpack to 0°C	MJ m^{-2} d^{-1} K^{-1}	0.3
cs	Ratio of stem area index to stand height	m	0.035
czr	Roughness/height ratio (rough closed canopies)	-	0.05
czs	Roughness/height ratio (smooth closed canopies)	-	0.13
dpsimax	Max vertical potential difference	kPa	0.01
drain	Drainage fraction to groundwater	-	1
fetch	Wind fetch length for weather station	m	5000
fxylem	Tree xylem conductivity	mm d^{-1} MPa^{-1}	0.5
grdmlt	Melt rate at snow-soil interface	mm d^{-1}	0.35
gsc	Groundwater outflow fraction	-	0
gsp	Groundwater seepage to deep storage	-	0
hr	Upper reference height for CZR	m	10
hs	Lower reference height for CZS	m	1
imperv	Impervious area fraction	-	0
infexp	Infiltration exponent	-	1
ilayer	Layers for infiltration distribution	-	3
intrainini	Initial rain interception	mm	0
intsnowini	Initial snow interception	mm	0
ksnvp	Snow evaporation correction factor	-	0.3
laimlt	LAI-dependent melt correction	-	0.2

Parameter	Description	Unit	Value
lpc	LAI at canopy closure	$m^2\ m^{-2}$	1.5
maxlqf	Liquid water flux in snow	$mm\ d^{-1}$	0.05
nn	Eddy diffusivity extinction coefficient	-	2.5
nooutf	Allow water flow from roots to soil (0 = yes, 1 = no)	-	1
qffc	Quick flow fraction at field capacity	-	0
qfpar	Quick flow threshold between FC and saturation	-	1
qlayer	Layers for “wetness” source area calc.	-	3
rm	Max incoming solar radiation on leaf	$W\ m^{-2}$	1000
rssa	Soil evaporation resistance at field capacity	$s\ m^{-1}$	100
rssb	Soil evaporation resistance exponent	-	1
saimlt	SAI-dependent melt correction	-	0.5
snoden	Snow density (SWE/depth ratio)	$mm\ mm^{-1}$	0.3
wndrat	Night/day wind speed ratio	-	0.3
z0s	Surface roughness of snow	m	0.001
z0w	Roughness at weather station	m	0.005
zw	Wind measurement height	m	10
initrlen	Initial root length density	$m\ m^{-2}$	10
initrdep	Initial root depth	m	0.25
rgroper	Net root growth period	years	0
rgrorate	Vertical root growth rate	$m\ yr^{-1}$	0
bypar	Bypass flow allowed (1=yes, 0=no)	-	0
zminh	Reference height for climate variables over canopy	m	2
slopelen	Slope length (custom param used)	m	200

Table 39. Species-Specific Parameters for LWF-Brook90 used in this Study - R Version

Parameter	Description	Unit	Spruce	Beech	Oak
budburst_species	Phenological species type	-	Picea abies (spaet)	Fagus sylvatica	Quercus robur
aspect	Slope aspect (0° = North)	degrees	185.6	185.6	185.6
dslope	Slope angle	degrees	13.8	13.8	13.8
length	Hillslope length	m	100	100	100
alb	Albedo without snow	-	0.13	0.21	0.21
albsn	Albedo with snow	-	0.34	0.47	0.47
cintsl	Snow interception capacity per LAI	mm	1.6	2.4	2.8
cintss	Snow interception capacity per SAI	mm	0.8	2.0	4.0
cintrl	Rain interception capacity per LAI	mm	0.4	0.6	0.7
cintrs	Rain interception capacity per SAI	mm	0.2	0.5	0.1

Parameter	Description	Unit	Spruce	Beech	Oak
cvpd	VPD at half max stomatal conductance	kPa	2	2	2
frintlai	Rain interception fraction per LAI	-	0.08	0.06	0.06
frintsai	Rain interception fraction per SAI	-	0.08	0.06	0.06
fsintlai	Snow interception fraction per LAI	-	0.08	0.04	0.04
fsintsai	Snow interception fraction per SAI	-	0.10	0.40	0.50
glmax	Max leaf conductance	m/s	0.0035	0.006	0.007
glmin	Min leaf conductance	m/s	0.0001	0.0002	0.0003
maxlai	Maximum leaf area index	m^2/m^2	3.0	6.0	4.5
lwidth	Leaf width	m	0.001	0.04	0.05
mxkpl	Max tree hydraulic conductivity	$mm\ d^{-1}\ MPa^{-1}$	8	8	8
maxrlen	Max root length per ground area	$m\ m^{-2}$	3000	3200	3200
psicr	Critical leaf water potential	MPa	-2.0	-2.5	-2.0
r5	Solar rad. threshold for half max conductance	W/m^2	100	100	100
rhotp	Total/projected leaf area ratio	-	2.6	2.0	2.0
sai	Stem area index	m^2/m^2	2.0	1.0	0.9
t1	Lower temp. threshold for stomatal opening	°C	10	10	10
t2	Upper temp. threshold for stomatal opening	°C	30	30	30
th	Temp. above which stomata fully closed	°C	40	40	40
tl	Temp. below which stomata fully closed	°C	0	0	0
betaroot	Root distribution parameter	-	0.976	0.966	0.966
winlaifrac	Winter LAI fraction	-	0.8	0.0	0.0
maxrootdepth	Max rooting depth	m	1.0	1.0	1.0

Table 40. Output Parameter LWF-B90 Model – R-Version

Parameter	Description	Unit
yr	Year	-
mo	Month	-
da	Day of month	-
doy	Day of year	-
aa	Average available energy above canopy	W/m^2

Parameter	Description	Unit
adef	Available water deficit in root zone	mm
asubs	Average available energy below canopy	W/m²
awat	Total available soil water in layers with roots between -6.18 kPa and psicr	mm
balerr	Error in water balance (daily value, output at the day's last precipitation interval)	mm
byfl	Total bypass flow	mm/d
dsfl	Downslope flow	mm/d
evap	Evapotranspiration	mm/d
flow	Total streamflow	mm/d
gwat	Groundwater storage below soil layers	mm
gwfl	Groundwater flow	mm/d
intr	Intercepted rain	mm
ints	Intercepted snow	mm
irvp	Evaporation of intercepted rain	mm/d
isvp	Evaporation of intercepted snow	mm/d
lngnet	Net longwave radiation	W/m²
nits	Total number of iterations	-
pint	Potential interception for a canopy always wet	mm/d
pslvp	Potential soil evaporation	mm/d
ptran	Potential transpiration	mm/d
relawat	Relative available soil water in layers with roots	-
rfal	Rainfall	mm/d
rint	Rain interception catch rate	mm/d
rnet	Rainfall to soil surface	mm/d
rsno	Rain on snow	mm/d
rthr	Rain throughfall rate	mm/d
sthr	Snow throughfall rate	mm/d
safrac	Source area fraction	-
seep	Seepage loss	mm/d
sfal	Snowfall	mm/d
sint	Snow interception catch rate	mm/d
slfl	Input to soil surface	mm/d
slvp	Evaporation rate from soil	mm/d
slrad	Average solar radiation on slope over daytime	W/m²
solnet	Net solar radiation on slope over daytime	W/m²
smlt	Snowmelt	mm/d
snow	Snowpack water equivalent	mm
snvp	Evaporation from snowpack	mm/d
srfl	Source area flow	mm/d
stres	Tran / ptran (daily value, output at the day's last precipitation interval)	-
swat	Total soil water in all layers	mm

Parameter	Description	Unit
tran	Transpiration	mm/d
vrfln	Vertical matrix drainage from lowest layer	mm/d

Appendix C – HBV-Light

GAP Calibration HBV-Light

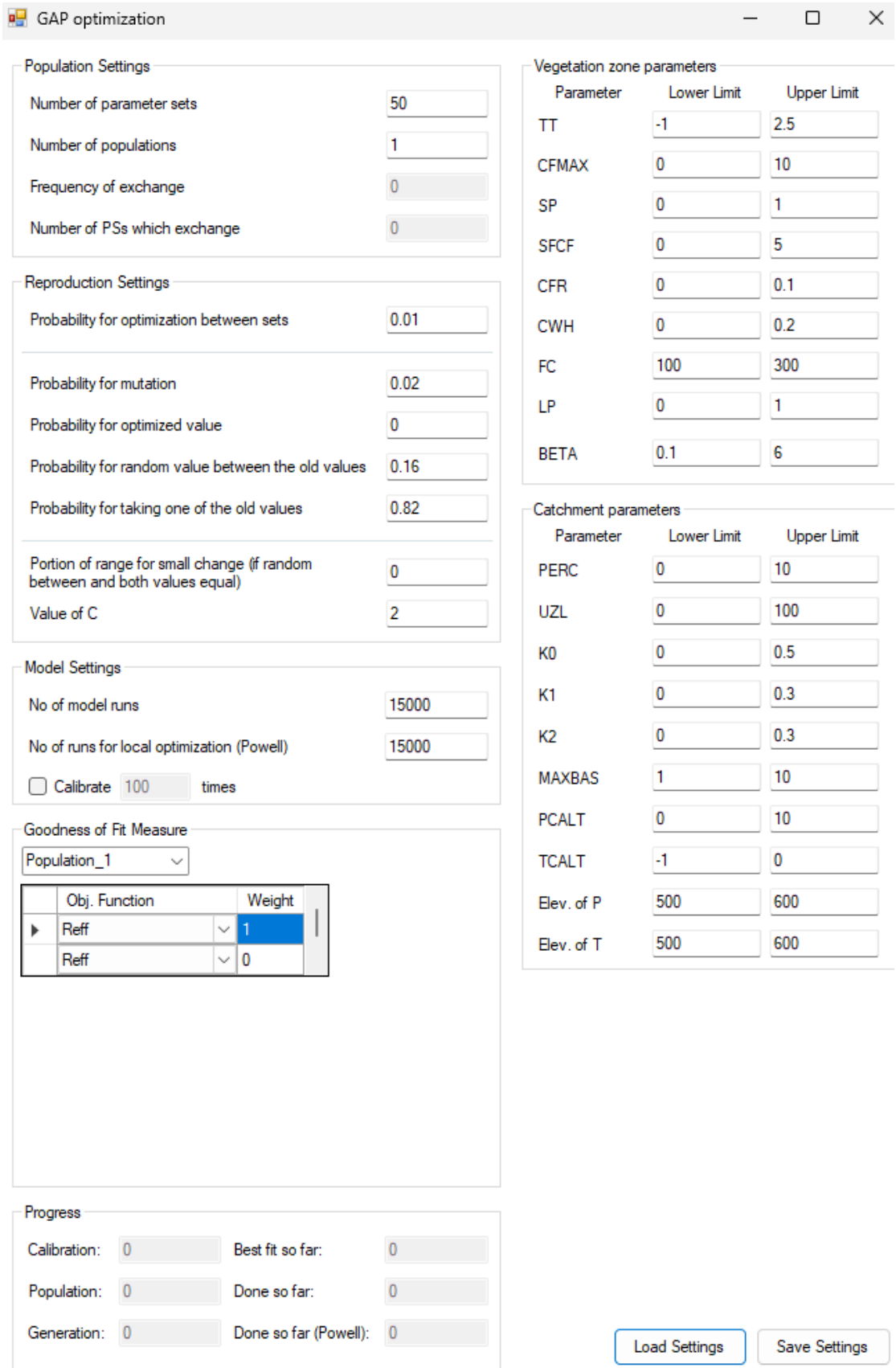

Figure 61. GAP Setup HBV-Light. General Setup parameters and specific Input parameter ranges.

Appendix D – TRAIN – Land-use classification

Table 41. TRAIN Land-Use Classification Scheme (All Applied Codes)

TRAIN Code	Class Name	Particular Feature
1	Sealed surfaces	No plant cover
2	Double cropping	Two harvests a year; applies only in GLOWA JR
3	Open water bodies (lakes, rivers)	Currently like class 95 (redundant)
5	Dichte Besiedlung (populous / highly urban)	Subdivided into (1), (60), (90); applies only in Germany
6	Lockere und mittlere Bebauung (urban)	Subdivided into (1), (60), (90); applies only in Germany
7	Industrie- und Gewerbeflächen (industrialised)	Subdivided into (1), (60); applies only in Germany
10	Verkehrsflächen (circulation areas)	Subdivided into (1), (60); applies only in Germany
11	Single cropping	One harvest a year; applies only in GLOWA JR
12	Cropland (Winterweizen)	Winter wheat; applies only in Germany
15	Abbauflächen und Deponien (landfill, deteriorated)	
19	Grazing land	Similar to shrublands (33), smaller LAI; applies only in GLOWA JR
20	Sonstige Grünflächen (green spaces)	Subdivided into (60), (90); applies only in Germany
30	Ackerland (undifferentiated arable land)	Applies only in Germany
32	Cropland/natural vegetation mosaic	Subdivided into (11), (33); applies only in GLOWA JR
33	Shrublands	Applies only in GLOWA JR
40	Obst- und Gartenbau (fruits and orchards)	Treated together with Weinbau (50); applies only in Germany
44	Grassland	Applies only in GLOWA JR
50	Weinbau (wine-growing)	Treated together with orchards (40); applies only in Germany
60	Wiesen, Weiden, Grünland (pastureland, grassland)	Applies only in Germany
66	Barren	Sparsely vegetated; applies only in GLOWA JR
70	Laubwald (deciduous forest)	Applies only in Germany
77	Urban and built-up area	Subdivided into (1), (33); applies only in GLOWA JR
80	Nadelwald (coniferous forest)	Applies only in Germany

TRAIN Code	Class Name	Particular Feature
90	Mischwald (mixed forest)	Applies only in Germany
95	Gewässer (open water bodies)	Currently like class 3 (redundant)
99	Wetlands	Reclassified to class 3; applies only in GLOWA JR
115	Vegetables	Applies only in GLOWA JR
116	Fruits	Parameterized as citrus; applies only in GLOWA JR
117	Cereals	Reclassified to single cropping (11); applies only in GLOWA JR
118	Other crops	Reclassified to single cropping (11); applies only in GLOWA JR
125	Unsustainable grazing	Smaller LAI than (19); applies only in GLOWA JR

Appendix E – Seasonal ETA & SM Trends by RCP Scenario

Table 42. Seasonal Sen's Slope and p-values for ETA Trends by Scenario and Model

Scenario	Model	Season	Sen's Slope (mm/year)	p-value
RCP2.6	LWF-B90	Autumn	-0.570	0.277
RCP2.6	LWF-B90	Spring	0.783	0.277
RCP2.6	LWF-B90	Summer	-0.027	0.973
RCP2.6	LWF-B90	Winter	-0.218	0.734
RCP2.6	TRAIN	Autumn	-0.190	0.475
RCP2.6	TRAIN	Spring	0.079	0.812
RCP2.6	TRAIN	Summer	0.602	0.277
RCP2.6	TRAIN	Winter	-0.058	0.760
RCP4.5	LWF-B90	Autumn	0.572	0.359
RCP4.5	LWF-B90	Spring	0.009	1.000
RCP4.5	LWF-B90	Summer	0.320	0.659
RCP4.5	**LWF-B90**	**Winter**	**1.134**	**0.007***
RCP4.5	TRAIN	Autumn	-0.193	0.518
RCP4.5	TRAIN	Spring	0.516	0.221
RCP4.5	TRAIN	Summer	0.643	0.234
RCP4.5	**TRAIN**	**Winter**	**0.536**	**0.035***
RCP8.5	LWF-B90	Autumn	-0.264	0.415
RCP8.5	LWF-B90	Spring	0.524	0.434
RCP8.5	LWF-B90	Summer	-1.005	0.185
RCP8.5	**LWF-B90**	**Winter**	**0.929**	**0.012***
RCP8.5	TRAIN	Autumn	0.322	0.096
RCP8.5	TRAIN	Spring	0.387	0.587
RCP8.5	TRAIN	Summer	-0.362	0.587
RCP8.5	TRAIN	Winter	0.452	0.118

Table 43. Seasonal Sen's Slope and p-values for SM Trends by Scenario and Model

Scenario	Model	Season	Sen's Slope (mm/year)	p-value
RCP2.6	LWF-B90	Autumn	-0.316	0.262
RCP2.6	LWF-B90	Spring	0.157	0.518
RCP2.6	LWF-B90	Summer	-0.061	0.708
RCP2.6	LWF-B90	Winter	-0.271	0.185
RCP2.6	TRAIN	Autumn	-0.350	0.110
RCP2.6	TRAIN	Spring	-0.019	0.734
RCP2.6	TRAIN	Summer	-0.304	0.415
RCP2.6	TRAIN	Winter	0.016	0.865

Scenario	Model	Season	Sen's Slope (mm/year)	p-value
RCP4.5	LWF-B90	Autumn	0.280	0.262
RCP4.5	LWF-B90	Spring	-0.151	0.541
RCP4.5	LWF-B90	Summer	-0.053	0.786
RCP4.5	LWF-B90	Winter	0.134	0.415
RCP4.5	TRAIN	Autumn	0.046	0.946
RCP4.5	TRAIN	Spring	-0.071	0.659
RCP4.5	TRAIN	Summer	-0.283	0.518
RCP4.5	TRAIN	Winter	0.099	0.153
RCP8.5	LWF-B90	Autumn	-0.246	0.083
RCP8.5	LWF-B90	Spring	-0.092	0.541
RCP8.5	**LWF-B90**	**Summer**	**-0.257**	**0.049 ***
RCP8.5	LWF-B90	Winter	-0.133	0.185
RCP8.5	TRAIN	Autumn	-0.025	0.919
RCP8.5	TRAIN	Spring	-0.206	0.359
RCP8.5	TRAIN	Summer	-0.278	0.683
RCP8.5	TRAIN	Winter	0.083	0.324

Appendix F – Model Key Features

Table 44. Key Features and Process Representations in TRAIN, HBV-Light, LWF-Brook90, and Raven-HMETS

Model Feature	TRAIN	HBV-Light	LWF-Brook90	Raven-HMETS
Model Type	SVAT model	Lumped/ Semi-distributed	Lumped (1D vertical)	Semi-distributed
Spatial Representation	Gridded (50×50 m resolution)	Single-point/Sub-catchment	Single-point (site-scale)	HRU-based (semi-distributed)
Temporal Resolution	Daily	Daily	Daily	Daily
Soil Layers	1 soil layer	1 soil box, 2–3 groundwater boxes	Up to 25 soil layers with matrix and macropore flow	modifiable
Snow Modeling	Degree-day method	Degree-day method	Degree-day method	Degree-day method with refreezing algorithm
Evapotranspiration (ETA)	Penman-Monteith with dynamic LAI and canopy resistance	PET corrected by temp & soil moisture; linear reduction	Shuttleworth–Wallace model with species-specific transpiration and canopy resistance	Penman-Monteith
Vegetation Representation	Dynamic LAI, albedo, height from phenological model	Monthly crop coefficient per zone	Species-specific phenology, rooting depth, LAI, stomatal resistance, transpiration etc.	Tree-type specific parameters
Routing / Discharge	Not explicitly modelled; soil balance only	Triangular weighting function	No routing; only gravity-driven drainage and seepage	Instant flow routing via subbasin connections
Climate Inputs	Precipitation, temperature,	Precipitation, temperature, PET	Precipitation, Tmax, Tmin, Tmean, solar	Precipitation, temperature,

Model Feature	TRAIN	HBV-Light	LWF-Brook90	Raven-HMETS
	radiation, humidity, wind		radiation, vapor pressure, wind	radiation, humidity, wind
Infiltration	Based on HBV conceptual approach	Conceptual; soil moisture dependent	Darcy's Law + macropore flow option	Land-use-based function of topsoil moisture
Soil Water Movement	One-layer model with percolation	Single box with threshold-based recharge	Multi-layer matrix and macropore flow via Richards' Equation	Layer-to-layer percolation based on linear functions
Snowmelt Refreezing	Not explicitly modelled	Included with refreezing coefficient	Not modelled; snowmelt only when temp > threshold	Included (Martel et al. 2017)
Canopy Interception	Simulated via LAI-based retention capacity	Simplified; via monthly crop coefficient	Interception + evaporation based on dynamic LAI and radiation	All intercepted water evaporates instantly
Scenario Capability	Applied in climate and land-use change studies	Used in glacier melt, recharge studies	RCP-ready; used for climate change, species drought risk, forest management	Supports climate scenarios; widely used in impact assessments
Typical Applications	Forest water balance, irrigation planning, droughts,	Runoff modelling, lowland hydrology, glacier melt	Forest drought stress, soil moisture mapping, species-specific water use	Climate impact, forest disturbance, depression storage